An Integrated Methodology for EV-oriented Lithium-ion Battery Rate-of-degradation Modeling and Region-based Control

by

Ruxiu Zhao

A dissertation submitted in partial fulfillment of

the requirements for the degree of

Doctor of Philosophy

(Mechanical Engineering)

at the

UNIVERSITY OF WISCONSIN – MADISON

2018

Abstract

This thesis investigates the physics-based modeling and active control schemes of the lithium-ion battery rate-of-degradation (ROD) for EV applications. An integrated methodology is proposed. It models battery electro-thermal responses during drive cycles, and analyzes different drive cycle current properties' effect on battery ROD during drive cycles. Also, it simplifies the complicated lithium-ion battery ROD model to a reduced-order model suitable to dynamically estimate battery ROD during drive cycles, and develops the active degradation control methodology via controlling the ROD for lithium-ion batteries.

A power-commanded lithium-ion battery electro-thermal model combining a recurrent neural network (RNN) electrical model with a lumped thermal model is developed to model battery electrical-thermal responses. Current properties associated with drive cycles such as current rate, the current RMS value, the presence of regeneration and their interactions with the temperature are experimentally analyzed. A reduced-order battery ROD model without partial differential equations (PDE) with accurate exchange current estimations is developed. Active degradation control schemes during drive cycles via controlling the ROD are developed, incorporating the proposed models and emphasizing on manipulating the aging factors associated with the drive cycle current properties. Trade-off between the degradation reduction and battery performance compromise is addressed and an adjustable ROD-limit boundary is proposed to help achieve better balances. The ROD control system is also integrated with conventional battery state estimation systems to extend the overall battery management system capability.

This research lays a foundation for applying active degradation control based on ROD control for lithium-ion batteries during drive cycles. This work can be valuable for EV applications for extending the battery life while maximizing the battery performance.

Acknowledgement

At the midnight of August 18 in 2008, the moment I stepped off the Van Galder bus in front of the Red Gym, I would never imagine spending the next decade of my life in this city and this university. Funny enough, ten years later, as approaching the end of my days in Madison, I wish I would never have to leave. I will cherish every piece of memory about every moment I have had about Madison. I appreciate every opportunity this city and this university had offered, all the bitter or joyful moments, all the people I met, all the support I had from my friends and teachers, and all the love from my loved ones. Madison will always be my other hometown.

The four-year undergraduate study was not too hard for me, instead, I had the opportunity to broaden my vision in a foreign country, feel the western culture, learn a thing or two, and get to know what I am interested about. After studying Mathematics and Physics for four years, I decided to do something more practical and therefore transitioned to engineering. I felt control was interesting so I just randomly emailed several ME professors and then Prof. Lorenz replied and asked for a meeting. I had no idea of WEMPEC until several weeks after I met with Prof. Lorenz discussing potential graduate study. Until this day, I still think this was unbelievable however I forever will be grateful for this "coincidence" and the turned-out-to-be an incredible journey.

Over all these Ph.D. years, I am particularly thankful to my advisor, Prof. Robert D. Lorenz. Prof. Lorenz has been more than my academic advisor. He is a faithful friend who is willing to help in whatever way he can. He teaches me not only the knowledge of engineering, but also the knowledge of life. In the technical world, he teaches me useful problem-solving skills. In the physical world, he teaches me invaluable lessons on how one socializes with others and deals with all the challenges. His mentality towards the life will be forever inspirational to me.

WEMPEC has been like a big family to me and I would like to express my gratitude to all the faculties, staff members, and the students I have met over these years for all the fun time. Among them, I would like to first thank Prof. Jahns, my co-advisor, who has been extremely

helpful and providing valuable advice for my research and my graduate school life. I also want to thank Prof's. Adamcyzk, Ludois, and Zinn for being on my committee and helping me through the last chapter. Over the years I have made many lifelong friends. Larry Juang was my first mentor leading me into the battery world and has been a wonderful friend to me. I wish the friendship will ever last. Phil Kollemeyer, who taught me so much about hand-on battery works, was another mentor of mine and has been a really good friend as well. Other colleagues who have helped on my research that I should not neglect include Kevin Frankforter, Jacob Dubie, and Ryan Hickey.

I also would like to thank WEMPEC students who share the journey with me over the years and make my Ph.D. life particularly memorable. These include but not limit to: Yuying Shi, Apoorva Athavale, Ruonan Zhou, Cong Deng, Yukai Wang, Kang Wang, Chen-Yen Yu, Wei Xu, He Niu, Le Chang, Mitch Marks, Yujiang Wu, Silong Li, Yingjie Li, Di Han, Yida Yang, Junjian Zhao, Ye Li, Bo Zhu, Jiyao Wang, Wenbo Liu, Jiangyang Liu, Jiejian Dai, and Baoyun Ge.

Friends I made outside of WEMPEC also have been supporting me and they have been always there for me. All the friendship prevented me from the lonely road. I am particularly thankful to Weinan Gong, Yiming Ma, Yixuan Long, Shengzhi He, and Bingming Chen.

Finally, I would like to express my deepest gratitude to my family for their unconditional support, encouragement, and love for all these years. I could not have done this without you.

Madison, WI

2018

Table of Contents

List of Figures

Chapter 1:

Chapter 2:

Chapter 3:

Chapter 4:

Chapter 5:

Chapter 6:

Chapter 7:

Appendix:

List of Tables

Chapter 5:

Chapter 6:

Chapter 7:

Appendix:

xviii

Nomenclature

Symbol	Description
E^a	Activation energy [J]
E^0	Electrode standard potential [V]
F	Faraday's constant 96485.3 $[\frac{C}{mol}]$
I_0	Exchange current [A]
I_{app}	Battery loading current [A]
I_s	Side-reaction current [A]
R	Gas constant 8.314 $[\frac{J}{mol\,K}]$
R_0	Battery series resistance [Ω]
$\dot{Q}$	Battery internal heat generation [W]
α	Charge transfer coefficient [\]
η	Overpotential [V]

Abbreviations

AC	Alternating Current
Ah	Amp-hours
ANCOVA	Analysis of Covariance
ANN	Artificial neural network
BMS	Battery Management System
BPNN	Back-propagated neural network
BV	Butler-Volmer
CC-CV	Constant current – constant voltage
DC	Direct Current
DFS	Deep Feature Selection
DOD	Depth-of-Discharge
ECM	Equivalent circuit model
EIS	Electrochemical Impedance Spectroscopy
EV	Electric vehicle

FF-NN	Feed-forward neural network
GRU	Gated Recurrent Unit
HPPC	Hybrid Pulse Power Characterization
KF	Kalman Filter
LIB	Lithium-ion battery
LPF	Low-pass filter
OCV	Open-circuit voltage
PDE	Partial differential equation
P2D	Pseudo 2D
RMS	Root mean square
RNN	Recurrent neural network
ROD	Rate-of-degradation
SEI	Solid-electrolyte-interphase
SOC	State-of-Charge
SOE	State-of-Energy
SOH	State-of-Health
SOP	State-of-Power
SPM	Single particle model
ΔS	Entropy change

Introduction

This section provides research background and motivation, an overview of the research, a summary of the research contributions, and a chapter-by-chapter list of the content included.

Background and Motivation

Lithium-ion batteries are an improvement in power and energy density compared to lead-acid, nickel-cadmium, and nickel-metal hydride cells. Among various applications, electric vehicles (EV) are one of the domains relying heavily on the Li-ion battery technologies. For the EV application, battery durability has been significantly emphasized and needs improvements.

Conventionally, both statistical and physics-based approaches have been investigated to model and predict lithium-ion battery aging performances pretty well while each has had limitations. The research in modeling lithium-ion battery aging process has led to investigations of degradation control schemes. Passive control schemes focusing on modifying battery materials have been investigated. Meanwhile, active control schemes have been focusing on balancing the temperature distribution and the electrical loading among cells in the battery pack.

The importance of battery rate-of-degradation (ROD) has been recognized in few research studies, and some work has been done to model the rate-of-degradation of batteries during operation. The results have been mostly focusing on optimizing charging trajectories and identifying suitable current rates for a constant-rate discharging process.

As the batteries on an EV undergo much more dynamic operations, an active cell-level degradation control that operates in real-time can be valuable and supplemental to existing technologies for better utilizing the batteries on the vehicle. Since the derivative of the controlled quantity is the starting point of a control system, such an active control requires a real-time battery ROD estimation technique. With the powertrain, drivetrain, and battery pack designs finalized, a smart battery operating strategy such as a region-based control scheme based on the real-time ROD estimation can simultaneously maximize the battery performance and reduce battery degradation.

Research Overview

The goal of this research is to develop methodologies for active degradation control of Li-ion batteries. The integration of different battery models and algorithms of both control and monitoring battery internal states is the fundamental part of this research. As the electic vehicle is the targeted application, the research starts with identifying different drive cycle properties that affect the rate-of-degradation (ROD) of Li-ion batteries. A combination of careful experimental deisgn and statistical analysis is used for evaluating different aging factors associated with less well-understood battery loading profiles, namely the drive cycle. Specifically, current RMS value, regeneration, temperature, and their interactions are evaluated with rigorous analysis.

Both electical and thermal models that are suitable for modeling batteries during drive cycles are developed. Machine learning techniques such as the recurrent neural networks (RNN), gated recurrent units (GRU), and deep feature selection (DFS) are integrated to formulate a compact battery electical model suitable for different drive cycles at different temperatures. A lumped thermal model based on the thermal equivalent circuit is developed for simulating battery dynamic thermal responses.

Moreover, a real-time ROD model of the battery that can dynamically estimate battery ROD during a drive cycle is proposed. The model takes advantages of both physics-based battery degradation modeling and the data-based parameter identification techniques, producing an accurate and computationally efficient model result. The proposed model is also evaluated for different Li-ion batteries and different temperature conditions.

A region-based Li-ion battery degradation control via dynamic ROD manipulations is subsequently proposed taking advantages of the real-time ROD model, which identifies vulnerable operating regions a battery suffers more degradation and then caps the battery with an acceptable level of ROD by limiting the loading current (power). As the region-based degradation control requires several pieces of information on the battery status, previously developed models such as

the electical model and the thermal model are integrated together to form a system. Dynamically controlling the degradation of the battery during drive cycles can then be achieved methologically.

The research also considers practical issues such as the implementation limitations. A temperature-dependent adjusting ROD threshold is proposed in order to achieve better balance between the degradation reduction and the battery output performance limitation. Such a dynamic threshold is established considering different driving scenarios such as highway and city drives, as well as different ambient temperature conditions. In addition, another impelementation issue regarding the integration capability of the proposed ROD control algorithm with the more conventional battery state estimation algorithms is invesitgated. An interactive algorithm system combining the ROD control algorithm with both SOC and SOP estimation algorithms is developed and evaluated through the simulation.

Research Contributions

The primary contribution of this research is an integrated methodology that controls battery degradation over dynamic drive cycles by manipulating the ROD. The proposed methodology lays a foundation for designing systems to dynamically control the degradation of EV batteries during driving, improving the durability of the EV batteries.

This research establishes the importance of the ROD variable for the batteries, develops and evaluates a reduced-order rate-of-degradation model for lithium-ion batteries. Such model is constructed with a physics-based approach, incorporating the electrochemical processes and the battery aging mechanism such as the solid-electrolyte-interphase (SEI) layer growth. This work simplifies the complex battery electrochemical model to meet the fast computation requirement for potential real-time implementation.

Moreover, the proposed reduced-order rate-of-degradation model has the capability for controls. Potential candidate control variables are identified, which can be manipulated to dynamically change the ROD of the batteries. A ROD-optimized battery current (power) shielding

control method is developed which, during a drive cycle, dynamically identifies "violations" of battery ROD bounds, and shields the current and power load of the battery to conform to these limits. The ROD control law is evaluated via aging experiments and shown to effectively reduce battery degradation during drive cycles.

This work also acknowledges the trade-offs between the degradation reduction from ROD control and the battery performance compromises. Analysis on the trade-off under different driving scenarios and temperature conditions is conducted. Potential ROD limit adjustments based on operating conditions are proposed to achieve more desirable and practical balance between the two parties in the trade-off.

Furthermore, the integration of the ROD control algorithms with the conventional battery state estimation algorithms is investigated. An integrated algorithm system is proposed to combine different algorithms together. The resulting system has an interactive nature and can extend ROD/SOC/SOP monitoring and control capabilities to a wide range of operating conditions.

In addition, this research extends previous analyses of battery aging factors, and investigates the aging effects of properties that are "unique" to drive cycles such as the current RMS value, the existence of regeneration, as well as their interactions with the temperature. An effective factorial design of experiment and a rigorous statistical analysis procedure are developed and utilized to analyze the effects of the interested factors on battery aging.

Finally, this work addresses the lack of suitable battery electro-thermal modeling for drive cycle simulations. A power-commanded electro-thermal battery model is developed and evaluated to effectively simulate battery electrical and thermal responses during drive cycles, extended from conventional current-commanded battery models. Machine learning techniques such as recurrent neural networks (RNN) are incorporated to support the modeling of the relevant battery nonlinear electrical processes, while a lumped battery thermal model is cross-coupled with the electrical model.

Summary of Chapters

Chapter 1 reviews the state-of-the-art of modern lithium-ion battery technologies. Li-ion battery electrochemistry is first reviewed. Then, both electrical and thermal modeling are discussed. Li-ion battery internal state estimation techniques are reviewed as well. In addition, topics regarding li-ion battery degradation including aging mechanisms, aging modeling, and both passive and active degradation control schemes are covered.

Chapter 2 discusses the development of a battery electro-thermal model for drive cycle simulations, incorporating RNN electrical model using with a lumped battery thermal model.

Chapter 3 investigates the aging effects of factors associated with drive cycles. A factorial design of experiment and a rigorous statistical analysis procedure are proposed to evaluate these factors. Both individual effects and interaction effects are analyzed.

Chapter 4 focuses on the development of a reduced-order battery ROD model. The resulting model can estimate battery ROD in real-time with the capability for active ROD control.

Chapter 5 proposes an active ROD control method via dynamic battery current (power) shielding. An integrated active ROD control methodology is then developed to enable battery degradation reduction of the lithium-ion batteries during drive cycles.

Chapter 6 analyzes the trade-off between battery degradation control and performance compromises. An adjustable ROD-limit boundary selection procedure is proposed to help achieve better balance between the control and the performance limitation at different conditions.

Chapter 7 proposes an integrated system combining ROD control algorithms with state estimation algorithms. It enhances battery managing capability over a wide operating range.

Chapter 8 presents the conclusions, contributions, and suggested future work.

Chapter 1 State-of-the-Art Review

1.1   Battery Introduction

One of the critical challenges today is to secure an energy supply that is sustainable and inexpensive. An energy storage system (ESS) is a critical piece for most methods intending to reduce or eliminate the need for fossil fuel consumption; examples include hybrid/electric vehicles, fuel cell technology, and biofuel synthesis. Of all the various technologies utilized for energy storage, perhaps the most ubiquitous is the battery. A battery is said to store energy electrochemically [2], by utilizing faradaic reactions in which electrons are either taken from or donated to a host atom, changing its oxidation state.

In general, batteries can be categorized as either primary or secondary. Primary batteries are non-rechargeable and are commonly found in consumer electronic products. Common primary batteries include zinc-carbon, zinc-alkaline-MnO_2, zinc-air, and lithium batteries. Secondary batteries are distinguished by their ability to recharge. Examples include lead-acid, Nickel-Cadmium (NiCd), Nickel-Metal Hydride (NiMH), and Lithium-ion (Li-ion) batteries. For vehicular applications, secondary batteries are the preferred candidates for a power source or load-leveling devices. The energy density and power density, as well as cost, are crucial factors for determining their suitability for an application [1].

Many commercial secondary batteries are manufactured as a series of cells packaged in a container [3]. A cell is defined as the primary electrochemical unit, while a battery is defined as two or more cells connected in series or parallel configurations to achieve specified operating voltage or current ratings. Since this configuration does not provide access to the internal anode and cathode terminals of each cell in the series string, it is difficult to determine much about the electrochemical status of individual cells from the available battery terminal measurements of voltage and current.

An electrochemical cell most likely contains the following essential components: anode, cathode, electrolyte, and separator [2]. An electrode can be thought of as the interface between an electrically conducting phase and an ionic conducting phase, through which charge is transferred during operation. Electrodes are classified as either a cathode or an anode. In electrochemical processes, an anode is an electrode where the oxidation reaction occurs, meaning that it releases electrons to the external circuit. A cathode is correspondingly the location where the reduction occurs, collecting the electrons from the anode through the external circuit. For a battery cell, the positive electrode is a cathode during discharge and an anode during charge, while the negative electrode is an anode during discharge and a cathode during charge. In the literature, however, the convention is to adopt the terminal name designations that are appropriate during the discharge operation. The electrolyte is the medium that conducts the ions between the cathode and anode of a cell. A separator is electrically insulating, yet permeable to ions, preventing the two electrodes from shorting together.

1.2   Comparison of Li-ion Cells to Other Secondary Batteries

Li-ion batteries are an improvement in power and energy density compared to lead- acid, nickel cadmium, and nickel metal hydride cells. They offer a higher cell voltage than any of the other technologies as well, with a nominal voltage of 3.7V. Fig. 1.1 shows the increased energy density of Li-ion cells over previous technologies regarding both weight and volume.
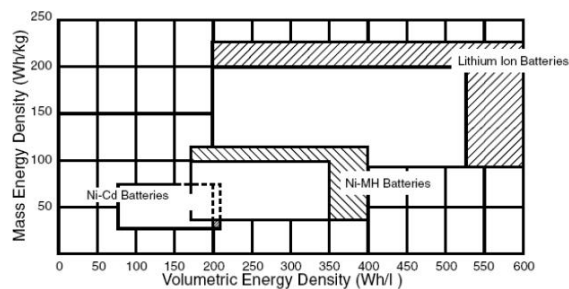
Fig. 1.1: Comparison of energy density in modern secondary batteries [4]

The increased energy density allows for extended operating times in modern digital products, such as cellular phones and laptops. It also allows for more efficient hybrid and electric vehicles, since the weight of a high-energy and high-power battery pack is much lower than what would be possible using previous technologies. In this thesis, Lithium-ion batteries are the primary research focus.

1.3 Lithium-ion Battery Chemistries

Since Lithium-ion batteries have become the most popular type of electrical power supply in today's electronic devices, as well as in electric vehicle applications, it is essential to understand and characterize the physics and electrochemistry in these cells.

Terminology

Battery technology includes some terms that are unique, and it is helpful to explain some of the most common terms here for those who may not be familiar with them.

Amp-hours (Ah) or milliamp-hours (mAh) – This unit is used as a measure of the amount of electric charge transferred into or out of a cell.

C or C-rate – The current corresponding to the manufacturer specified cell capacity. A cell with a 2Ah capacity would have a C-rate of 2A. This is often used as a basis for defining current.

Capacity – Battery capacity is most often specified in Ahs. For example, a 18650 Lithium-ion battery may be specified as 3.7V, 2.9Ah. This means the battery can source 2.9A for 1 hour if it is fully charged. The actual capacity of a cell may vary from the manufacturer's specified value and will decrease with time and cycling.

Cycle – Typically, a complete discharge and a complete charge are called "one cycle".

State-of-Charge (SOC) – An estimation of the amount of charge remaining in the cell.

It is expressed as a percent of the cell's capacity, where 100% is a fully charged cell.

1.3.1   Lithium-ion Battery Structure and Electrode Material

Lithium-ion batteries are characterized by the chemistry of lithium-ion flow. One Lithium-ion cell usually consists of the following components: two current collectors that conduct electrons; positive and negative electrodes, where two half-reactions happen; electrolyte as the medium for lithium-ion transfer; a permeable membrane separator in between to prevent short circuits; and the solid-electrolyte-interphase (SEI) formed between the electrolyte and the anode material. Typically, lithium ions (Li^+) transfer from the anode to the cathode during discharge, and back to the anode during charging. The cathode material of Lithium-ion batteries commonly is composed of Li_xMO_y, where M can be Nickel, Manganese, Cobalt, or their mixtures [5]. On the other hand, the anode material commonly is graphite or other carbonaceous materials. Lithium ions are intercalated in the graphite structure during charging and are released during discharge in a highly reversible process [5]. A typical Lithium-ion cell structure and its intercalation process, characterized by Li^+ ion insertion or de-insertion at the carbon anode, are shown in Fig. 1.2 and Fig. 1.3.
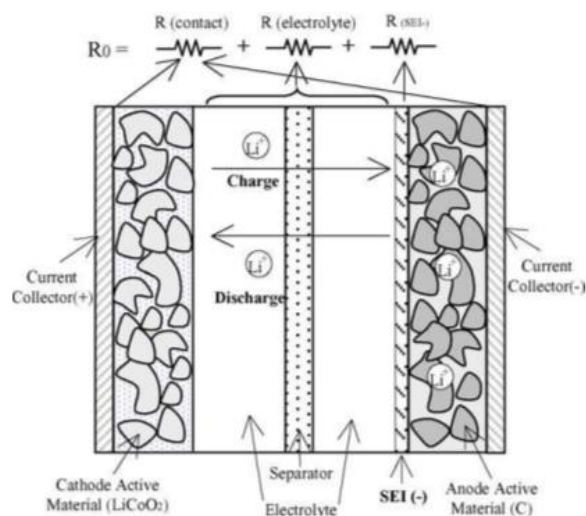
Fig. 1.2: Conceptual diagram of a Li-ion cell [6]
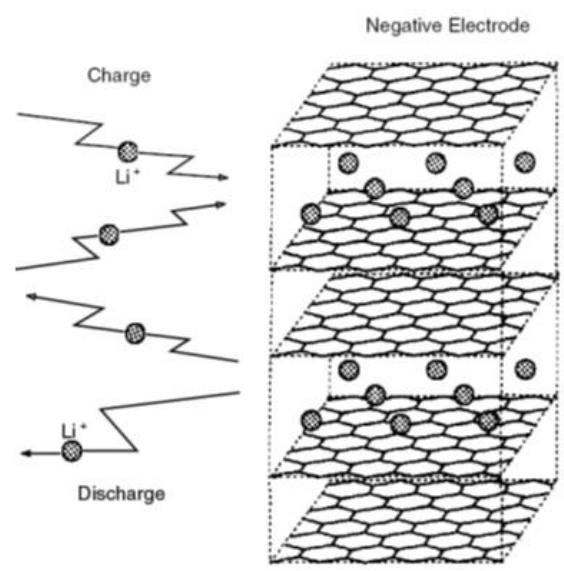
Fig. 1.3: Carbon planes in anode allow Li+ ions to intercalate between them [7]

Lithium-ion cells for commercial purposes can be in a cylindrical or prismatic package for higher capacity, with a pressure release valve built in for safety concerns. Another option is to stack electrodes, separators, and seal inside a thin plastic laminated foil. This type of cell is called a pouch cell. Examples of different packaging are shown below in Fig. 1.4.

(a) Cylindrical Cell   (b) Prismatic Cell
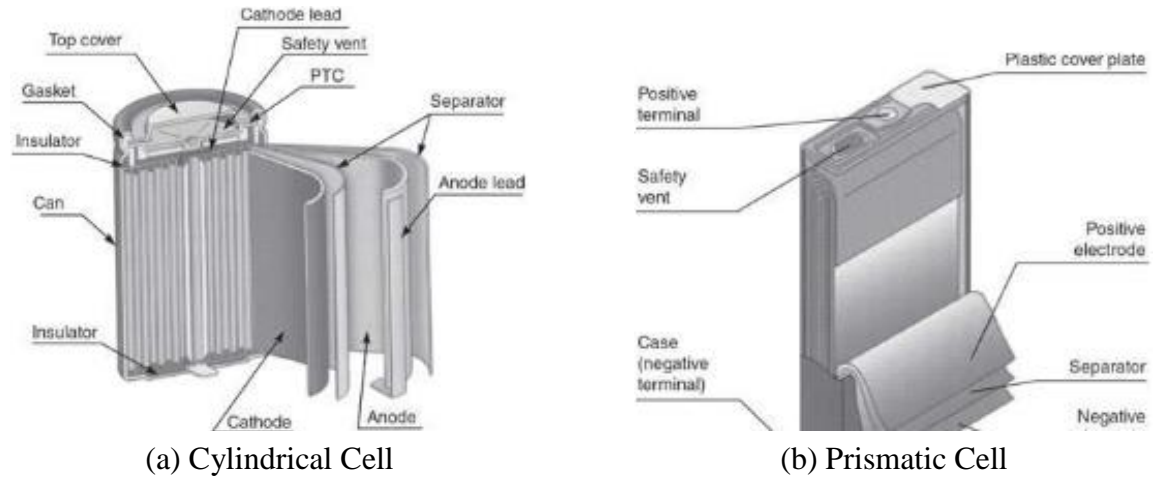
(c) Pouch Cell

Fig. 1.4: Examples of common battery packaging. From [8].

Typically for a Lithium-ion cell, the two half-reactions are described as the following, where "Me" is short for "Metal" and can be different for different types of Lithium-ion batteries.

Cathode: $LiMeO_2 \leftrightarrow Li_xMeO_2 + (1 - x)\ Li^+ + (1 - x)\ e^-$

Anode: $(1-x)Li^+ + (1-x)e^- + C \leftrightarrow Li_{1-x}C$
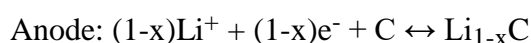
1.3.2   Electrochemical Process in Lithium-ion Cells

Since potential is an important electrochemical variable in the batteries, exploring the physical meaning of this variable in detail is needed. Several electrochemical mechanisms in Lithium-ion cells explained below are established by potential difference.

1.3.3.1 Thermodynamics and Nernst's Equation

Thermodynamics, strictly speaking, encompass only systems at equilibrium [9]. Therefore, it is a prerequisite for the system to have reversibility. A system is said to be thermodynamically reversible if an infinitesimal reversal in a driving force causes direction reversal. Similarly, a chemically reversible system describes a system that reverses its direction of reaction when reversing the DC current polarity. A chemically irreversible system cannot be thermodynamically reversible, while a chemically reversible one may or may not be thermodynamically reversible [9].

In a thermodynamically reversible system, as a Lithium-ion cell, Nernst's equation describes the connection between electrode potential, E, and the concentrations of participants in

the electrode process.

$$E = E^0 + \frac{RT}{nF}\ln\frac{C_O}{C_R} \tag{1.1}$$

E is the electrode potential in [V], E^0 is the standard potential of the electrode in [V]. R is the universal gas constant of 8.314 in $[\frac{J}{mol\ K}]$, T is the temperature in [K], n is the stoichiometric number of electrons in the reaction, F is the Faraday constant of 96485.337 in $[\frac{C}{mol}]$, C_O is the concentration of the oxidant in $[\frac{mol}{cm^{-3}}]$, and C_R is the concentration of the oxidant in $[\frac{mol}{cm^{-3}}]$. The electrode process is described in ((1.2) below, where O is the oxidant and R is the reductant.

$$O + ne \leftrightarrow R \tag{1.2}$$

Now, the potential of a Lithium-ion cell or a cell in general, with the two electrodes and electrolyte, is:

$$E_{cell} = E_{cathode} - E_{anode} \tag{1.3}$$

Table 1.1, shown below, tabulates various standard electrode potentials of interest.

1.3.3.2 Electrode Kinetic Overpotential and the Butler-Volmer Equation

For a battery cell, electrode reactions are characterized by interfacial charge-transfer dynamics, and the reaction rate is a function of potential [9]. To quantitatively relate the electrode kinetics observations with electrode potential and concentration, it is necessary to establish a potential dependent law for such a phenomenon.

In the theory of interfacial kinetics, mass transfer is considered not a limiting factor, meaning there is a low current and an efficiently stirred electrolyte [9]. In 1905, Tafel showed an exponential relationship between the current and the overpotential in the following form known as the Tafel equation:

$$\eta = a + b \log(i) \tag{1.4}$$

This equation has frequently been the valid basis for successful models of electrode dynamics.

Table 1.1: Standard electrode potentials for various reactions of interest [87]

Reaction (Roman numeral superscript indicates oxidation state)	Standard Potential (V) vs. H_2/H^+	Remarks
$F_2 + 2e^- \leftrightarrow 2F^-$	+2.87	Strongly Oxidizing
$Co^{3+} + e^- \leftrightarrow Co^{2+}$	+1.81	
$Pb^{IV}O_2 + 4H^+ + SO_4^{2-} + 2e^- \leftrightarrow Pb^{II}SO_4 + 2H_2O$	+1.69	Lead-Acid Battery Positive Electrode [5]
$Pb^{4+} + 2e^- \leftrightarrow Pb^{2+}$	+1.67	
$2HOCl^I + 2H^+ + 2e^- \leftrightarrow Cl_2 + 2H_2O$	+1.63	Water disinfection with Chlorine (a)
$Mn^{3+} + e^- \leftrightarrow Mn^{2+}$	+1.51	
$Cl_2 + 2e^- \leftrightarrow 2Cl^-$	+1.36	Water disinfection with Chlorine (b)
$O_2 + 4H^+ + 4e^- \leftrightarrow 2H_2O$	+1.23	Acidic (pH 0) Water Oxidation
$Mn^{IV}O_2 + 4H^+ + 2e^- \leftrightarrow Mn^{2+} + 2H_2O$	+1.23	Production of Electrolytic MnO_2
$Hg_2^{2+} + 2e^- \leftrightarrow Hg^0$	+0.79	
$Fe^{3+} + e^- \leftrightarrow Fe^{2+}$	+0.77	
$Hg_2SO_4 + 2e^- \leftrightarrow 2Hg^0 + SO_4^{2-}$	+0.62	Mercury Sulfate Reference Electrode
$Ni^{III}OOH + H_2O + e^- \leftrightarrow Ni^{II}(OH)_2 + OH^-$	+0.49	Positive Electrode for Nickel-Metal Hydride and Nickel-Cadmium Batteries
$O_2 + 2H_2O + 4e^- \leftrightarrow 4OH^-$	+0.40	Alkaline (pH 14) Water Oxidation
$Hg_2Cl_2 + 2e^- \leftrightarrow 2Hg^0 + 2Cl^-$	+0.27	Saturated Calomel Reference Electrode
$Ag^ICl + e^- \leftrightarrow Ag^0 + Cl^-$	+0.22	Silver-Chloride Reference Electrode
$Ti^{4+} + e^- \leftrightarrow Ti^{3+}$	0.00	
$2H^+ + 2e^- \leftrightarrow H_2$	±0	Reference, Acidic Water Reduction
$Fe^{3+} + 3e^- \leftrightarrow Fe^0$	-0.04	
$Pb^{2+} + 2e^- \leftrightarrow Pb^0$	-0.13	
$Ni^{2+} + 2e^- \leftrightarrow Ni^0$	-0.23	
$Co^{2+} + 2e^- \leftrightarrow Co^0$	-0.28	
$Pb^{II}SO_4 + 2e^- \leftrightarrow Pb^0 + SO_4^{2-}$	-0.36	Lead-Acid Battery Negative Electrode
$Ti^{3+} + e^- \leftrightarrow Ti^{2+}$	-0.37	
$Cd^{2+} + 2e^- \leftrightarrow Cd^0$	-0.40	
$Cr^{3+} + e^- \leftrightarrow Cr^{2+}$	-0.41	
$Fe^{2+} + 2e^- \leftrightarrow Fe^0$	-0.44	
$Zn^{2+} + 2e^- \leftrightarrow Zn^0$	-0.76	
$Cd^{II}(OH)_2 + 2e^- \leftrightarrow Cd^0 + 2OH^-$	-0.81	Nickel-Cadmium Battery Negative Electrode
$M + H_2O + e^- \leftrightarrow MH + OH^-$	-0.83	Nickel-Metal Hydride Battery Negative Electrode [5]
$2H_2O + 2e^- \leftrightarrow H_2 + 2OH^-$	-0.83	Alkaline (pH 14) Water Reduction
$Cr^{2+} + 2e^- \leftrightarrow Cr^0$	-0.91	
$Mn^{2+} + 2e^- \leftrightarrow Mn^0$	-1.17	
$Ti^{2+} + 2e^- \leftrightarrow Ti^0$	-1.63	
$Al^{3+} + 3e^- \leftrightarrow Cd^0$	-1.66	
$Mg^{2+} + 2e^- \leftrightarrow Mg^0$	-2.36	
$Na^+ + e^- \leftrightarrow Na^0$	-2.71	
$Ca^{2+} + 2e^- \leftrightarrow Ca^0$	-2.87	
$K^+ + e^- \leftrightarrow K^0$	-2.93	
$Li^+ + e^- \leftrightarrow Li^0$	-3.05	Strongly Reducing

To better associate with the reversibility of electrode process, an advanced equation describing the electrode kinetics was discovered and named after John Alfred Valentine Butler and Max Volmer [10][11]. The known Butler-Volmer equation, in equilibrium conditions, is:

$$i = i_0[\exp(-\alpha\frac{\eta F}{RT}) - \exp((1-\alpha)\frac{\eta F}{RT})] \tag{1.5}$$

i_0 is called the exchange current, which is the limiting current when the oxidation and reduction reach equilibrium. η is called the overpotential, which drives the current and thus battery dynamics. α is the charge transfer coefficient. As a dimensionless parameter between zero and one, it measures the symmetry of the oxidation and reduction reactions. When $\alpha = 0.5$, these two reactions are symmetric.

Exchange current and charge transfer coefficients, as the two critical parameters in Butler-Volmer equation, show their effects on the plots that describe the relationship between terminal

current and overpotential. Fig. 1.5 shows the effect of the exchange current on the Butler-Volmer equation, while Fig. 1.6 shows the effect of the charge transfer coefficient [9].
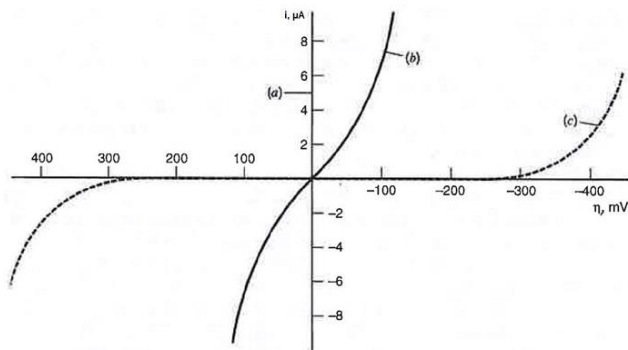
Fig. 1.5: BV equation with diff. exchange currents (α=0.5, 298K). (a)1mA, (b)1μA, (c)1nA
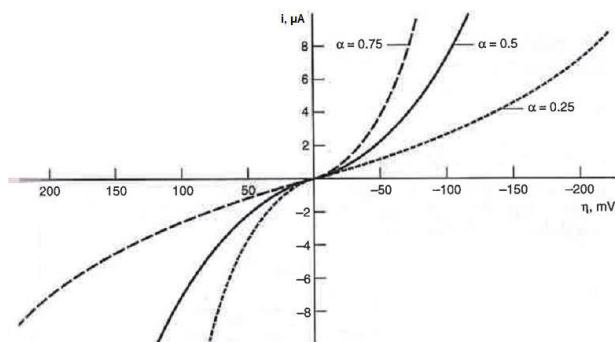
Fig. 1.6: Butler-Volmer equation with diff. transfer coefficients (1μA, 298K)[9]

It is noted that the Butler-Volmer equation describes the steady-state behavior of the electrode. If the battery is not in steady-state, the voltage across the electrodes is also governed by the transient response of the double-layer capacitance. Such phenomenon refers to a charge separation that occurs at the interface between the electrode and the electrolyte, where the electrode surface attracts ions of the opposite sign as in the electrolyte [1].

1.3.3.3 Mass Transfer of Ions

Mass transfer describes the movement of ions in the solution from one location to the other. It usually is considered in three types of modes.

1. Migration - Movement of charged species caused by potential gradients in a bulk solution.

2. Diffusion - Movement of species caused by concentration gradients.

3. Convection - Stirring of the hydrodynamic transport.

For linear mass transfer, the Nernst-Planck equation describes the mass transfer in an electrode as the following, where each term describes one of the three modes:

$$J_i(x) = -D_i \frac{\partial C_i(x)}{\partial x} - \frac{z_i F}{RT} D_i C_i \frac{\partial \varphi(x)}{\partial x} + C_i v(x) \tag{1.6}$$

$J_i(x)$ is the flux of species I in at a distance x from the surface. D_i is the diffusivity in $[\frac{cm^2}{s}]$. $\frac{\partial C_i}{\partial x}$ is the concentration gradient at x, and $\frac{\partial \varphi(x)}{\partial x}$ is the electric potential gradient at x. z_i is the charge of the species, and C_i is the concentration of the species. $v(x)$ is the velocity $[\frac{cm}{s}]$ of the element.

If the electrolyte is assumed to be plentiful and the stirring at the electrode is assumed to be inefficient, ((1.6) reduces to only the second term, which is the diffusion term. Therefore, the rate of mass transfer is proportional to the diffusion term. Suppose at $x \geq \delta_0$, the concentration of the species is the same as the bulk solution concentration, C_i^*. In this case, the species concentration profile is described below in Fig. 1.7, based on a linear concentration gradient.
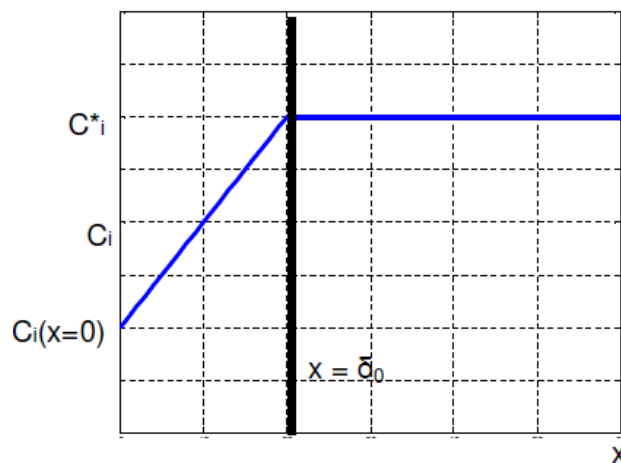
Fig. 1.7: Example species concentration profile (diffusion only)

In this case, the current is related to the concentration profile as:

$$\frac{i}{nFA} = m_i(C_i{}^* - C_i(x=0)) \tag{1.7}$$

A is the surface area of the electrode in [cm^2], and m_i is the mass transfer coefficient in $[\frac{cm}{s}]$. $\frac{i}{nFA}$ has the unit $[\frac{mol}{s\ cm^2}]$, which is the unit of the reaction rate. It is also clear that the maximum mass transfer rate occurs at the position x=0, and the current reaches the limited value.

When considering the diffusion effect into the Butler-Volmer equation, a more realistic version of it can be deducted, which considers the ion concentration at the interface between the electrode and the electrolyte of both the cathode and the anode.

$$i = i_0[\frac{C_O(x=0)}{C_O{}^*}exp(-\alpha\frac{\eta F}{RT}) - \frac{C_R(x=0)}{C_R{}^*}exp((1-\alpha)\frac{\eta F}{RT})] \tag{1.8}$$

In ((1.8), O and R represent oxidation and reduction.

1.4 Lithium-ion Battery Electrical Modeling

This section discusses several types of approaches in the literature modeling lithium-ion battery electrical responses. When such model is intended for online, vehicular applications, it is needed to be computationally manageable for onboard computing. Alternatively, for applications associated with battery material development or manufacturing, much more complicated models are needed to include the various physical aspects of the battery.

For these two application domains, two general categories of lithium-ion battery electrical models are listed:

1. Electrical equivalent circuit models: a category of less-complex models that captures the relationship between battery terminal voltage and current via the electrical circuit network.

2. Physics-based model: a set of complex models trying to reconstruct the physical structure of the battery and simulate the electrochemical process inside the battery.

1.4.1 Battery Electrical Equivalent Circuit

Several different equivalent circuits have been developed to describe the electrical response of a lithium-ion cell. The different components within an equivalent circuit related to different physical aspects of the cell, including the electrode impedance, electrolyte impedance, solid-state diffusion, and charge transfer process. Both a full-order equivalent circuit and reduced-order equivalent circuits have been proposed in the literature and utilized widely in different applications. Detailed explanations and illustrations of the equivalent circuit models could be found in [12] -[16]. These models applied to most lithium-ion cells because they had the same basic components.

In the full-order equivalent circuit model, different physical aspects of a lithium-ion cell have been represented by different electrical components as shown in Fig. 1.8.
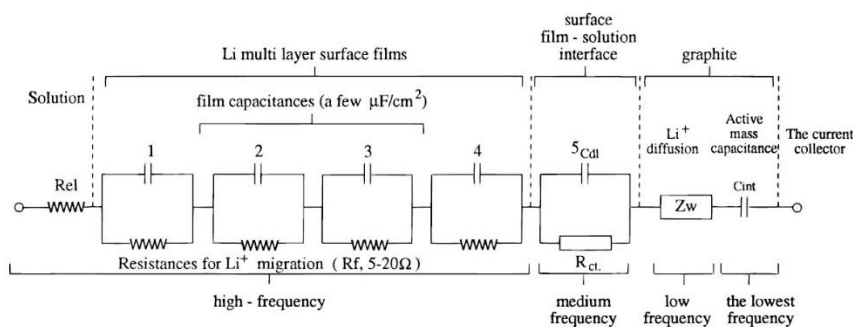
Fig. 1.8: Full-order electrical equivalent circuit for a lithium-ion cell

The electrolyte solution had a relatively constant resistance, R_{el} , which increased slightly, when the electrolyte was consumed during undesired side reactions [12]. At high frequencies, at or above several kilohertz, the electrical response of the cell has been dominated by inductive effects. This impedance has been usually neglected because it has been found to contain no useful data about the cell and might not be included in equivalent circuit models. At lower frequencies, SEI resistance and capacitance dominated [12]. Since the SEI layer separated the positive Li+ ions from the negatively charged solution ions and appears to be a double-layer capacitor, a parallel RC component have been used to model the combined effect of SEI resistance and capacitance. At

medium frequency, another parallel RC component have been used to model the slower charge transfer process occurring at the interface between the SEI and the graphite anode [86]. At low frequencies, a Warburg impedance element has been used to represent the Li+ ions diffusion in the graphite [12][13].

Fig. 1.8 shows all the elements described above except the inductance due to its insignificance in understanding cell behavior. This full-order equivalent circuit offered the most effective and direct representation relating to the physical process in the lithium-ion cell [13]. It included all the impedances that a Li^+ ion would have encountered as it moved through the cell.

Moreover, to simplify the electrical equivalent circuit model, reduced-order models that capture the most noteworthy features have been proposed [18]. Fig. 1.9 below shows a simplified equivalent circuit, where L represents the inductance, R_E represents solution resistance, $Z_{electrode}$ and parallel RC components represent the combination of the charge-transfer resistance, double layer capacitance, and Warburg impedance.
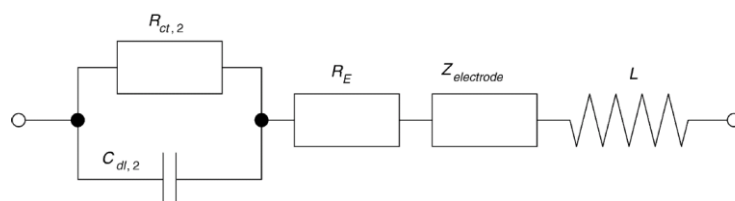
Fig. 1.9: Reduced-order electrical equivalent circuit for a lithium-ion cell [18]

The above reduced-order model can be further simplified to Fig. 1.10 below, where the parallel RC component combines the effects of all the RC parallel combinations in the full model and R_Ω includes the resistance of the electrolyte, current collectors, battery terminals and internal connections. Also, the inductance has been neglected for its mere effect as ultra-high frequencies.

A different equivalent circuit approach was introduced in [17], and the equivalent circuitry is shown in Fig. 1.11. In this model, it adopted the idea of the previous approaches that separated the network into different elements. The most significant difference was that the linear RC component representing charge transfer process was replaced by a nonlinear component. "LPF"

represents "low-pass filter" and $V_{ct}(i)$ is the steady-state response of the charge transfer process following the inversion of the Butler-Volmer equation. (1.9) shows the modeling equation for this nonlinear component, where b_1 and a_1 are parameters for the low-pass filter and I_0 is the exchange current parameter, predetermined by experiments.
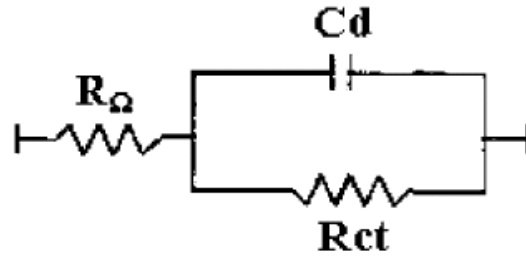
Fig. 1.10: Minimal-order equivalent circuit [19]

This model recognized that the characteristics of the voltage drop due to charge transfer has been nonlinear with respect to the current, while the traditional equivalent circuits inherited linearity between the charge transfer voltage drop and the current. Under the assumption of reaction symmetry, the Butler-Volmer equation could be inverted to the form calculating the overpotential using the current as the input. The overpotential calculated was the steady-state response of the charge transfer voltage drop.

$$LPF(V_{ct}(I)) = \frac{b_1}{1 + a_1 q^{-1}} \sinh^{-1}(\frac{I}{2I_0}) \qquad (1.9)$$

This model has been shown to have better performance for large current and/or low-temperature conditions, where the traditional RC components have been shown to suffer inaccuracy. This improvement was especially beneficial for battery state estimation areas, which will be further discussed in later sections.
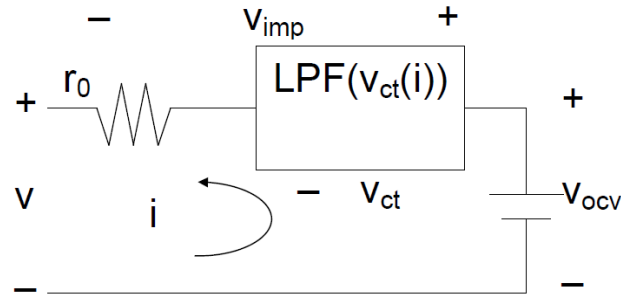
Fig. 1.11: Nonlinear battery model incorporating Butler-Volmer electrode equation

Overall, equivalent circuit models have been formulated in different ways. However, they all shared similar background knowledge that such models have been using different electrical circuit components to represent different physical domains of the battery cell. Such models have been widely utilized in electric vehicle applications for its simplicity and onboard implementation suitability.

1.4.2   Physics-based Model Developed by Doyle et.al

The Newman model considered the cell structure in Fig. 1.12 and was based on the galvanostatic charging and discharging behavior.
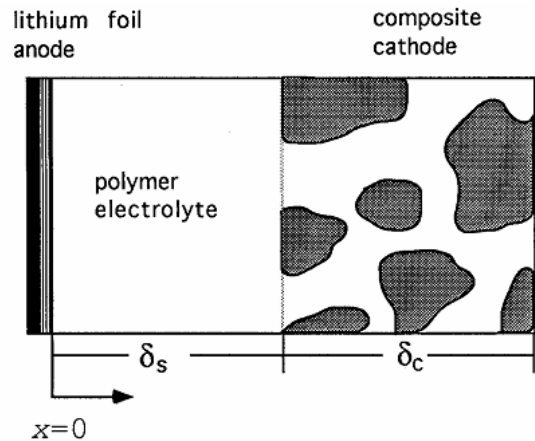
Fig. 1.12: One-dimensional lithium cell structure in Newman model [22]

A list of the symbols, subscripts, and superscripts from [22] is introduced in the following table.

Table 1.2: List of symbols, subscripts, and superscripts used in Newman Model

Symbol	Interpretation	Unit
a	specific interfacial area	m^{-1}
c	the concentration of the electrolyte	$\frac{mol}{m^3}$
c_0	the concentration of polymer solvent	$\frac{mol}{m^3}$
c_i	the concentration of species i	$\frac{mol}{m^3}$
c_T	maximum concentration in solid	$\frac{mol}{m^3}$
c_s	concentration in solid	$\frac{mol}{m^3}$
c_{max}	maximum concentration in polymer	$\frac{mol}{m^3}$
c^0	initial concentration in the polymer	$\frac{mol}{m^3}$
D, D_s	the diffusion coefficient of electrolyte in the polymer and of lithium in the solid matrix	$\frac{m^2}{s}$
f	activity coefficient	/
F	Faraday's constant = 96487	$\frac{C}{eq}$
i	the current density	$\frac{A}{m^2}$
i_0	exchange current density	$\frac{A}{m^2}$
I	superficial current density	$\frac{A}{m^2}$
j_n	pore wall flux of lithium ions	$\frac{mol}{s\ m^2}$
k_2	the reaction rate constant at cathode/polymer interface	$\frac{m^4}{mol\ s}$
k_{a1}	the anodic reaction rate constant	$\frac{m^3}{s}$

k_{c1}	the cathodic reaction rate constant	$\dfrac{m^3}{s}$
K_{i_j}	the frictional coefficient	$\dfrac{J\ s}{m^5}$
n	number of electrons transferred in the electrode reaction	/
N_i	molar flux in x direction of species i	$\dfrac{mol}{s\ m^2}$
r	distance normal to the surface of the cathode material	m
R	universal gas constant = 8.3143	$\dfrac{J}{mol\ K}$
R_s	the radius of cathode material	m
s_i	the stochiometric coefficient of species i in the electrode reaction	/
t	time	s
$t^{0,i}$	transference number (fraction of total electric current that anions and cations carry in passing through an electrolytic solution) of species i	/
T	temperature	K
u	utilization of intercalation material	/
U	open-circuit potential	V
v_i	the velocity of species i	$\dfrac{m}{s}$
x	distance from the anode	m
z_i	charge number of species i	/
α	transfer coefficient between 0 to 1, as in the Butler-Volmer equation	/
β	activity coefficient correction	/
δ	dimensionless current density	/
δ_s	thickness of the separator	m
δ_c	the thickness of the composite cathode	m
ε	the porosity of the electrode	/
ζ	activity coefficient correction	s
η	the surface potential	V
Θ_p	site concentration in the polymer	/
Θ_s	site concentration in solid matrix	/

κ	the conductivity of the electrolyte	$\dfrac{S}{m}$
ν	dimensionless exchange current density	/
ν_+, ν_-	number of cations and anions into which a mole of electrolyte dissociates	/
σ	the conductivity of the solid matrix	$\dfrac{J}{mol}$
τ	dimensionless time	/
υ_i	electrochemical potential of species i	V
Φ	electrical potential	V
Subscript	**Interpretation**	
c	the cathode	
r	the reference state	
s	solid state	
T	maximum concentration in intercalation material	
1	the solid matrix	
2	solution phase	
Superscript	**Interpretation**	
0	solvent, or initial condition	
θ	the standard cell potential	

In the model presented in [22], it was noted that secondary mechanisms such as film formation and volume change were not included. Therefore, this original physics-based model was not used to evaluate aging characteristics of a battery cell. However, this model has served as a foundation to developing physics-based equations that could model the primary reactions of the electrochemical process inside a battery. Many equations presented in [22] have been consistently used later for developing physics-based models of specific batteries for specific applications, as well as for developing battery degradation models.

In [22], at the lithium anode, which has been replaced by graphite in modern batteries, x was set to be 0 and the charge transfer reaction, i.e., primary reaction, followed the Butler-Volmer equation and was summarized in (1.10).

$$i = i_{01}[\exp(-\alpha_{a1}\frac{\eta_{s1}F}{RT}) - \exp(\alpha_{c1}\frac{\eta_{s1}F}{RT})]$$

$$\eta_{s1} = \Phi_1 - \Phi_2 - U_1 \qquad (1.10)$$

$$i_{01} = F(k_{a1})^{\alpha c1}(k_{c1})^{\alpha a1}(c - c_{max})^{\alpha c1}(c)^{\alpha a1}$$

In addition, the flux and concentration of flowing species and the potential at the boundary were assumed to be continuous. Since the composite cathode included both the solid active particles, and the polymer/salt electrolyte and the fraction of each component was assumed as known, the two phases were assumed as superimposed, and the material balance of the lithium on the cathode was described with the following partial differential equation in (1.11).

$$\varepsilon\frac{\partial c}{\partial t} = \nabla(\varepsilon D(c)\nabla c) - \frac{i_2 \nabla t_+^0(c)}{z_+ v_+ F} + \frac{aj_n(1 - t_+^0)}{v_+}$$

$$aj_n = \frac{-s_i}{nF}\nabla i_2 \qquad (1.11)$$

j_n in (1.11) is the pore wall flux of lithium ions across the interface.

Moreover, due to the composite nature of the cathode, the consequent length of the ions' traveling length required modification. The coefficients for modification were assumed as known and shown in (1.12).

$$k_{eff} = k\varepsilon^{1.5} ; D_{eff} = D\varepsilon^{1.5} \qquad (1.12)$$

Furthermore, assuming the active cathode particles were spherical geometrically, and the transport of the lithium was only in the form of diffusion, the material balance partial differential equation has been described as in (1.13).

$$\frac{\partial c_s}{\partial t} = D_s[\frac{\partial^2 c_s}{\partial r^2} + \frac{2\partial c_s}{r \ \partial r}] \qquad (1.13)$$

In (1.13), r is the direction normal to the spherical surface. When considering the (de)insertion process in the cathode, kinetic expressions based on the Butler-Volmer equation is the following.

$$i = Fk_2(c_{max}\text{-}c)^{\alpha c}c^{\alpha a}[c_s exp(\frac{\alpha_a F}{RT}(\eta\text{-}U)) - (c_T - c_s)exp(\frac{\alpha_c \eta_{s1} F}{RT}(\eta\text{-}U))]$$

$$\eta = \Phi_1{}^\theta - \Phi_2{}^\theta \qquad\qquad (1.14)$$

$$U = U_2{}^\theta - U_{ref}{}^\theta + \frac{RT}{F}(\beta c_s + \zeta)$$

The model equations in [22] have been used to simulate the physical phenomena in the example system, including a lithium anode, polymer electrolyte, and a composite cathode. It also simulated the charging/discharging behavior of such system.

The model developed by Doyle et al. has been also called the pseudo-two-dimensional (P2D) model, and as mentioned has been the most used by researchers. There have been several other transformations of this model, some of which were reduced-order, and some were extended versions [29]. Namely, they have included models such as single-particle model (SPM), multi-physics model, and molecular/atomistic model.

Fig. 1.13 shows a plot comparing model accuracy (predictability) and complexity (CPU time) for different types of cell-level physics-based models. It has been shown that the model developed by Doyle et al. had an average accuracy and complexity. Single-particle model, which simplified mass transport phenomena and neglected concentration and potential effects in the solution phase, was a reduced model from the P2D model. Multi-physics models usually have been extended from modeling electrochemical process to other domains such as battery's thermal behavior or mechanical behavior, such as the P3D stack/Thermal Model and P2D + Stress-strain listed in Fig. 1.13 [29].

These physics-based models have provided plenty of insights for researchers to analyze and optimize lithium-ion batteries in many ways. Many issues have been addressed from these models, including [29]:

1. Identification of base transport and kinetic parameters

2. Capacity fade modeling (continuous or discontinuous)

3. Identification of unknown mechanisms

4. Improved life by changing operating conditions

5. Improved life by changing material properties

6. Improved energy density by manipulating design parameters

7. Improved energy density by changing operating protocols

8. Electrolyte design for improved performance

9. State estimation in packs

10. Model predictive control that incorporates real-time estimation of State-of-Charge (SOC) and State-of-Health (SOH)

11. Improved protocols for optimum formation times
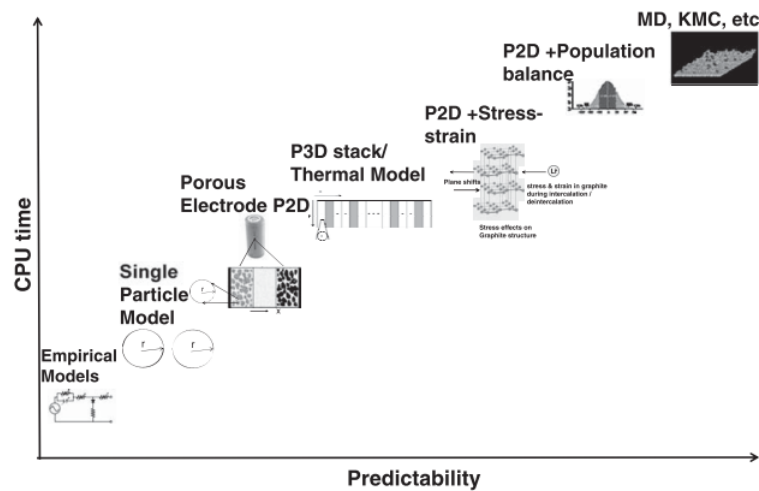
Fig. 1.13: Predictability and complexity plots for different cell-level models

1.5 Lithium-ion Battery Thermal Modeling

Besides significant efforts for lithium-ion battery electrical modeling, another key area regarding modeling has been the lithium-ion battery thermal modeling. Temperature has been identified as one of the dominant factors affecting battery performance, durability, and safety [20].

While the surface temperature of a battery can be directly measured by several types of thermal sensors, the internal temperature of a battery can be difficult to measure for in-situ applications. Inserting thermal sensors into the battery is limited by the space inside the battery, and usually requires specialized manufacturing such as drilling holes into the battery. This may lead to further safety concerns and therefore is not used for commercial applications.

However, it is essential to have access to the internal temperature information since the internal temperature of the battery has been shown to be significantly higher than the surface temperature even under regular operating conditions [24]. Relying only on the surface temperature measurement could lead to underestimation of potential thermal runaway situations, and methods to estimate the internal battery temperature are necessary. The following three types of approaches have been the primary methods for battery thermal modeling from a holistic point of view:

1. Impedance-based methods.

2. Electrochemical-thermal modeling.

3. Finite element analysis.

1.5.1 Impedance-based Battery Internal Temperature Estimation

The electrical equivalent circuit shown in the previous section showed that a lithium-ion battery can be analyzed like other electronics via an impedance spectrum. It has been shown that temperature is an important factor to consider when estimating the parameters from the equivalent circuit model. The solution resistance, as well as the resistance of both the current collectors and terminals, can be affected by the temperature [20]. Such relationship has been explained by an Arrhenius equation [27] based on the activation energy, E_a, at a given SOC, and a pre-factor, A_0, in (1.15).

It should be noted that the surface film resistance and charge transfer resistance are temperature-dependent as well, following a similar Arrhenius relationship.

$$\frac{1}{R_1} = A_0 \exp(\frac{-E_a}{RT}) \qquad\qquad (1.15)$$

As the temperature "T" in (1.15) is more accurate to be interpreted as the internal temperature of the battery instead of the surface temperature, a measured solution resistance can be used to estimate the internal temperature. Such resistance can be characterized through electrochemical impedance spectroscopy, and with post data processing, the internal temperature of the battery can be estimated. In Fig. 1.14, an exemplary plot from [28] has shown the "exponential" relationship between the solution resistance, a.k.a series resistance R_0, and the temperature for a lithium-ion cell.
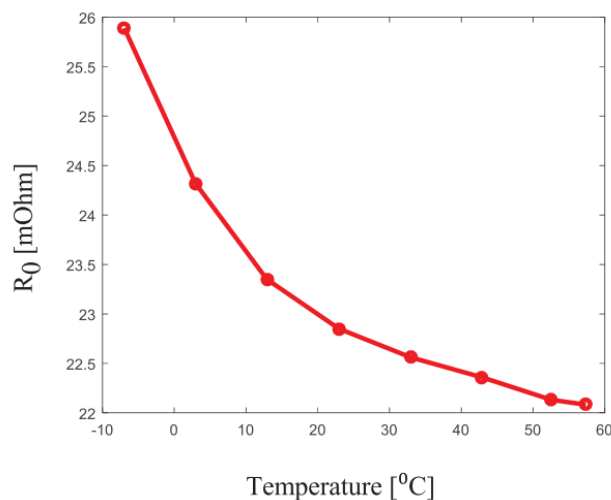
Fig. 1.14: Temperature-dependent solution (series) resistance plot

1.5.1.1 Electrochemical Impedance Spectroscopy (EIS)

The equivalent circuit models describe the impedance characteristics of lithium-ion cells when excited with a range of frequencies. An impedance spectrum contains a wealth of information about a cell's condition. The spectral data have been used to estimate various parameters in an equivalent circuit model [18], showing various aging and degradation effects throughout the cell's lifetime.

Impedance spectroscopy can be performed across a wide range of frequencies, and the

impedance spectrum exhibits different behavior at different frequencies. The battery is stimulated with a sinusoidal alternating current of a defined frequency and amplitude. The resulting voltage answer is measured. With voltage and current known the system's impedance can be easily calculated for the specific frequency. The cell will appear capacitive at low frequencies but will appear inductive at a relatively high frequency (>1kHz typically). The impedance can be typically separated into real and imaginary components and plotted with the real impedance on the x-axis, and the negative imaginary component plotted on the y-axis as shown in Fig. 1.15.
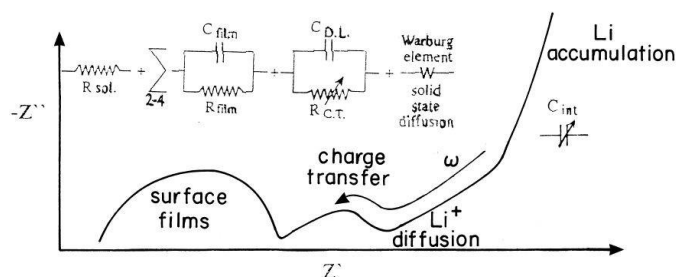
Fig. 1.15: EIS spectrum with full-order circuit model relationship

Fig. 1.15 shows a typical impedance spectrum for a lithium-ion cell, where the two semicircles represented the RC circuits. The high-frequency portion of the spectrum has not been shown here since the inductive behavior of such lithium-ion cell is insignificant as explained before.

The resistance of the surface film corresponds to the width of the large semicircle. The film capacitance is found using the frequency at the peak of the semicircle as shown in Fig. 1.16 below. Similar estimations can be done with respect to the smaller semicircle. These estimations are sensitive to measurement errors since they are based on single-point measurements.

$$f_g = \frac{1}{2\pi RC}$$
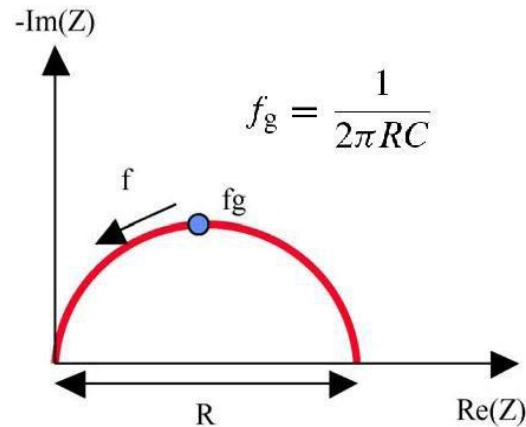
Fig. 1.16: Resistance and capacitance calculation from impedance spectrum [93]

In addition, due to the capacitive nature of the double-layer capacitance inside the battery, SOC has been shown as another important factor that shifted the spectrum. An example from [25] showed the spectra of a pristine NCA cell at -10°C at different SOC in Fig. 1.17. SOC undoubtedly played a significant role especially in characterizing the surface film impedance. The changing SOC during charge transfer process was responsible for the changes in both the resistive and capacitive behaviors.
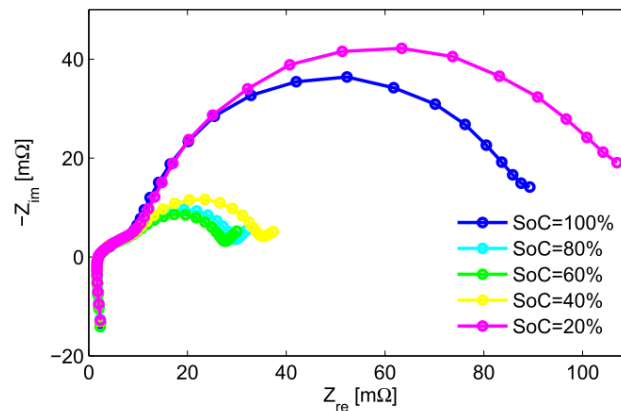
Fig. 1.17: EIS spectrum of a pristine NCA cell at -10°C with varying SOC

1.5.1.2 Internal Temperature Estimation Using the EIS Spectrum

Since both temperature and SOC affect the EIS spectrum, the SOC effect needs to be either isolated or decoupled from the temperature effect to have an accurate internal temperature estimation. Different approaches have been used in literature to find an EIS related signal that had

very weak SOC dependency while the temperature dependency was strong enough. [23], [25] and [26] identified three different signals that could be extracted from the EIS spectrum, containing strong temperature dependency and weak/no SOC dependency. While there might be other useful signals, these three signals are shown here as examples since the essential method is based on the Arrhenius equation introduced previously.

In [23], the authors identified that at 40Hz, the EIS spectrum had almost no SOC dependency at a given temperature, as shown in Fig. 1.18. The authors further transformed the impedance spectrum into a bode plot and find that the phase-shift value at 40Hz could be used as the signal associated with the temperature.
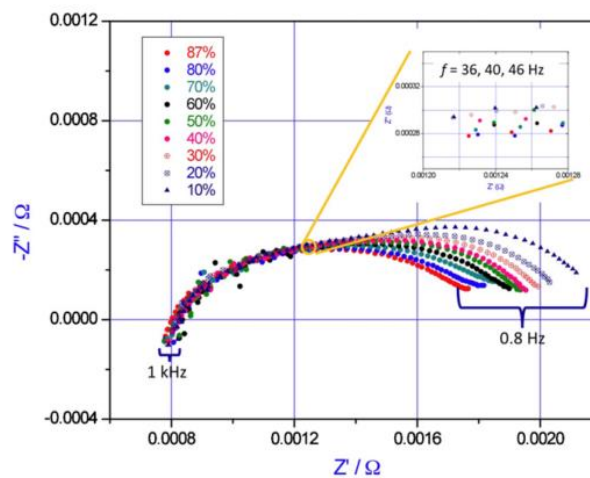
Fig. 1.18: Impedance of a tested battery at 16°C with varying SOC

Considering the small SOC effect at 40Hz, the authors took an average of three phase values at 20%, 50%, and 80% and plot the averaged values versus different temperature conditions. As shown in Fig. 1.19, an Arrhenius relationship can be fitted, and the small error bars validate the weak SOC effect. After formulating a model based on the fitted line, the internal temperature of the battery can be estimated from a fast impedance measurement at 40Hz.

A similar approach could be found in [25], where the authors found that the intercept frequency (phase lag is zero) had a strong relationship with the temperature. As shown in Fig. 1.20,

the frequencies with 0 phase shift are temperature dependent. Since the interested frequency range was high, the SOC effect was minimal. Fig. 1.21 shows the temperature dependency of such frequency and an Arrhenius relationship can be seen, while the SOC effect is minimal. Based on this plot, the internal temperature can be then inversely found based on the impedance bode plot.
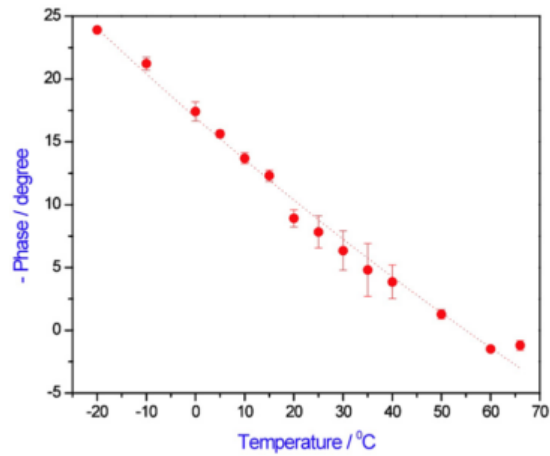
Fig. 1.19: Averaged phase shift at 40Hz of the tested battery vs. temperature
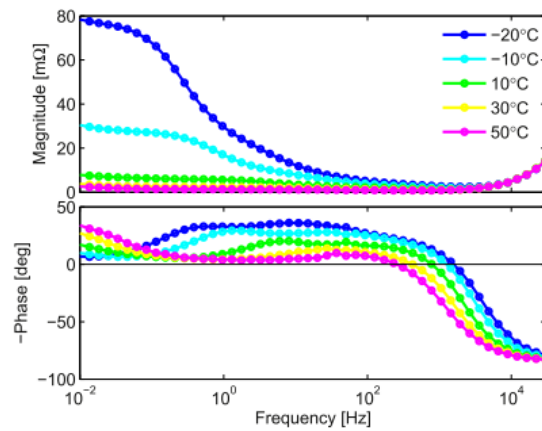
Fig. 1.20: Impedance bode plots of the tested battery at different temperatures
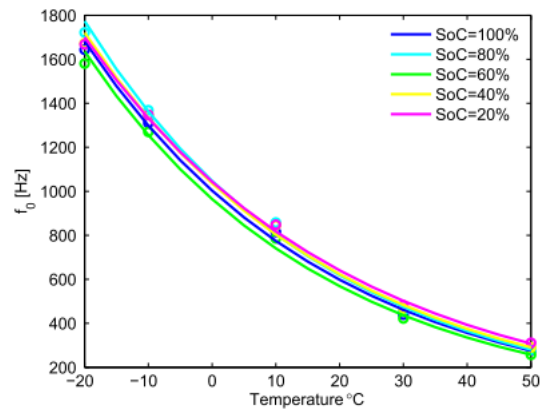
Fig. 1.21: Intercept frequency vs. temperature for the tested battery

The approach in [26] focused on the impedance spectrum at the very high-frequency range where the SOC effect is small. The 10.3kHz impedance is then identified as the signal of interest. Fig. 1.22 shows the Arrhenius relationship between the real part of the impedance at 10.3kHz and the temperature, as the SOC effect is shown to be small.
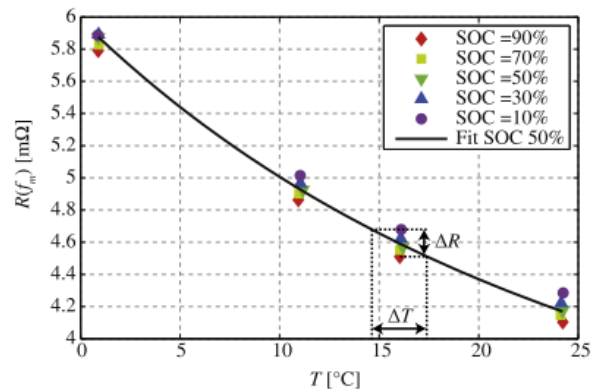
Fig. 1.22: Real part of impedance at 10.3kHz vs. temperature

Other signals have been also identified and investigated for their temperature dependencies in the literature. However, the overall method stays similar, and the temperature relationship has been identified following the Arrhenius equation. Such types of approach require extensive offline characterizations, and the resulted relationship cannot be extended to other batteries. Also, the internal temperature estimation is offline as well, requiring separate impedance measurements and data processing.

1.5.2   Electrochemical Thermal Modeling

The physics-based approach has been another way to estimate battery internal temperature. This type of approach, when the model is computationally light, can be used online since the electrochemical process generates heat inside the battery, and the internal temperature distribution can be calculated given a known physical structure of the battery.

There are two difficulties when formulating such electrochemical thermal models. One is the calculation method used for heat generation, and the other is the identification of various physical parameters both in the electrochemical domain and in the thermal domain.

1.5.2.1 Lithium-ion Battery Internal Heat Generation

There are three main heat sources inside the battery: interfacial kinetics, species transport, and ohmic heating from the movement of charged particles. In [30], several different methods calculating overall heat generation inside a battery were discussed. (1.16) provides a detailed expression for battery heat generation based on energy balance, where the first term is the battery electrical power produced, the second term is a combination of producible reversible work and entropic heat, and the third term is the heat generated from mixing.

$$q = - IV - \sum_l I_l T^2 \frac{d\frac{U_{l\ avg}}{T}}{dT}$$
$$+ \sum \frac{d}{dT}[\int_{vj}\sum_i c_{ij} RT^2 \frac{\partial}{\partial T}\ln(\frac{\gamma_{ij}}{\gamma_{avg\ ij}})dvj]$$
$$+ \sum_j \sum_i [(\Delta H_{ij} - RT^2 \frac{d}{dT}\ln\frac{\gamma_{ij}}{\gamma_{avg\ ij}})\frac{dn_{ij}}{dt}]$$

$$(1.16)$$

The heat generation calculation has been approached by integrating local heat generation and can be divided into different electrodes. (1.17) is another form of the heat generation calculation based on energy balance excluding the entropic heat effects. (1.18) is an area differential form of (1.17). In (1.18), it shows that variables such as overpotential η, solid/electrolyte phase potential ϕ are included, and this means that a physics-based thermal model

is highly coupled with the physics-based electrochemical models introduced in the previous section.

$$q = -\int_v(\sum_l ai_{nl}U_{Hl}dv) - IV \tag{1.17}$$

$$-q'' = i(\eta_a + \Delta\phi_s) + \int(ai_n\eta_c - i_1\frac{d\phi_1}{dx} - i_2\frac{d\phi_2}{dx})dx \tag{1.18}$$

A simplified form of (1.16) has been commonly used, in which the phase change and mixing effects have been neglected. Such a simplified calculation method is shown in (1.19), where U is the open-circuit voltage, OCV. The first term the heat generation due to overpotential and the second term is the entropic effect.

$$q = I(U - V) - I(T\frac{\partial U}{\partial T}) \tag{1.19}$$

Using (1.19) relies on the characterization of the entropic term, especially the change of OCV with respect to temperature at different SOC stages, a.k.a. entropic coefficient. In [31], the authors provided two methods to characterize the entropic coefficient. Based on (1.20), the entropic coefficient could be either calculated by fitting the slope of OCV vs. Temperature at varying SOC, or by measuring the reversible heat generation $\dot{Q}_{rev}$. Using "gradient heat flux sensor (GHFS)", $\dot{Q}_{rev}$ between charging and discharging could be measured. In Fig. 1.58, a typical plot of entropic coefficient vs. SOC is shown.

From the plot one could find that at high SOC, the entropic coefficient was greater than 0 while at low SOC, it was less than 0. Also, the entropic coefficient did not have a clear trend against varying SOC, and therefore extrapolation was needed to calculate the coefficient at any SOC that was not characterized.

$$\Delta S = nF\frac{\partial U}{\partial T} = \frac{nF\dot{Q}_{rev}}{IT} \tag{1.20}$$
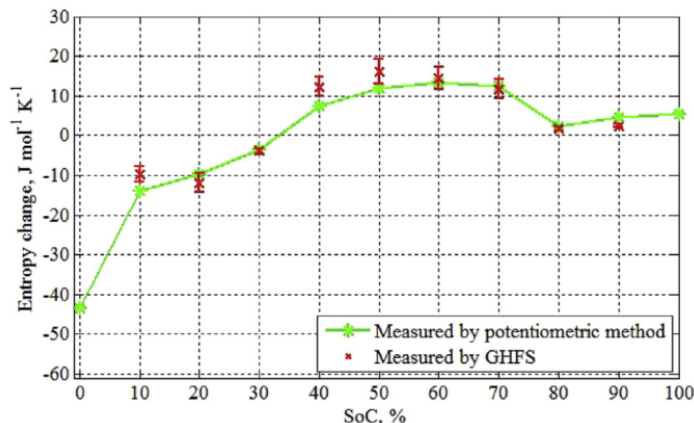
Fig. 1.23: Entropic coeff. vs. SOC for the tested battery using different methods

With fitted entropic coefficients with respect to SOC, the heat generation can be calculated. Different electrochemical thermal models have utilized (1.19) either in the exact form or a slightly-modified form to calculate the heat generation, with the help of the electrochemical models estimating battery terminal voltage.

1.5.2.2 Thermal Model Formulation

As shown in the previous section, the basis for battery thermal modeling was to calculate the internal heat generation accurately, and this required either accurate battery electrode potential modeling in the porous electrode models or accurate battery terminal voltage modeling in the lumped parameter models. Especially when electrode potentials are needed for the heat generation calculation, physics-based electrochemical models introduced in 1.4.2 are needed and therefore coupled with the thermal model. In fact, these two types of models are cross-coupled since the internal temperature estimated by the thermal model can be further fed back in the electrochemical models, i.e., in the Butler-Volmer electrode kinetics equation.

There has been extensive research conducted coupling the electrochemical model and the thermal model. Different degrees of model complexity have been chosen to formulate either model to achieve a balance between accuracy and overall model complexity.

In [33], the P2D lithium-ion battery electrochemical model was extended by adding the

thermal effects. The total reaction heat generation Q_{rxn}, the total reversible heat generation Q_{rev}, and the total ohmic heat generation Q_{ohm} were all included to model the thermal effect given by the energy balance equation in (1.21). Q_{rxn} is the heat generation by overpotential, Q_{rev} is the heat generation due to entropy change, and Q_{ohm} is calculated as in (1.22). The boundary conditions for this thermal model followed convection shown in (1.23) and (1.24).

$$\rho C_p \frac{dT}{dt} = \lambda \frac{\partial^2 T}{\partial x^2} + Q_{rxn} + Q_{rev} + Q_{ohm} \tag{1.21}$$

$$Q_{ohm} = \sigma_{eff}(\frac{\partial \phi_1}{\partial x})^2 + k_{eff}(\frac{\partial \phi_2}{\partial x})^2 + \frac{2k_{eff}RT}{F}(1\text{-}t_{0+})\frac{\partial \ln c}{\partial x}\frac{\partial \phi_2}{\partial x} \tag{1.22}$$

$$-\lambda \frac{\partial T}{\partial x}|_{x=0} = h(T_\infty - T) \tag{1.23}$$

$$-\lambda \frac{\partial T}{\partial x}|_{x=L_p+L_s+L_n} = h(T - T_\infty) \tag{1.24}$$

In Fig. 1.24, the battery surface temperature progression during discharge is shown with different constant discharge current rates. The simulations were performed in the COMSOL environment, showing the capability of coupling thermal model with the existing electrochemical model.

In [32], the authors formulated the electrochemical model using a reformulation of the existing complex porous electrode pseudo three-dimensional (P3D) model. The thermal model developed was a 2D model with carefully-structured boundary conditions, ensuring its convenient coupling with the electrochemical model. The authors utilized Chebyshev-based orthogonal collocation and several other numerical methods to reformulate the P3D model (RFM), and compared both the electrochemical model results and thermal model results with a previously-developed P2D model in the COMSOL simulation environment, as shown in Fig. 1.25. The RFM had similar model accuracy compared to the P2D model but took much less time to simulate.
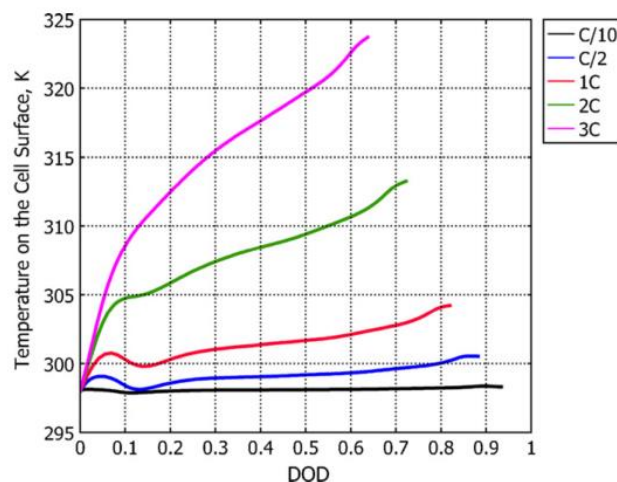
Fig. 1.24: Battery surface temperature simulation results during discharge with various rates
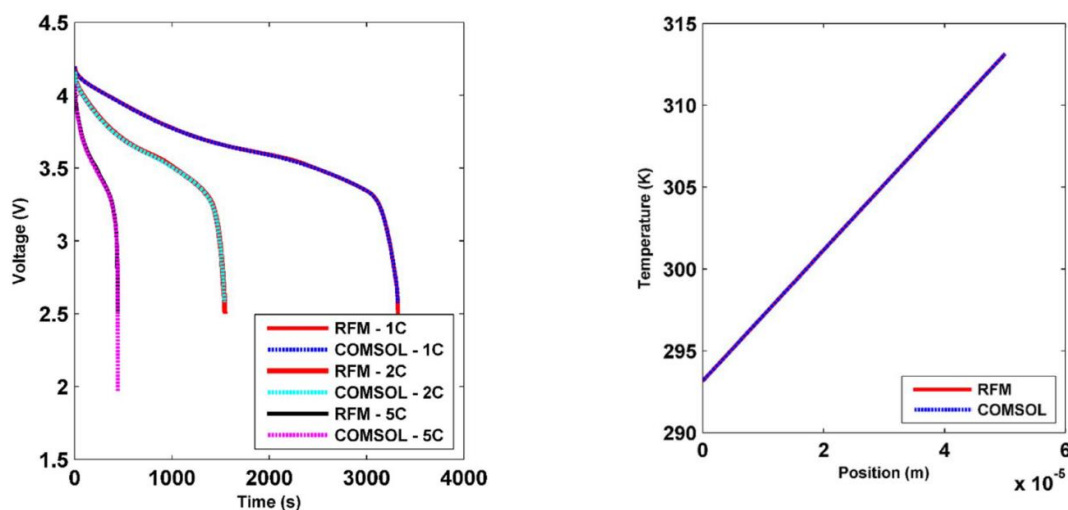
Fig. 1.25: Results comparison between RFM and P2D models

In [34], the electrochemical model selected was the single-particle model, a reduced-order model from the P2D model. The thermal model coupled was also reduced by neglecting the ohmic heat generation term. The simplification was acceptable since heat generation due to overpotential activation and entropy change accounted for most of the heat generated. By simplifying both the electrochemical and thermal models, the model complexity and computational requirement were both reduced. It is shown in Fig. 1.26, the accuracy of the thermal model based on the single-particle model did not deteriorate compared to that based on the porous electrode model.

A similar coupled electrochemical-thermal model has been extended to model lithium-ion

battery packs in EV applications [35]. Under different drive cycle profiles, the modeled battery surface temperature was compared with the measured temperature and shows good accuracy, as shown in Fig. 1.27.
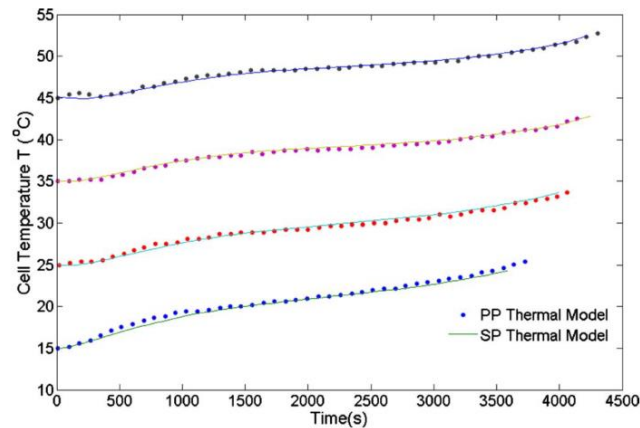
Fig. 1.26: Cell temperature estimation comparison between SP and PP models (1C discharge)
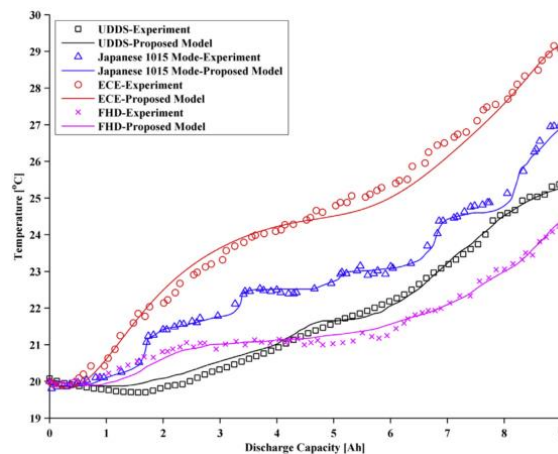
Fig. 1.27: Cell surface temperature model results under different drive cycles

However, [31] - [35] all assumed the core temperature of the battery was the same as the surface temperature and did not consider the temperature distribution inside the battery because of the heat flux flowing from the inner center of the battery to the battery surface.

Considering the physical structure of a battery, [24] developed a lumped-parameter thermal model for a cylindrical battery. In order to validate the thermal model, a customized thermal sensing setup was made, and a thermocouple was inserted into the battery, as shown in Fig. 1.28.

Thermal circuits were formulated to show the thermal loop inside the battery. In Fig. 1.29, both a detailed thermal equivalent circuit and a simplified thermal equivalent circuit are shown.
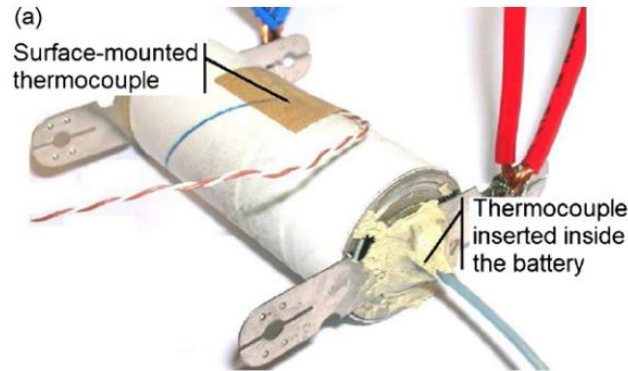
Fig. 1.28: Battery with inserted and surface mounted thermocouples
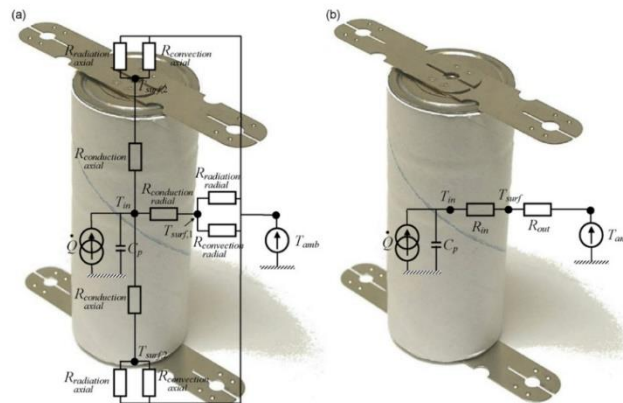
Fig. 1.29: (a) Complete battery thermal circuit; (b) Simplified battery thermal circuit

The heat generation calculation in [24] included both the overpotential term and entropy term, while instead of using a separate electrochemical model to estimate the battery voltage, the measured battery voltage was used, with a sampling frequency at 100 Hz. Based on the equivalent thermal circuit, the core temperature of the battery was estimated and compared with the measured temperature data with the current/voltage data collected after a consecutive-pulse test. The model showed good accuracy with less than 1°C error, shown in Fig. 1.30.
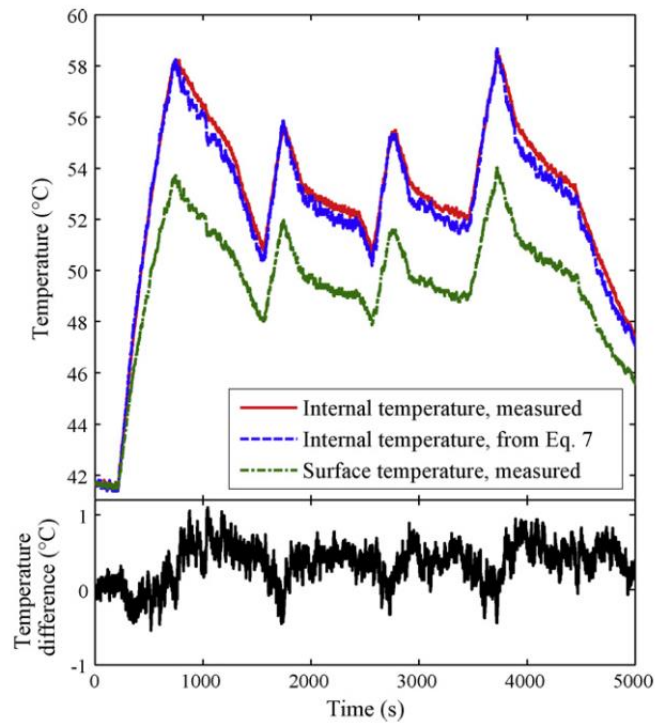
Fig. 1.30: Battery core temperature estimation result and error

Moreover, a coupled electro-thermal model was developed in [37] with the lumped model. The electrical model used for battery voltage estimation was a 2RC model, and the thermal model was formed similarly to the simplified thermal circuit in Fig. 1.29 (b). Thermocouples were placed on the battery surface and inside the battery to validate the model. After characterizing all the parameters of both the electrical equivalent circuit and the equivalent thermal circuit, medium-dynamic cycles were performed on the test battery to validate the model. Estimated battery voltage from the electrical model was fed into the thermal model to estimate both the surface temperature and core temperature. In Fig. 1.31, the current profile, SOC profile, and the FFT of the current are shown for the validation experiment.
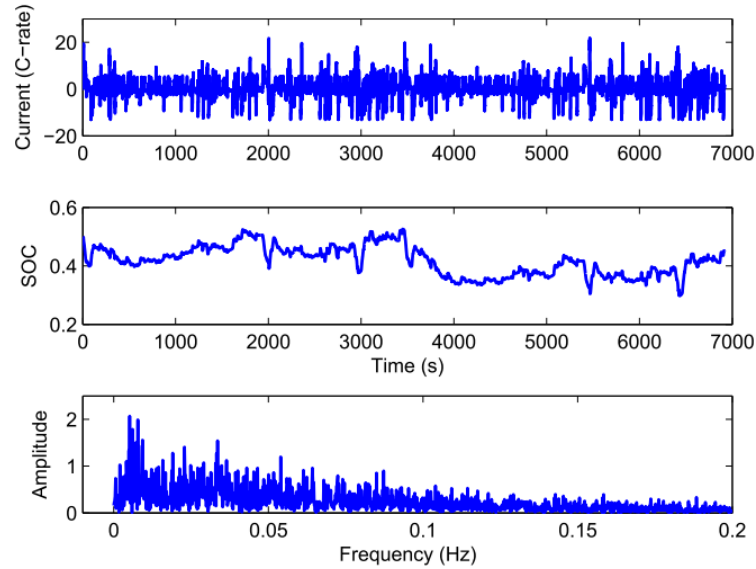
Fig. 1.31: Tested cycle profiles (Current, SOC, Current FFT)

Validation results for the electro-thermal model are shown in Fig. 1.32, yielding good agreements with the measured voltage data and measured surface/core temperature data. It shows that with carefully-characterized parameters, electrical equivalent circuit model can provide accurate voltage estimations as accurate as the electrochemical models. Also, the estimated voltage can be further fed into the thermal model for internal battery temperature estimation.
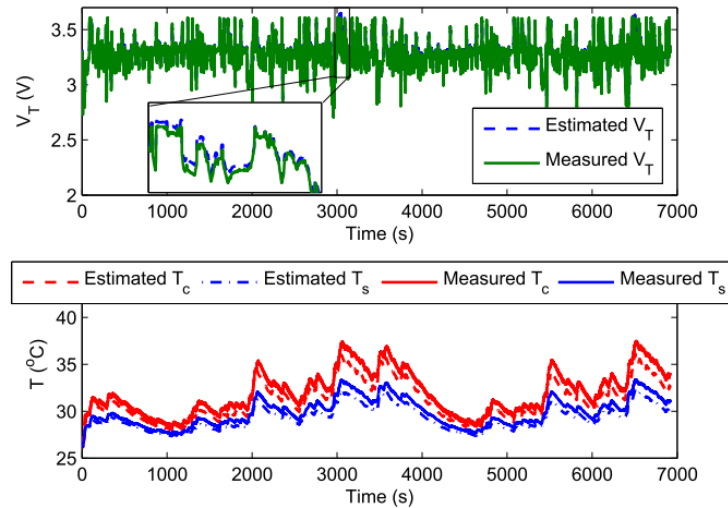
Fig. 1.32: Electro-thermal model results compared to measured data

1.5.3   Battery Thermal Model Using FEA Methods

Another thermal modeling approach is through finite-element analysis using specific software. This type of modeling has been offline and usually provides steady-state results. These results can be further analyzed to understand battery thermal limits and optimize battery thermal management strategies or battery material selection.

Since FEA is not the focus of this thesis, it will not be discussed in detail. An example from [36] showed the steady-state temperature distribution across the battery physical structure after a high current cycle, shown in Fig. 1.33.
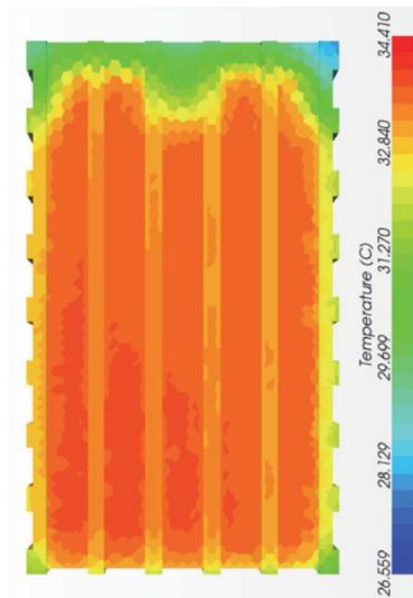
Fig. 1.33: FEA result of the temperature distribution after a high current discharge

The biggest advantage of the FEA approach is the access to the temperature distribution in the battery, while the other modeling approaches only provide a lumped single-point temperature estimation. On the other hand, the disadvantages using FEA include 1) its long simulation time, and 2) its limit for offline simulations.

1.6   Lithium-ion Battery State Estimation

As the lithium-ion batteries are widely used for various applications, monitoring battery

internal states' status becomes crucial for adjusting the controls of the load dynamically to optimize the usage. Several battery internal states have received the highest attention, including state-of-charge (SOC), state-of-power (SOP), state-of-energy (SOE), and state-of-health (SOH). The biggest difficulty is the fact that there has been no direct measurement of these internal states, and therefore different modeling, estimation, and statistical analysis techniques are required and have been investigated extensively in the literature. Among these internal states, SOC, SOP, and SOE can be categorized as the short-term states since they change much more often than the long-term state SOH. Since these short-term states are not of high relevance to this thesis, the associated estimation techniques will not be discussed extensively.

1.6.1   State-of-Charge (SOC) Estimation

One of the most studied metrics in a battery management system (BMS) is the SOC. For an EV application, the keen interest on the SOC metric is due to the perceived utility of the SOC in predicting the remaining battery use time/vehicle mileage until depletion. SOC estimation techniques in the literature have been divided into four main categories:

1. Coulomb counting

2. Voltage-based methods

3. Impedance-based methods

4. Empirical data-driven methods

1.6.1.1 Coulomb Counting

The most direct method to estimate SOC is coulomb counting. Assuming a fixed amount of charge, Q_{total}, is available after the battery is fully charged, the SOC can be calculated as in (1.25).

$$SOC = \frac{Q_{total} - Q_{out}}{Q_{total}} * 100\% \qquad (1.25)$$

However, one difficulty for characterizing Q_{total} is that different discharge current

magnitudes would result in different available charges before the battery voltage crosses the lower voltage safety limit. Therefore, even though the theoretical total available charge is usually fixed for a battery, in an application scenario it needs to be somewhat modified to avoid overestimating SOC. One can refer to [39] for an example using the Peukert modification to calculate Q_{total}.

A couple of other issues regarding coulomb counting included 1) current sensor error, and 2) imperfect coulomb efficiency during charge [40]. Methods to reset the coulomb counter and prior information about coulomb efficiency may be needed to mitigate these two issues.

1.6.1.2 Voltage-based Methods

The most common methods used to estimate SOC has been estimating the OCV of the battery and correlating the OCV to the SOC value since the OCV-SOC relationship is based on thermodynamics and can be treated as fixed. The preparation for such methods requires an experimentally determined OCV vs. SOC curve, recording the OCV of the battery after resting the battery for a couple of hours at different SOC. After the formulation of the curve, while the battery is under loading, various methods involving observers and/or filters have been developed to estimate the OCV based on the measured battery terminal voltage, loading current, and/or temperature. Subsequently, the SOC is estimated by looking up the corresponding OCV on the predetermined curve.

The standard methodology sequence is first to formulate a battery through either ECM or electrochemical approaches, then record measurements at every sample instant and estimate the state by the developed analysis method at that sampling instant. The most commonly used filter approach is the Kalman Filter (KF). The KF can be divided into both the Linear KF and the Extended Kalman Filter (EKF), suitable respectively for linear state space models and nonlinear state space model. [41] contained the computation sequence using the KF at any sampling instant, including a "predict" step and a "correct" step. Such sequence was the same for both linear and nonlinear KFs. In Fig. 1.34, the flowchart including the matrix calculation for an EKF is shown.
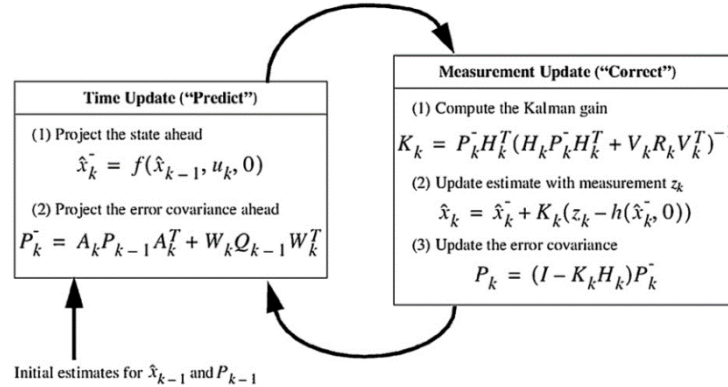
Fig. 1.34: Flowchart for a nonlinear Kalman Filter at any sampling instant

Based on this flowchart, G.L Plett has developed the voltage-based KF approach for lithium-ion battery state estimation [42], which laid the foundation for almost every subsequent state estimation method development using the KF. ECM was used, and a sample result of the SOC estimation is shown in Fig. 1.35.

In the literature of recent battery SOC estimation research, the KF has been commonly used, despite minor changes regarding the filter structure and the battery model are made. There have been also few cases where Particle Filter is proven to be effective.

For example, in [43], an estimation method for SOC using the Particle Filter was developed, where unlike the KF, the noise was no longer assumed to be Gaussian. The performance of both the SOC and SOH estimations is shown in Fig. 1.36 with a photovoltaic current profile as for a grid application. The SOC estimation was accurate compared to the reference measured and calculated by coulomb counting.
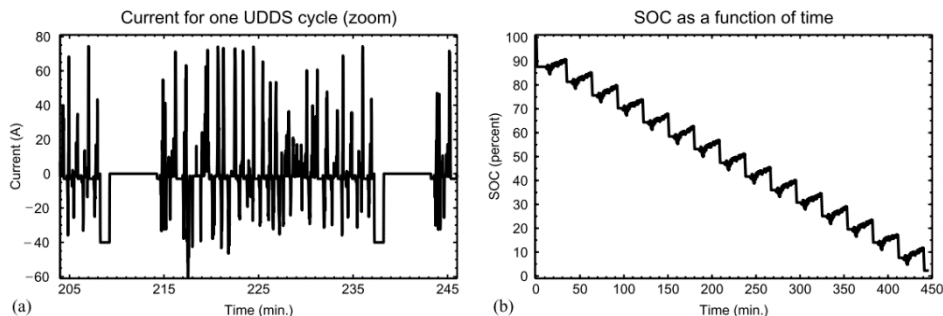
Fig. 1.35: Drive cycle current profile & SOC estimation using the particle filter
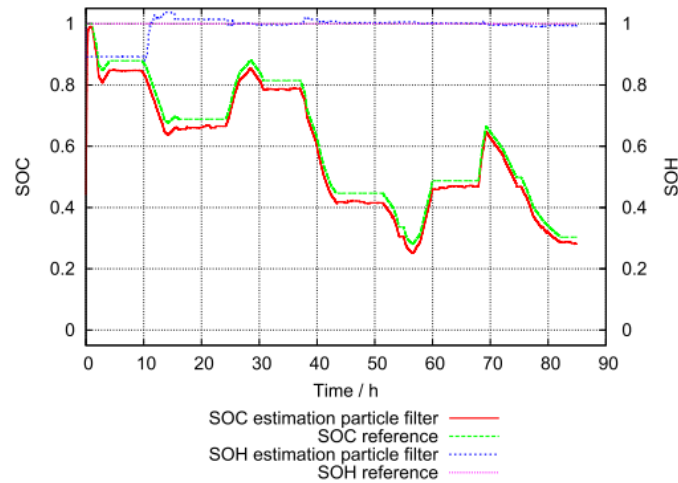
Fig. 1.36: SOC/SOH estimation results using a Particle Filter

On the other hand, SOC estimation technique based on observers have been investigated. Formulating the battery model with a state-space modeling approach provides opportunities to apply modern control methods such as sliding mode observers and nonlinear observers for state estimations.

For example, in [44], a sliding mode observer was connected to a 2RC battery ECM. The adaptive switching gain sliding mode observer (ASGSMO) system is shown in Fig. 1.37, and a good SOC estimation result is shown in Fig. 1.38 for a suburban drive cycle.
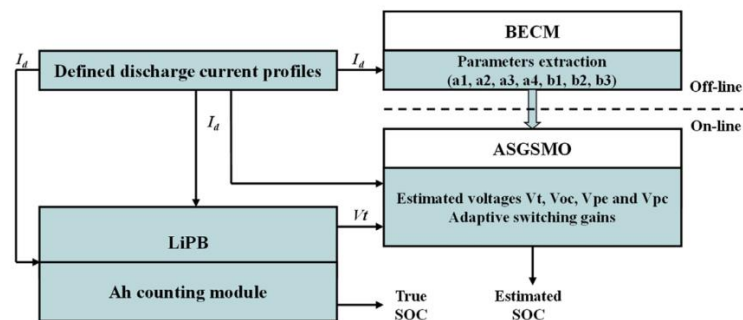
Fig. 1.37: Flowchart using ASGSMO for SOC estimation
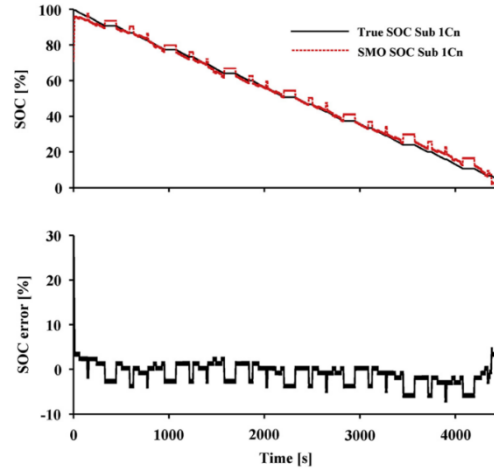
Fig. 1.38: SOC estimation performance during a suburban drive cycle

Alternatively, nonlinear observers can be constructed based on either ECM or electrochemical models. In [45], the authors developed the SOC estimation method using nonlinear observers based on a 1RC ECM. In Fig. 1.39, it shows a comparison of the SOC estimation performance using an EKF, a sliding mode observer (SMO), and a nonlinear observer (NLO), where the NLO shows similar performance as the EKF and better performance than the SMO.

As mentioned, the state space model can be constructed based on either an ECM or an electrochemical model. When constructing using the electrochemical model, the complexity is significantly increased. In [46] for example, a nonlinear SOC observer was developed based on a P2D electrochemical model. Both the state space model and the observer structure became much more complicated than those in [45]. However, the observer could not only provide SOC estimation, but also estimate other electrochemical states such as concentrations. This improvement provided deeper insight into the process inside the battery than using the ECM. The SOC estimation result is shown in Fig. 1.40 for an AUDC drive cycle, in which a good agreement between estimation and reference was achieved barring a rather slow initial convergence.
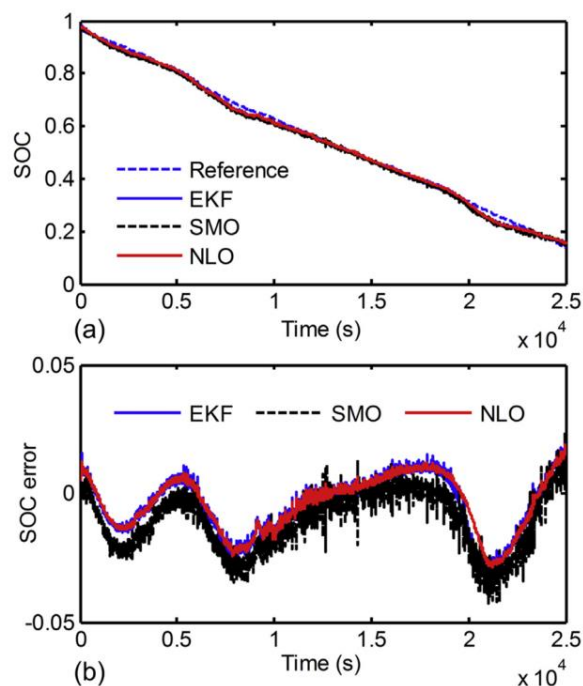
Fig. 1.39: Flowchart for a nonlinear Kalman Filter at any sampling instant
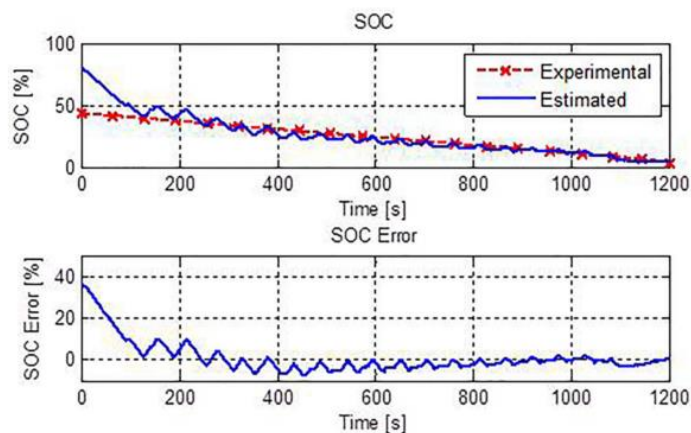
Fig. 1.40: SOC estimation performance using a NLO with an electrochemical model

1.6.1.3 Impedance-based Methods

For various types of batteries, impedance-based methods have been proposed to estimate SOC. The background of this method has been to measure the impedance spectra at different SOCs beforehand, and later correlate the measurements with the SOC values as determined by the coulomb counting method. Several parameters have been proposed as candidates for the SOC

indicators. These included the high-frequency resistance, the resonant frequency, and the voltage relaxation time constant [47] [48] [49][50].

There are a couple of disadvantages for the impedance-based SOC estimation methods. The first one is that measuring impedance at different frequencies requires specific EIS apparatus, and the battery needs to be at no load condition. This limits such a method to be performed offline and thus is less appealing compared to the dynamic estimation using voltage-based methods. Another disadvantage is that the impedance measurements could be polluted by factors other than SOC, such as temperature and aging. This leads to an inaccurate estimation of the SOC and therefore undesirable for many applications.

1.6.1.4 Data-driven Methods

While filter approaches are more common for SOC estimation, data-driven methods such as neural networks have been used to represent a complicated state transition process that a battery's SOC represents. This genre of methods first constructs the structure by selecting suitable input variables, as in time series. Such variables include battery terminal voltage, load current, temperature, and/or SOC value from the previous sample instant. The output is usually the SOC value of the next sample instant. By gathering voltage, current, temperature data, as well as the calculated SOC values based on Coulomb-counting for a wide range of different experiments, the neural network is then trained, leading to the convergence of all the hyperparameters inside the complex network. After the training, with the hyperparameters fixed, the ANN then predicts the SOC for the next sample instant from the inputs.

In the literature, artificial neural networks (ANN) with different structures have been developed for SOC estimation of different battery types. One example of an estimator for SOC using a recurrent neural network (RNN) structure could be found in [58]. The network structure is shown in Fig. 1.41.
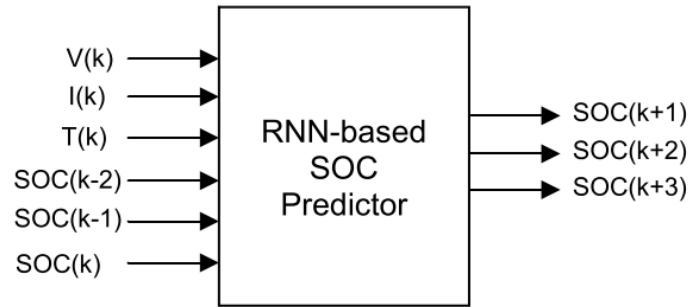
Fig. 1.41: RNN structure for predicting Li-ion cell SOC

After the successful training of the RNN shown above, the validation results of SOC estimation, as well as the estimation error, is shown in Fig. 1.42, achieving good estimation accuracy.
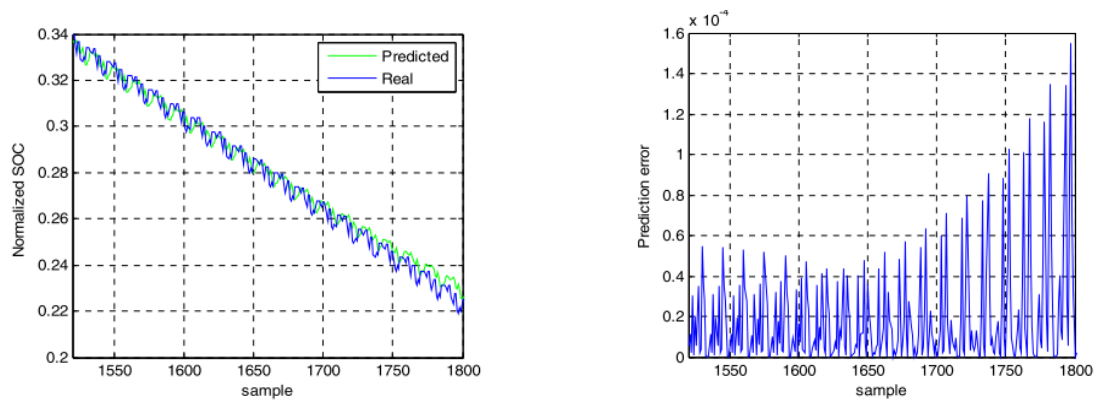
Fig. 1.42: SOC estimation validation results and the error

A similar structure was used for the case of lead-acid batteries, where both battery voltage and SOC are outputs [59]. Compared to [58], more layers were introduced, so the ANN was multi-layered, commonly seen for AI deep learning. Also, each layer contained more neurons, trying to compensate for the more complex electrochemical process inside the lead-acid battery. The multi-layer structure is shown in Fig. 1.43.
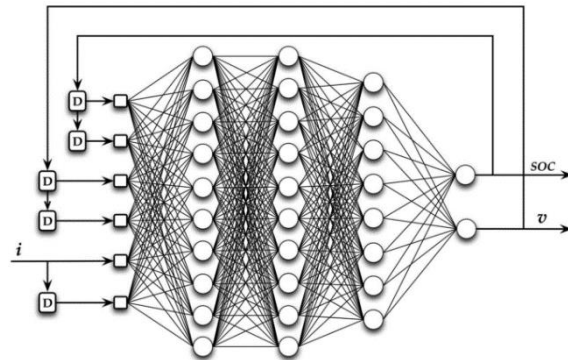
Fig. 1.43: RNN structure for predicting lead-acid battery voltage and SOC

Other research in the literature proposed several other neural-network-related approaches for battery SOC estimation. [60] proposed a method to predict the end of discharge of lithium-ion batteries using a combination of the particle filter and the neural network with radial basis functions instead of the conventional sigmoid basis functions. Fig. 1.44 shows the estimation performance of this proposed method.
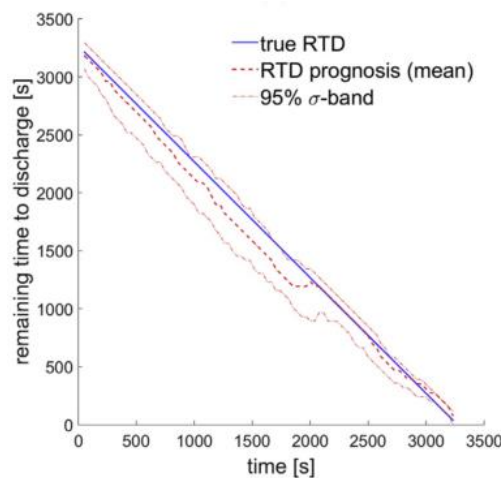
Fig. 1.44: Remaining time to discharge estimation

In [61], a neuro-controller was also included in the proposed structure together with an ANN-based battery system model. In Fig. 1.45, the combined structure is shown, while the ANN-based battery system model predicted battery voltage and self-tuned the parameters based on the measured data, and the neural-controller helped predict the SOC. Both battery voltage and SOC were accurately estimated, as shown in Fig. 1.46.

Other ANN-based models were also developed to consider the effect of battery aging. One can refer to [62] for details.
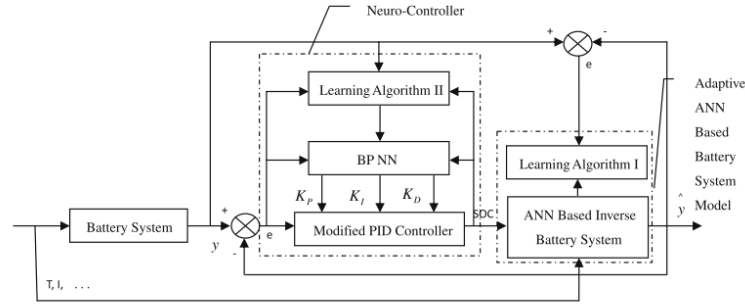
Fig. 1.45: Combined ANN-based battery model and neuro-controller
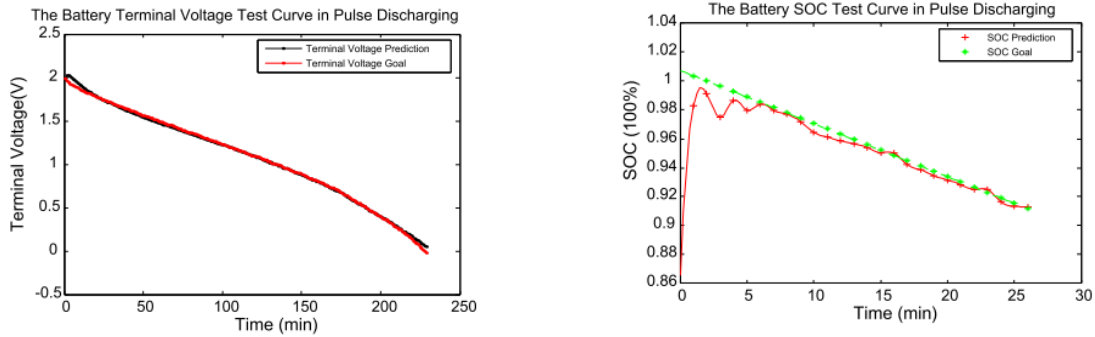
Fig. 1.46: Voltage and SOC estimation results compared to measured data

1.6.2   State-of-Power/Energy (SOP/E) Estimation

For a battery to fulfill its tasks, it not only requires the battery to have sufficient stored charge, but also requires the battery to have enough power capability and remaining energy to sustain the operation. SOP and SOE estimations become important for power applications such as in automobile industry, where an EV is built to have desirable range, as well as good power ratings. On the other hand, SOE is directly correlated to the remaining range of an EV. With the fast development of the EV industry, an accurate SOE estimation gradually becomes more important.

1.6.2.1 SOP Characterization and Estimation

Two metrics characterize battery power capability: state-of-function (SOF) and state-of-power (SOP). SOF was first introduced in [64], and since then, various definitions of SOF have

been proposed [63] [64] [65], which have been all related to the battery power capability. The SOF represents a binary yes/no answer to the question whether the battery can fulfill its task, while the SOP is a signal representing how much power is available. The SOF and SOP are defined as the following.

$$SOF = \begin{cases} 1 \text{ if } V_{min} \geq V_{limit} \\ 0 \text{ if } V_{min} \leq V_{limit} \end{cases} \tag{1.26}$$

$$SOP = \frac{V_{limit}(V_{ocv} - V_{limit})}{R} \tag{1.27}$$

V_{min} is the minimum voltage reached when the battery is under load, V_{limit} is the low voltage limit specified by the battery manufacturer, and R is the steady state resistance of the battery under the linear circuit model assumption. The definitions in (1.26) and (1.27) are for the discharging limit, while the charging version can be derived similarly. The HPPC test proposed by the FreedomCAR consortium has been the most straightforward short-term power capability tool [92]. By observing the voltage drop during the fixed-time current pulse at various SOC, the resistance and OCV for the associated condition can be used to help predict power performance.

Moreover, there has been some research investigating different estimation methods for battery SOP during operation. The approaches have been divided into two categories [66]:

1. Methods based on adaptive characteristic maps (CM)

2. Methods based on ECMs

The methods based on CMs require extensive experimental characterizations, generating a look-up table of static interdependences between battery power capability and various battery parameters and states. Such parameters and states include SOC, temperature, duration of the power pulse, required power, and battery voltage. Such characterization tests include HPPC tests and EIS tests.

The biggest advantage of using CMs is its simple implementation and clear characteristics. However, such methods suffer from their uncertainty of the battery's previous history as well as

the potential lack of recognition of other parameters. An example lookup table is shown in Fig. 1.47, showing the dependency between the available power on battery current, SOC, and temperature, for the tested battery.
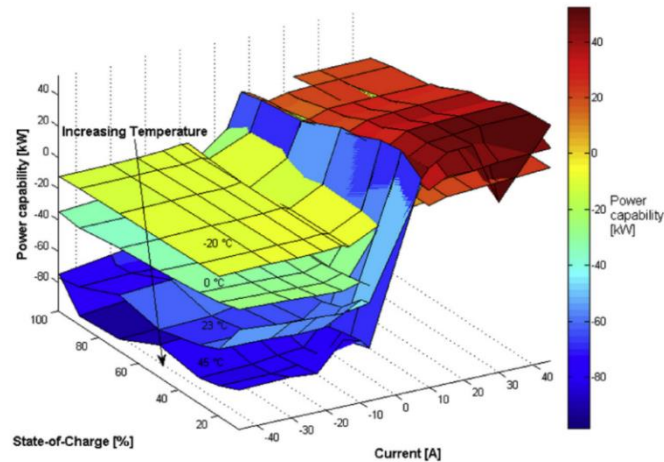
Fig. 1.47: Dependence of available battery power on battery current, SOC, and temperature

The other category of methods based on ECMs can be divided into: 1) Kalman filter based methods, 2) least-square-based methods, and 3) other adaptive filters and observer methods. Kalman filter based methods are the most commonly used methods. At any sampling instant, the Kalman filter provides estimations of the states in the ECM. Based on the parameters and estimated states of the ECM, one can calculate the possible minimum voltage the battery could reach, or the potential maximum loading current the battery could have at the next sample instant. This estimated voltage can then be compared with the voltage limit and determine whether the battery's power capability reaches the limit. Alternatively, one can calculate the maximum possible current given the battery voltage limit.

In [68], a 1RC ECM was used, and the Kalman filter was applied to estimate OCV and the resistance of the battery at any sampling instant. The estimated maximum current or minimum current at next sample instant depending on charging or discharging was then calculated. In Fig. 1.48, it shows the charge/discharge current limit, and the associated charge/discharge power limit during a FUDC drive cycle.
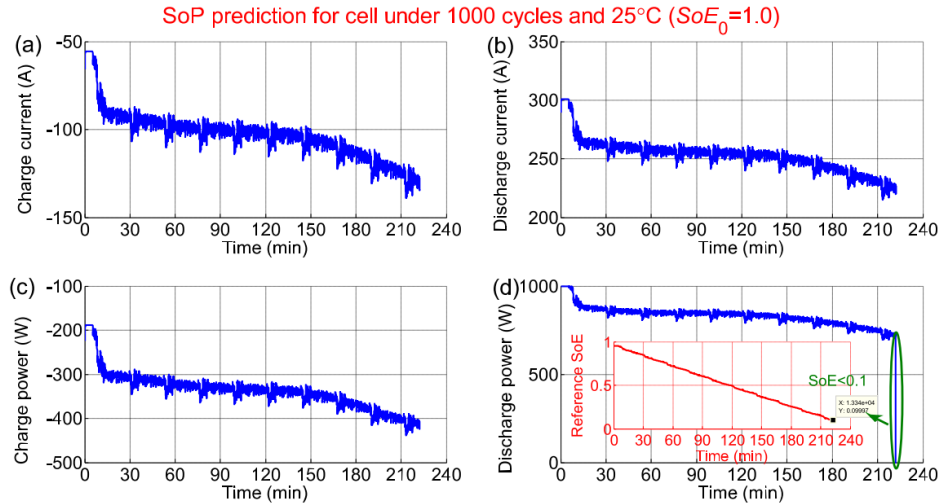
Fig. 1.48: Estimated current limit and SOP during a drive cycle

A similar approach using 1RC ECM could be found in [68], and another approach applying the Kalman filter on a differently structured ECM was shown in [69]. A nonlinear Butler-Volmer (BV) circuit element is used to replace the RC component in the ECM. The resulting SOP estimation was more temperature compatible and smoother regarding noise compared to using RC ECM. The comparison is shown in Fig. 1.49 and the BV model resulted in more accurate and stable SOP estimation, especially at low temperatures. This was because the battery resistance shows high nonlinearity at low temperatures.

-20°C   25°C
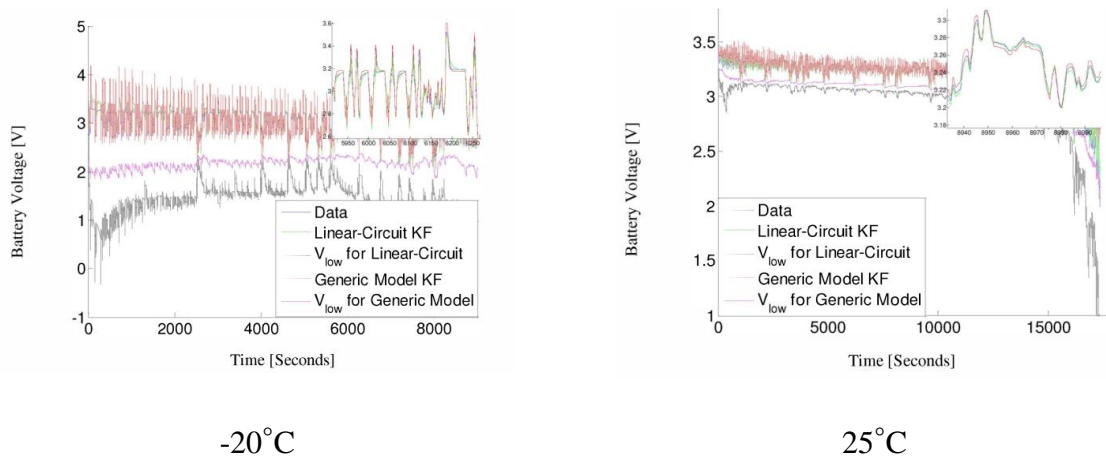
Fig. 1.49: SOP comparison between the linear model and BV model at diff. temp.

1.6.2.2 SOE Estimation Methods

Unlike SOC estimation, SOE estimation recently started to draw research attention due to the fast growth of the EV industry. There has not been much research done to investigate SOE estimation techniques. As the SOE estimators are intended mostly for onboard implementations, it requires a fast computation speed while maintaining acceptable reliability. Like the SOC definition, SOE is defined as in (1.28), where E_N is the nominal battery energy. However, the integral of power suffers from errors from both the current sensor and the voltage sensor, and E_N can be different under different power loading conditions. Thus, other approaches to estimating SOE have been investigated.

$$SOE(t) = SOE(t_0) + \frac{\int_{t_0}^{t} P(\tau)d\tau}{E_N} \tag{1.28}$$

Like SOP estimation methods, SOE estimation methods can be categorized into two types: 1) methods based on the characteristic maps (CM), and 2) methods based on filters.

In [70], a look-up table containing the remaining energy with respect to different starting SOE and the operating discharge power was constructed based on experiments, as shown in Fig. 1.50. Though this look-up table was only valid for 25°C, it was validated to be effective estimating SOE during a pure-discharge dynamic cycle at 25°C, shown in Fig. 1.51.

Another look-up table based SOE estimation could be found in [71], where experiments helped construct graphs of the total available energy in terms of SOC and discharge current rates, as shown in Fig. 1.52 and Fig. 1.53.
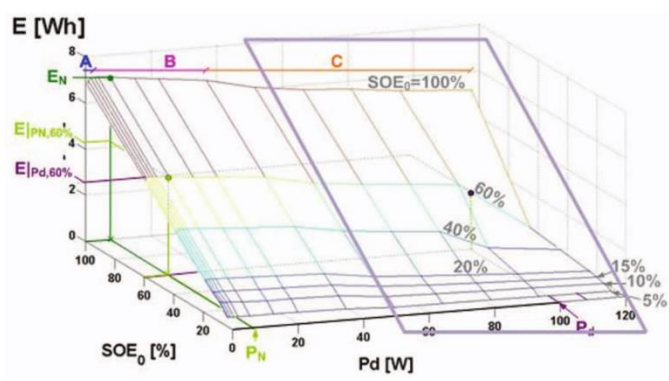
Fig. 1.50: Look-up table of rem. energy vs. initial energy and discharge power at 25°C
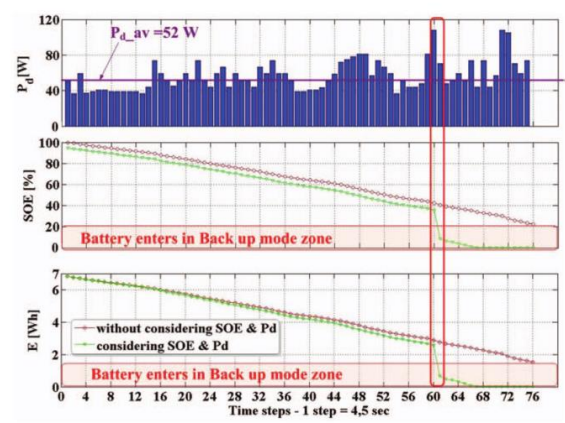
Fig. 1.51: Comparison between look-up table estimated SOE and cumulative calculated SOE
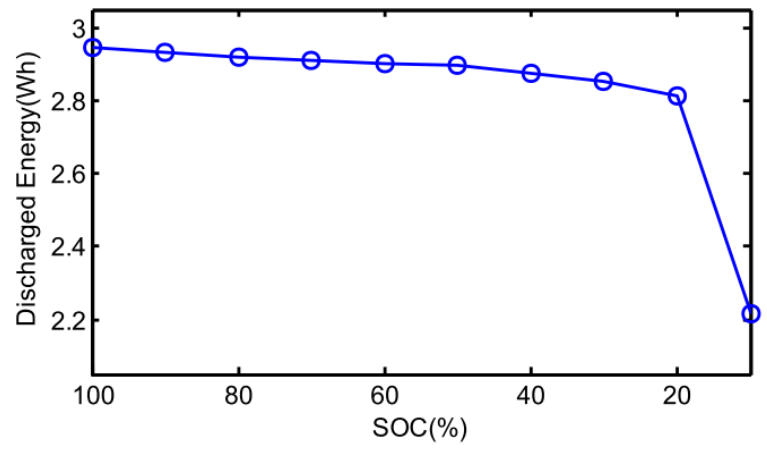
Fig. 1.52: Look-up table of avail. energy vs. SOC
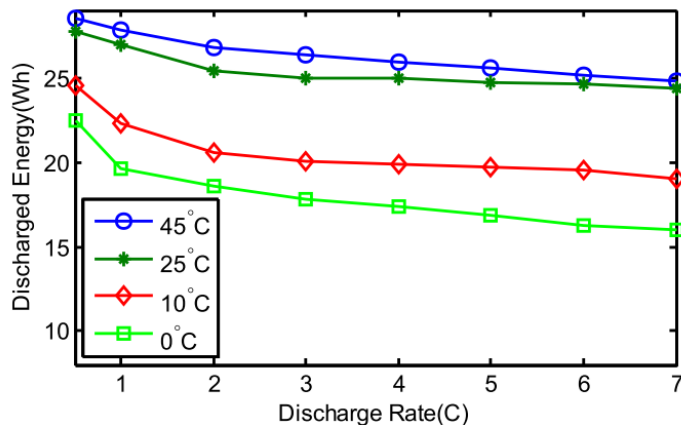
Fig. 1.53: Look-up table of avail. energy vs. discharge current rates at different temperatures

Based on the correlation plots, a back-propagated neural network (BPNN) was constructed linking voltage, current, and temperature to remaining energy (SOE). The BPNN structure is shown in Fig. 1.54, and Fig. 1.55 shows a good agreement between the estimated SOE from the trained BPNN and the measured SOE using accumulation of power.
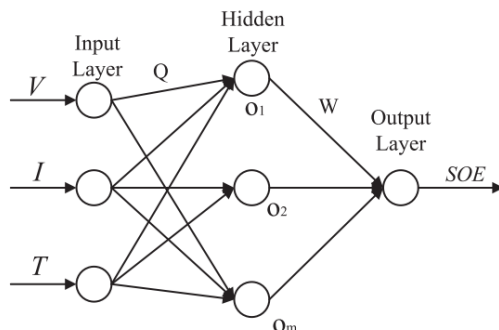
Fig. 1.54: BPNN structure for the SOE estimation
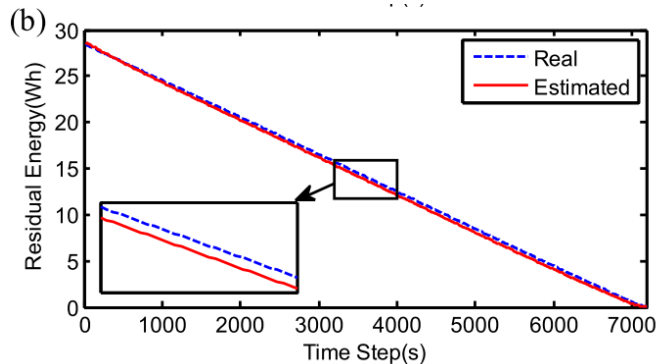
Fig. 1.55: SOE estimation performance based on the BPNN

On the other hand, another category of SOE estimation has been based on filter-based methods. Different types of filters could be found in [67], [72], and [73]. In [67], an unscented KF was applied based on the 1RC ECM model and the SOE estimation error of such model was kept under 1% under the FUDS drive cycle, as shown in Fig. 1.56 and Fig. 1.57.
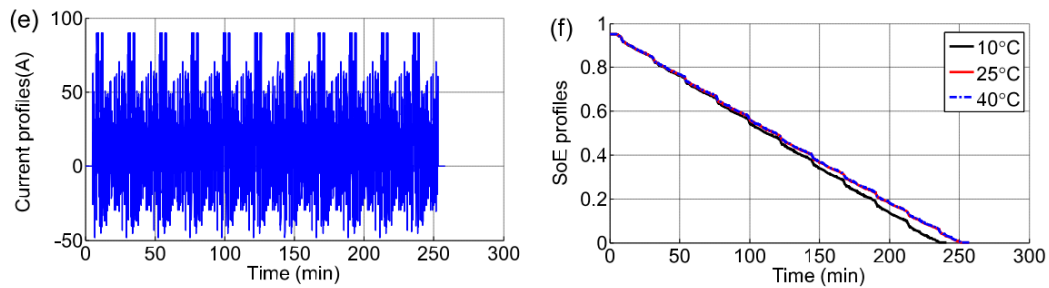
Fig. 1.56: FUDC current profile and SOE estimation at diff. temperatures
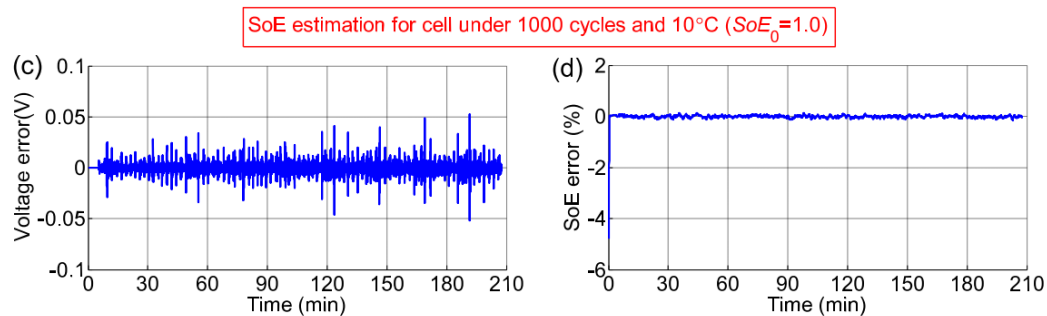
Fig. 1.57: ECM voltage model error and SOE estimation error at 10°C

An approach using central-difference Kalman filter (CDKF) could be found in [72], while [73] used Particle filter approach. The SOE estimation performances in both cases were shown to be effective. One can refer to the papers for details.

1.7   Lithium-ion Battery Aging Mechanism

As the Lithium-ion battery is widely used in the modern electronics area, as well as the power source for electric vehicles and energy storage, its durability has been significantly emphasized to improve productivity. Therefore, its aging mechanisms are worthy of extensive review and investigation.

Both the cathode and anode of a lithium-ion battery experience aging, and the mechanisms can be different from each other [74]. In addition, electrolyte influences the aging at both electrodes and ages itself mainly at the interface between itself and electrodes.

1.7.1   Aging of Carbonaceous Anodes

Though anode materials like lithium storage metals and alloys have recently been found increased attention, a much more complete understanding of anode aging has been accomplished with graphite-based cells [75]. In general, the aging effects are influenced by the different chemistry and the nature of the specific cell components for different Lithium-ion batteries. However, the physical theory behind dominant aging mechanisms of graphite anodes is similar and will be discussed. It is pointed out that changes of the electrode at the electrolyte interface and in the electrolyte, of the active material, and of the composite electrode including the current collector, active materials, conductive additives, binders, or porosity, can be the sources of anode aging with time and use [74]. Among these three different regions of sources, changes at the electrode/electrolyte interface are believed to be the primary source of aging at the anode.

1.7.1.1 SEI Formation, Function, and Relation to Aging

During the first cycles of a lithium-ion battery, electrolyte decomposition occurs together with irreversible consumption of lithium ions at the electrode/electrolyte interface as the electrode is in the charged state. The decomposition results in the build-up of "protective layers" that cover the electrode's surface. At specific graphite surface sites, where intercalation/deintercalation occurs between lithium ions and graphite structure, the layers there are called the solid-electrolyte-interphase, SEI. SEI layers protect reduction of the electrolyte compounds and corrosion of the charged electrode by approximately allowing lithium cations and electrons, but not other electrolyte components, to permeate into the graphite structure [74]. However, throughout the entire battery life, some charged and neutral species still diffuse through the SEI layer and these result in irreversible charge capacities and self-discharge reactions. As a result, corrosion happens

at the anode, and the electrolyte decomposes, causing electrolyte loss, SEI layer growth, and battery capacity loss. As summarized in [74], SEI layer formations occur during the first few cycles to protect the battery anodes. However, SEI conversion, stabilization, and growth occur during the entire life of Lithium-ion battery usage, during which aging phenomenon happens.
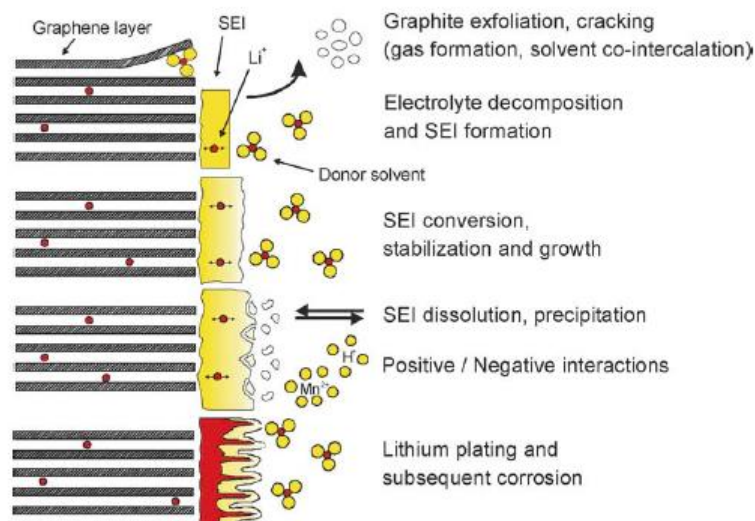
Fig. 1.58: Graphical demonstration of aging mechanisms at anode/electrolyte interface

Moreover, SEI thermal behavior plays an essential role when operating temperature affects cell properties like power fade and impedance rise [76]-[77]. It is shown that SEI layer breaks down or dissolves at a higher rate-of-degradations at elevated temperatures, while the reconstruction of the damaged SEI layer produces inorganic components, reducing ionic conductivity of the SEI layer for lithium [74]. A graphical illustration of the aging mechanism at the anode/electrolyte interface is shown in Fig. 1.58:

1.7.1.2 Changes of the Active Material and the Composite Electrode

Besides the important aging mechanism happening at the SEI layer, minor aging effects occur within the bulk of the active material, as well as the composite electrode. The changes within the active materials mostly result in structural cracking or damage on the graphite. Examples include graphite exfoliation and graphite particle cracking, because of solvent co-intercalation, electrolyte reduction, or gas evolution inside graphite [78]. The aging effect within the composite

electrode mainly is due to contact loss between carbon particles resulting from the volume changes of the active material, and thus mechanical disintegration within the composite electrode. Moreover, internal cell pressure and current collector corrosive both play a role in aging as well [79] - [84].

In summary, Table 1.3 summarizes the aging mechanisms at the carbonaceous anode describing causes, effects, and influences. It is shown in Table 1.3 that SEI layer growth appears in most of the aging causes. Therefore, insight may be provided by a quantitatively model of the aging mechanisms of a Lithium-ion battery, especially its anode aging, SEI layer thickness can be a possible measure to take most of the aging causes into account.

Table 1.3: Lithium-ion battery anode aging – causes, effects, and influences [74]

Cause	Effect	Leads to	Reduced by	Enhanced by
Electrolyte decomposition (→SEI) (Continuous side reaction at low rate)	Loss of lithium Impedance rise	Capacity fade Power fade	Stable SEI (additives) Rate decreases with time	High temperatures High SOC (low potential)
Solvent co-intercalation, gas evolution and subsequent cracking formation in particles	Loss of active material (graphite exfoliation) Loss of lithium	Capacity fade	Stable SEI (additives) Carbon pre-treatment	Overcharge
Decrease of accessible surface area due to continuous SEI growth	Impedance rise	Power fade	Stable SEI (additives)	High temperatures High SOC (low potential)
Changes in porosity due to volume changes, SEI formation and growth	Impedance rise Overpotentials	Power fade	External pressure Stable SEI (additives)	High cycling rate High SOC (low potential)
Contact loss of active material particles due to volume changes during cycling	Loss of active material	Capacity fade	External pressure	High cycling rate High DOD
Decomposition of binder	Loss of lithium Loss of mechanical stability	Capacity fade	Proper binder choice	High SOC (low potential) High temperatures
Current collector corrosion	Overpotentials Impedance rise Inhomogeneous distribution of current and potential	Power fade Enhances other ageing mechanisms	Current collector pre-treatment (?)	Overdischarge Low SOC (high potential)
Metallic lithium plating and subsequent electrolyte decomposition by metallic Li	Loss of lithium (Loss of electrolyte)	Capacity fade (power fade)	Narrow potential window	Low temperature High cycling rates Poor cell balance Geometric misfits

1.7.2   Aging of Lithium Metal Oxide Cathodes

Cathode materials affect Lithium-ion battery performance and calendar life significantly. Lithium manganese oxides ($LiMn_2O_4$), lithium nickel cobalt mixed oxides ($LI(NiCo)O_2$), and

lithium cobalt oxide ($LiCoO_2$) have been the most common cathode materials for Lithium-ion cells [74]. Since the different aging mechanisms at the cathodes highly depend on the materials, some basic aging mechanisms are summarized in this section.

Usually, the chemical reaction of the cell cathodes is described as following:

$$LiMeO_2 \leftrightarrow Li_xMeO_2 + (1 - x) Li^+ + (1 - x) e^-$$
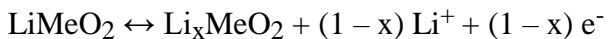
As the insertion/extraction of lithium ions occurs during the reaction, several changes may happen on the cathode that affect the lifetime of a lithium-ion cell. As stated in [74], there could be aging of active material, degradation or changes of electrode components, oxidation of electrolyte components and surface film formation, and even interaction of aging products with the negative electrode. These different effects were found to occur simultaneously and cause cell capacity fading in three ways [74]:

1. Structural changes during cycling

2. Chemical decomposition/dissolution reaction

3. Surface film modification

A comprehensive schematic overview is shown in Fig. 1.59 to describe aging mechanisms for lithium-ion cell cathodes.

It is noted that though cathode aging mechanisms are difficult to quantitatively model due to the following reasons:

1. Cathode materials vary based on cell type and therefore surface film components are undetermined.

2. Structural damage could happen randomly in terms of both time and position and therefore be difficult to physically model and quantitatively calculated.
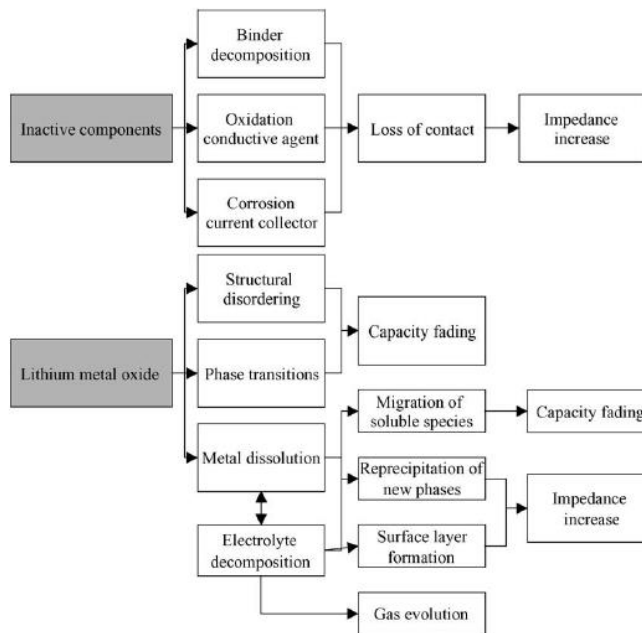
Fig. 1.59: Aging mechanisms of lithium-ion cells cathode materials [85]

1.8 Lithium-ion Battery Degradation Metrics

To quantitatively represent the current aging state of any lithium-ion cell and improve lifetime predictions, two primary degradation metrics, capacity and resistance, have been found and evaluated to be appropriate.

1.8.1 Capacity and Capacity Loss as an Indicator of Degradation

Capacity loss is the most fundamental measurement of cell degradation. The capacity of a cell is the number of amp-hours it can provide when taken from a fully charged state to a fully discharged state at a specified discharge rate [92]. Capacity is a relatively easy battery characteristic to measure and is often used as a benchmark for when a battery is no longer useful as an energy storage device for an application. Often, the lifetime of a cell is specified as the number of cycles until the capacity drops to 80% of its original value, but this threshold varies based on the application.

The amp-hours amount required to charge a cell entirely is always higher than the available

amount to be fully discharged due to different loss mechanisms. The difference is dependent on the rate of discharge. The high discharge rate of 1C or more makes the cell reach the discharge cut-off voltage prematurely due to the higher voltage drop across the cell internal impedance. As a result, the cell shows significantly lower apparent capacity and could be misleading. Therefore, when measuring capacity to indicate cell health state, it is necessary to compare the amp-hours discharged with the same discharge rate and temperature, to be able to predict the capacity under similar conditions.

1.8.2   Measuring Capacity

The capacity of a cell is theoretically a definite and measurable quantity. However, temperature and discharge rate significantly affect the apparent capacity. As a result, the real capacity is impossible to measure. Using very low currents will provide the best estimation of the actual capacity, since the effect of the internal impedance will be negligible at very low currents such as C/20, and temperature changes are small in such cases.

Practically, an entire charge-discharge cycle is performed at a controlled current rate and constant temperature to measure cell capacity repetitively. However, performing a complete cycle with a low discharge current rate is not desirable in most applications due to its time-consuming nature. Therefore, other methods to estimate the capacity may be used.

1.8.3   Impedance as an Indicator of Degradation

Since direct capacity measurement is undesirable, it has been found that cell impedance can be another useful metric to represent cell degradation states. It has been found that, for the specific cells under investigation, the 1kHz impedance of the cell has a strong correlation to the capacity and can be used to predict cell capacity [88]. For other cells, this frequency can be different, but it always corresponds to the frequency in which the impedance of the cell is entirely real, denoted as R_0 in the following sections. This method does not require measuring capacity, but instead uses the cell impedance at a specific frequency to represent cell degradation state. Fig.

1.60 below shows the comparison between the 1kHz impedance and cell capacity during the cell cycling.
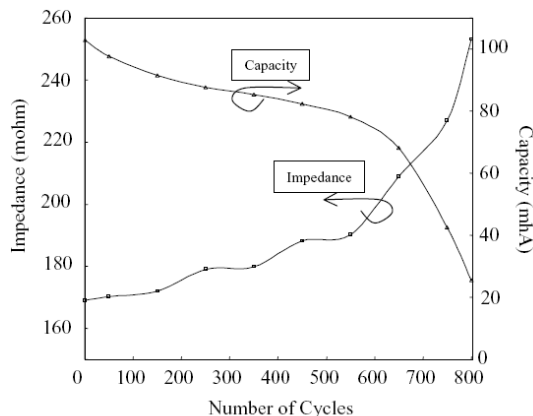
Fig. 1.60: Relationship between 1kHz impedance and cell capacity

Estimating the values of the different components in the model can be challenging. The solution resistance, R_0 , is approximately the impedance where the spectrum crosses the real axis at high frequencies [19]. In addition, since EIS is based on a single frequency signal injection FFT methodology, impedance responses at different frequencies are measured individually. To characterize the degradation of a lithium-ion cell, R_0 is measured since it is highly correlated to the capacity [88]. Therefore, a limited spectrum form of EIS is sufficient if it contains the two consecutive impedance points across the real axis. This adjustment could significantly improve the sampling rate of measuring battery resistance. A complete EIS spectrum takes typically about 10 minutes to finish, whereas two frequency responses at around 1 kHz would only take seconds to measure.

1.8.4   Impedance Spectrum Variations During Aging Process

Impedance characteristics of a cell change through cycling or storage and can be used to quantify the amount of degradation within the cell. Since the cell capacity fades over aging process, and there is a negative correlation between cell capacity and cell impedance, the real component of impedance increases, and the semicircles become larger over time [5]. Changes in parameter

estimates in the equivalent circuit after cycling can be used to identify what specific parts of the cell experienced degradation. Fig. 1.61 shows a typical cell impedance spectrum shifting as the cell experiences aging.
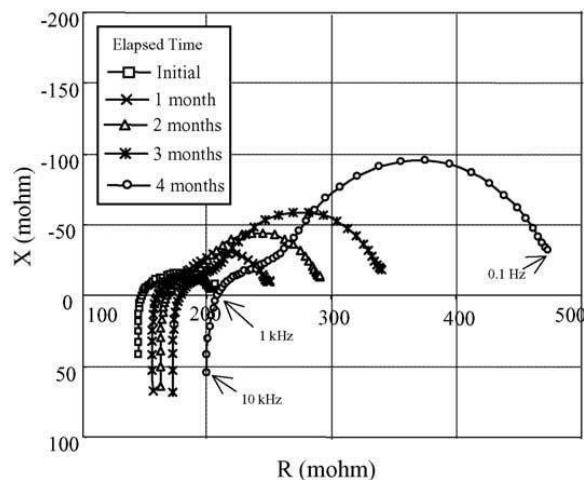
Fig. 1.61: The shifting aging cell impedance spectrums [5]

It is also noted that there are several effects, such as state-of-charge (SOC) and temperature, affecting cell impedance spectrum intrinsically. As a cell is being discharged, SOC of the cell decreases, and cell impedance in low-frequency regions increases in both real and imaginary components, while high-frequency impedances show slight changes. The high-frequency impedance is dominated by inductance, which is almost entirely a characteristic of the cell geometry and cables, and thus would not be expected to change [21]. The series resistance corresponding to the electrode and solution resistance does not change as a function of SOC either. The concentration of the solution ions remains constant as a function of SOC; therefore, its resistance is not expected to change [21]. Fig. 1.62 shows the impedance spectrums of a typical lithium-ion cell at different SOC. It is shown that the low-frequency impedances show much more significant variations than that of the high-frequency impedances.
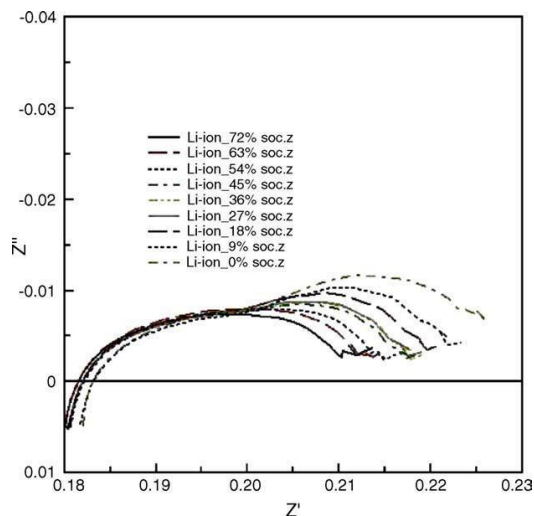
Fig. 1.62: Impedance spectrum variations at different SOC [94]

Since factors such as SOC and temperature affect the impedance spectrum, it would be more appropriate to perform impedance spectroscopy on a cell at the same SOC and temperature, if one wants to compare the spectrum shift through the aging process. The impedance spectrums would be incomparable if the other potential variables were not fixed.

1.9   Lithium-ion Battery Offline SOH (Degradation) Modeling Approaches

Since battery aging could lead to undesirable failure or even chemical pollution, the capability to predict the aging performance of batteries has been widely investigated. There have been a few classes of methods that are discussed in the literature. The most-used two types of approaches are:

1. Statistical approach: Empirical fitting of aging metrics based on aging data

2. Physics-based approach: Constructing physics-based model to include secondary reactions responsible for aging

Both approaches have respective advantages and disadvantages. Since this thesis focuses on physics-based modeling, the statistical approach will be shortly introduced, and more emphasis will be put into introducing physics-based approach.

1.9.1   Statistical Methods for Aging Prediction

Statistical approaches relate the quantities of interests, such as SOC and temperature, with other measured quantities, such as resistance and capacity, to describe battery aging performance. This type of approach usually includes the following three steps [90][95][96]:

1. Operating batteries under specified test conditions. Test conditions are experimentally designed based on the relationship interested, e.g., effects of SOC and temperature on aging performance.

2. Periodic measurements of battery aging performance metrics, i.e., capacity and resistance.

3. Using statistical methods such as curve-fitting and parameter estimation to analyze the data. Fitted models could be used to predict battery performance in the future with similar conditions.

A few examples of statistical approaches for aging performance predictions will be introduced next to better explain both the advantages and the disadvantages of such approach.

In [95], Hochgraf et al. investigated the effect of cycling dynamics on lithium-ion cell degradation. A total of six cells were studied, two repetitive cells for each of three different cycling dynamics conditions. The three drive conditions included baseline dynamics, reduced dynamics, and calendar storage. Fig. 1.63 shows that the reduced dynamics drive cycle could have had a slower degradation compared to that of baseline dynamics. It is noted that in this study, resistances were normalized and measured consistently at 50% SOC, and the temperature was kept at 40oC. These fixed conditions ensured the comparability of the results under different conditions.
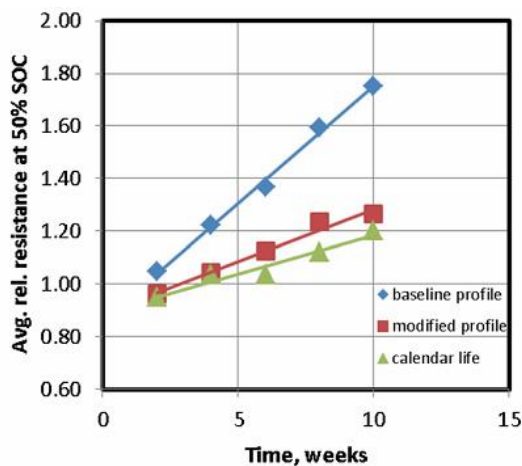
Fig. 1.63: Average normalized resistance at 50% SOC vs. time [95]

In another study, Ecker et al. investigated the effects of both calendar storage conditions and cycling conditions on cell aging performance [90]. Based on their data, they concluded that the storage conditions affect their cell degradation more significantly than cycling conditions. They further developed a life prediction model for different storage conditions, which presented a quantitative relationship between cell impedance and both the SOC of cells and the temperature during calendar storage. Fig. 1.64 shows some of their results that lead to the observation on the significant effect of storage conditions.
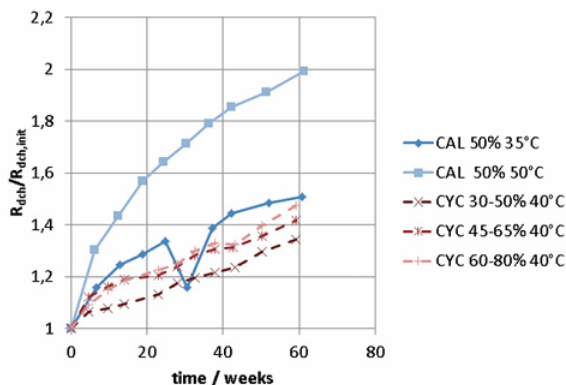
Fig. 1.64: Resistance growth under different storage and cycling conditions [90]

As discussed before, temperature plays a vital role in influencing battery aging. Thomas et al. presented a method to predict battery life with a statistical model based on the accelerated aging process [96]. A statistical model was constructed based on cell resistance data with respect to both

temperature and time. Such fitted model further helped predict cell resistance in the future at room temperatures. Fig. 1.65 shows the resistance data and fitted curves under their experiments with respect to different temperatures.
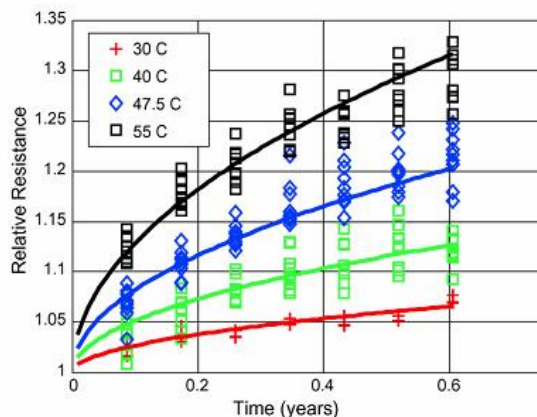
Fig. 1.65: Resistance and fitted curves vs. time under different temperatures [96]

In summary, statistical approaches remain a powerful tool to analyze battery aging performance. It bypasses the extreme difficulties regarding complex battery electrochemical process modeling and high uncertainty on physical parameters involved in such process. It also utilizes mathematical and statistical computation methods to better analyze the data and concludes accurate and comprehensive results. It is usually oriented to specifically investigate cell aging performance with respect to interested variables, which had been proven significant to aging characteristics. As a result, it has a drawback that such approaches require specifically designed experiments for specific conditions. One set of experiments could only help investigate one specific variable. This feature also limits the capability of the statistical approach for prediction, because any prediction will be constrained by the variable investigated previously.

1.9.2   Physics-based Approaches for Battery Aging Prediction

Physics-based modeling on the electrochemical process happening inside a battery has recently become an attractive research area. It helps relate theoretical electrochemical phenomena, such as diffusion and charge transfer with terminal characteristics measurements, such as voltage

and current. Doyle, Fuller, and Newman first published their work on developing a physics-based model for the battery electrochemical process in 1993 [22]. Other physics-based models that may focus on other applications have been developed using this original model as the starting point. Moreover, physics-based models to describe battery degradation are extensively investigated as a critical extension of Doyle, Fuller, and Newman's work. In the following, the derivation of Newman model is summarized using the original notation.

Since Newman's battery model published, extensive works have been done to improve battery performance simulation techniques. As lithium-ion cells become the most popular battery used in electric vehicles (EV) and hybrid EV applications nowadays, aging of lithium-ion cells becomes more of a concern. As a result, there has been a need for developing lifetime prediction methods for lithium-ion cells. Physics-based models based on a physical description of the aging phenomena are a significant part of these methods.

Physics-based models usually are divided into two groups. One is called as "phenomenological", where aging sources are described with several governing equations and interact directly with other model features. The other group uses mathematical models based on pristine cells, and some of the model parameters are updated through separate experimental relationships or statistical curve-fitting [97]. Between the two groups, phenomenological physics-based models describe the battery aging characteristics more comprehensively, yet have a more complex structure. The real battery system is too complicated to be analyzed thoroughly, and some aging sources like structural degradation of active materials are challenging to model. As a result, most physics-based models focus on a single aging source [97].

Before summarizing the work has been done on modeling lithium-ion battery aging, a list of the symbols, subscripts, and superscripts for the rest of this section is introduced in the following table.

Table 1.4: List of symbols and subscripts used in [22][97][98][99][100]

Symbol	Interpretation	Unit
a	interfacial area per unit volume	cm^{-1}
A_{anode}	anode area	cm^2
c_{eq}	equilibrium solvent molar concentration	$\frac{mol}{m^3}$
c_{Li}	lithium concentration in the carbon electrode	$\frac{mol}{m^3}$
c_{Li_max}	maximum lithium concentration in the carbon electrode	$\frac{mol}{m^3}$
c_p	product molar concentration in the SEI phase	$\frac{mol}{m^3}$
c_s	concentration in solid	$\frac{mol}{m^3}$
D_s	the diffusion coefficient of electrolyte in the polymer and of lithium in the solid matrix	$\frac{m^2}{s}$
i	the current density	$\frac{A}{m^2}$
i_0	exchange current density	$\frac{A}{m^2}$
F	Faraday's constant = 96487	$\frac{C}{eq}$
J_1	local current density for intercalation reaction	$\frac{A}{m^2}$
J_s	the current density of the solvent reduction reaction	$\frac{A}{m^2}$
k	the proportionality constant	/
k_0	the rate constant for solvent reduction	ms^{-1}
L	SEI thickness	m
M_p	the molecular weight of the newly formed surface film	$kg\ mol^{-1}$
n	number of electrons transferred in the electrode reaction	/

N_0	the initial number of moles of lithium available for cycling	mol
N_L	moles of lithium lost	mol
Q_s	capacity loss	Cm^{-2}
R	universal gas constant = 8.3143	$\dfrac{J}{mol\ K}$
R_P	the resistance of the film products	Ωm^2
R_{film}	film resistance at the electrode/electrolyte interface	Ωm^2
t	time	s
T	temperature	K
T_s	total parasitic reaction time	s
U	open-circuit potential	V
V	the terminal voltage	V
x	fractional capacity loss	/
X	SEI electronic conductance	mho
Z_p	stoichiometric coefficient of Li in P	/
α	anodic and cathodic transfer coefficients	/
λ	a constant in the similarity solution	/
ρ_P	the density of the newly formed surface film	$kg\ m^{-3}$
η_s	overpotential for the solvent reduction reaction	V
φ	the local potential of a phase	V
Subscript	Interpretation	Work Cited
n	the normal direction	[97]
s	side reaction	[97]
p	active material particles	[97]
0	exchange current density	[99]
c	the cathodic reaction	[99]
1	solid phase	[100]
2	solution phase	[100]
j	n (negative electrode), p (positive electrode)	[100]
ref	reference	[100]

Darling and Newman first tried to model side reactions that cause lithium-ion battery aging by introducing a solvent oxidation reaction into the lithium-ion battery model [98]. They adopted Newman's previous work on physics-based modeling of battery [97] and identified electrolyte oxidation during electrolyte decomposition as the failure mechanism of lithium-ion cells. In [97], a positive electrode was the focused electrode for analysis and the failure mechanism proposed is as following, where the perchlorate anion oxidizes in propylene carbonate on porous platinum around a specific range of voltage.

$$ClO_4- \rightarrow ClO_4 + e^- \rightarrow ClO_2 + 2O_{ad} + e^-$$
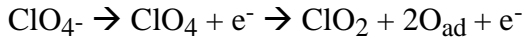
The adsorbed oxygen was suspected to be consumed in the oxidation of the propylene carbonate (PC) and resulted in the loss of active materials, as well as structural damage, such as a gas leak.

The proposed model adopted (1.29) described the intercalation of Li^+ following the Butler-Volmer kinetics and calculates the current density of primary reactions. In addition, since the potential of interest in their work was far from the equilibrium potential, they modeled the side reaction with Tafel kinetics:

$$i_{ns} = i_{0s}\exp(\frac{\alpha_s F(V-U_s)}{RT}) \quad\quad (1.29)$$

This side reaction equation allowed calculation on side reaction current density. Based on conservation of charge, a relationship was proposed between the divergence of the current density in the electrolyte phase and the reaction rates of both the primary and secondary reactions.

$$\nabla i = a_p i_p + a_s i_s \quad\quad (1.30)$$

Results from [98] showed some self-discharge processes in the cells under consideration, where self-discharge processes represented the PC oxidation and caused failure. Some of their results are shown below in Fig. 1.66 and Fig. 1.67.
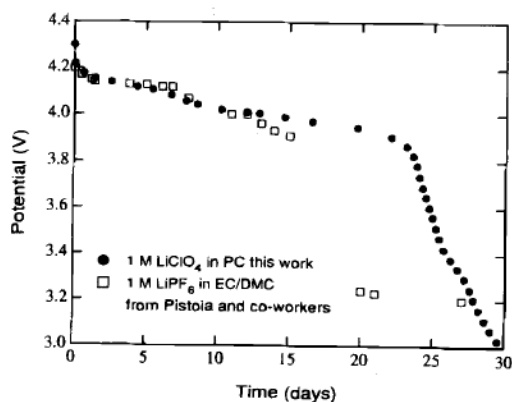
Fig. 1.66: Self-discharge of cell b52 after a galvanostatic charge at 30uA/cm^2 to 4.3V [98]
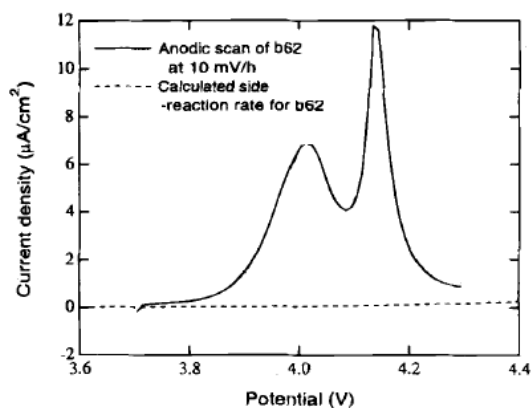
Fig. 1.67: Comparison of an anodic scan of b62 to the calculated side reaction current density

Fig. 1.66 shows that the cell suffered a self-discharge process, where its potential continually dropped after fully charged and even had a significant drop at about 4.15V. Meanwhile, Fig. 1.67 shows a comparison between the total current and the calculated side reaction current, where side reaction current could be up to 20% of the total current at high voltage.

After Darling and Newman published their work on modeling aging states of lithium-ion cells, research on this area has been widely recognized and developed. Ploehn et al. in [99] presented a "solvent-diffusion" model to predict capacity fading of lithium-ion cells during storage at different temperatures. They proposed the failure mechanism as that even though solid-electrolyte-interface (SEI) between the electrolyte and negative electrode primarily serves as a crucial passivating layer to minimize reduction of electrolyte components, some "poor" electrolyte

reduction accumulates on the SEI film, causes the SEI layer to grow, and results in lithium-ion cell aging [98]. This phenomenon backs the model that uses SEI layer growth as the metric to describe the cell degradation states. Therefore, the rate of lithium loss is proportional to SEI electronic conductance as in the following (1.31).

$$\frac{dN_L}{dt} = kX \qquad (1.31)$$

The aging mechanism diagram in [99] is shown in Fig. 1.68, and the model assumes a two-electron reduction at the carbon-SEI interface:

$S + 2e^- + 2Li^+ \rightarrow P$
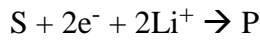
where, S is the solvent component and identified as ethylene carbonate (EC), and P is an insoluble product of either Li_2CO_3 or lithium alkyl carbonates based on EC concentrations level.
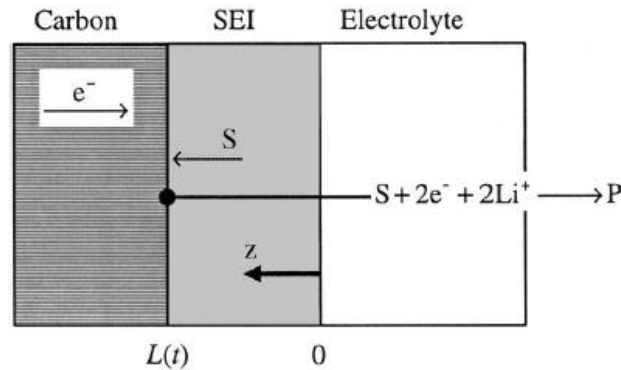
Fig. 1.68: Schematic of SEI growth via solvent diffusion [98]

In [99], the planar symmetry of the anode was assumed, and Fick's second law of diffusion (1.32) was also utilized to describe the solvent diffusion through the SEI.

$$\frac{\partial c_S}{\partial t} = D_S \frac{\partial^2 c_S}{\partial z^2} \qquad (1.32)$$

By applying the boundary condition that $c_S = 0$ at $z = L(t)$, a relation between the SEI layer thickness and storage time was proposed, as shown below.

$$L(t) = 2\lambda\sqrt{D_S t} \qquad (1.33)$$

$$\lambda = \frac{c_{eq} \exp(-\lambda^2)}{\sqrt{\pi}c_p \ erf(\lambda)}$$

A square root relationship was found, and since the capacity loss was linearly proportional to the SEI layer thickness, the partial capacity loss was calculated according to (1.34).

$$x(t) = \frac{2Z_p c_p A_{anode}\lambda}{N_o}\sqrt{D_s t} \qquad\qquad (1.34)$$

Based on this square root relation, simulation results were compared with experimental results with lithium-ion cells stored with a constant voltage. Simulation results for different temperatures during storage were also compared with experimental results. The results are shown in Fig. 1.69 and Fig. 1.70. The simulation results agreed with the experimental results in all cases.
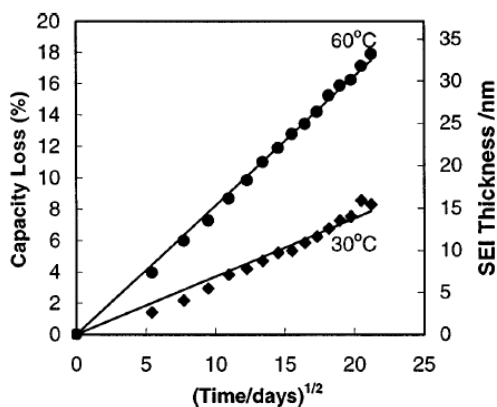
Fig. 1.69: Measured capacity loss and estimated SEI thickness vs. time stored at 3.9V [99]
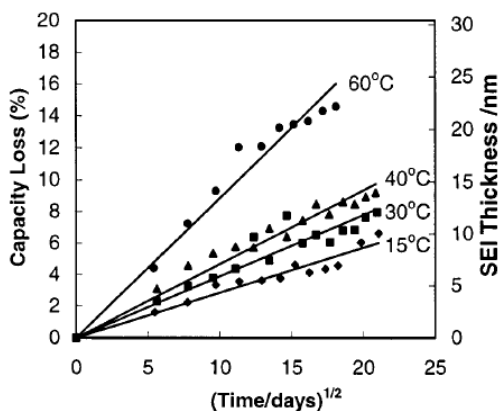
Fig. 1.70: Measured capacity loss and estimated SEI thickness vs. time stored at 3.8V [99]

Since in [99] no secondary reaction related equation was used to model capacity fading, Ramasamy et al. used similar modeling principles in [99], to improve the model to include secondary reaction equations, and develop a physics-based model to predict the lithium-ion cells capacity loss in carbon electrode during storage [100]. The aging mechanisms in [100] followed what had been stated in [99], that the two-electron reduction process of ethylene carbonate on the carbon anode into insoluble product caused the aging. As a result, SEI layer thickness increases and can be used as the metric to describe lithium-ion cell degradation states.

In this work [100], the solvent reduction reaction was modeled in a similar way as (1.29) with Tafel kinetics, since the potential window of interests is far from the reversible potential for EC reduction.

$$J_s = J_{s0}(\frac{c_{Li}}{c_{Li\_max}})^2 exp(-\frac{\alpha_c F}{RT}\eta_s)$$
$$J_{s0} = nFk_0\, c_{Li}^{2(1-\alpha_c)}$$
(1.35)

The relationship between the lithium concentration and side reaction current density was also bounded by the fact that the lithium depletes as fast as the solvent reduces, as shown in (1.35). This led to (1.36), where the rate of lithium concentration decreased was proportional to side reaction rate.

$$-\frac{1}{A}\frac{dc_{Li}}{dt} = \frac{J_s}{nF}$$
(1.36)

Moreover, the loss of active lithium-ions per unit surface during storage could be estimated by summating the side reaction current density over time.

$$Q_s = \int_0^{T_s} J_s dt$$
(1.37)

The SEI layer thickness was then calculated by relating the total occurrence of lithium-ion loss side reaction to SEI layer component physical parameters.

$$\delta_{film} = \frac{Q_s M_p}{n \rho_P F} \qquad (1.38)$$

Following the model presented, Ramasamy et al. carried out a set of simulations, where several lithium-ion cells were stored under different SOCs. The plots in Fig. 1.71 showed a square root trend, which reasonably agreed with their previous work in [99].
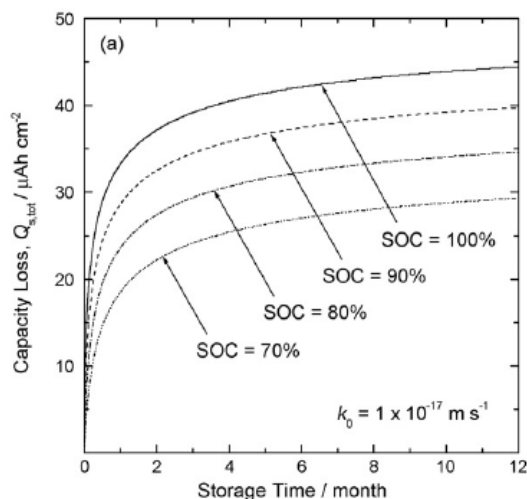
Fig. 1.71: Simulated capacity loss due to the self-discharge of the carbon electrode [100]

Except for the storage conditions, Ramadass et al. also considered the cycling scenario for lithium-ion cells and developed first principles of a capacity fade model for both the storage and cycling conditions [101]. It is noted firstly that this model used a similar thought process as introduced in [100], and both works assumed no transport limitation for the solvent across the SEI layer, i.e., the solvent was assumed to be abundant at the electrode. Secondly, this model assumed the same aging mechanisms used in [99] and [100].

In [101], since the test cases were no longer limited to storage, the primary reaction during battery cycling needed to be considered as well. Butler-Volmer kinetics were used to describe both the lithium-ion intercalation reaction, i.e., primary reaction, and the solvent reduction reaction. These two Butler-Volmer dynamic systems were considered separately. Therefore, an important assumption was made that the local volumetric charge transfer current density was defined as a

superposition of the intercalation and side reaction current densities. This relationship is given by

$$J = J_1 + J_s \tag{1.39}$$

Both primary reaction and side reaction current density were then calculated by the Butler-Volmer kinetics expression and Tafel kinetics expression with irreversible reactions. The expression for the primary reaction is listed in (1.40), and the expression for the secondary reaction was given in (1.35).

$$J_1 = a_j i_{0j} [\exp(-\alpha_{aj} \frac{\eta_j F}{RT}) - \exp(\alpha_{cj} \frac{\eta_j F}{RT})]$$
$$i_{0j} = k_j (c_{1j}{}^{max} - c_{1j}{}^s)^{\alpha_{aj}} (c_{1j}{}^s)^{\alpha_{cj}} (c_2)^{\alpha_{aj}}$$
$$\eta_j = \varphi_1 - \varphi_2 - U_{jref} - \frac{J}{A} R_{film} \tag{1.40}$$
$$j = n,p$$

In the expression to calculate the overpotential, the voltage drop due to the SEI layer was included based on Ohm's law and R_{film} was a metric other than the capacity loss used to define degradation state. R_{film} was defined as a summation of the initial SEI layer resistance and the increasing resistance portion caused by growing SEI layer thickness and is given by

$$R_{film} = R_{SEI} + R_p(t) \tag{1.41}$$

The progressing resistance, R_p, relates to the growth thickness of the SEI layer and is given by

$$R_p = \frac{\delta_{film}}{k_p} \tag{1.42}$$

The mass transfer differential equation that was given in (1.36) was also incorporated in this model to describe the solvent reduction reaction. The calculation of the capacity loss was the same as introduced in (1.37).

Based on the model, Ramadass et al. simulated the aging process for lithium-ion cells with different cycling cases. Some of their simulation results are listed in Fig. 1.72, Fig. 1.73, and Fig. 1.74.
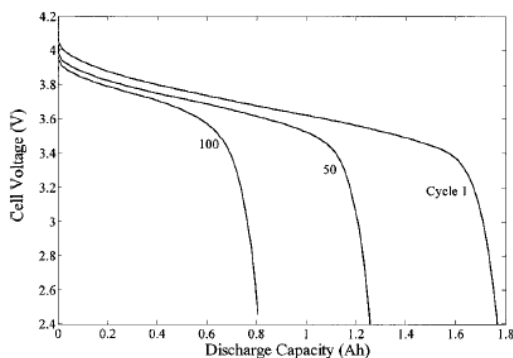
Fig. 1.72: Simulated discharge characteristics of lithium-ion cells for various cycles [100]
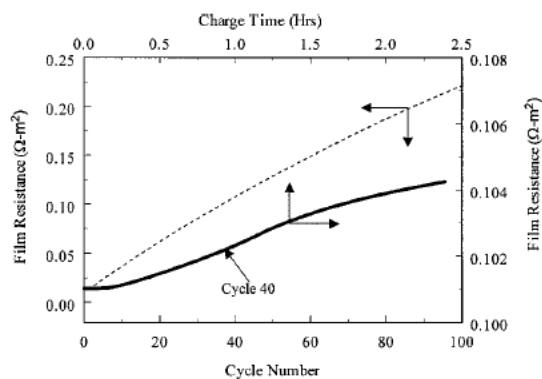
Fig. 1.73: Film resistance vs. cycle (solid line) & film resistance vs. charge time [100]
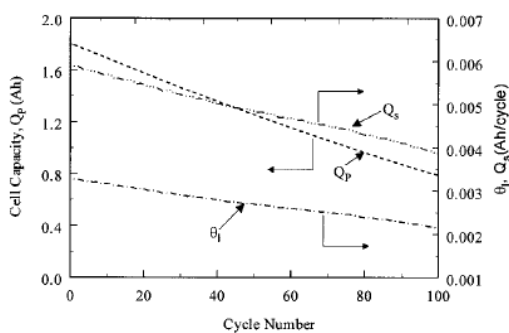
Fig. 1.74: Cell cap. (Q_p), cap. loss per cycle (Q_s), SOC loss per cycle (θ_1) vs. cycle[100]

The simulation results showed the capability of the model to describe two degradation metrics, resistance, and capacity, during the aging process of lithium-ion cells. It is noted that in [100][101], though lacking experimental evaluation of the proposed aging model, these models set the foundation for subsequent research, in which experimental results were used to evaluate the

model. Prada et al. followed the model Ramadass proposed and evaluated with storage aging experiments on lithium-ion cells, specifically lithium-ion iron-phosphate cells [89]. Lithium-ion cells were stored with different SOC with a fixed temperature, and the comparison between simulation results and experimental results are shown in Fig. 1.75. The model was evaluated to be reasonably accurate and can predict degradation states for the storage case. Prada.et.al later improved the model by incorporating a thermal model that could be used to provide a more accurate estimation of the battery temperature change during either storage condition or cycling condition [91]. Some results in [91] for both storage and cycling conditions are shown in Fig. 1.76 and Fig. 1.77, and there is a good agreement between simulation results and experimental results.

The model approaches discussed in this section are often used for battery offline degradation modeling. They provide insights on various aging factors and battery durability under different loading conditions for different applications. These insights help the manufacturer modify the cell designs to accommodate customers for different application requirements.
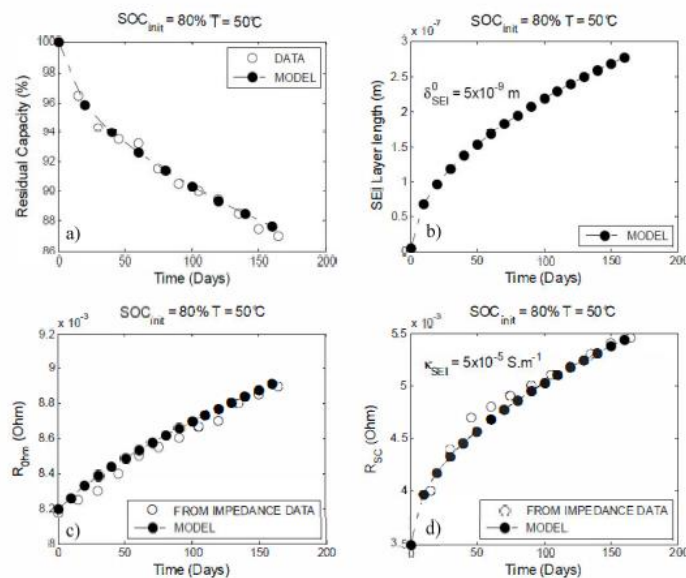
Fig. 1.75: Capacity, SEI thickness, series & charge transfer resistances vs. time[89]
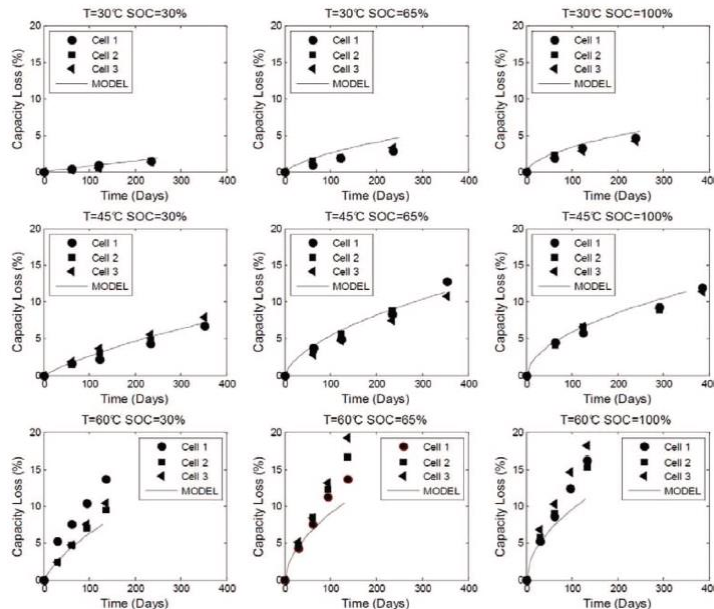
Fig. 1.76: Sim. & exp. capacity loss @ diff. ambient temperatures [91]
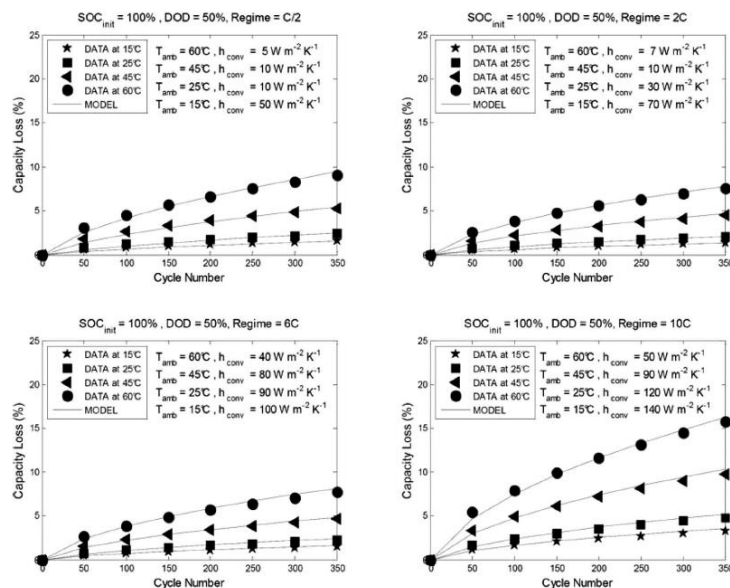
Fig. 1.77: Sim. & exp. capacity loss @ diff. cycling conditions[91]

1.10 Lithium-ion Battery Online SOH (Degradation) Estimation

Another set of SOH estimation technique is developed for online purposes. Based on the data gathered during operations, different state estimation techniques have been developed to

extract the information of the current health status of the batteries. As introduced in the previous section, capacity and resistance are the two metrics indicating battery SOH. Together with the direct SOH index estimation methods, these form the three categories of online SOH estimation methods.

1.10.1   Direct SOH Index Estimation

In some research, the brand-new battery has been designated with a SOH index of 1, which gradually decreases as the battery ages. As the battery is under loading, measured data are collected, while some states or parameters are filtered at the same time. The researchers try to find a correlation between one of these quantities and the SOH index.

For example, in [102], the authors proposed a method correlating the SOH index with the diffusion capacitance in a 2RC ECM. They applied a generic algorithm (GA) on the measured data gathered while the battery was under operation and estimated the diffusion capacitance value. The overall GA parameter estimation process is shown in Fig. 1.78.
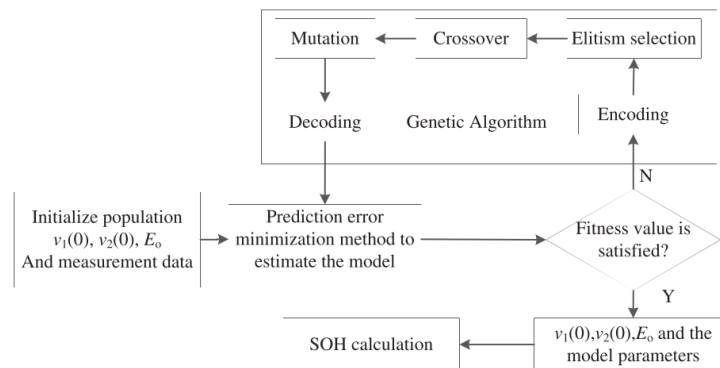
Fig. 1.78: GA parameter estimation flow chart

Since the diffusion capacitance, C_{diff}, was temperature dependent, they also proposed a health index function in terms of both C_{diff} and the temperature, as shown in ((1.43), where C_{diff_rat} was the rated diffusion capacitance at $25°C$ and other parameters in the equations were pre-determined.

$$h = f(C_{diff}, T) = (\frac{(a_1 T^2 + a_2 T + a_3) * C_{diff\_rat}}{1000 * C_{diff}} + b_0) * 100\% \qquad (1.43)$$

Another example was shown in [43], where the authors incorporated the SOH index in the standard coulomb-counted SOC calculation equation (1.44). C_r was the rated capacity.

$$S_{SOC\_t} = S_{SOC\_t-1} + \frac{(I_{batt} + \varepsilon) * \Delta t}{SOH * C_r} \qquad (1.44)$$

By applying a particle filter on estimated SOC rate of change between samples, the SOH index was then estimated. In Fig. 1.79, it shows both the SOC and SOH estimations for several runs on the same data. The results showed stable and rather robust SOC and SOH estimation performance.
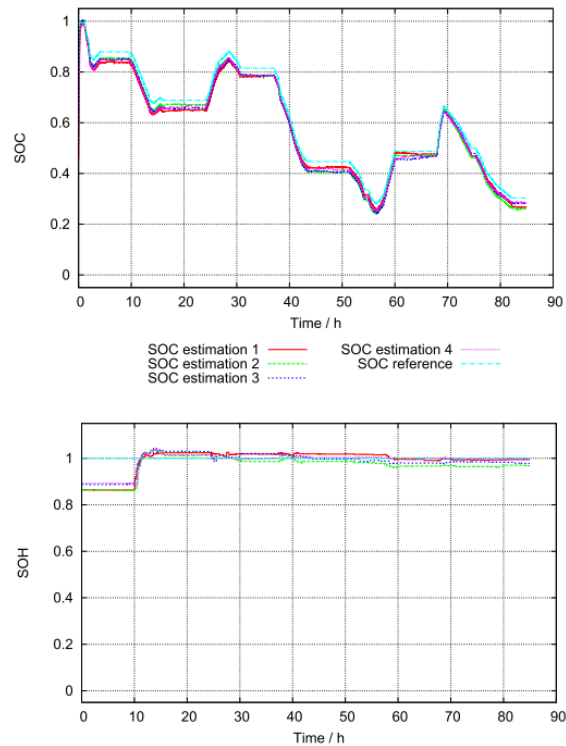
Fig. 1.79: SOC/SOH estimation results with the applied particle filter

In addition, some researchers have found that SOH index could also be estimated based the battery voltage curves during charging [103]. The authors analyze the standard CC-CV charging curves for a battery at different ages, shown in Fig. 1.80, and determine that the time

constant of the battery voltage increase during CC stage correlates to the battery SOH. After developing an ECM and including a SOH index in the time constant term, the authors apply least square methods to find the best estimated SOH index by fitting the voltage data during CC charging stage. SOH estimation results for three different batteries are shown in Fig. 1.81, demonstrating the generality of such method for different batteries.
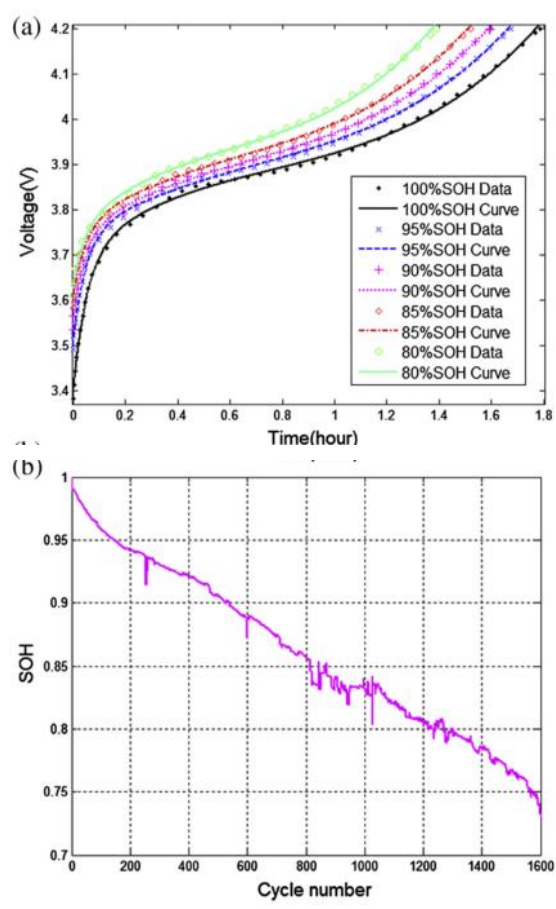
Fig. 1.80: Battery charging voltage curves at different SOH stages
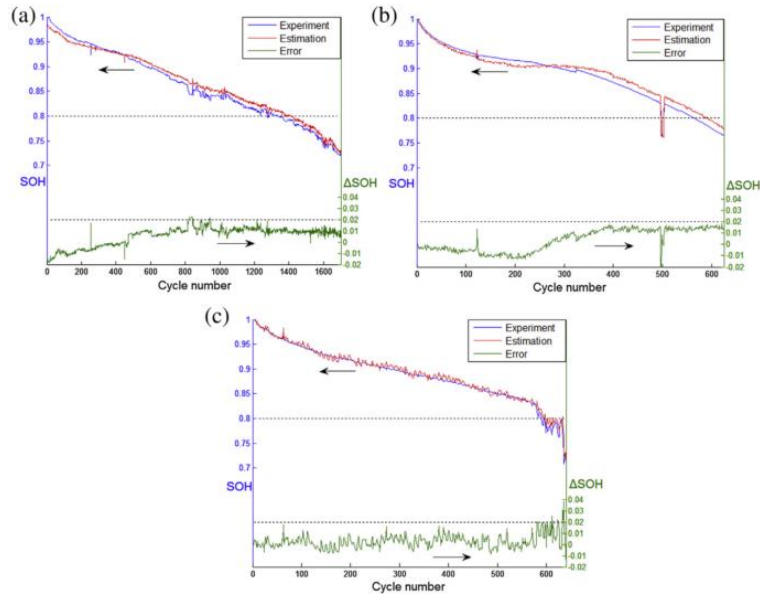
Fig. 1.81: SOH estimation based on charging curves for different batteries

1.10.2   Online SOH Capacity Estimation Methods

Capacity is a direct indicator of battery SOH, and different techniques have been developed to online estimate the capacity based on the sensing data collected during battery operations. In [104], the authors summarized different techniques estimating the capacity. The basic idea behind the algorithms was to formulate a model that can calculate the battery capacity. By inverting the coulomb counting SOC estimation equation, the capacity could be calculated as in (1.45).

$$C = \frac{\int_{t_1}^{t_2} \frac{\eta\, i(t)}{3600}\, dt}{SOC(t_2) - SOC(t_1)} \tag{1.45}$$

The charge change between two samples can be measured using an onboard coulomb counter or as the integral of current, while the SOC differences between two samples are based on other SOC estimation techniques such as filters. The capacity estimation steps are shown in Fig. 1.82. During the battery operation, the charge change measured by a coulomb counter is much easier to determine than the SOC change, which requires estimations. Since these SOC estimation techniques are crucial for the capacity estimation, such techniques are subdivided into two groups

[104]:

    1. Adaptive joint estimation techniques

    2. Adaptive dual estimation techniques

While the joint estimation techniques usually use a single state vector for parameter and state estimation, the dual estimation techniques formulate two filters, one for state estimation and one for parameter estimation. The filters used in these techniques can be divided into two groups as well:

    1. Methods based on least squares estimation

    2. Methods based on the Kalman filter, similar filters, and observer estimation

In some cases, the capacity is inserted as a state, while sometimes it is treated as a parameter. With a carefully formulated ECM, both approaches have been investigated and shown their effectiveness estimating capacity.

One interesting approach proposed in [105], not only considers the importance of achieving accurate SOC estimation, but also takes the sensing error within the coulomb counter into account.

While the method belongs to the least squares type, it extends to "total least squares (TLS) estimation" for its inclusion of the charge counting errors. As shown in ((1.45), the equation can be treated as a linear fit while the capacity is the slope value. The conventional least squares methods only consider the error on the y data, while the TLS method considers errors on both x and y, as illustrated in Fig. 1.83. This approach is then suitable for the capacity estimation.
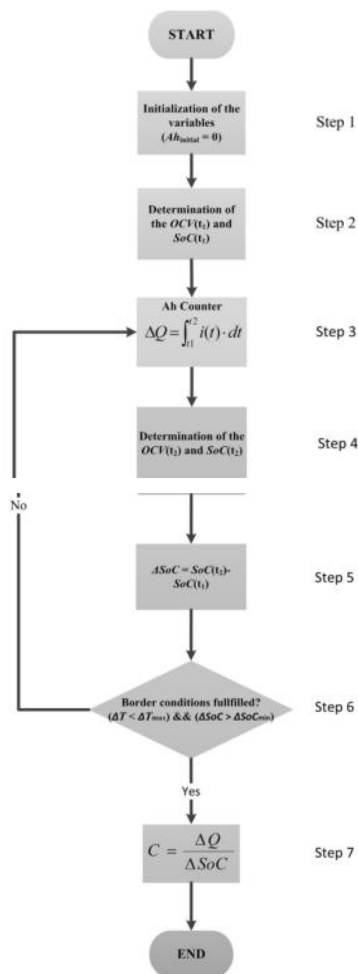
Fig. 1.82: Capacity estimation flow chart
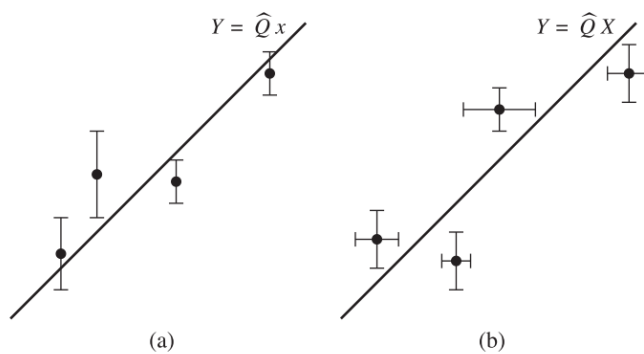
Fig. 1.83: Linear fitting (a) errors only on y, (b) errors on both x and y

The author proposed several different TLS methods and evaluates their effectiveness for a

hybrid electric vehicle application simulation. In Fig. 1.84, the simulation results are shown, and some types of the TLS approaches were evaluated to be effective.
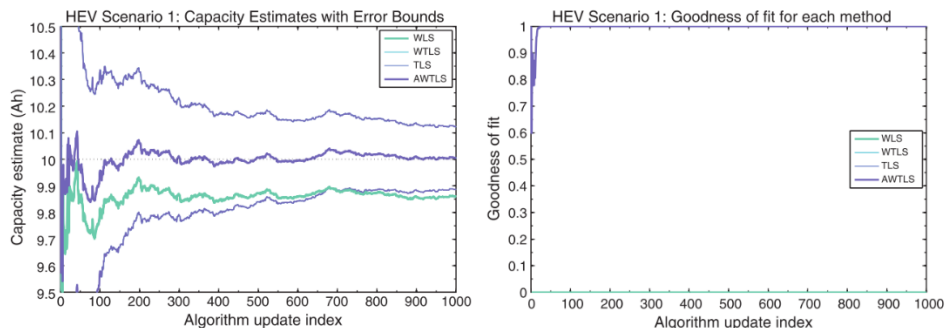
Fig. 1.84: TLS for capacity estimation for a hybrid electric vehicle application simulation

Overall, various capacity estimation methods have been developed. For onboard monitoring purposes, these methods are required to be stable, accurate, and most importantly, computationally light and fast.

1.10.3   Online SOH Resistance Estimation Methods

As discussed in a previous section, other than capacity, battery internal resistance can be another SOH indicator. The basic idea of resistance estimation is to formulate a battery model with resistance as one of the states, and online estimate the state based on the terminal data measured. There are three difficulties on estimating resistance: 1) constructing a suitable battery model, 2) compensating effects from other factors (i.e., temperature), and 3) controlling the estimation noise to an acceptable level because the resistance value is generally small.

Based on the requirements, two types of approaches have been investigated:

1. Filter-based approaches

2. Data-driven approaches

The filter-based approaches are generally developed based on the battery ECM since resistance is always one of the components in an ECM. As an example, in [106], a 1RC ECM was adopted, and the resistance was estimated by a least-square method. The authors also compensated

the temperature influence by a predetermined Resistance vs. Temperature look-up table based on the Arrhenius relationship. The estimated resistance values were also passed through a low pass filter to mitigate the noise level. In Fig. 1.85, resistance estimations for both the new and the aged cells are shown to demonstrate the online monitoring performance.
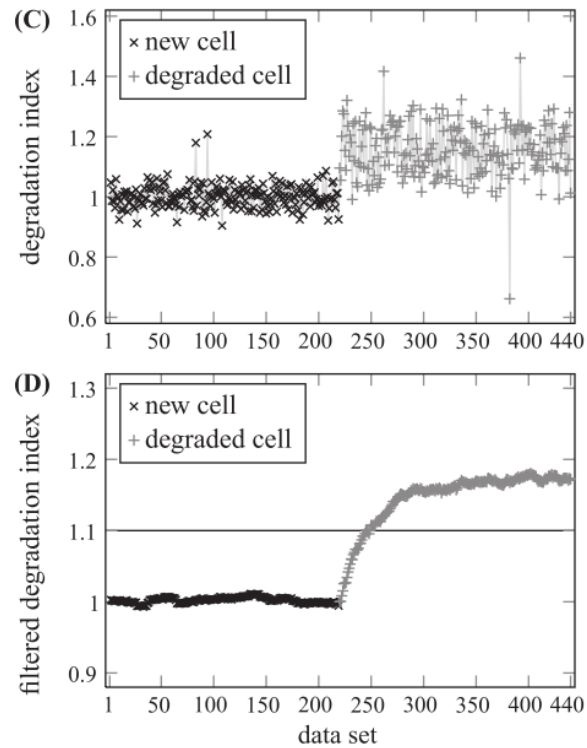
Fig. 1.85: Linear fitting (a) errors only on y, (b) errors on both x and y

Another set of online resistance method is using data-driven machine learning techniques. By formulating an NN battery model with resistance component in it and training it with data collected from both new and aged cells, a nonlinear resistance modeling can be achieved and used for online monitoring. An interesting NN structure was developed in [107], where the NN battery model was specially structured to include both the conventional charge transfer RC parallel ECM components and the ohmic resistance component represented by a neural network. Moreover, both the temperature effect and SOC effect on the ohmic resistance were considered. This structured neural network (SNN) is shown in Fig. 1.86.
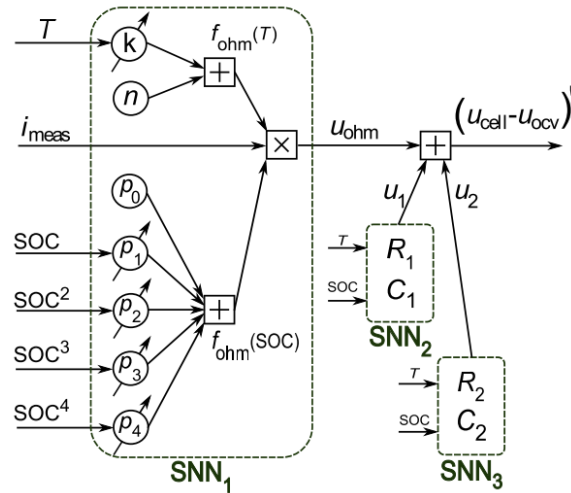
Fig. 1.86: SNN for the ohmic resistance and corresponding weights for a lithium-ion cell

After training the SNN with already collected battery cycle data from the battery BOL to the battery EOL, the parameters were identified in the model. The authors also compared the resistance estimation performance between using the SNN and using an EKF. The comparative results of the ohmic resistance estimations are shown in Fig. 1.87. Both methods achieved similar outcomes. However, since the SNN was trained offline, the online estimation took less time to compute compared to the EKF.
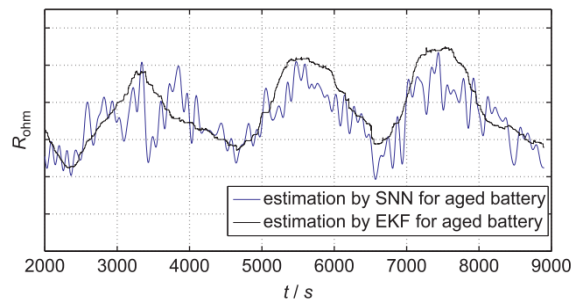
Fig. 1.87: Resistance estimation performance comparison between SNN and EKF

Overall, several resistance estimation methods have been developed. The onboard implementation of such estimations requires fast computation as well. Different from the capacity estimation, the resistance estimation could suffer from uncertainties from factors like temperature and SOC but could also be used as an indicator of battery power.

1.11   Lithium-ion Battery Degradation Control Schemes

Since the lithium-ion battery has become a significant part of modern energy storage applications, there has been extensive work to investigate different methods of enhancing battery performance and extending battery life. Different control schemes have been investigated, evaluated, and applied for different applications. In this section, different degradation control schemes, including both the passive control and the active control, will be introduced and discussed briefly.

1.11.1   Passive Control Schemes: Electrolyte Additives

There has been extensive work in the material area to improve lithium-ion type batteries' performance by investigating and experimenting with new materials for the cathode, the anode, and other cell components. Since this thesis focuses on the degradation investigation for general lithium-ion batteries, specific material science development for novel lithium-ion battery components will not be discussed in detail. Instead, another typical passive control scheme, applying electrolyte additives, will be briefly introduced for its use of generally improving lithium-ion battery performance.

There have been different additives used in lithium-ion batteries, which are categorized by their different functions. These include SEI forming improver, cathode protection agent, $LiPF_6$ salt stabilizer, safety protection agent, Li deposition improver, and other agents like solvation enhancer, Al corrosion inhibitor, and wetting agent [108].

Usually, less than 5% by weight or by volume of such an additive is added into the electrolyte mainly to improve cyclability and cycle life [108]. The typical functions these additives serve are summarized below [108]:

1. Facilitate SEI formation on the graphite anode surface.

2. Reduce irreversible capacity loss and gas leak during SEI formation and cycling.

3. Improve thermal sustainability.

4. Prevent dissolution and overcharge of cathode materials.

5. Improve physical property of electrolyte for better performance.

6. Reduce flammability of organic electrolyte.

7. Prevent overcharge conditions.

8. Terminate operation for ill-diagnosed batteries.

According to Table 1.3 presented in the previous sections, lithium-ion batteries suffer degradation in many situations. These could be that the SEI layer is not smoothly formed during first cycles, or the battery experiences extreme operating temperatures, there is a gas leak, or there is overcharging to cause lithium plating. Among all the functions of the electrolyte additives introduced, facilitating SEI formation, reducing capacity loss, and preventing gas leaks, as well as improving thermal stability and overcharge protection, are all valid ways to mitigate lithium-ion battery degradation. Fig. 1.88 below presents one brief example of the effectiveness in terms of degradation control by adding sodium salts to the electrolyte.
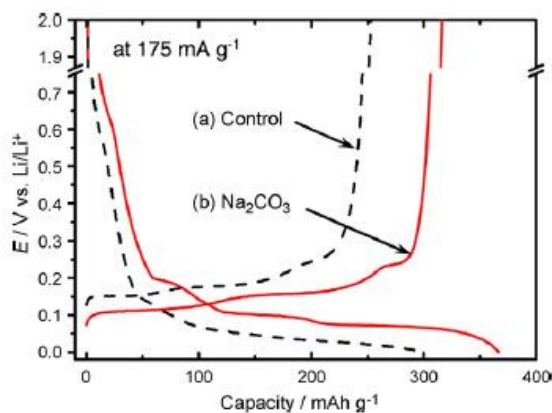
Fig. 1.88: Graphite electrode voltage (a)w/out (b)w/ a Na_2CO_3 solution pretreatment[108]

By adding sodium salt, there appears to be a small potential elevation of the intercalation between lithium anions and the graphite. This potential elevation helps keep the lithium-ion cell out of the sensitive voltage range of lithium plating on the anode, which will cause irreversible

lithium loss and capacity fading [108]. In addition, this potential elevation helps improve the cell power density to enhance performance.

In summary, passive control schemes have been extensively investigated in the recent literature and have proven to be effective enhancing battery performance and slowing battery degradation mechanisms. However, such an approach requires a physical modification of cell structure and is limited to in-situ situations. Therefore, active control schemes should be explored, especially for electric vehicle applications, where the batteries have already been manufactured and installed.

1.11.2   Thermal Management & Battery Voltage Balancing

Lithium-ion batteries have been widely used in all kinds of electrical applications, such as supplying power to electronics and serving as the primary energy source for electric vehicles. Many battery management systems (BMS) have been designed to monitor battery performance, prevent safety issues, and control degradation to improve cell durability. In this section, degradation control schemes based on thermal management and cell level equalization will be introduced.

Lithium-ion batteries are recommended to operate within specific operating regions restricted by temperature and voltage, to remain safe and reliable [109]. Fig. 1.89 below shows the proper temperature and voltage windows that a lithium-ion cell is advised to operate within.

It shows that lithium-ion batteries are recommended to operate within a temperature region generally from -20C to 50C and a voltage range from about 1.5V to 4.2V [109]. The plot only provides a general requirement, and different types of lithium-ion cells will have specific temperature and voltage ranges. Typically, elevated temperature leads to electrolyte decomposition and other structural damages that shorten cell lifetime, while low temperatures accelerate other degradation mechanisms, such as lithium plating. High voltages will cause overcharging and lead to lithium loss, while low voltages cause structural damage and active

material loss. For the rest of this section, degradation control schemes based on either proper thermal management or battery voltage balancing will be introduced, specifically for EV applications.
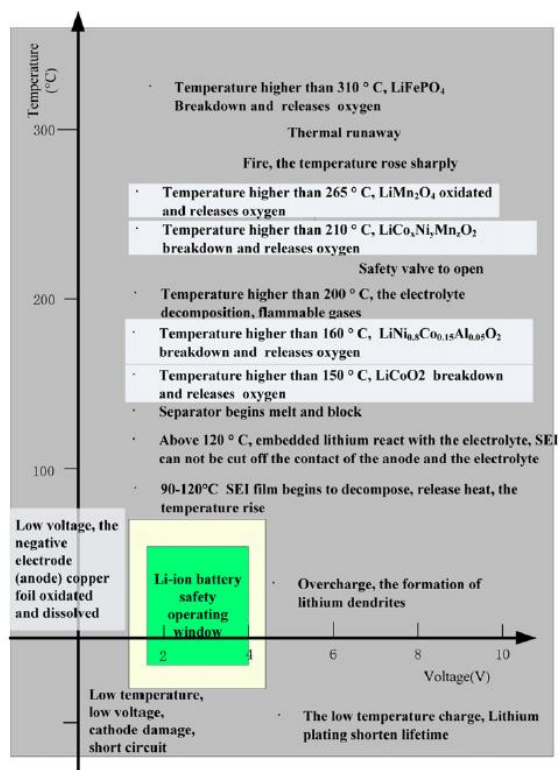
Fig. 1.89: Proper operating window for lithium-ion battery [109]

Thermal Management:

In EV applications, a battery pack of hundreds of cells is installed, and thermal management is a much more significant aspect to consider compared to temperature control in the single-cell situation. Elevated temperatures during operation lead the battery to exceed permissible temperature levels and decrease performance, while non-uniform temperature distribution in the battery pack causes local deterioration and reduces cell lifetime [109]. The thermal management systems usually focus on optimizing operating temperature range for every cell and all battery modules, maintaining small temperature variations in the module, and providing proper ventilation for hazardous gases [109]. It is also noted that a thermal management system may be passive and

mostly driven by the ambient environment. This passive approach can be modified to be active with a built-in source in the battery module to provide heating or cooling [109]. Usually, the thermal management system can be divided into the following four categories:

1. Air heating/cooling/ventilation

2. Liquid heating/cooling

3. Phase change materials (PCM)

4. Combination of 1, 2, and 3.

The following figures list out the basic schematics for the first three categories, including the passive design and active design.
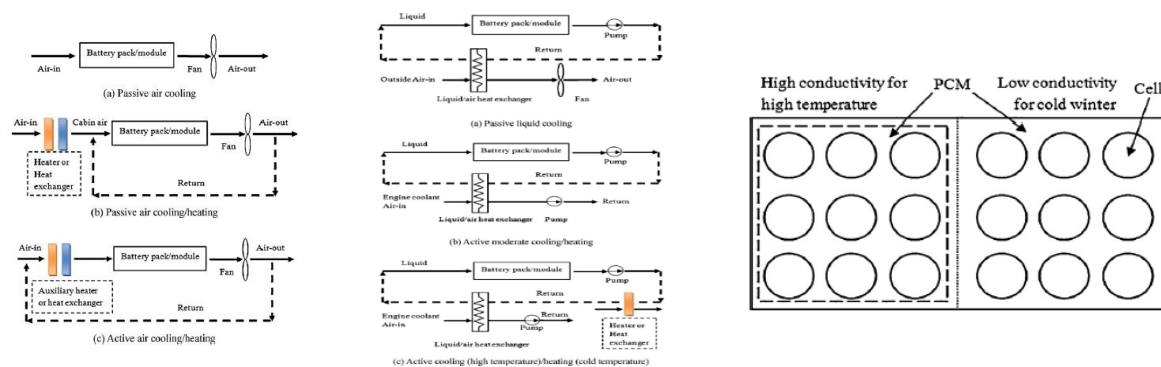
Fig. 1.90: Thermal management system using air/liquid/PCM [109]

Air cooling and liquid cooling share similar topologies and utilize the heat exchanger's concept in the respective thermal management system design. Built-in heat exchangers can help actively control the temperatures inside the battery modules. Thermal management systems using PCM, on the other hand, utilize the thermal properties of specific materials for the battery packaging and actively help maintain the battery pack within the ideal operating temperature range [109]. Further details on the thermal behavior modeling and analysis will not be discussed in this thesis.

Battery Voltage Balancing:

Imbalance of cells is common and results from both internal and external factors. Internal

factors include differences between cells in terms of the manufacturing volume, internal impedance, and self-discharge rate. External factors include unequal power draining for different cells, and thermal differences among cells. Without the balancing system, there will be voltage drift over time for some of the individual cells and the capacity of the whole pack will quickly decrease [110]. Fig. 1.91 shows three imbalance conditions that may or may not need cell balancing [109].
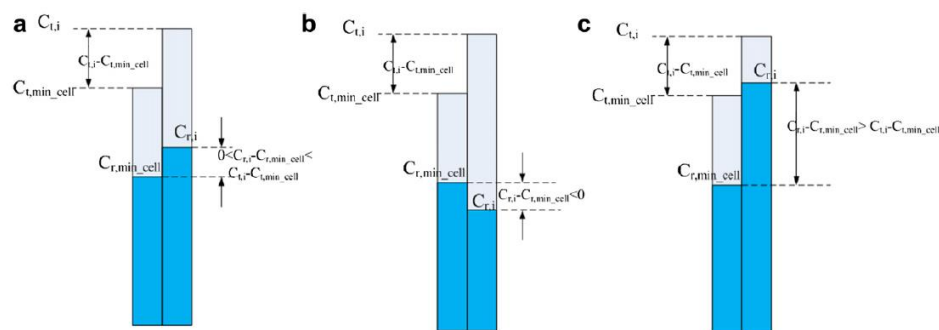
Fig. 1.91: Battery equalization cases (a)no need (b)overcharge (c)overdischarge[109]

In Fig. 1.91, $C_{t\ min\_cell}$ is the total capacity of the individual cell with minimum capacity. $C_{r\ min\_cell}$ is the current remaining capacity of this cell. $C_{t\ i}$ and $C_{r\ i}$ denote the total capacity and current capacity for another cell i. Fig.1.7-6(a) shows the situation when the cell with minimum capacity can be fully discharged or charged without causing any other cell over-discharged or overcharged. In this situation, no cell equalization is needed. However, Fig. 1.91 (b) and (c) show that situations when the other cells could be over-discharged or overcharged when the cell with minimum capacity is fully charged or discharged. Then cell balancing is needed in these cases [109].

There are both passive and active balancing methods. The passive methods can be only used for lead-acid batteries and nickel-based batteries because they can be overcharged without permanent damage [110]. Since the lithium-ion battery is the focus of this research, passive battery balancing methods will not be discussed further.

Active balancing follows the idea of using the external circuit to transfer energy among

cells to keep them balanced actively. Active battery balancing methods have been extensively applied to lithium-ion battery packs and can be categorized into three groups by circuit topology, shunting methods, shuttling methods, and energy converter methods [110].

Shunting active balancing methods remove the excess energy from the cells with higher voltages and let the cells with lower voltages catch up. Shuttling active balancing methods use external energy storage devices such as capacitors to transfer energy among cells to balance. Energy converter methods utilize isolated converters to release the excess energy from one cell to the whole battery pack [110]. Fig. 1.92 through Fig. 1.94 below show some example circuits for each type of balancing method. Table 1.5 gives a comprehensive comparison between these methods [110]. These figures and the table show the background of battery balancing development and details on circuitry theory and circuit analysis will not be discussed.

(a)   (b)
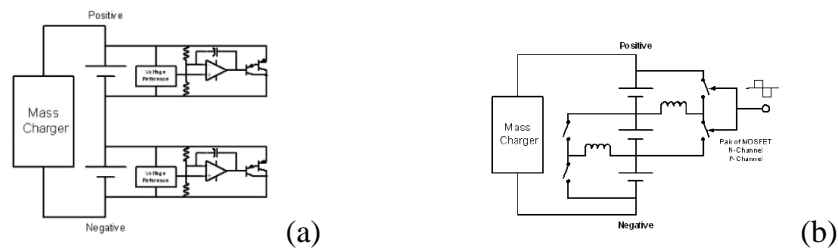
Fig. 1.92: Shunting methods (a)analog dissipative (b)PWM controlled [110]

(a)   (b)
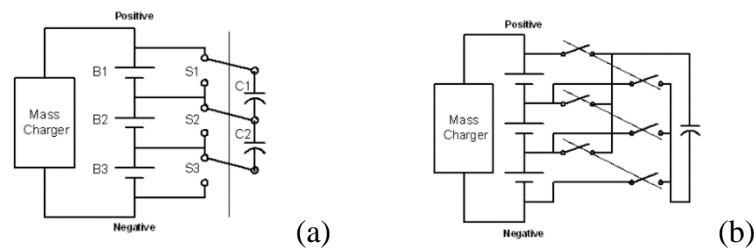
Fig. 1.93: Shuttling methods (a)switched capacitor (b)single switched capacitor [110]
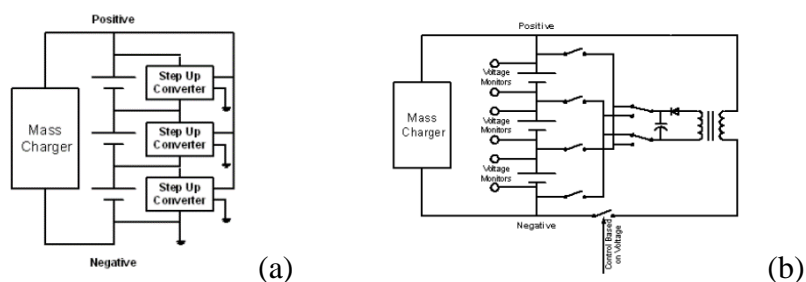
Fig. 1.94: Energy converter methods (a)step-up converter (b)switched transformer [110]

Table 1.5: Comparison between balancing methods

Balancing Methods	Balancing Nature	Major Components Needed to Balance an n Cell String	Best Effective Period	Modular Design Capability
Dissipative Shunt Resistor	Shunting	n Switches, n Resistors	Recharging	Easy
Analog Shunting	Shunting	n Transistors	Recharging	Very Easy
PWM Controlled Shunting	Shunting	2(n-1) Switches, n-1 Inductors	Recharging	Moderate
Boost Shunting	Shunting	n Switches, n Inductors	Recharging	Moderate
Complete Shunting	Shunting	2n Switches, n Diodes	Recharging	Moderate
Switched Capacitor	Shuttling	2n Switches, n-1 Capacitors	Recharging & Discharging	Easy
Single Switched Capacitor	Shuttling	2n Switches, 1 Capacitor	Recharging & Discharging	Poor
Step-up Converter	Energy Converter	n Isolated Boost Converters	Recharging	Easy
Multi-winding Transformer	Energy Converter	1 n Winding Transformer	Recharging	Very Poor
Ramp Converter	Energy Converter	1 n/2 Winding Transformer	Recharging	Very Poor
Multiple Transformer	Energy Converter	n Transformers	Recharging	Easy
Switched Transformer	Energy Converter	n+3 Switches 1 Transformer	Recharging	Moderate
Resonant Converter	Energy Converter	2(n-1) Switches, 2n inductors	Recharging	Easy

In summary, both passive and active approaches have been investigated in literature to control lithium-ion battery degradation. Passive control schemes mostly involve cell component material modifications. Such schemes will be limited in applications because the battery pack is physically inaccessible for any modifications once installed. On the other hand, active degradation control schemes have been developed in two aspects. One is to utilize a thermal management system to maintain the cell temperature in the desirable range. The other is to utilize external circuits to balance the energy among cells inside a battery pack to improve durability. These two active approaches can be summarized as active degradation control based on cell thermal loading balancing and active degradation control based on cell electrical loading balancing.

1.11.3 Battery Rate-of-degradation (ROD) Modeling

The cell level material modifications are usually investigated and developed by battery cell manufacturers to improve the cell performance and durability. The pack level thermal/electrical load balancing methods are widely investigated in both research and industry. However, based on

modern process/system control theories, it is also possible from the cell level, to develop direct control algorithms focusing on the interacting electrical and thermal loadings. Such approaches focus on manipulating some metric that indicates the rate-of-degradation (ROD) of the battery while it is operating. So far, these degradation control methods have been recognized recently, and only investigated in limited research. There has not been any industrial implementation seen yet.

As developing any ROD control scheme, a ROD model is required in the first place, and the battery degradation models serve as the basis for developing any ROD model. Between the statistical aging models and physics-based aging models introduced in the previous section, statistical aging models are not suitable to formulate ROD model since they only provide long-term aging trend insights and require a significant amount of aging data. The physics-based degradation models are then the best candidate as the foundation of developing any sort of ROD model for batteries.

Exploring the physics-based battery degradation models developed in the literature [91][97][98][99][100][101], the purposes of the models have been to simulate battery degradation progression under certain operations. There have been ROD related variables within those models. As in the very first paper regarding modeling battery degradation [98], the side reaction current i_{ns}, could be calculated following (1.29). A similar form of this equation was adopted in [101], where the first principle capacity fade model was developed. Instead of using side reaction current, the side reaction rate, which was proportional to side reaction current, was calculated using (1.46).

$$J_s = -i_{os}a_n\exp(-\alpha_c nf\eta_s) \tag{1.46}$$

As the SEI layer growth is the aging source, (1.42 shows that the battery resistance, R_p, is proportional to SEI layer thickness, δ_{film}. On the other hand, the increasing rate of the film thickness is given by (1.47). This shows that the rate-of-change of the SEI layer thickness is proportional to the side reaction rate. Thus, the rate-of-change of the battery resistance is proportional to the side reaction rate as well. Since the resistance is an indicator of battery

degradation, the rate-of-degradation is proportional to the side reaction rate.

$$\frac{\partial \delta_{film}}{\partial t} = -\frac{J_s M_p}{a_n \rho_p F} \tag{1.47}$$

Similarly, the capacity loss shown in (1.37) has the lost capacity as the integral of the side reaction current over time. Therefore, the rate-of-change of battery capacity can be calculated as in (1.48), where vol is the volume of the electrode of aging.

$$\frac{dQ_{loss}}{dt} = -i_s = -J_s \text{ vol} \tag{1.48}$$

Even though the ROD calculation metric has been "hiding" in the developed physics-based electrochemical model, it has not been paid attention to because of two reasons. One is the fact that the papers in the literature focus on evaluating the simulation results of battery degradation and comparing the results with measured capacity and/or resistance either during storage or during cycling. The ROD has never been the important variable for investigations. The other reason is that there have not been any methods to measure ROD practically, so the modeled ROD cannot be evaluated thoroughly.

In the literature, though the identified aging mechanisms or the electrochemical models can be different, the equation calculating the side reaction current or side reaction rate usually follows Tafel's equation (1.46). Since the electrochemistry remains similar for capacity loss or resistance increase even from different aging mechanisms, the ROD metric, either capacity-based or resistance-based, is modeled similarly.

Overall, constructing a physics-based electrochemical model for the battery aging process contains the ROD model in it. This allows simulation of ROD when the full electrochemical degradation model is simulated. This posts one significant challenge in terms of model complexity and computational burden since manipulating degradation by applying a ROD control would require a fast calculation of ROD.

1.11.4   Lithium-ion Battery ROD Control Methods

Depending on the ROD metric simulations within the physics-based battery electrochemical degradation model simulations, there have been few propositions for battery life maximization purposes. The battery operations can be divided into the charging process and the discharging process. As the charging process can be easily customized rather than the more "customer-driven" discharge process, most battery degradation control propositions via ROD manipulation are intended for the charging process.

In [112], the authors proposed charging rate optimizations to maximize the life of a lithium-ion cell. The physics-based battery model adopted the single-particle model (SPM), which simplifies the battery structure from a complex P2D model. The ROD metric in the SPM is the side reaction current density. The assumptions associated with SPM are as follows:

1. The concentration of the electrolyte is constant and uniform for all time across the cell sandwich (cathode, separator, and anode).

2. The potential in the solution phase is constant and uniform for all time across the cell.

3. Positive and negative electrode potentials depend on time only.

4. The side reaction is the reduction of ethylene carbonate.

The cell life threshold was assumed to be 20% capacity drop. The authors fixed the requirement for discharge process which was always 40% depth-of-discharge (DOD) in 35 minutes, as well as for the maximum charge time to be 61 minutes. In addition, the total cycle number was set to 320. Since the battery lower voltage limit was fixed, the charging current could not be very low. Otherwise, the discharge task could not be fulfilled. However, higher charge current would have resulted in worse degradation, and therefore there was an optimal charge current to fulfill all the requirements.
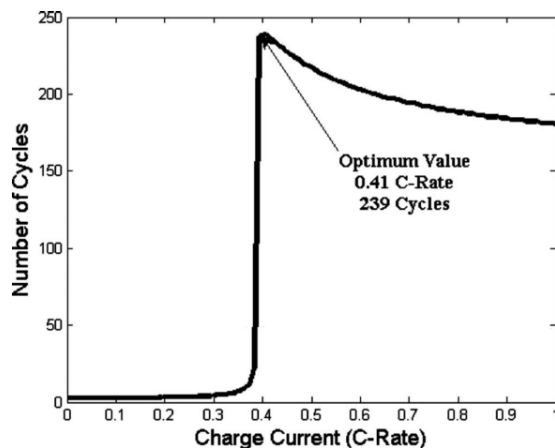
Fig. 1.95: Single charging current rate optimization [112]

After applying the nonlinear programming (NLP) optimization technique based on the SPM battery cycle life simulation, the authors found that different charging rates could be selected based on the current cycle number to improve the cell life. The authors first assumed a single charging current rate and determined that between 0 to 1 C-rate, 0.41 C-rate charging current resulted in the longest cell life of 239 cycles, as shown in Fig. 1.95.

Using the single charge rate case as the baseline, the authors continued to explore using different charge current rates at various stages of the overall cycling. As shown in Fig. 1.96, 4 to 20 different current rates were optimized respectively and simulated, achieving about 30% less capacity loss compared to the baseline simulation results.

Table II. Dynamic optimization results.

Number of charge currents	Objective function value	Percent increase with respect to the case with one charge current	Number of objective function evaluations
1	239.043741	0	957
2	255.036768	6.6904	4354
4	297.045917	24.2643	11,274
5	305.043895	27.6101	11,522
8	306.038250	28.0260	42,883
10	309.038612	29.2812	20,641
16	306.038768	28.0263	45,441
20	309.038792	29.2813	80,801

Fig. 1.96: Summary table for simulated cell life improvement with diff. charge rates [112]

In another approach [115], for the case of a prior fixed charge current rate, the authors proposed life optimization methods for battery packs via smartly controlled relay switches. The

authors adopted the electrochemical degradation model from [101] and simulated short-term battery responses starting at various SOC with different charge/discharge current rates. The instantaneous rate-of-change value of the SEI film thickness, $\dot{\delta}$, (i.e., the ROD metric), was recorded and plotted as a look-up table against both current and SOC, shown in Fig. 1.97.
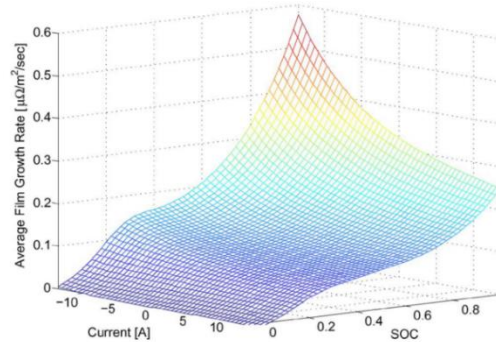
Fig. 1.97: Rate-of-change of SEI layer thickness vs. Current and SOC [115]

Assuming identical two cells in parallel, each with a relay switch to control the current flow as shown in Fig. 1.98, the authors proposed two different optimization methods, the deterministic dynamic programming (DDP) and a heuristic control mapping, to optimize the relay on/off sequence during a 1C charge process. The SOC trajectories of both simulated cells under a standard charge process without any relay were plotted together with the optimized SOC trajectories generated by both the optimization methods, as shown in Fig. 1.99.
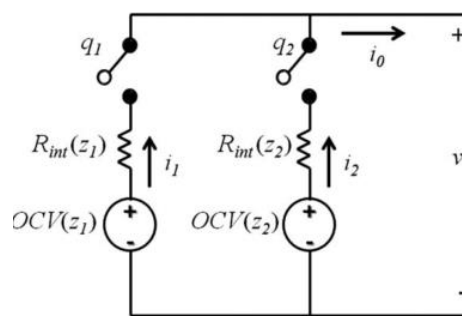
Fig. 1.98: The simulation circuitry of two parallel cells with relays [115]
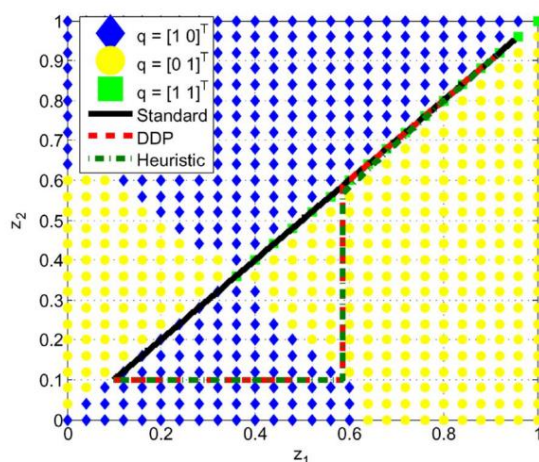
Fig. 1.99: SOC trajectories of both cells w/ and w/out optimization [115]

Based on the simulation results, Fig. 1.100 contains a summary table showing the cell life-saving results due to optimized relay switching sequences. The simulation results showed approximately 50% of improvement.

TABLE I
CONTROLLER PERFORMANCE COMPARISON ON THE CONTROL AND FULL ELECTROCHEMICAL MODELS

Control Scheme	Control Model		Full Model		
	Resistance of Total Film Buildup	Reduction in Film Buildup	Resistance of Total Film Buildup	Reduction in Film Buildup	Control vs. Full Error
Standard	3.20 mΩ/m²	0%	2.95 mΩ/m²	0%	8.47%
DDP	1.55 mΩ/m²	51.8%	1.49 mΩ/m²	49.5%	4.03%
Heuristic	1.56 mΩ/m²	51.2%	1.51 mΩ/m²	48.7%	3.31%

Fig. 1.100: Cell life improvement summary with optimized charge trajectories [115]

In both [112] and [115], the complicated electrochemical battery degradation model was adopted. Since such model linked both the primary and secondary reactions of the cell, several partial differential equations (PDE) regarding ion concentration change and mass transfer were involved, making the model complicated and usually requiring offline simulation on a specific software. To implement such control on board, it was necessary to develop a simplified ROD model in which the ROD metric can be fast computed. In [113], the authors developed a simplified ROD model calculating the side reaction current density at any time instant, J_s (t), resulted from lithium-plating on the cathode of the battery during charge. The resulted reduced-order ROD model was compared to the full model in the simulation environment and evaluated to have small

errors, as shown in Fig. 1.101.
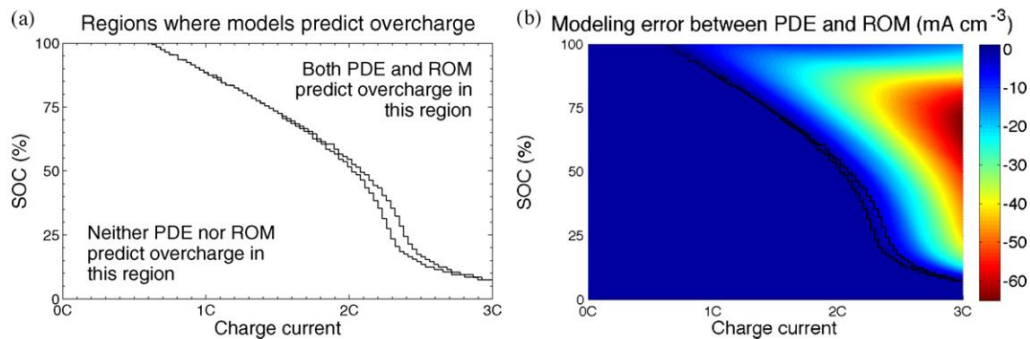
Fig. 1.101: ROD comparison between the simplified model and the full model [113]

For the aging mechanism on the anode, the SEI layer growth, authors in [114] proposed a simplified model calculating the side reaction current density $J_s(t)$ as well. Assuming the exchange current I_0 of the primary reaction only depends on SOC in a function format, PDEs associated with I_0 were eliminated. As a result, a simplified J_s calculation is given in (1.49).

$$J_s = -i_{os}a_n\exp(\frac{-F(U_n^{ref} - U_{ref\_s})}{2R_gT}) * \exp(-asinh(\frac{-i_{app}/Vol_n - J_s}{2a_nI_0})) \tag{1.49}$$

By a simple recursive root-finding algorithm, J_s can be calculated for a given current I_{app} at a given temperature and SOC. Fig. 1.102 shows the comparison between this reduced-order model and the full model, evaluated to have less than 1.5% error.
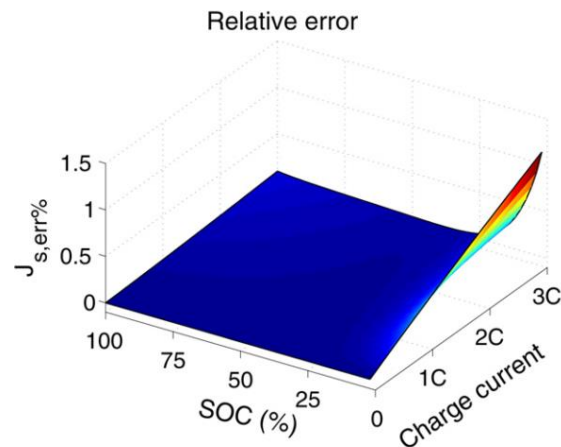
Fig. 1.102: ROD comparison between the simplified model and the full model [114]

This reduced-order model was adopted in [116], where dynamic programming was used to develop an optimized charging process. The authors compared the optimized charge trajectory with several standard CC-CV charge processes at different CC rates via simulations. The trajectories' comparison is shown in Fig. 1.103, and in Fig. 1.104, a table summary shows the effective battery life-saving benefited from the optimized charge trajectory, as well as time-saving during charge.
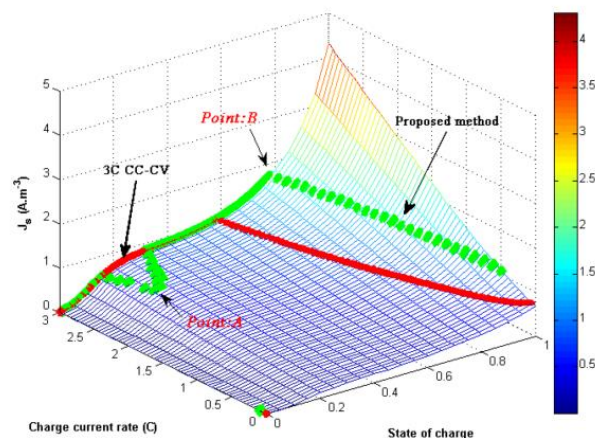
Fig. 1.103: Optimized charge trajectory compared to standard trajectories [116]

Type	Charging time	Js accumulated
1/3C CC-CV	11973 sec	4592.2 A.m^{-3}
1C CC-CV	6083 sec	3277.1 A.m^{-3}
3C CC-CV	3612 sec	2603.4 A.m^{-3}
Proposed method	1882 sec	1636.6 A.m^{-3}

Fig. 1.104: Summary of life-saving and time-saving with optimized charge trajectory [116]

There is little research regarding optimizing the battery degradation during discharge via a ROD control strategy. This is because most of the times there is no prior knowledge of the discharge process. On the other hand, though research shows that different discharge currents, temperature, different operating voltage windows all play roles affecting battery degradation rate, it is difficult to subjectively avoid harsh conditions since the discharge process can happen

anytime, at any operating condition, with any loading condition, and at the "customers" will.

There have been some investigations into degradation control for some specific discharge conditions. In [115], under a fixed constant rate discharge process, the authors utilized dynamic programming technique to smartly switch relays on and off so that two cells in parallel could be discharged via a degradation-optimized trajectory. The optimized trajectories are shown in Fig. 1.105, similar to the trajectories of an optimized charge process introduced previously.
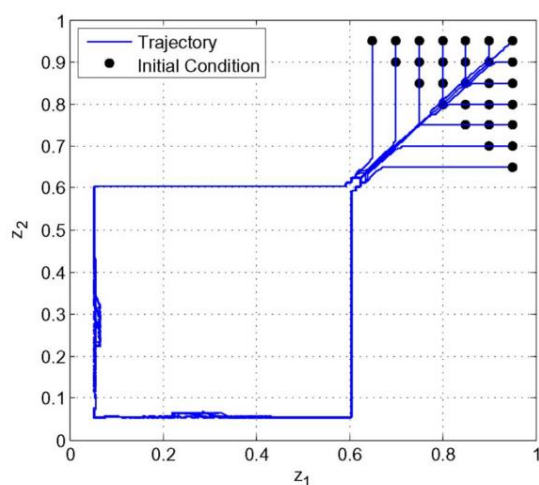
Fig. 1.105: Degradation-optimized discharge trajectories for two parallel cells [115]

Another paper [117] focused on the aging mechanisms of the battery under low discharge current rate conditions. The authors adopted the P2D model and simulate various conditions in the COMSOL software environment.
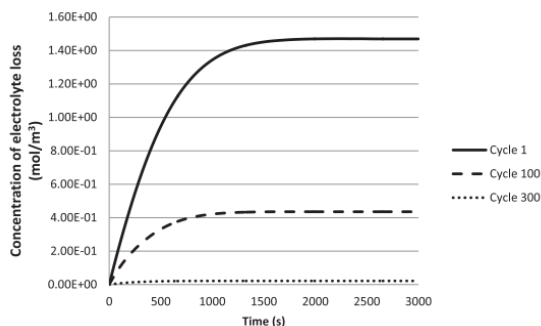
Fig. 1.106: Simulated electrolyte loss at different cycles [117]

Based on the simulation results of the electrolyte loss at different cycles shown in Fig.

1.106, the authors proposed several suggestions regarding the discharge rate selection at the battery's different stages. They suggested that the discharge current should remain at least 1C at the beginning of the discharge when the cell was new to avoid significant electrolyte loss due to the low discharge current. As the cell lives through its lifetime, the current at the beginning of a discharge cycle could be reduced without triggering high electrolyte degradation rate.

Overall, some battery degradation control strategies via ROD manipulation have been investigated in literature, although they are limited in research without practical implementation. Most of the investigations have been focusing on optimizing the charging process, and little research has analyzed the discharge process.

1.12   State-of-the-Art Summary

This chapter has outlined and discussed the recent development in the literature regarding lithium-ion battery electrochemistry, electrochemical-thermal modeling, state estimation, degradation mechanisms and modeling, and different passive and active degradation control schemes. Several key conclusions are summarized below.

A lithium-ion battery electrochemical process includes the electrode kinetics (charge transfer) modeled by the Butler-Volmer equation, and the mass transport (diffusion) modeled by Fick's laws of diffusion.

Both ECM and physics-based electrochemical models have been developed, modeling battery electrical responses. Both types of models use current as the input, estimate battery voltage and have been evaluated for various cycling conditions.

Both full and lumped lithium-ion battery thermal models have been developed. Coupled with the electrical models, the thermal models have been evaluated to estimate both the battery surface and battery core temperatures.

Characteristics mapping, filter-based algorithms, and data-driven methods have been

widely used for lithium-ion states' estimations, including SOC, SOP, SOE, and SOH.

Lithium-ion battery degradation mechanisms have been extensively investigated, and different mechanisms have been described in different sections of a typical lithium-ion cell. Capacity and resistance have been identified as the two major metrics of indicating battery degradation state.

SEI layer growth has been identified as the dominant aging source on the battery anode. Physics-based electrochemical degradation models have been developed characterizing this aging mechanism and have been evaluated for both storage and constant-rate cycling conditions.

Schemes such as material modifications, thermal management, and voltage balancing have been developed for lithium-ion battery (pack) degradation control, and widely implemented in applications.

Lithium-ion battery degradation control schemes via ROD manipulations have been investigated in the research literature but have been focused only on battery charge trajectory optimization and discharge rate selection.

1.13 Summary of Research Opportunities Identified

The following research opportunities have been identified in the state-of-the-art review:

- Li-ion Battery Rate-of-degradation (ROD) Model for Drive Cycle Operations

The ROD models in the literature have been mostly offline and computationally heavy. There is also a lack of experimental evaluations for the developed ROD models, especially under the drive cycle aging condition. Development of a reduced-order ROD model compatible with drive cycle operations is important for monitoring battery aging rate during drive cycles. Such reduced-order ROD model should be computationally efficient and can be used for real-time applications. Also, such ROD model should be control oriented.

- Li-ion Battery Degradation Control during Drive Cycles via ROD Manipulations

Battery degradation control via ROD manipulations has been investigated mostly for the battery charge process. There has been very little work investigating the degradation control schemes during drive cycles via ROD manipulations. ROD-based active degradation control schemes integrated with the electro-thermal modeling, aging factor identification, and reduced-order ROD modeling are important and valuable for improving battery durability in EV applications.

- Li-ion Battery Electro-thermal Modeling for Power-commanded EV Drive Cycles

Battery electro-thermal models developed in the literature took current as the input and are incompatible and inconvenient carrying EV drive cycle simulations. Moreover, the coupling between a thermal model and an electrochemical model requires heavy computational efforts and is ineffective for drive cycle simulations. Development of a computationally efficient electro-thermal model with power input is essential and valuable for EV drive cycle simulations.

- Operating-condition Dependent Degradation Control Analysis

For EV applications, the driving scenario and ambient temperature can be two important factors. A degradation control strategy should consider different operating conditions and be flexible enough to adjust to different conditions. The resulting control strategy should aim for practical and feasible manipulations.

- Integration Potential of Proposed ROD Control with Conventional Li-ion Battery Algorithms

Many battery algorithms have been investigated in the literature regarding monitoring and control battery internal states such as SOC, SOP, SOE and etc. A more active control-oriented algorithm such as the ROD control should have the compatibility to be integrated into standard battery management systems and communicate with other algorithms. An integrated algorithm system can be beneficial for battery overall management in EV applications.

- Investigation of Aging Factors during Drive Cycle Aging Tests

Aging factors such as temperature, SOC, and cycling rate have been evaluated in the literature for lithium-ion batteries based on constant-rate cycling experiments. However, there has been little work investigating aging factors during drive cycle aging tests. Besides the commonly investigated factors, aging factors in a drive cycle such as the current RMS and the regeneration are important and valuable to be investigated for a better understanding of battery life limitations for EV applications.

Chapter 2 EV-oriented Li-ion Battery Electro-thermal Modeling

As discussed in the state-of-the-art review, almost all lithium-ion battery electrical models are either formulated using equivalent circuits or constructed via physics-based electrochemical models. Both types of models take the loading current as the input and the battery voltage as the output. However, for an EV application, experimentally testing a battery over different drive cycles is necessary to understand how the battery voltage changes under a dynamic environment instead of standard constant-rate cycling. The battery voltage change becomes much more volatile, and lower voltage limit could be reached unexpectedly during a drive cycle due to the changing overpotential. In addition, due to the nature of how inverters and electric motors work, the inverter control does not take current commands and draw the respective current from the battery. Instead, the driver steps on the pedal and sends out speed command, and it later converts to the power command signal for the inverter. Based on the power command and battery voltage at present, the resulted current will then be drawn from the battery. Therefore, when testing battery for any drive cycle, the command profile is actually a power profile converted from the speed command by the driver via a vehicle model.

In this thesis, the focusing application is the EV industry. Thus, the batteries are extensively tested in experiments operating under drive cycles. It is necessary to develop a battery electrical model that is suitable for simulating battery voltage responses during drive cycles. The most important requirement of such a model is the model can take power profiles as the input and still estimating the battery voltage output. The solution to such requirement is not trivial since the power, as the product of current and voltage, inherently has voltage information within. Using an equivalent circuit or modeling the electrochemical process both in fact are following rules of physics, while using power to predict voltage is unorthodox and indeed is somewhat violating the

rule of physics.

Therefore, conventional ways of modeling will not work well, and a potential approach is using machine learning techniques such as the neural networks. A neural network treats the system as a black-box and links the input with the output via a mathematical model, seeming to be a suitable candidate for our unorthodox requirement.

If a neural network (NN) lithium-ion battery model could be successfully formulated and predict the battery voltage based on power commands, the loading current through the battery would have been estimated as well, just by dividing the power with the estimated voltage. This benefit could be beneficial since this would allow this neural network based electrical model to integrate with a physics-based lithium-ion battery thermal model and estimate both the surface and core temperature of the battery during a drive cycle. This provides an efficient way to simultaneously modeling both the battery electrical response and the battery thermal responses during drive cycles that have to be separately modeled in the literature. Such a holistic lithium-ion battery electro-thermal model can be valuable simulating the battery performance for EV applications.

In this chapter, an unconventional approach to modeling Li-ion batteries using the recurrent neural network (RNN) is proposed. Similar to the conventional ECMs, a current-based RNN battery model is proposed to demonstrate the concept of using machine learning techniques to model Li-ion batteries. Apart from the current-based RNN battery model, a power-based RNN is also proposed, showing the generality of using RNN to model Li-ion batteries for needs from different applications. A battery thermal model using the thermal equivalent circuit is also constructed to supplement the RNN models, so a completely offline battery model is formulated.

2.1 Lithium-ion Battery Electrical Modeling Using a RNN

The first step is to select the most suited neural network structure for modeling a lithium-ion battery. There are two main categories of NNs: feedforward neural networks (FF-NN) and

recurrent neural networks (RNN). The most significant difference between a FF-NN and a RNN is that as the NN evolves, the current hidden state in a RNN depends on the previous hidden state besides the current input, whereas in a FF-NN the current hidden state only depends on the current input. Because of this difference, a FF-NN has a simpler structure, is easier to train, but only represents time-independent relationships. On the other hand, a RNN has a more complex structure, could be computationally more burdensome to train, but is particularly suitable to model time-dependent responses. Machine learning techniques have been accepted as a powerful tool to model highly-nonlinear systems and have also been used in battery research. Machine learning has mostly been applied to battery state estimation (i.e., state of charge, power, energy, and health) research though. Typically support vector machines (SVMs) [51][52] and artificial neural networks (NNs) [53][54][58] have been investigated. Moreover, recent advancements in machine learning can be partly attributed to a subset of NNs, recurrent neural networks (RNNs) [55] with long short-term memory (LSTM) cells [56]. Compared to conventional NNs, RNNs with LSTM can be a more suitable candidate to model battery related systems since battery dynamics usually have long time constants and [57] shows that such techniques can be applied to formulate an accurate SOC estimator. As discussed in the state-of-the-art review, NN approaches have been used for battery SOC estimation. According to several examples in the literature [58][59], it has been the RNN adopted for lithium-ion battery cases. As the internal states of a lithium-ion battery depend on the states in the history, in other words, lithium-ion battery is a dynamic system with time-dependent responses. Therefore, although it is not the SOC of a lithium-ion battery that is modeled in our interests, if we treat the lithium-ion battery itself as a black-box, a RNN should be the better candidate to model such a system.

2.1.1   Overall RNN Structure with DFS and GRU

A typical RNN structure is shown in Fig. 2.1. Unlike a FF-NN, the hidden state h_t depends not only on the input x_t, but also on the previous hidden state h_{t-1}, as shown in (2.1) and (2.2). This

addition of "recursive" state feedback changes the neural network structure significantly. The output data are no longer calculated solely based on the instantaneous inputs at each time instant, but remain dependent on information from previous samples compared to a FF-NN.
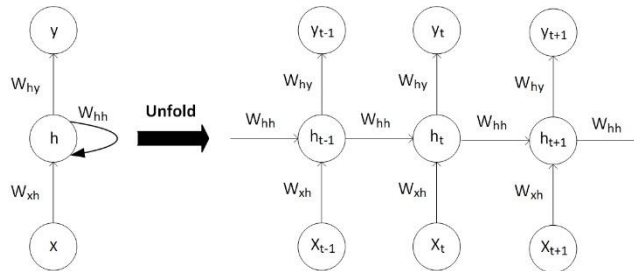
Fig. 2.1: Basic RNN structure

However, a traditional RNN has a significant drawback that must be addressed before applying it to LIB modeling. More specifically, the backpropagation step in the typical RNN structure suffers from a phenomenon called "Vanishing Gradient" [119]. This refers to small gradients that make it difficult for the baseline RNN model to learn the correlation between temporally distant events. In the case of LIB modeling, the diffusion phenomenon is a critical part of the battery dynamics and often has a time constant larger than 500s. As a result, it is essential that, during training, the RNN must can recognize and remembering the correlation between data points that are separated significantly in time.

$$h_t = H(W_{xh}x_t + W_{hh}h_{t-1} + b_h) \tag{2.1}$$

$$y_t = H(W_{hy}h_t + b_y) \tag{2.2}$$

One solution to this Vanishing Gradient problem is to implement a GRU algorithm [120] as shown in Fig. 2.2 and (2.3) to (2.6). A GRU has two gates: a reset gate *r*, and an update gate *z*. The reset gate determines how to combine a new input with the previous inputs in its memory, and the update gate defines how much of the previous memory to retain. This gating mechanism can be explicitly tailored to model long-term dependencies. By learning the parameters for its gates, the network learns how its memory should behave.
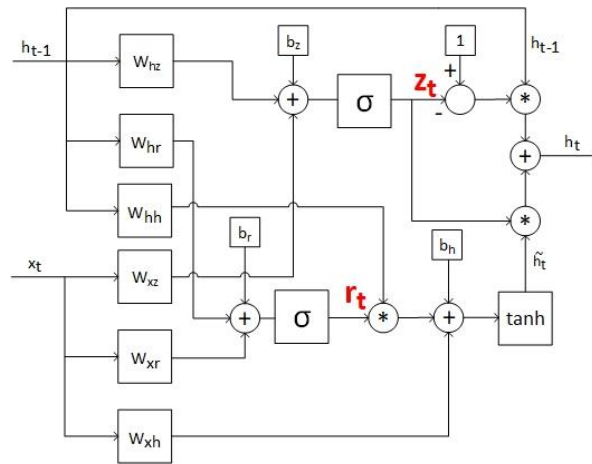
Fig. 2.2: Gated Recurrent Unit (GRU) structure

$$z_t = H(W_{xz}x_t + W_{hz}h_{t-1} + b_z) \tag{2.3}$$

$$r_t = H(W_{xr}x_t + W_{hr}h_{t-1} + b_r) \tag{2.4}$$

$$\tilde{h}_t = \tanh(W_{xh}x_t + W_{hh}h_{t-1}r_t + b_h) \tag{2.5}$$

$$h_t = (1 - z_t)h_{t-1} + z_t\tilde{h}_t \tag{2.6}$$

In addition, most machine learning algorithms normalize the input data for better convergence. For this case, it is better to weight the LIB model inputs since all the inputs are actual physical quantities. There is a DFS algorithm that has been successfully used in protein promoter identification applications [121]. This structure has been adapted for this new application by multiplying each of the physical inputs to the LIB model by an adjustable weighting parameter. These weighted inputs are then fed to the GRU structure. By implementing both the DFS and GRU, a structured RNN appropriate for modeling LIBs has been constructed.

A sample code written in Python is provided in Fig. 2.3 to show the mathematical structure of GRU and DFS, as well as a table summarizing the RNN internal structure information. It constructs a 2-level GRU system together with DFS. Typically, u_t denotes the input vectors, while y_t is the RNN output. E_0 denotes the weight vector that propagates the input vector through DFS, essentially an elementwise weighting process. In terms of other variables, zm_t/zs_t, rm_t/rs_t, and cm_t/cs_t are the different gates described in Fig. 2.2. The hidden states are hm_t and hs_t. Since this is a

2-level GRU system, a propagated input x_e is the input of the 1st level GRU, and the output hidden state of the 1st level GRU is the input of the 2nd level GRU. The other variables are called the hyperparameters.

```
def recurrent_fn(self, u_t, hm0_tm1, hs0_tm1, E0, E, W_xz, W_hz, W_xr, W_hr, …
                               … W_xh, W_hh, b_z, b_r, b_h, W_hy, b_hy):
    # 1st level GRU
    x_e0 = u_t*E0
    x_t = E.dot(x_e0)
    zm_t = T.nnet.hard_sigmoid(W_xz[0].dot(x_t) + W_hz[0].dot(hm0_tm1) + b_z[0])
    rm_t = T.nnet.hard_sigmoid(W_xr[0].dot(x_t) + W_hr[0].dot(hm0_tm1) + b_r[0])
    cm_t = T.tanh(W_xh[0].dot(x_e) + W_hh[0].dot(hm0_tm1 * rm_t) + b_h[0])
    hm_t = (T.ones_like(zm_t) - zm_t) * hm0_tm1 + zm_t * cm_t

    # 2nd level GRU
    zs_t = T.nnet.hard_sigmoid(W_xz[1].dot(hm_t) + W_hz[1].dot(hs0_tm1) + b_z[1])
    rs_t = T.nnet.hard_sigmoid(W_xr[1].dot(hm_t) + W_hr[1].dot(hs0_tm1) + b_r[1])
    cs_t = T.tanh(W_xh[1].dot(hm_t) + W_hh[1].dot(hs0_tm1 * rs_t) + b_h[1])
    hs_t = (T.ones_like(zs_t) - zs_t) * hs0_tm1 + zs_t * cs_t

    yt = W_hy.dot(hs_t) +b_hy
    return [hm_t, hs_t, yt]
```

Fig. 2.3: Sample codes for a 2-level GRU with DFS

A summarized network configuration is shown below in Table 2.1 for a better understanding of the network complexity. It shows that the largest matrix involved is 30*30, which is small enough that will not cause any computational burden for a modern computer once all the hyperparameters are trained and converged to fix values.

Table 2.1: Network configuration summary

Network Specs	Size
# of neurons	30
# of network layers	3 (i.e. 2-level GRU + 1-level DFS)
u_t	1 x 4
E0	1 x 4 (elementwise multiplication with u_t)
E	4 x 30
$W_{xz}/W_{hz}/W_{xr}/W_{hr}/W_{xh}/W_{hh}$	30*30*2 (one for each GRU level)
$b_z/b_r/b_c$	1 x 30

W_{hy}	30 x 1
b_{hy}	1 x 1
y_t	1 x 1

2.1.2 Definition of Inputs and Outputs for the RNN Models

While the output of the battery model is its terminal voltage (V), the selection of inputs for the structured RNN is flexible but needs to be physically meaningful. Two different sets of inputs are considered, and each has its own advantages and disadvantages. The first set of inputs includes measured battery terminal current (I), integrated battery amp-hours (Ah), battery temperature (T) measured with a thermocouple on the battery surface, as well as the estimated battery voltage at the previous sampling instant ($\hat{v}_{-1}$). Fig. 2.5 displays the RNN structure with this first set of inputs. With DFS included in the model, the input x_t in (2.3) for the GRU is the weighted input vector [I_w T_w Ah_w $\hat{v}_{-1w}$], and the weight value associated with each physical input is optimized during the training stage.
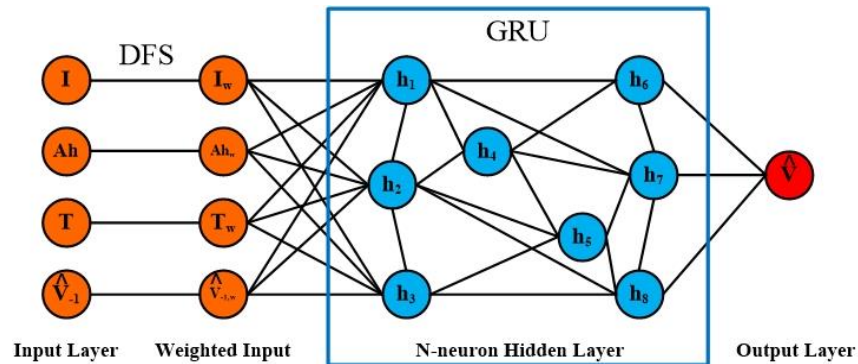
Fig. 2.4: Current-based LIB RNN using DFS and GRU structures

During the training stage, measured voltage data are used as V_{-1} to allow the model to learn the LIB dynamic behavior. However, after the training is finished, only the initial measured battery voltage at t=0 (V_0) is used to forward predict the battery voltage at t=1 ($\hat{v}_1$). At every other subsequent time instant, the estimated battery voltage at the previous sampling instant ($\hat{v}_{t-1}$) is used as one of the four inputs to predict the battery voltage ($\hat{v}_t$) at the next time instant. This approach insures that the model is operating as a predictive model.

For the other input set, power and watt-hours replace current and amp-hours in the model input vector. This approach is appropriate when testing the battery using drive cycles for which power is the key command variable. This second set of inputs includes the battery power command (P), the integrated battery watt-hours (Wh), measured battery temperature (T), and the predicted battery terminal voltage at the previous sampling instant ($\hat{v}_{-1}$). Fig. 2.5 exhibits the structure with the second set of inputs. Both the DFS and GRU structures are the same for both cases. Since power is one of the inputs of this proposed model and the predicted battery voltage is the output, the used charge of the battery can be estimated as well. This estimation can be compared with the integral of the measured current as a second model validation metric and the charge (amp-hours) calculation sequence is shown in Fig. 2.6.
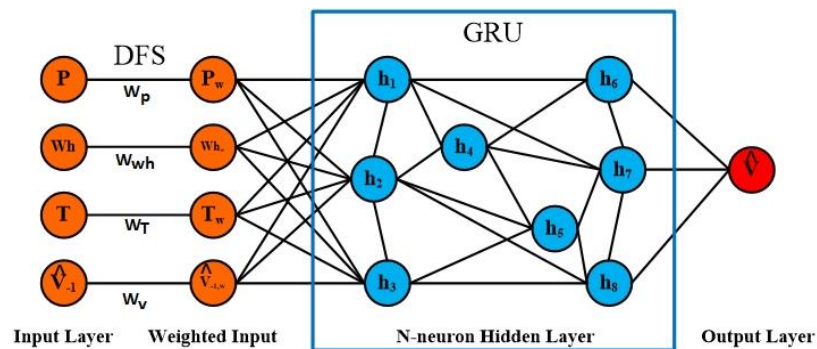
Fig. 2.5: Power-based LIB RNN using DFS and GRU structures
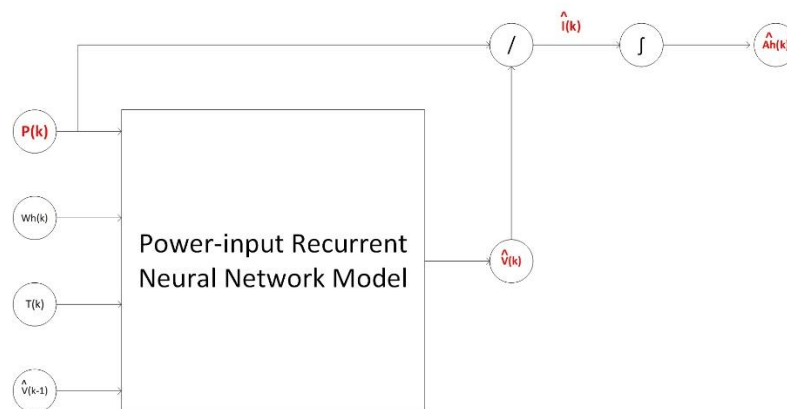
Fig. 2.6: Block diagram for voltage modeling and prediction of consumed amp-hours

2.2 RNN Battery Electrical Model Training & Evaluation

2.2.1 Training Procedure for RNN

A standard neural network training procedure, including forward prediction and backpropagation through time (BPTT) via gradient descent, is utilized. The loss function computed at the end of each forward prediction step is the difference between the RNN's estimated battery voltage and the measured voltage. In (2.7), N is the length of the training dataset in the process and $\hat{V}_k$ and V_k are the RNN-estimated and the measured voltage values at time step k, respectively.

$$L = \sum_{k=1}^{N} (\hat{V}_k - V_k)^2 \tag{2.7}$$

During one training step, it consists of one forward path and one backpropagating path. Based on all the model parameter values at the end of the previous training step, the RNN model generates the kth voltage estimate, and the associated error is calculated. Based on the loss function, the backpropagation is taken place following the gradient descent algorithm as shown in (2.8), where $Param_i(k)$ denotes the ith model parameter at the kth time step, and lr denotes the learning rate. $\nabla L(Param_i, k)$ is the gradient of L with respect to the ith model parameter at k^{th} time step. In this paper, the learning rate is set to 0.002, and the model parameters are initialized randomly with a normal distribution with 0 mean and 0.01 standard deviation.

$$Param_i(k) = Param_i(k-1) - lr*\nabla L(Param_i, k) \tag{2.8}$$

It should be noted that although the model structures of the proposed current-input and power-input models are identical except different input variables, their model parameters require separate training and are independent from each other. In the next section, model validation results for both proposed models are shown.

2.2.2 Experimental Testing of Battery Cells

Two batteries with different cathode chemistries have been tested, the Panasonic

NCR18650PF shown in Fig. 2.7 and the Sony VTC6 shown in Fig. 2.8. Their key specifications are listed in Table 2.2. The batteries were tested by applying power profiles calculated for four standard drive cycles including HWFET, LA92, UDDS, and US06. The batteries were also tested for a fifth drive cycle, referred to as the NN drive cycle, which was created from a random combination of the other drive cycle power profiles. The power profiles are scaled for a single cell of a 35kWh electric vehicle battery pack. The drive cycle power profiles are calculated for an electric Ford F150 truck with a 35kWh battery pack [122][123]. The profiles are scaled for a single cell of the 35-kWh battery pack, which is defined to consist of 3680 of the 18650 cells.

Table 2.2: Specifications for tested Panasonic NCR18650PF & Sony VTC6 batteries

	Panasonic	Sony
Nominal Voltage:	3.6V	3.6/3.7V
Nominal Capacity	2,900mAh	3,000mAh
Cathode Chemistry	NCA	NMC

Fig. 2.7: Panasonic NCR18650PF cells   Fig. 2.8: Sony VTC 6 cells

The tests are performed at four discrete temperatures ranging from -10ºC to 25ºC. For each test the cell is first fully charged and then the drive cycle power profile is drawn from the battery until the cell reaches a cut off voltage of 2.5V. Due to the Panasonic battery only being rated to charge at temperatures of 10ºC and higher, there is no regeneration (charging) portion for the 0ºC and -10ºC tests for both batteries. The measured Panasonic cell power profiles for each temperature for the NN cycle is shown in Fig. 2.10 and the current profiles are shown in Fig. 2.9. The profiles for the Sony cells are not presented here since they are only slightly different from those of the

Panasonic cells.

Table 2.3: Summary of power-cycle profiles

Test	Use	Mean Power [W]	RMS Power [W]	Peak Power [W]
HWFET	Training	-4.8 -5.2*	6.2 5.9*	-15.7 -15.7*
LA92	Training	-2.4 -3.4*	7.3 6.0*	-26.5 -26.5*
UDDS	Training	-1.6 -2.4*	4.5 3.8*	-18.9 -18.9*
US06	Training	-7.0 -9.0*	14.1 13.2*	-53.6 -53.6*
NN	Validation	-2.7 -4.7*	10.0 8.8*	-38.8 -38.8*
*: low temperature case, no regeneration				
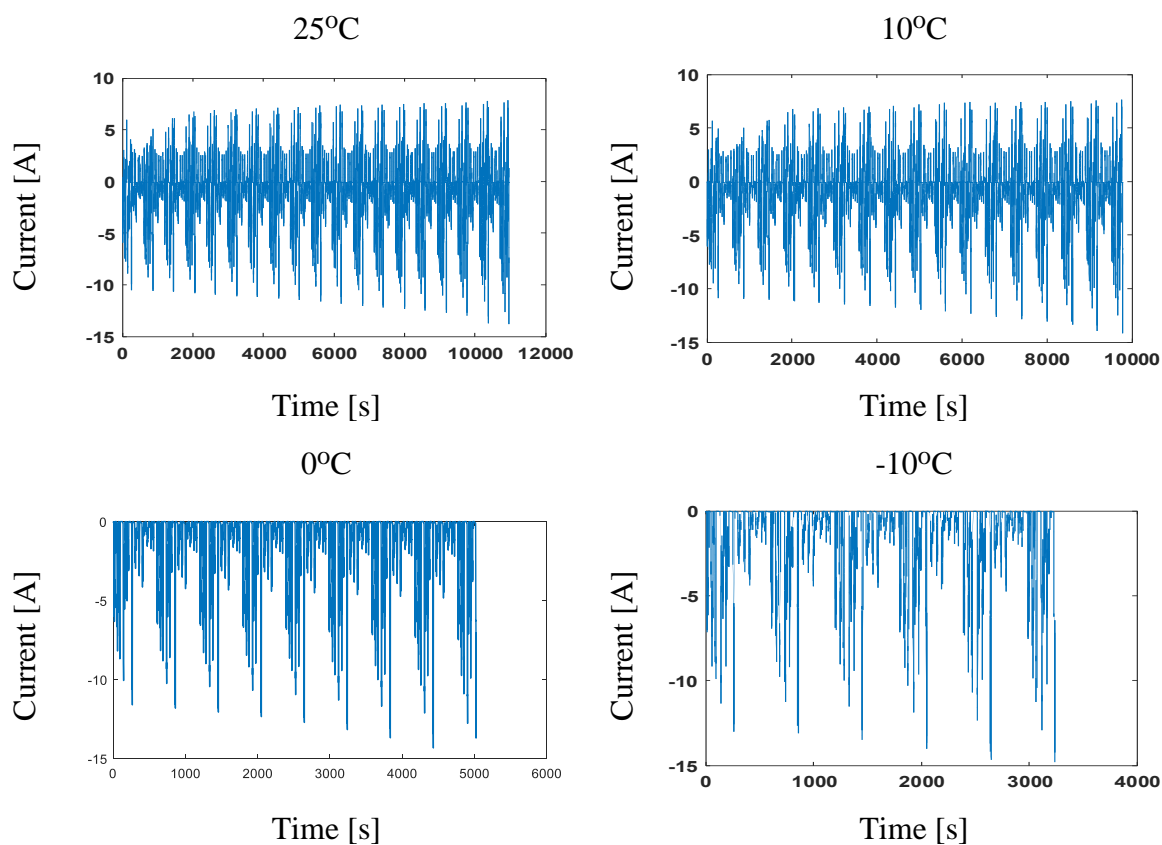
Fig. 2.9: Current profiles for NN drive cycle at 25°C, 10°C, 0°C, and -10°C

In Table 2.3, a summary of the power cycle profiles is presented and it is shown that the

HWFET, LA92, UDDS, and US06 cycles are used to train the RNN and the NN cycle is used to evaluate the accuracy of the RNN model. The cycles respective mean, RMS, and peak power values are included for the with and without regeneration cases. The cycles cover a wide range of mean and peak power values, ensuring the network is well trained for different scenarios. It should be noted that negative sign is chosen in this paper to represent discharge power.
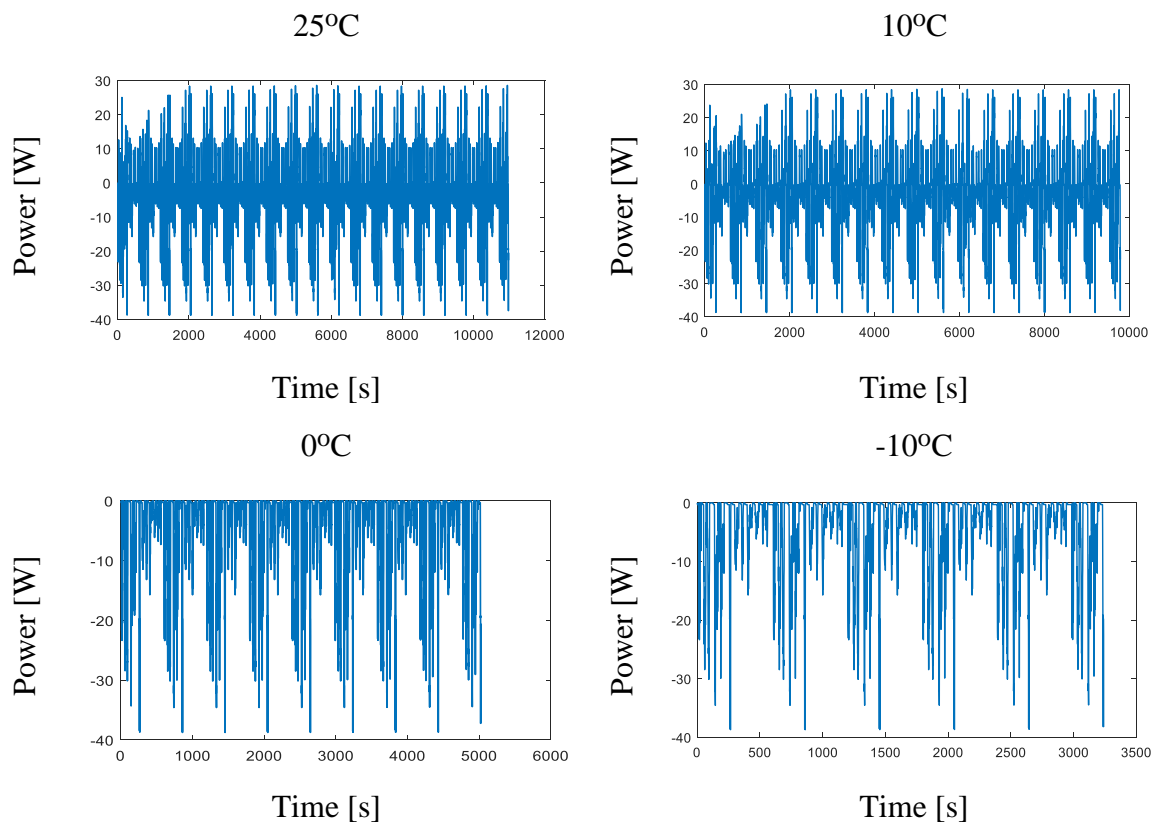
Fig. 2.10: Power profiles for four NN drive cycle datasets at 25°C, 10°C, 0°C, and -10°C

In total, there are 16 (= 4 x 4) datasets available for training, and a training sequence through all these 16 datasets is defined to be one epoch. The training continues for a total of 800 epochs during which the voltage estimation error reduces as the model fit improves. It is important to note that the order of the 16 datasets is randomized during each epoch to improve the training robustness.

The RNN is trained separately for the Panasonic and Sony batteries as the different

chemistries and capacities result in different model parameters. The power- and current-input RNNs are also trained separately, since they are distinct models. The results of both the current- and power-input RNN models for the Panasonic cells are presented first in the following subsection, whereas only the power-input modeling results for the Sony cells are shown since the power-input model proposed in this paper can be a more significant contribution to the battery research. After training the RNN structures shown in Fig. 2.4 and Fig. 2.5 with the Panasonic cell data, the average voltage errors for each sequential training epoch are plotted in Fig. 2.11 for the current- and power-input models, respectively.

Current-input: [I Ah T $\hat{V}_{-1}$] Power-input: [P Wh T $\hat{V}_{-1}$]
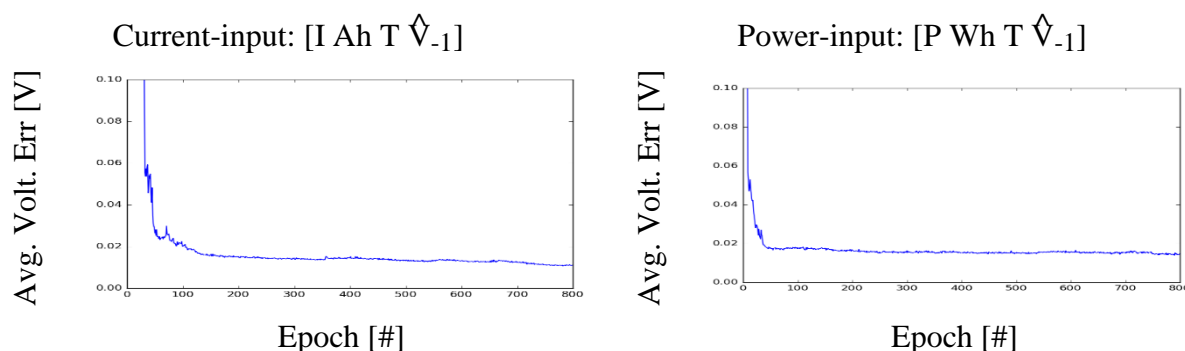
Fig. 2.11: Training error plots for current- and power-input RNN model for Panasonic cells

2.2.3   Trained Current-based RNN Model Evaluation

The voltage prediction accuracy of the current- and power-input RNNs is evaluated using the measured NN drive cycle data, which was not utilized in the training of the RNN. The model is therefore tested using independent data, showing that the RNN successfully learned the general dynamic characteristics of the battery cells. The model is tested by inputting measured temperature, current, and amp-hours and measured temperature, power, and watt-hours for the current- and power-input models respectively, and by comparing the RNN estimated voltage to the measured voltage.

The model could also be tested by inputting the commanded power profile, rather than the measured power profile. The commanded power is typically the same, but the battery tester does for example limit the charging power at high SOC to prevent the battery voltage from exceeding

the set limit. This can be observed from time 0 to 2000s in Fig. 2.10, where the charge power is less than later in the test where the battery voltage has decreased. The developed RNN model has not been formed in a way that can limit power as described though, so testing the RNN with commanded power would result in higher error under these power limited circumstances. It is desirable for a battery model to account for voltage and power limits, and this is therefore a recommended area for future development.

In Fig. 2.12, predicted voltage versus measured voltage for the current-input RNN is shown for the NN profile evaluation dataset at four different temperatures, as well as zoomed-in views and the prediction error. These results show that the trained RNN model performs well, capturing the nonlinear cell behavior which is present at low temperatures fairly accurately. In Table 2.4, several different error metrics are summarized for the four different temperature conditions, including the mean absolute error (MAE), the root-mean-square error (RMSE), the maximum error (MAX), and the standard deviation of the error (STDDEV).

The prediction error is much smaller than 0.5V and is generally lower at the higher temperatures. This could be because that, at low temperatures, the battery is more resistive and the nonlinear Butler-Volmer effect and diffusion are more prevalent, contributing to greater model error. The low temperature cases may also have higher error because the drive cycles are shorter at low temperatures due to the cut off voltage being reached sooner and to the lack of regenerative braking energy. This results in less overall training data being available at low temperatures, which may cause the RNN to bias towards minimizing error at higher temperatures where there is more data.
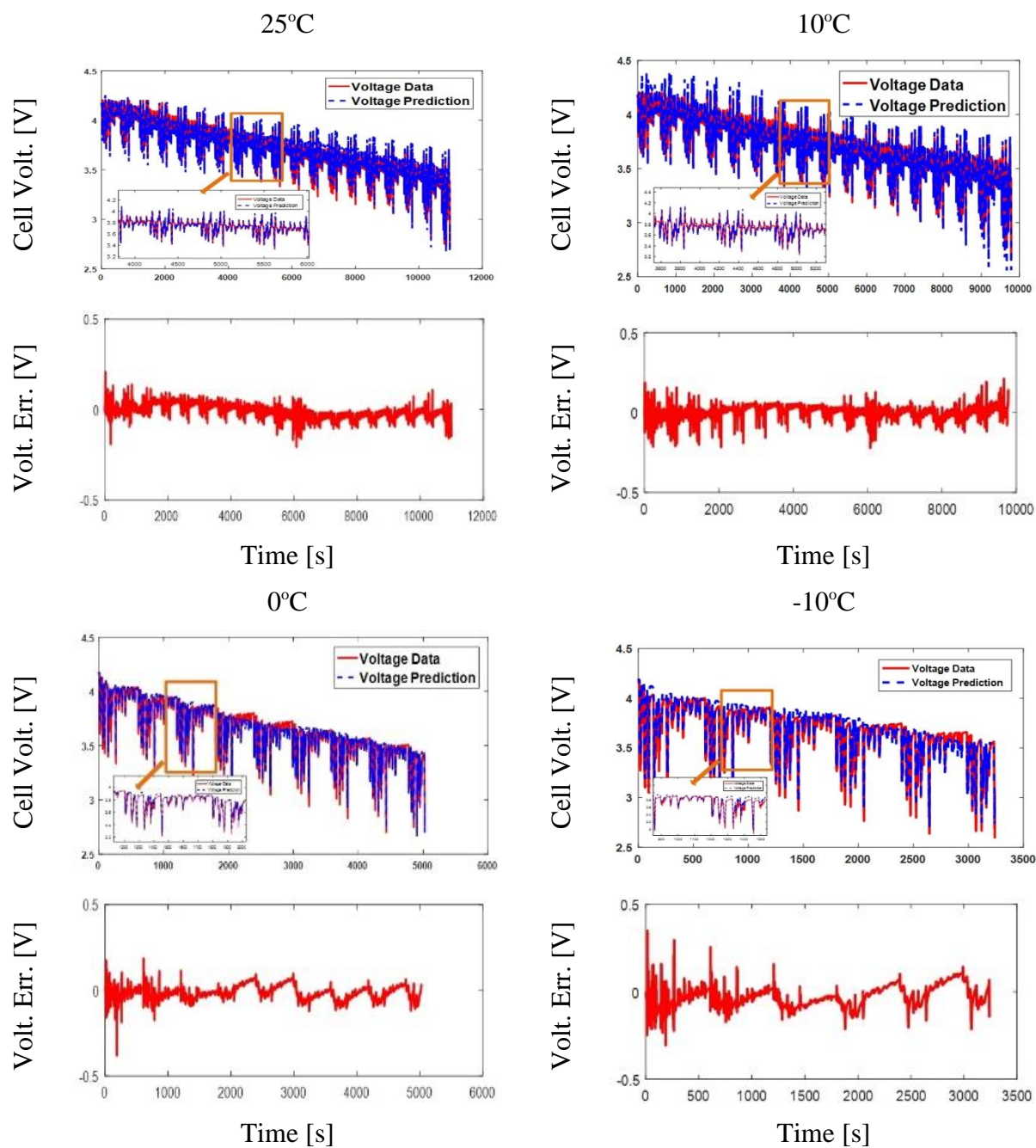
Fig. 2.12: Current-input RNN model validation results for Panasonic cells

Table 2.4: Summary of voltage prediction error for current-input RNN model (Panasonic)

	25ºC	10ºC	0ºC	-10ºC
MAE [V]	0.029	0.029	0.033	0.053
RMSE [V]	0.037	0.039	0.041	0.066
MAX [V]	0.21	0.22	0.38	0.35
STDDEV [V]	0.036	0.038	0.039	0.060

To illustrate how well the proposed current-input RNN model performs it is compared to traditional ECMs. In [124], three typical ECMs have been evaluated for the same Panasonic 18650PF cell investigated here, including an "R-only" model, "R-Zwb model", and "R-RC-RC-Zwb model". R, C, and Zwb represent resistor, capacitor, and the Warburg impedance respectively. All three models have been evaluated using the same "NN" validation profile and an RMS error comparison between the three ECMs and the proposed current-input RNN model is shown below in [124]. It shows that the proposed RNN model can achieve a similar accuracy as the traditional ECMs, without requiring the specialized parameterization tests and processes needed for the ECM models.
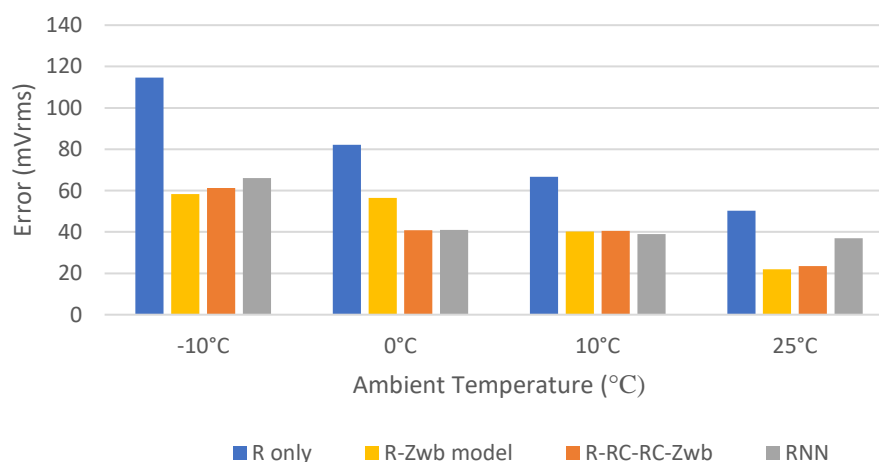
Fig. 2.13. Comparison of RNN current-input model error to equivalent circuit model error from [124] for Panasonic cells at different temperatures

2.3 Electro-thermal Model Formulation

2.3.1 Combination Between RNN Electrical Model and Thermal Model

Based on the RNN model developed in the previous section, the lithium-ion battery electrical responses during a drive cycle can be accurately simulated. With the power input and the voltage output, the loading current through the battery during the drive cycle can be estimated as in (2.9).

$$\hat{I} = \frac{P}{\hat{V}} \tag{2.9}$$

For the three evaluation datasets at three different temperatures, the estimated battery current is plotted in Fig. 2.14, Fig. 2.15, and Fig. 2.17, as well as the error between the estimated current and the experimentally measured current.
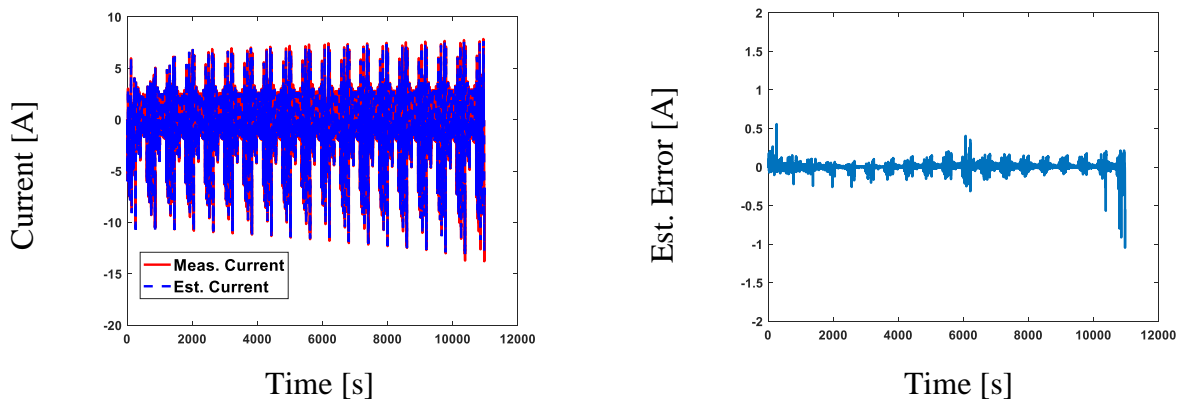
Fig. 2.14: Current estimation using the RNN model for Panasonic cell at 25°C
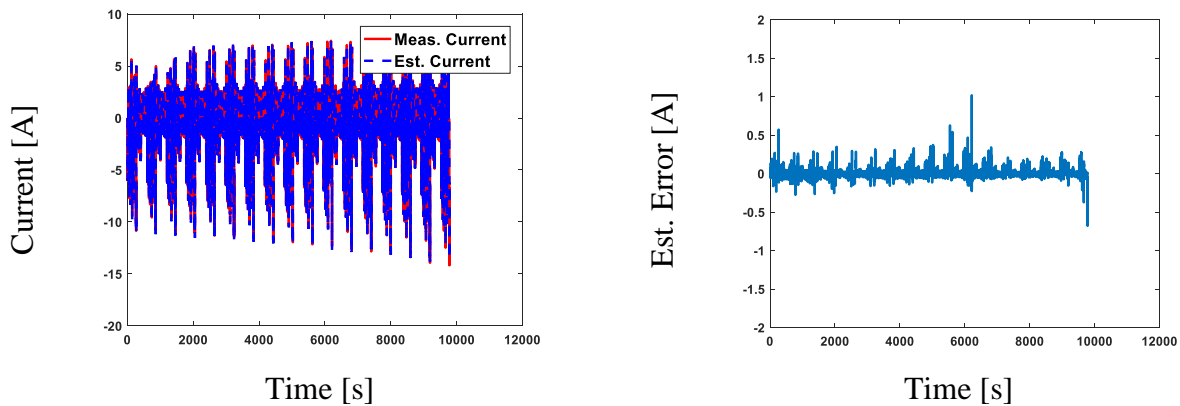
Fig. 2.15: Current estimation using the RNN model for Panasonic cell at 10°C
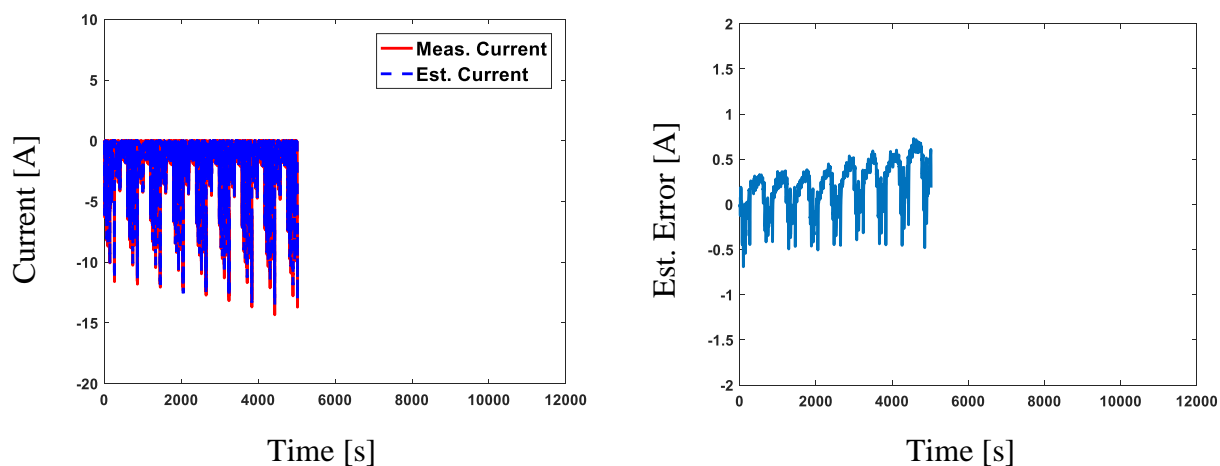
Fig. 2.16: Current estimation using the RNN model for Panasonic cell at $0°$C
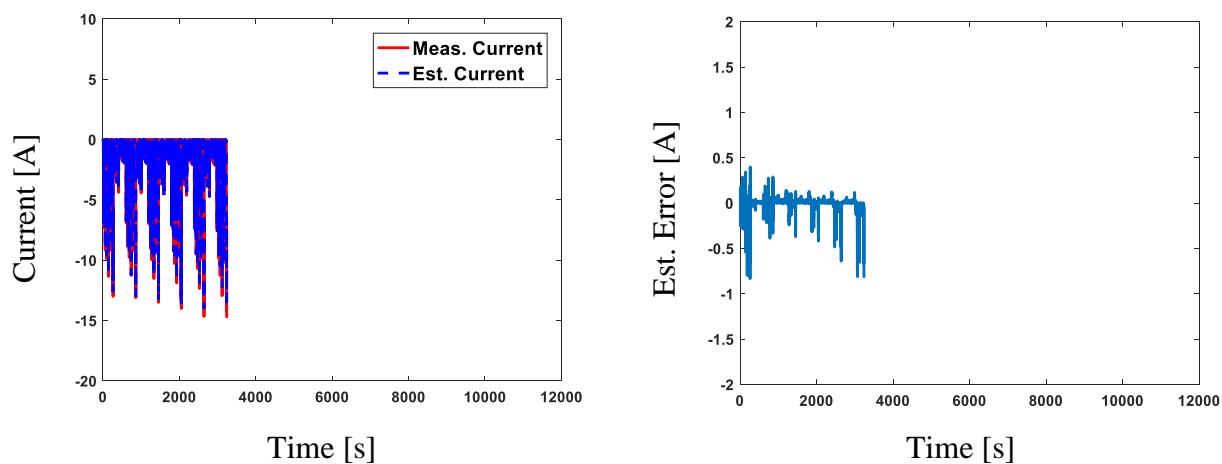
Fig. 2.17: Current estimation using the RNN model for Panasonic cell at $-10°$C

The estimated current is shown to have good accuracy with the measured current at all three temperatures. The estimation error has been kept less than 10%, except one endpoint for the $25°$C case. This is mainly due to these are step simulations, and the model has not enough information to estimate the last point.

2.3.2   Battery Thermal Equivalent Circuit Model

With the accurately estimated current and voltage, a lithium-ion battery thermal model can be developed and integrated with the RNN model. As mentioned in the state-of-the-art review, lithium-ion battery thermal models rely heavily on an accurate battery internal heat generation

calculation. As different heat generation calculation methods have been discussed in the state-of-the-art review, the most efficient and effective method here is to adopt (1.19), where the heat generations due to overpotential and entropy change are included as the dominant generation source. Also, this equation calculates the heat generation with a lumped battery model and the simplicity of the model fits with requirements for the electro-thermal model developed in this thesis.

The lithium-ion battery of interests is still the Panasonic 18650PF used for the RNN modeling. The battery is a cylindrical cell, and a top view of such cell is shown in Fig. 2.18.
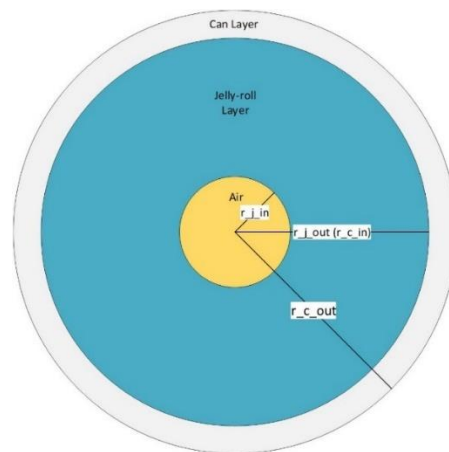
Fig. 2.18: Top view of testing batteries

The internal structure of cylindrical cells is similar. There is an air conduit in the middle for venting and short-circuit protection. The bulk part surrounding the air conduct is called the "jelly roll", which is consists of a rolled cathode layer and a rolled anode layer, separated by a membrane "separator". For a lumped battery model, this "jelly roll" is treated a lumped portion. In addition, there is an outer can layer served as the battery case. Can material is highly thermally conductive and contributes to a tiny temperature drop.

Based on the internal structure of the cylindrical model, an equivalent thermal circuit can be developed, similar to Fig. 1.29(b). Both the "jelly roll" and the can layer are included in the equivalent thermal circuit. The circuit scheme is shown in Fig. 2.19. $\dot{Q}$ denotes the internal heat

generation, T_c, T_j, T_s, and T_f denote core temperature, jelly roll temperature, surface temperature, and the outside fluid temperature respectively. When the battery is placed in a thermal chamber, the outside fluid is the air.
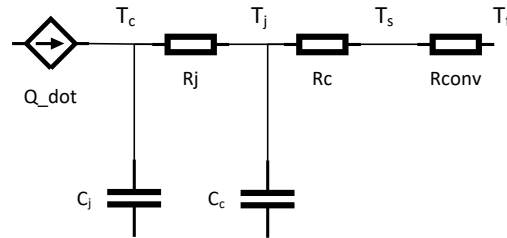
Fig. 2.19: A lumped thermal equivalent circuit for testing batteries

Thermal resistances and capacitances for different battery parts are included as well. R_j and R_c denote the thermal resistance for the jelly roll and the can layer. C_j and C_c are the thermal capacitances for the jelly roll and the can layer. R_{conv} is the convective thermal resistance between the battery surface and the ambient environment.

The heat generation $\dot{Q}$ is calculated as in (2.10). The first term is the heat generation by the overpotential, and the second term is the entropy change. The partial derivative of the battery OCV with respect to the core temperature is called the entropy coefficient. The value for this partial derivative can be measured by experiments.

$$\dot{Q} = I(V - V_{ocv}) - IT_c\frac{\partial V_{ocv}}{\partial T_c} \qquad (2.10)$$

To measure the entropy coefficient, the battery is first charged or discharged to one certain SOC stage, then resting at one specific temperature for a couple of hours. After that, the battery OCV with respect to that temperature and SOC is recorded. By changing the ambient temperature to different values, the battery OCV usually slightly changes. By recording different OCV values at different temperatures for one specific SOC stage, a linear line can be fitted through those OCV values, and the slope is then the entropy coefficient at that particular SOC stage. By repeating the same experimental sequence at different SOC stages, a look-up table of the entropy coefficient

against different SOC stages can be formulated. Such look-up table for the tested Panasonic 18650PF cell is shown in Fig. 2.20. The entropy coefficient is nonlinear and could change signs, positive at medium to high SOC and negative at low SOC. This finding agrees with the results in the literature. From Fig. 2.20, the entropy coefficient can be significant at some SOC stages, and therefore the entropy change term contributes to the internal heat generation and should not be neglected.
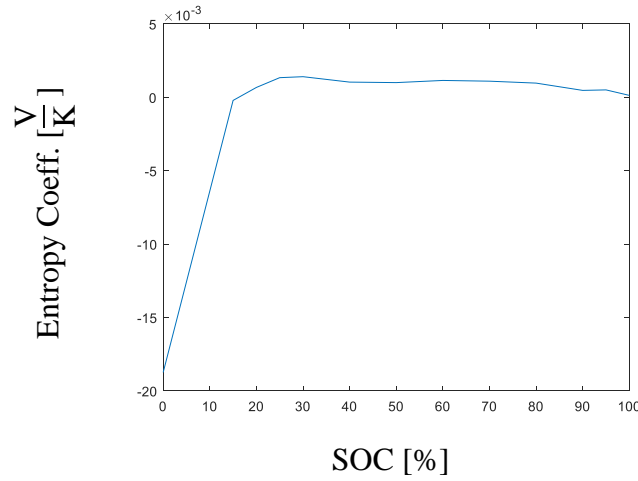
Fig. 2.20: Entropy coefficient vs. SOC for the Panasonic 18650PF cell

Based on the equivalent thermal circuit, the energy balance can be applied to the circuit, and both the battery surface and battery core temperature can be calculated from the variables and parameters shown on the circuit. The calculations in the discrete time format for both quantities are shown in (2.11) and (2.12).

$$T_c(k) = (1 - \frac{\Delta t}{R_j C_j} \frac{R_{conv}}{R_j + R_{conv}}) \, T_c(k\text{-}1) + \frac{\Delta t}{C_j} \, \dot{Q}(k\text{-}1) + \frac{R_{conv}\Delta t}{R_j + R_{conv}} \, T_{amb}(k) \qquad (2.11)$$

$$T_s(k) = \frac{R_{conv}}{R_{conv} + R_c} \, T_j(k) + \frac{R_c}{R_{conv} + R_c} \, T_{amb}(k) \qquad (2.12)$$

As shown in the heat generation equation, the battery voltage and current are both inputs, assuming the core temperature of the battery initially is the same as the ambient temperature, the heat generation can be calculated in a stepped-time fashion, and the battery surface temperature and battery core temperature at the following timestamps can be calculated following (2.11) and

(2.12).

2.3.3   Li-ion Battery Thermal Model Evaluation

To validate the lumped battery thermal model developed for testing cells, the evaluation datasets used for RNN model evaluation are used again, and for now, measured voltage and measured current from the experimental data are used. In Fig. 2.21, Fig. 2.22, Fig. 2.24, and , the estimated surface temperature, the estimated core temperature, and the measured surface temperature from a thermocouple attached in the middle of the battery surface, are plotted for the evaluation datasets at three different temperatures. In addition, the estimation errors between the estimated surface temperature and the measured surface temperature for different evaluation cases are plotted. Unfortunately, the core temperature of the battery is not measured due to the tool limitation and safety concerns since it would require drilling hole into the battery.
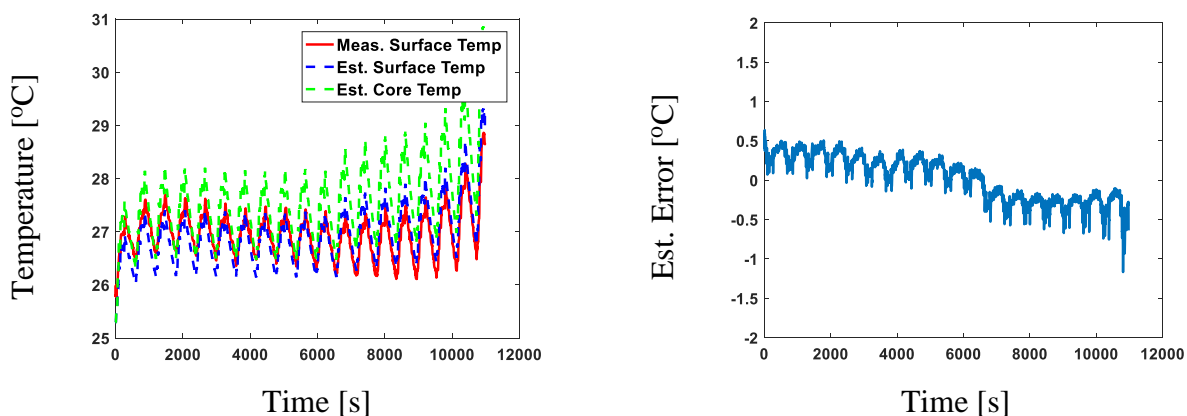
Fig. 2.21: Lumped thermal model evaluation at 25°C
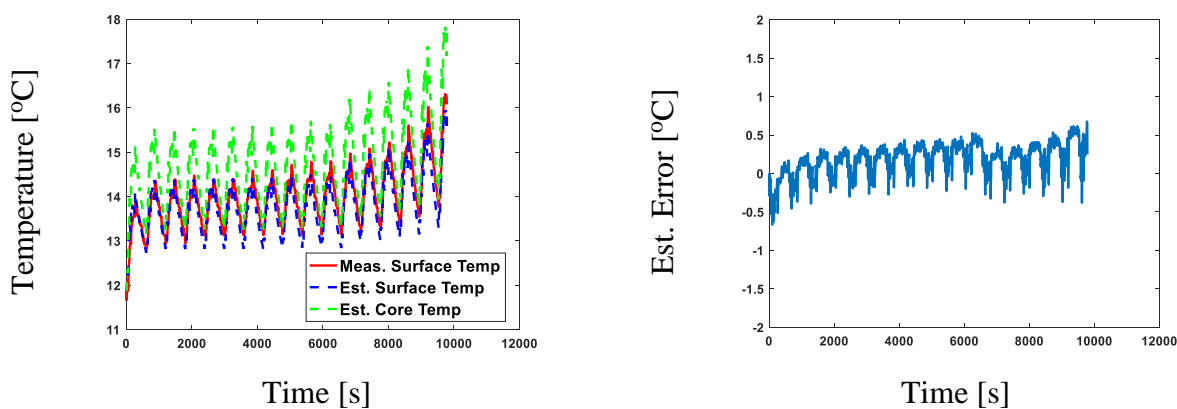
Fig. 2.22: Lumped thermal model evaluation at 10°C
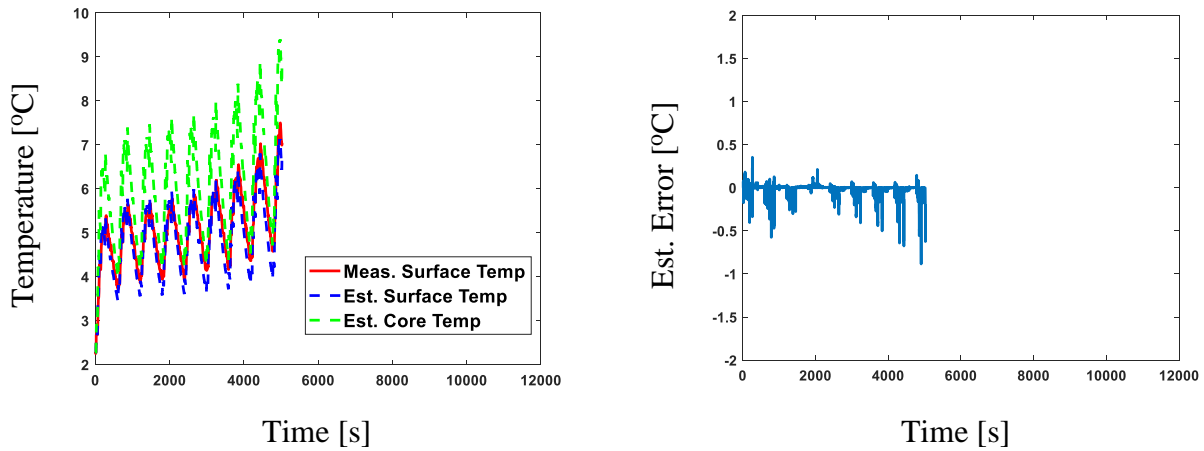
Fig. 2.23: Lumped thermal model evaluation at 0°C
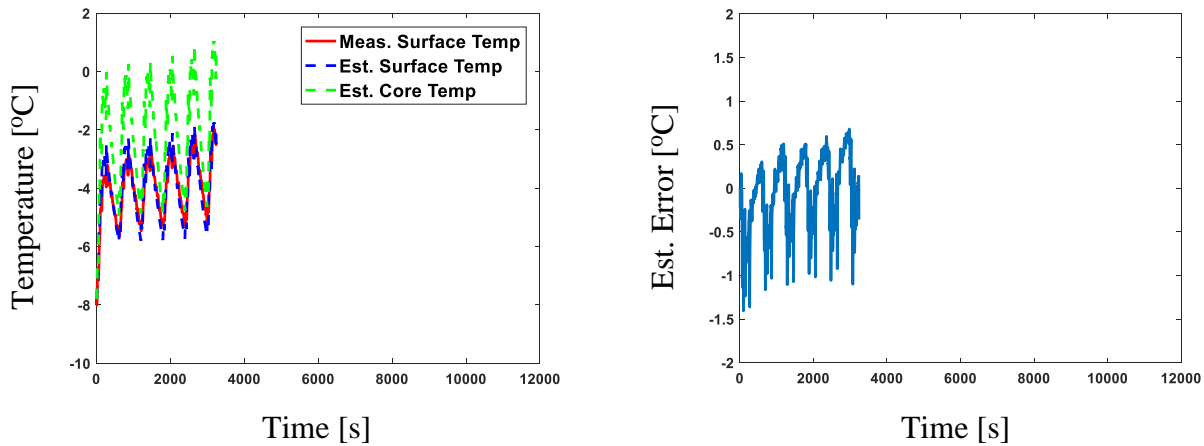
Fig. 2.24: Lumped thermal model evaluation at -10°C

The estimated battery surface temperature agrees well with the measured battery surface temperature at all three temperatures, confirming the validity of the developed lumped thermal model. For 25°C and 10°C cases, the estimation error is kept within 1°C. For -10°C, the estimation error is less than 1.5°C. This is due to the increased ohmic heating loss from the exponentially increased battery internal resistance at low temperatures.

2.4 Power-commanded Electro-thermal Model Evaluation

2.4.1 Model Evaluation for the Panasonic Cell

The lithium-ion battery RNN electrical model and the lumped battery thermal model developed from the previous sections can be further integrated into one holistic lithium-ion battery

electro-thermal model specifically for the power-commanded drive cycle simulation purposes.

Given a drive cycle power profile, such electro-thermal model can be simulated in the discrete fashion. Initially, the battery surface temperature is assumed to be the same as the ambient temperature, and the cell voltage is assumed to the idle voltage. At time stamp 2, the input vector consists of [P(2), Wh(2), $T_S(1)$, V(1)] can be fed into the RNN model and predicts $\hat{V}(2)$, the estimated cell voltage at time 1. Then, the loading current at time 1, $\hat{I}(2)$, can be estimated and fed into (2.11 and (2.12 to estimate both the surface temperature and core temperature at timestamp 2, $\hat{T}_c(2)$ and $\hat{T}_s(2)$. For the subsequent simulation time steps, the input vector into the RNN model is [P(k), Wh(k), $\hat{T}_S(k\text{-}1)$, $\hat{V}(k\text{-}1)$], the outputs of the electro-thermal model are $\hat{V}(k)$ and $\hat{T}_c(k)$.

The same training process has been applied to the RNN model with the power-input dataset as shown in Fig. 2.5. The associated training error plot is provided in Fig. 2.11. The results in Fig. 2.25 show that the power-input RNN is also able to accurately model the battery dynamic performance. Similarly, a summary of the error metrics is shown in Table 2.5. The prediction error is again slightly larger at low temperatures, attributed to similar reasons explained for the current-input model case. The results also show that the overall estimation error utilizing this power-input RNN is slightly higher than the previous case for which current/amp-hours are used as inputs. One hypothesis for explaining this difference is that the RNN model with the first input set does a better job of modeling the electrochemical nature of the battery in which induced current results in voltage differences, and battery amp-hours are closely related to battery open-circuit voltage. According to this argument, the relationships captured by the equations for the power-input set do not model the underlying electrochemical reactions in the cell as well as the RNN for the current-input set.
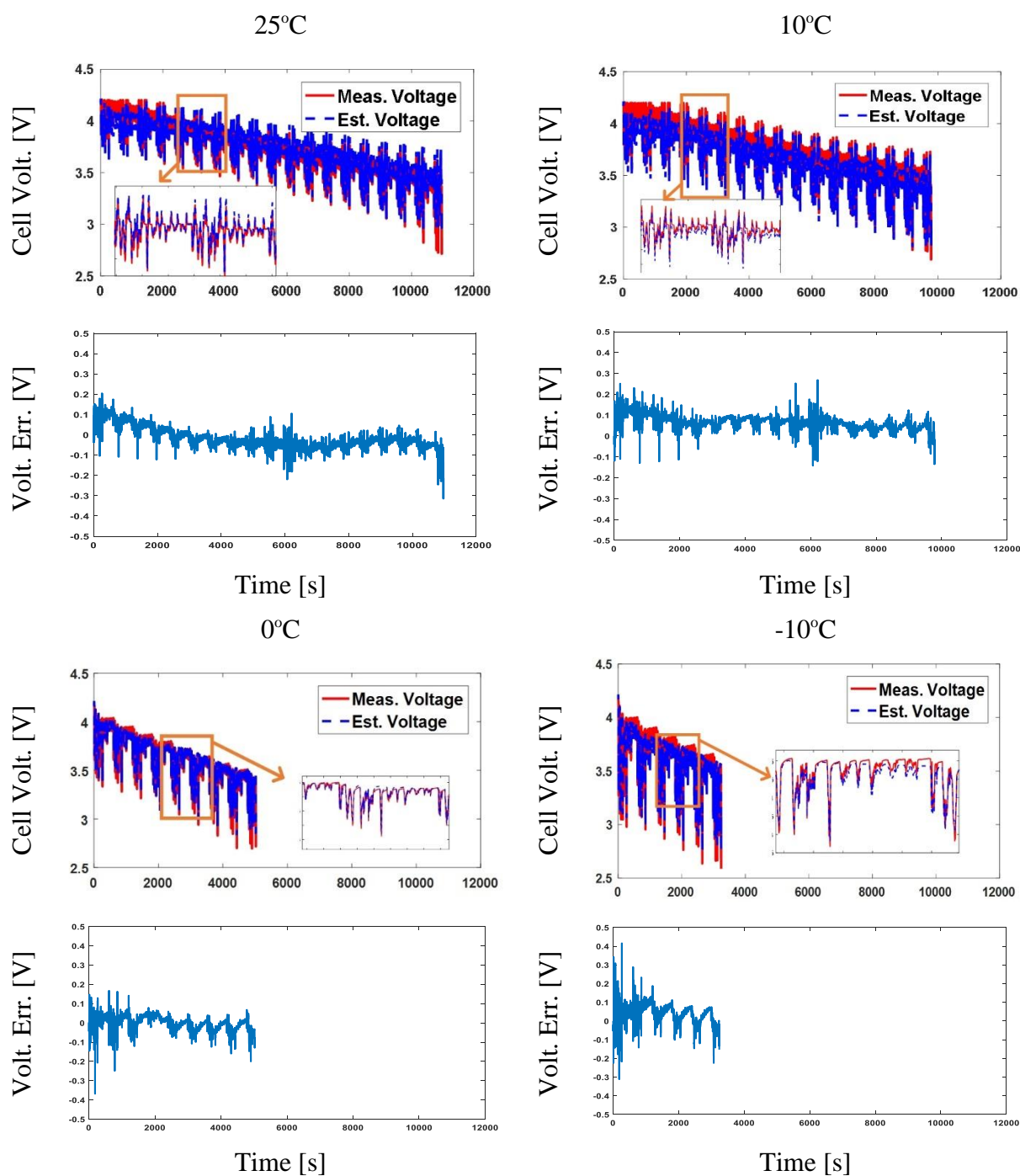
Fig. 2.25: Power-input RNN model validation results for Panasonic cells

While acknowledging this difference, the model with the power-input set offers an advantage noted earlier associated with its ability to estimate the amp-hours consumed from the battery for a given power profile. This feature is particularly appealing for automotive industry

since the vehicle controller delivers torque/power commands instead of current commands. By using the power command and the estimated battery voltage, the estimated amp-hours can be conveniently calculated using the relationship in (2.13).

$$\hat{Ah}(k) = \sum_{1}^{k} \frac{P(i)}{\hat{V}(i)} \tag{2.13}$$

Table 2.5: Summary of voltage prediction error for power-input RNN model (Panasonic)

	25ºC	10ºC	0ºC	-10ºC
MAE [V]	0.046	0.064	0.028	0.049
RMSE [V]	0.055	0.072	0.036	0.060
MAX [V]	0.315	0.269	0.368	0.417
STDDEV [V]	0.052	0.035	0.036	0.049

Fig. 2.26 plots the RNN predicted amp-hours vs. the measured amp-hours for the four validation datasets using the model with the power-input set. These overlaid waveforms show that the amp-hour estimations using (2.13) are quite accurate for all four validation datasets. However, similarly at all four temperature cases, the amp-hour prediction error tends to increase as the drive cycle goes on. This is because the model estimates current and the amp-hour is essentially accumulated current. Therefore, amp-hour prediction error will accumulate based on the current error over time.

25ºC

10ºC
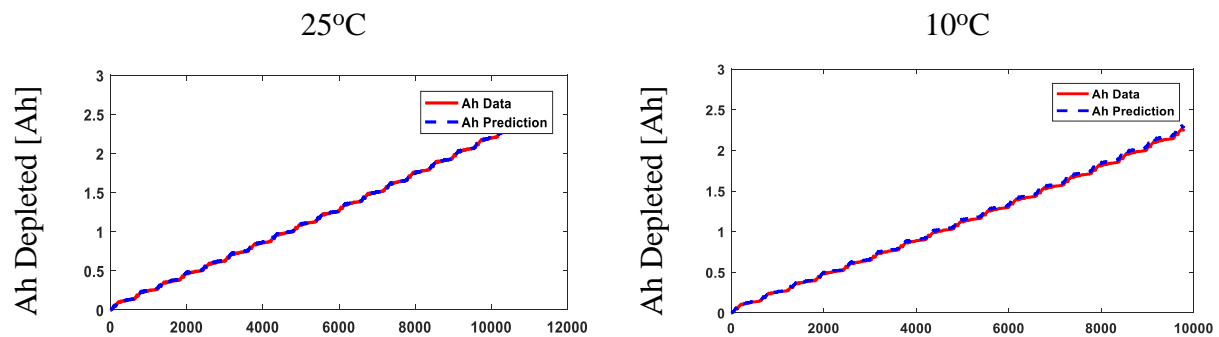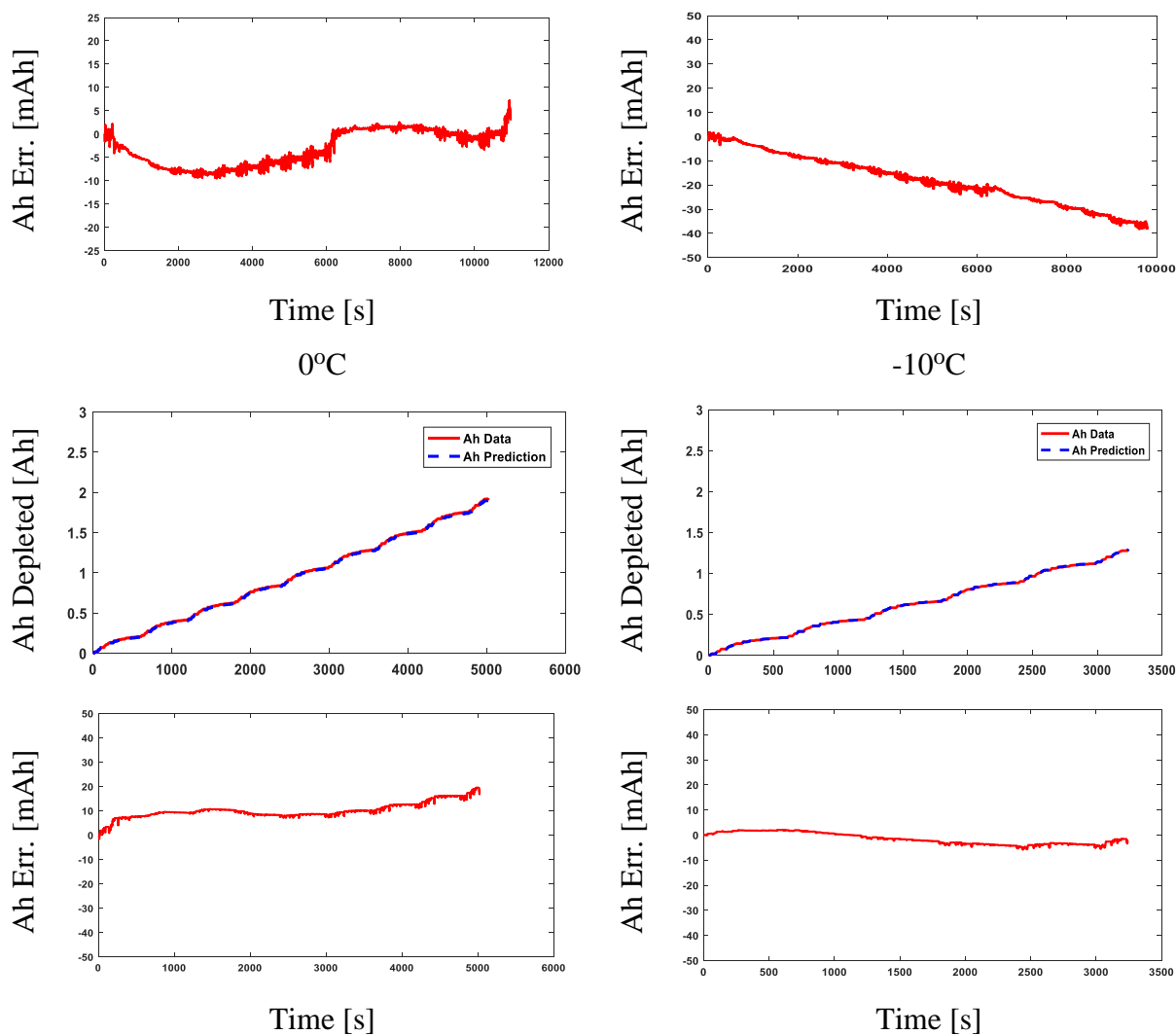
Fig. 2.26: Panasonic measured versus modeled amp-hours for power profiles

Table 2.6 provides the summary of the error metrics for the consumed amp-hour prediction. Generally, it can be observed that the model has worse performance at higher temperatures. This seems to contradict with the previous observation that the model works better at higher temperatures. However, since the battery can operate longer until reaching cut-off voltage at higher temperatures, the validation datasets at higher temperatures have more data at low SOC and this could lead to higher accumulated error for the amp-hour prediction.

Table 2.6: Summary of Ah prediction error for power-input RNN model (Panasonic)

	25°C	10°C	0°C	-10°C
MAE [mAh]	3.89	18.08	10.13	2.38
RMSE [mAh]	4.90	20.82	10.62	2.72
MAX [mAh]	9.54	38.31	19.50	5.84
STDDEV [mAh]	3.79	10.37	3.20	2.29

2.4.2   Model Evaluation for the Sony Cell

The proposed power-input RNN model is evaluated for the Sony VTC6 cells, which have a different chemistry from the Panasonic cells. Fig. 2.27 shows the battery voltage estimation results for the Sony VTC6 cells at different temperatures using the power-input RNN model. Similar to the results achieved for the Panasonic cells, the voltage estimation errors are well under 0.5V for different temperatures. Enlarged plots for small sections in the plots also show that the RNN model can capture the nonlinearity within the battery electrical behavior. Such results demonstrate the generality of the proposed RNN model for batteries with different chemistries over a wide range of temperatures. The voltage prediction error metrics are summarized in Table 2.7. The results are similar to those of the Panasonic cells in that the model has generally higher errors at low temperatures.

0°C   -10°C

Time [s]   Time [s]
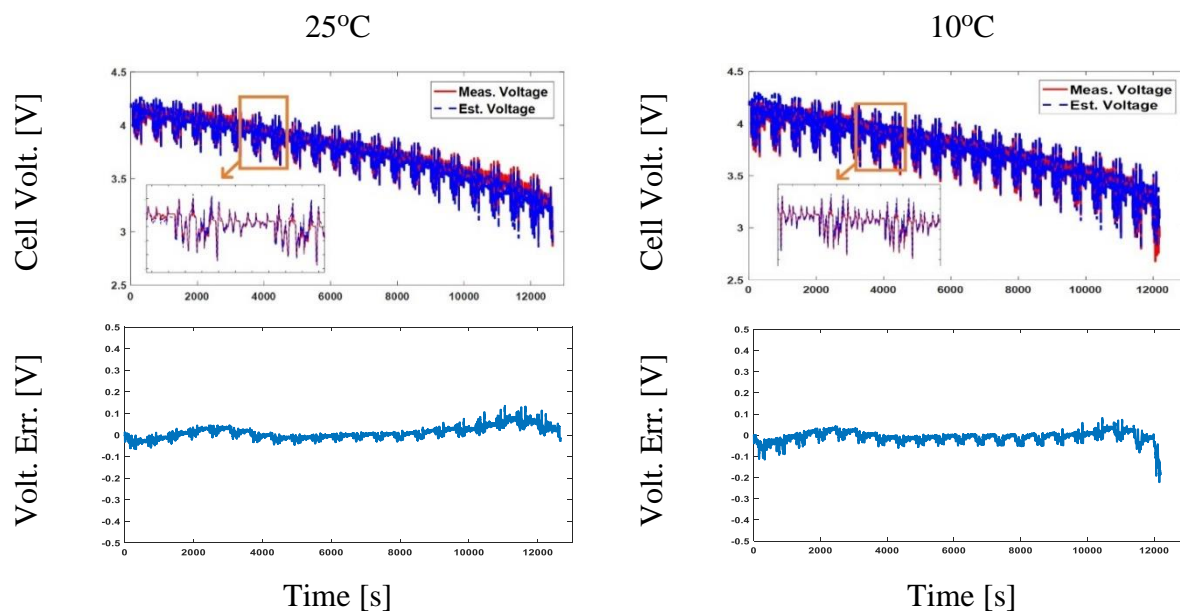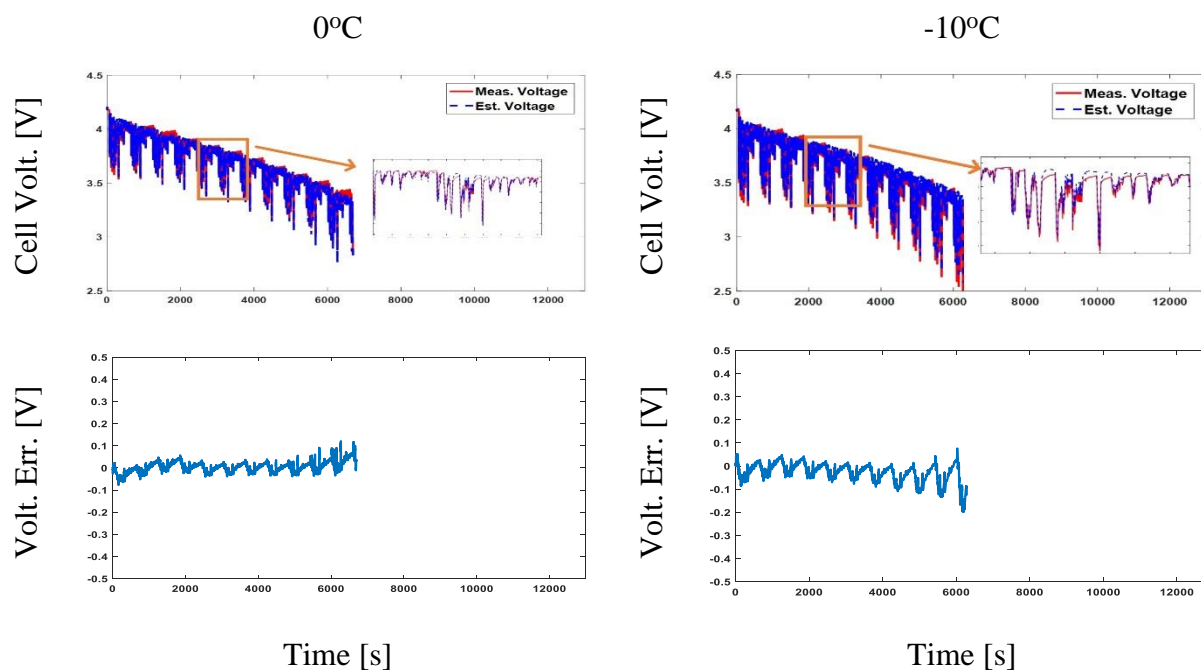
Fig. 2.27: Power-input RNN model validation results for Sony cells

For the Sony cells, the amp-hour prediction accuracy is analyzed as well. The results are shown

in Fig. 2.28 and the amp-hour predictions agree well with the measured amp-hour data for all three

temperatures. The associated error metrics are summarized in Table 2.8. The error metrics fall over

the similar ranges as those of the Panasonic cells and have the similar trends as stated earlier.

Therefore, the proposed power-input RNN model can be a quite robust model for both voltage and

amp-hour predictions over a wide temperature range. Such amp-hour prediction capability can be

helpful for battery energy estimation and consequently vehicle range prediction as well.
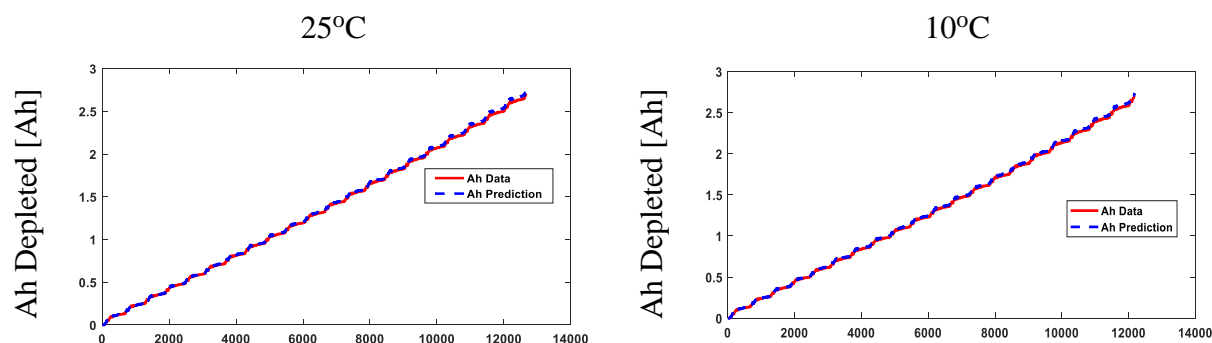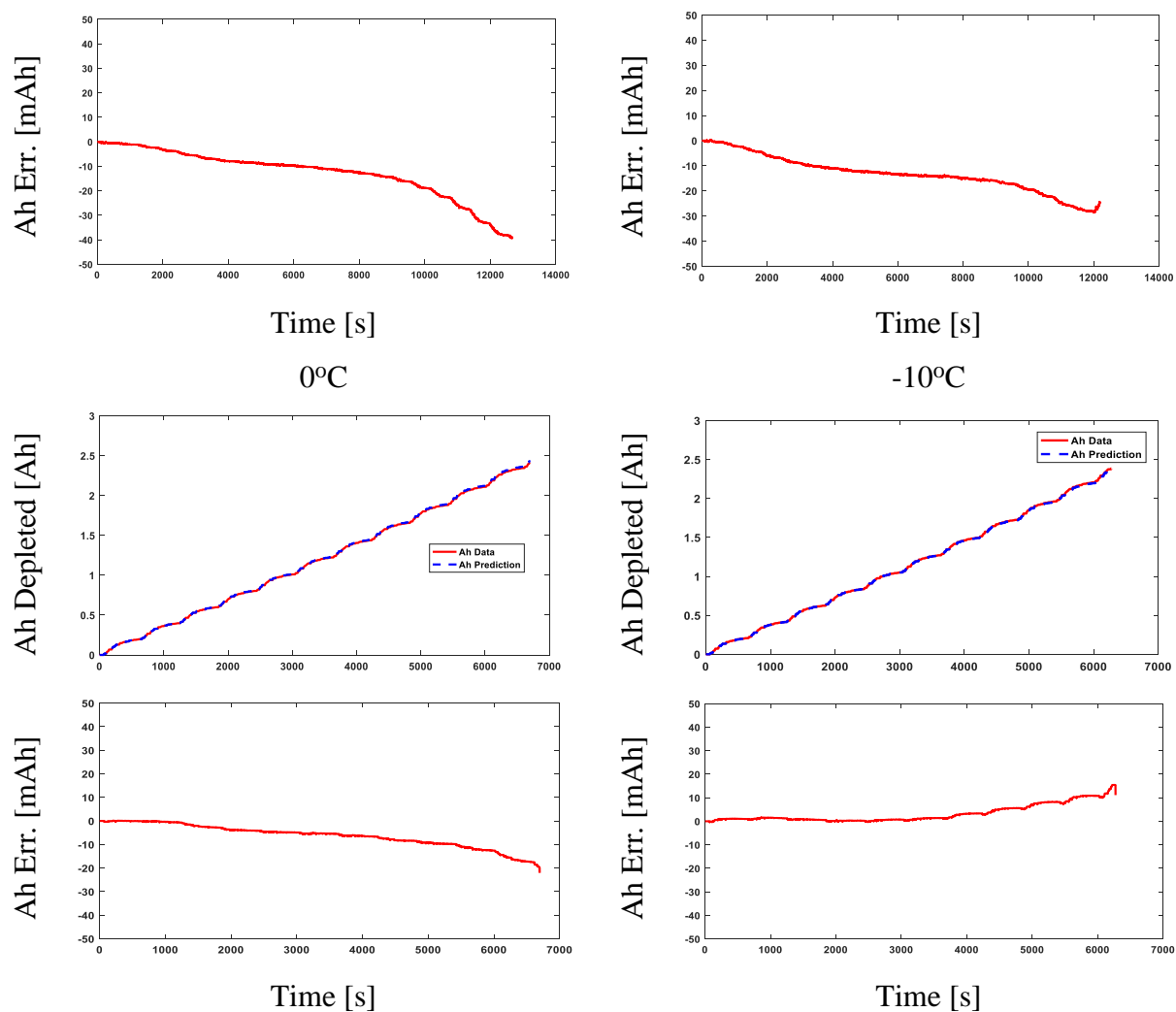
25°C   10°C

Fig. 2.28: Sony measured versus modeled amp-hours for power profiles

Table 2.7: Summary of voltage prediction error for power-input RNN model (Sony)

	25ºC	10ºC	0ºC	-10ºC
MAE [V]	0.023	0.020	0.019	0.037
RMSE [V]	0.030	0.028	0.025	0.050
MAX [V]	0.14	0.22	0.12	0.20
STDDEV [V]	0.028	0.026	0.025	0.040

Table 2.8: Summary of Ah prediction error for power-input RNN model (Sony)

	25ºC	10ºC	0ºC	-10ºC
MAE [mAh]	12.64	13.22	6.29	3.29
RMSE [mAh]	15.98	15.01	7.95	4.97
MAX [mAh]	39.66	28.61	22.04	15.46
STDDEV [mAh]	9.78	7.11	4.86	3.73

2.5   Chapter Summary

In this chapter, a lithium-ion battery electro-thermal model is developed, coupling a RNN electrical model with a lumped parameter thermal model. The RNN electrical model takes advantages of modern machine learning techniques and adopts GRU and DFS structures so that the long-time dependence of lithium-ion battery electrical responses are correctly modeled. Two types of RNN electrical models are proposed, one with current as the main input variable while the other using power as the main input variable. The current-input RNN model has been evaluated to achieve accurate voltage estimation very comparable to the traditional equivalent circuit models (ECMs). Meanwhile, the power-input RNN model is specifically useful for drive cycle simulations with power-commanded profiles and has been evaluated to achieve accurate voltage estimations for different drive cycles over a wide range of temperature.

On the other hand, a lumped parameter thermal model is developed for the cylindrical cell of interests. The internal heat generation due to overpotential and entropy change is carefully modeled. With identified thermal properties identified for different parts of the battery, the thermal model has been evaluated to accurately estimate both the battery surface temperature and the battery core temperature during drive cycles at different temperature conditions.

Although the developed thermal model uses current as one of the inputs, because of the feature of the power-input RNN model developed, both battery voltage and current can be estimated via the RNN model under power-commanded drive cycles simulations. Therefore, the

developed lithium-ion battery electro-thermal model can be integrated together and has been evaluated to accurately estimate both the electrical and thermal responses during drive cycles at various temperature conditions. Moreover, the proposed RNN models have been evaluated for batteries with different cathode chemistries and show consistent accuracy.

This provides a valuable tool for the EV manufacturers to model the battery and simulate its performance during drive cycles. The full vehicle simulation can also benefit from this holistic model.

Chapter 3 Investigation of Drive Cycle Properties Affecting Li-ion Battery ROD

The purpose of this chapter is to investigate the influence of dynamic drive profile properties on lithium-ion battery aging, distinguished from the steady-state current waveforms used in the previous work. Besides the aging factors commonly investigated, this investigation also focuses on the impact of several potential but less well-known aging factors. For example, it examines whether the existence of regeneration intervals interspersed with discharge periods during a dynamic discharge current profile influences the aging rate. In addition, statistical analysis techniques introduced in [17] are utilized to analyze two aging models: 1) linear regression, and 2) log regression. Finally, the aging influence of discharge temperature, and, more importantly, the interactions between temperature and the RMS current value, are explored using similar approaches.

3.1   Aging Analysis for RMS Current and Regenerative Conditions

3.1.1   Aging Experiment Design and Data Analysis Procedure

The three test conditions include one pure DC discharge, one non-regenerative stepped discharge waveform, and one-stepped discharge with roughly 8% regeneration (i.e., the ratio of regenerative power to discharge power). The two stepped drive profiles were carefully selected to mimic a dynamic drive cycle with the same average current (DC) value as a constant DC discharge condition at 2.9A. The two stepped cycle waveforms have the same RMS value of 3.7Arms, higher than the DC case. The three groups are denoted as "DC", "RMS", and "RMSw/reg", respectively.
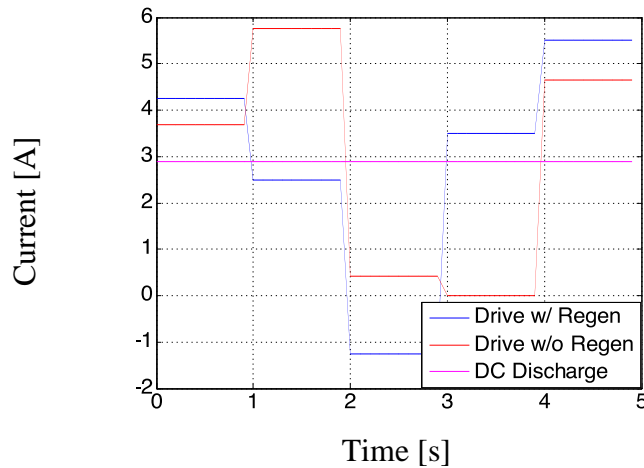
Fig. 3.1: Proposed drive profiles for aging experiments

Table 3.1: Summarized discharge waveform specifications

Treatments	DC	RMS	AC	Regen
AC w/o Regen	2.9 A	3.7 A	+	-
AC w/ Regen	2.9 A	3.7 A	+	+
DC	2.9 A	2.9 A	-	-

This experiment is designed to examine the influence of regeneration on battery aging by comparing the results of two stepped drive groups. It is also designed to reconfirm the significance of the RMS current value as an aging factor using a more dynamic drive profile than the pure sinusoids used in [17]. This aging experiment used nine Panasonic NCR18650PF lithium-ion cells rated at 2.9Ah and 3.7V.

Fig. 3.2 shows the experimental test configuration. Nine cells were evenly divided into three groups, and each underwent a 300-cycle aging process. Fig. 3.1 shows the one-period (5s) discharge waveforms for three test conditions, and the specifications of the three discharge waveforms are summarized in Table 3.1. For recording the battery aging characteristics, Electrochemical Impedance Spectroscopy (EIS) was carried out at the beginning of the experiment, and after every 30 cycles to measure R_0 at 80% SOC (0.58Ah discharged).

Fig. 3.2: 9-cell aging experimental setup

Analysis of covariance (ANCOVA) is used to linearly fit the response and covariate, i.e., initial resistance, and evaluate the effect of the different treatments [125]. The linear regression model used for the analysis of the experimental results follows ANCOVA procedure as shown in (3.1). Adopting a similar model configuration and parameter nomenclature as in [17], R_{ij} is the jth resistance measurement for the ith cell, and X_{ij} is the jth normalized cycle stamp for the ith cell. The actual cycle number C_j is normalized using (3.2) and (3.3). $\hat{\beta}_0$ is the intercept term, and $\hat{\beta}_1$ allows the initial values of different cells to be included as a predictor term, as well as helping to maintain physical units for the linear regression model.

After regression, $\hat{\beta}_2$ to $\hat{\beta}_{10}$ are the corresponding aging rate coefficients for each of the 9 cells. Grouping the coefficients for each of the three treatments and comparing the average aging rates between pairs of treatments using a Student's t-test according to (3.4) - (3.6), the statistical significance of the candidate aging factors is evaluated.

$$R_{ij} = \hat{\beta}_0 + \hat{\beta}_1 R_{i0} + \hat{\beta}_2 X_{1j} + \ldots + \hat{\beta}_{10} X_{9j} + \varepsilon_{ij} \qquad (3.1)$$

$$X_{kj} = Z_j \delta(i - k) \qquad (3.2)$$

$$Z_j = \frac{C_j - \bar{C}}{\Delta C} \tag{3.3}$$

$$\hat{\beta}_{avg} = \frac{\sum \hat{\beta}_i}{n} \tag{3.4}$$

$$Var\left(\hat{\beta}_{avg}\right) = \frac{Var\left(\hat{\beta}_i\right)}{n} \tag{3.5}$$

$$t = \frac{\hat{\beta}_{avg1} - \hat{\beta}_{avg2}}{\sqrt{Var\left(\hat{\beta}_{avg1}\right) + Var\left(\hat{\beta}_{avg2}\right)}} \tag{3.6}$$

3.1.2   Statistical Analysis of RMS and Regeneration Effects

In Fig. 3.3, the corrected resistance values (i.e., $R_{ij} - \hat{\beta}_1 R_{i0}$) and each treatment's average model (i.e., $\hat{\beta}_0 + \hat{\beta}_{avg} Z$) are plotted together, accompanied by a plot of the residuals. The average aging rates of different treatments and the t-test results between each pair of treatments are summarized in Table 3.2 and Table 3.3. The resulting coefficients are summarized in Table 3.4. In Fig. 3.4, the residuals are small, ensuring the validity of the linear model. The statistical hypothesis testing threshold is selected to be 10% considering the manufacturing variations among the cells and the imperfect current regulation accuracy.
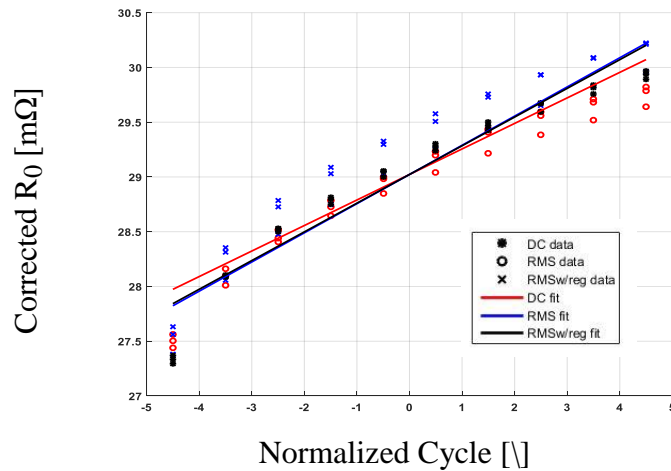
Fig. 3.3: Corrected Ro for every cell, group averaged fitted model
(linear regression model)
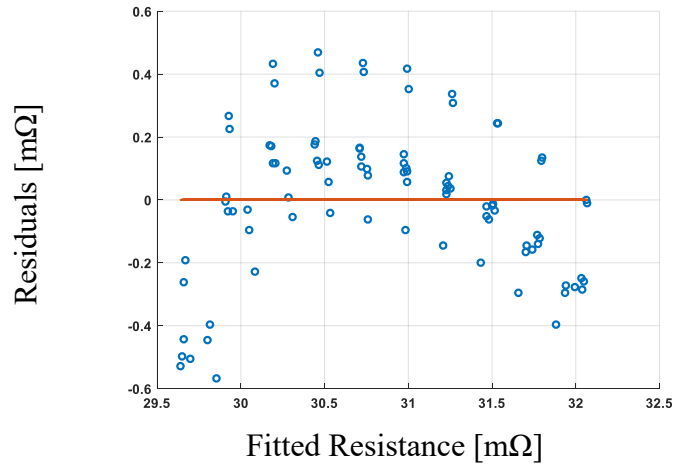
Fig. 3.4: Residuals for the linear regression
model

Table 3.2: Estimated avg. slopes for linear regression model (25⁰C)

	$\hat{\beta}_{avg}$	Std-dev ($\hat{\beta}_i$)
DC	0.233	6.98e-3
RMS	0.266	7.40e-4
RMSw/reg	0.262	6.10e-3

Table 3.3: T-test results for linear regression model (25⁰C)

	t-statistic	p value	Significant
RMS vs. DC	8.22	1.36%	Y
RMS w/reg vs. DC	5.42	0.59%	Y
RMS vs. RMSw/reg	1.21	34.7%	N

Table 3.4: Fitted coefficients (β_i's) for the linear regression model (25⁰C)

Index	Coeff.	Index	Coeff.
0	29.02	6	0.2656
1	0.065	7	0.2664
2	0.2251	8	0.2647
3	0.2380	9	0.2551
4	0.2361	10	0.2665
5	0.2671	/	/

Based on the t-test statistical significance results, the aging rates in the RMS and RMSw/reg cases are both higher than that in the DC case, confirming that when the discharge current follows a dynamic drive profile, higher RMS current values will result in faster aging. In addition, the high p-value of 34.7% for the RMS vs. RMSw/reg t-test in Table 3.3 indicates that one cannot statistically distinguish between the aging rates of the two cases with and without regeneration. That is, the test results indicate that two cells tested with dynamic cycles that have the same RMS current value can be expected to age the same regardless of whether the cycles include regenerative intervals or not.

Examination of the resistance curves in Fig. 3.3 suggests that R_0 deviates somewhat from following a straight line, showing signs of plateauing during the later stages of the test. Therefore, even though the linear regression model captures the overall aging trends, it would be worthwhile to investigate a higher-order model to better capture the gradually slowed aging. For this purpose, a log regression model is a suitable candidate to capture any aging saturation effects at high cycle numbers. The differential equation form of the proposed log regression model is provided in (3.7). The rate of change of R_0 per 30-cycle is merely the difference between two consecutive R_0 measurements (j^{th} and $j+1^{th}$) for the ith cell. $\hat{\beta}_0$ is the offset term and $\hat{\beta}_{i1}$ is the aging rate coefficient for the ith cell.

$$\frac{dR_{ij}}{dX_j} = \hat{\beta}_0 + \hat{\beta}_{i1}R_{ij} + \varepsilon_{ij} \tag{3.7}$$

$$t = \frac{(\hat{\beta}_{avg1} - \hat{\beta}_{avg2}|T_+) - (\hat{\beta}_{avg1} - \hat{\beta}_{avg2}|T_-)}{\sqrt{Var(\hat{\beta}_{avg1} - \hat{\beta}_{avg2}|T_+) + Var(\hat{\beta}_{avg1} - \hat{\beta}_{avg2}|T_-)}} \tag{3.8}$$

In Fig. 3.5 and Fig. 3.6, the differential R_0 data for each cell are plotted together with the fitted responses (i.e., $\beta_0 + \beta_{i1}R_{ij}$), accompanied by a plot of the residuals. Table 3.5, Table 3.6, and Table 3.7 summarize the average aging coefficients by treatments, the t-test results, and the aging coefficients. These results agree with the results from the linear regression model, indicating that higher RMS current values result in faster aging and that the cells do not age differently

because of the presence of regenerative operation.
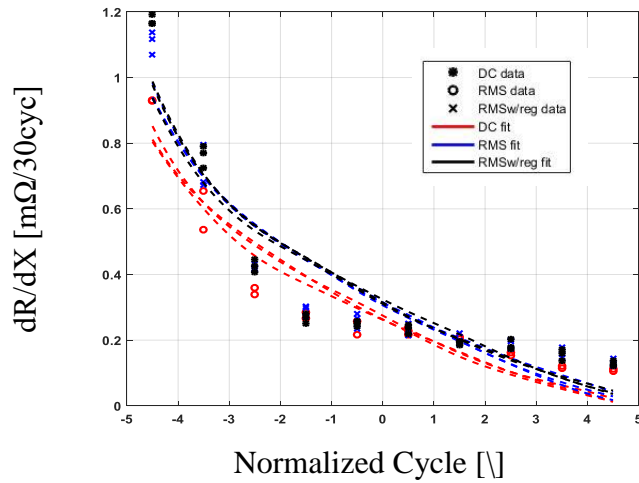
Fig. 3.5: Rate-of-change of Ro for every cell (log regression model)
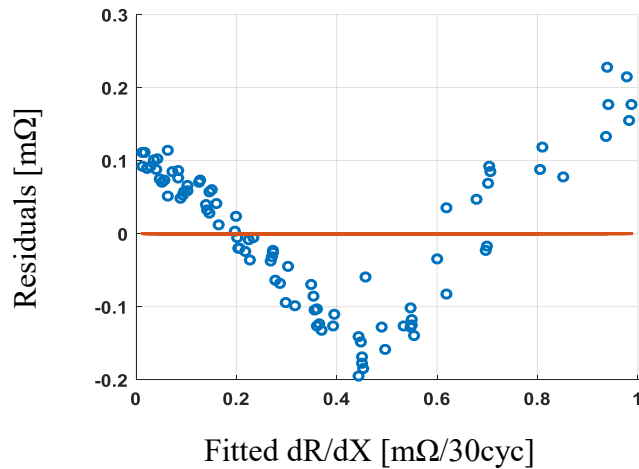
Fig. 3.6: Residuals for the linear regression model

Table 3.5: Estimated avg. slopes for log regression model (25ºC)

	$\hat{\beta}_{avg}$	Std-dev ($\hat{\beta}_i$)
DC	-0.359	1.25e-3
RMS	-0.355	2.10e-3
RMSw/reg	-0.357	4.73e-4

Table 3.6: T-test results for log regression model (25⁰C)

	t-statistic	p value	Significant
RMS vs. DC	3.26	4.19%	Y
RMS w/reg vs. DC	3.29	5.80%	Y
RMS vs. RMSw/reg	1.66	22.67%	N

Table 3.7: Fitted coefficients (β_i's) for the log regression model (25⁰C)

Index	Coeff.	Index	Coeff.
0	11.37	51	-0.3570
11	-0.3606	61	-0.3537
21	-0.3582	71	-0.3563
31	-0.3588	81	-0.3572
41	-0.3531	91	-0.3565

The results from both the linear modeling and the log modeling imply the benefits of reducing the AC content of the battery current to extend the battery life. On the other hand, they also suggest that regenerative operation does not appear to influence battery aging considerably and can be given less attention when designing battery systems.

3.2 Aging Analysis of Interactions Between Temperature and RMS Current

3.2.1 Low Temperature Aging Experiment Design

Temperature data gathered during the battery aging tests suggests a close relationship between the battery aging process and temperature. Based on the temperature readings collected from the surface of each cell, the surface temperature of the DC group cells rose from 25⁰C to ~31⁰C during each discharge cycle, while the surface temperatures of cells in the other two groups both rose to ~34⁰C. Such temperature differences agree with the observations in [17].
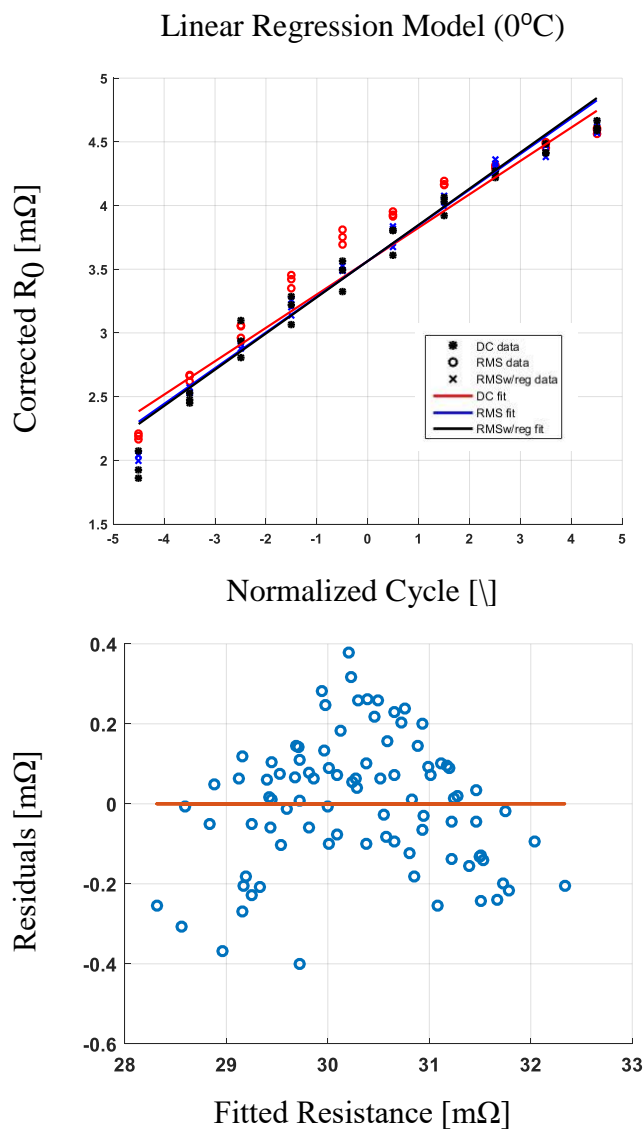
Fig. 3.7: Corrected R_0, group averaged fitted model, and residuals (0^0C)

The effects of this temperature difference can be expected to accumulate over extended numbers of cycles and contribute to faster aging. The similarity of the observed temperature rises in the RMS and RMSw/reg cell groups is one more piece of evidence that supports the analytical result that the presence of regeneration during the discharge profile does not have any significant influence on battery aging.

To more carefully explore interactions between the discharge current RMS value and the discharge temperature, a second experiment has been performed. The second experiment was

designed very similarly to the first aging experiment except that the battery discharge temperature was changed from 25^0C to 0^0C. For this second experiment, another set of nine Panasonic cells was used, and they were grouped the same way as during the first experiment. 300 aging cycles were performed on each cell, and their series resistances were measured using EIS every 30 cycles.

The low-temperature data were analyzed using the same linear regression model as in (3.1). In Fig. 3.7, the corrected R_0 progressions for every cell are plotted together with the group averaged fitted models in the low-temperature experiment. The linear regression model based on ANCOVA fits the data well with small and random residuals. The aging coefficients are presented in Table 3.8.

Table 3.8: Fitted coefficients (βi's) for the linear regression model (0°C)

Index	Coeff.	Index	Coeff.
0	3.5601	6	0.2803
1	0.9521	7	0.2789
2	0.2657	8	0.2903
3	0.2605	9	0.2821
4	0.2601	10	0.2807
5	0.2818	/	/

Table 3.9: Estimated average slope (0°C experiment)

	βavg	Std-dev (βi)
DC	0.2621	3.1e-3
RMS	0.2803	1.5e-3
RMSw/reg	0.2843	5.2e-3

Table 3.10: T-test Results (0°C experiment)

	p-value	Significant
RMS vs. DC	0.3%	Y
RMSw/reg vs. DC	0.5%	Y
RMS vs. RMSw/reg	30.89%	N

Utilizing similar Student's t-test techniques as for the first experiment, the average slopes of different treatments are calculated and compared in Table 3.9 and Table 3.10. The results indicate that, when discharging at low temperatures, there is strong statistical evidence that cells cycling with a discharge current of higher RMS value age faster. Furthermore, the statistical results also suggest that the presence of regeneration does not influence battery aging during these tests.

Consistent with this observation, battery surface temperatures increase similarly in the RMS and RMSw/reg groups but are higher than in the DC group. These results suggest that a larger temperature difference between the cell surfaces and the ambient may lead to faster aging during cycling experiments.

It should be noted that the log regression model was not necessary for the low-temperature data since the linear regression model is better suited for evaluating the aging progression and interpreting the aging rates, especially when considering the comparison between the high-temperature and low-temperature aging rates.

3.2.2 Interacting Aging Effects Analysis

In addition, the data from both experiments can be effectively combined for analysis utilizing an extended form of (3.1). The new linear regression model is expressed in (3.9), where the model is extended to 18 cells including nine cells from the first experiment and nine cells from the second experiment:

$$R_{ij} = \hat{\beta}_0 + \hat{\beta}_1 R_{i0} + \hat{\beta}_2 X_{1j} + \ldots + \hat{\beta}_{19} X_{18j} + \varepsilon_{ij} \qquad (3.9)$$

300 cycle data for both experiments were extracted and combined for analysis. It should be noted that, due to test equipment availability limitations, the second experiment could not be carried out simultaneously with the first experiment. Any storage-based aging of the cells that were used for the second experiment while the first experiment was running is neglected in this analysis.

Combined Linear Regression Model
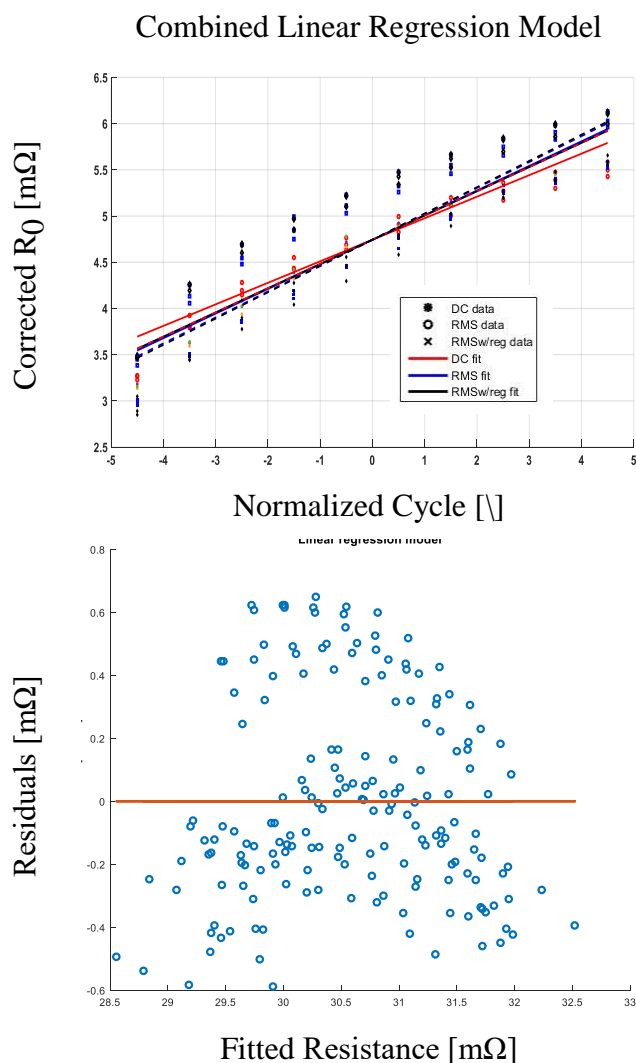
Fig. 3.8: Corrected R_0, group-averaged fitted model, and residuals (25°C and 0°C)

In Fig. 3.8, the corrected R_0 for each of the 18 cells, their respective group-averaged fitted model, and the residuals are plotted. The data are well-fitted with reasonably small residuals. The 18 coefficients $\hat{\beta}_2$ to $\hat{\beta}_{19}$ from the fitted results using (3.9) are provided in Table 3.11. They have been categorized according to six different test conditions covering the 3 treatments and 2 temperatures. By comparing the averaged slopes of groups with the same discharge current profile but at different temperatures, Table 3.12 shows that there is strong evidence that the batteries age faster at 0°C compared to 25°C for all three discharge current profile cases. This result is expected since known aging mechanisms at low temperature reduce the lithium intercalation stability and

kinetics, lose lithium to passive surface films, and lead to irreversible capacity fading [126][127].

The t-test equation (3.8) can be used to investigate whether the aging effects caused by different RMS values are statistically different at different temperatures (i.e., interaction between the RMS current value and the battery discharge temperature). One would expect that the temperature rise caused by inducing more RMS current would result in a faster change in series resistance at low temperatures since in Fig. 3.9, the resistance gradient is sharper at low temperatures.
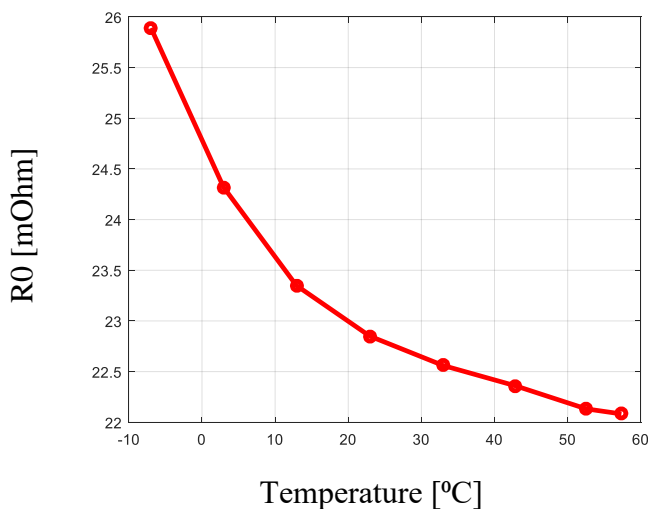
Fig. 3.9: Cell series resistance vs. temperature

Table 3.11: Fitted coefficients (βi's) for the combined linear model (0ºC & 25ºC)

Index	Coeff.	Index	Coeff.
0	4.7433	10	0.2665
1	0.9177	11	0.2657
2	0.2251	12	0.2605
3	0.2380	13	0.2601
4	0.2361	14	0.2818
5	0.2671	15	0.2803
6	0.2656	16	0.2789

7	0.2664	17	0.2903
8	0.2647	18	0.2821
9	0.2551	19	0.2807

Table 3.12: T-Test results for temperature effect on aging

	t-statistic	p value	Significant
0⁰C vs. 25⁰C (DC)	6.59	0.90%	Y
0⁰C vs. 25⁰C (RMS)	14.81	0.07%	Y

Table 3.13: T-test results for interaction results (RMS & T)

	t-statistic	p value	Significant
(RMS-DC)*T	3.69	0.61%	Y

However, Table 3.13 summarizes the t-test results and suggests that discharging the battery with a high RMS current value at 25°C would affect the battery aging performance more significantly than at 0°C.

This result leads to questions about whether the temperature rise due to the induced RMS current is not the only factor that should be considered when comparing the low-temperature aging rate to high-temperature aging rate. For instance, as indicated previously, the end-of-discharge voltage is also an aging factor. While cycling at low temperature, the difference of the end-of-discharge voltage between the "RMS" testing group and the "DC" testing group is noticed to be smaller than during cycling at room temperature. This observation suggests that such aging effects would share the role of affecting aging together with the temperature rise from high RMS current at room temperature. Based on the analysis in this paper, it suggests that the RMS current may impact aging more significantly at room temperatures.

3.3   Chapter Summary

This chapter has investigated the aging influences of critical but less well-known discharge current properties during cycling for lithium-ion batteries. Specifically, the current RMS value, the

presence of regeneration, and interactions between the RMS current value and the battery discharge temperature are the primary aging factors of interest.

An effective analysis methodology incorporating ANCOVA, log regression modeling, and Student's t-test provides statistical rigor and a basis for confidence in the analytical results. A careful design of experiments also strengthens the reasoning process.

Important results include: 1) higher RMS current results in faster aging, 2) the presence of regeneration in the current profile does not affect aging, 3) low-temperature results in faster aging, and 4) interaction between the aging effects of RMS current and temperature appears to be significant.

These conclusions have many practical implications that are expected to be helpful for future battery system design. For instance, the clear coupling effect between the RMS current value and cell temperature implies a necessity of combining both current regulation and thermal balance in a battery management system.

Chapter 4 Reduced-order Li-ion Battery ROD Modeling

As discussed in the state-of-the-art, the rate-of-degradation (ROD) of the lithium-ion batteries is one of the variables within a physics-based lithium-ion battery electrochemical degradation model. It has not been widely investigated because of its insignificance in terms of the monitoring and predicting the degradation status of the lithium-ion batteries. However, from the stand-of-point of the modern system/process control, the ROD is a suitable control variable that could lead to overall battery degradation control. This has not been widely recognized either in research or in the industry yet, and only little research has paid attention to the potential control variable [112] - [117]. In this chapter, a reduced-order lithium-ion battery ROD model is developed, and it is suitable for effective and computationally-light ROD estimation when the battery is operating during drive cycles.

4.1   Reduced-order ROD Model Development

To develop a ROD model, different battery aging rate factors need to be understood, and preferably they can be included and represented in the ROD model. In the literature, factors such as the current rate, the battery SOC, and the battery temperature have been evaluated to have substantial effects on the battery degradation rate. In addition, in the previous chapter, it has been shown that during a drive cycle, the current RMS is another aging rate factor. Since the RMS value is calculated based on one type of average of current values over a period of time, a ROD model that includes the current as one of the variables inherently includes the current RMS value as well. In terms of the high-frequency noise on the loading current, as discussed from the previous chapter, it should be controlled by physical filters and is out of the scope of this research.

In addition, based on the nature of the Butler-Volmer equation, it is better to use the core temperature of the battery instead of the surface temperature. As shown in the state-of-the-art review as well as in a previous chapter, the core temperature can be noticeably higher than the surface temperature during a drive cycle or a conventional constant-rate cycling. Though the temperature difference is not significant, with the help of a battery thermal model as the one developed in a previous chapter, an estimated battery core temperature could help reduce the ROD estimation error.

Overall, the goal of a ROD model is to at least include the battery current rate, the battery SOC, and the battery core temperature as the associated variables. In addition, for an EV application, the dynamics change fast, and the switching frequency of the electronics is also high. Thus, another requirement for the ROD model is that it can be computed fast.

4.1.1   Reduced-order ROD model development

As discussed in the state-of-the-art, the lithium-ion battery suffers from numbers of different aging mechanisms and identifying one dominant aging source to model is a crucial step to develop any degradation model. The idea should be the same when modeling the ROD.

As there are many ways and positions that a lithium-ion battery can degrade, some of which are suitable for quantitative modeling. It has been shown that cathode aging mechanisms are much more difficult to model due to the high variability of the materials. On the other hand, the SEI layer between the electrolyte and the carbonaceous anode has been found to grow because of known chemical reactions, which results in anode aging. It also has been discussed in the state-of-the-art that electrolyte decomposition because of these parasitic chemical reactions contributes to the total battery aging much more than that of structural damages or other mechanical disintegration within the electrodes.

In addition, since most of the current commercialized battery cells used for EV applications are using graphite as the anode material but have different types of cathode materials, modeling

the anode aging mechanism has much more generality.

As a result, the following assumption from [99][100][101] is adopted in the reduced-order ROD model development in this thesis.

Assumption 1:

Anode degradation mechanism, specifically SEI layer growth due to parasitic side reactions, dominates the whole aging mechanisms and is assumed to be the sole source of aging considered in the rate-of-degradation model in this thesis.

Different lithium-ion batteries have different physical structures. As seen in Fig. 1.4, the cylindrical cell, prismatic cell and pouch cell can look very different. Even though every cell consists of an anode, a separator, electrolyte, and a cathode, they are physically distributed and assembled can vary case by case. In terms of a microscopic view, how graphite particles distribute on the anode, or how lithium-ions intercalate through the film at the graphite anode, is not observed to be in a certain way in every cell. Therefore, a geometric assumption is needed as a starting point to model the physical system.

There are three structural model assumptions typically used for a lithium-ion cell. The 2D model shown in Fig. 4.1(a) that was introduced by Doyle et al. [22] considered the whole physical process. It calculates the concentration of lithium on electrodes and in the electrolyte in terms of both solid and solution phases and with respect to both x and y directions. This assumption considers the electrochemical process thoroughly but introduces extreme complexity for equation formulation and computation. The introduction of several time-variant physical parameters could over-complicate the model and make it extremely hard to converge.

To simplify the model, the pseudo-2D model was developed by Fuller et al. [22]. In this approach, the solution phase concentration was assumed to only vary in the x-direction, and the solid phase was assumed to be identical spherical particles of a determined size. The dominant diffusion form was in the radial direction [111]. However, this approach showed some instability

issues when dealing with both the radial direction and y-direction simultaneously. It later had been adjusted with coordination scaling.

In this thesis, the third geometric model, single particle (SP) model shown in Fig. 4.1(c), is used as a further simplification of the P2D model. According to the SP model, the following assumptions are used:

Assumption 2:

1. The graphite anode is assumed to consist of identical spherical particles of a predetermined size.

2. The porous electrode is treated as many identical single particles that uniformly distribute across the electrode.

3. The diffusion phenomenon is dominant in the radial direction.

4. The local potential and concentration gradients in the solution (electrolyte) phase are ignored and accounted for using a lumped solution resistance term

5. The SP model accounts for solid diffusion in the electrode particles and the intercalation reaction kinetics.

The SEI component that involves the secondary reaction is assumed to be ethylene carbonate. It reacts with lithium-ion and will eventually form lithium ethylene dicarbonate $(CH_2OCO_2Li)_2$, the insoluble component. A detailed formation flowchart is shown below in Fig. 4.2. A simpler RDS schematic can be found in Fig. 1.68, which shows the 2-electron deduction side reaction.
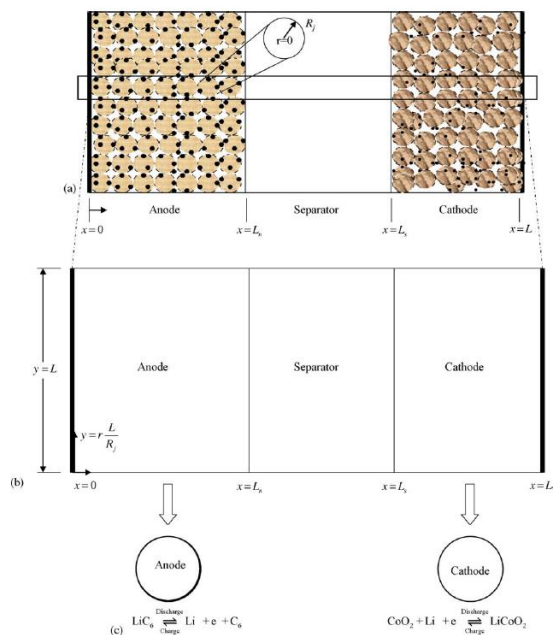
Fig. 4.1: Diff. Li-ion Cell Physical Models (a) 2D (b)P2D (c) SP [111]

The rate-determine-step (RDS) in this reduced-order ROD model contains a two-electron reduction scheme for every secondary reaction. This reaction is assumed to be the dominant side reaction, and the complete chemical reaction sequence consists of four steps of reactions and is well summarized by Safari et al. in [97].
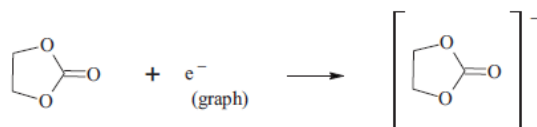
Step 1: Ethylene carbonate (EC) receive one electron to form an anion
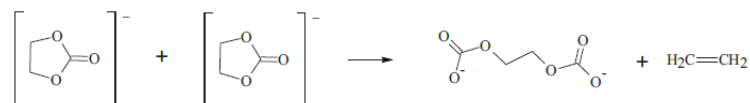
Step 2: Two anions could react with each other to form new organic compounds
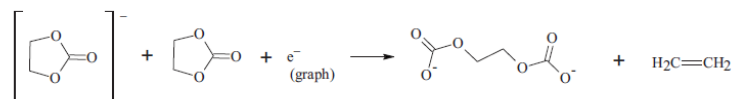
Step 3: One anion could react with another EC by receiving one electron to have the same reaction as in Step 2
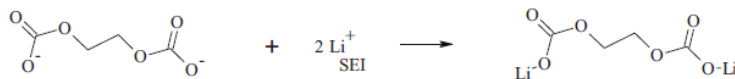
Step 4: The compound reacts with Li^+ to form insoluble lithium ethylene dicarbonate

Fig. 4.2: Insoluble component formation flow chart

Considering the electrochemical degradation models developed in the literature, the parts that cause the most computational burden and limits the simulation to offline are the PDEs associated with either the electrode kinetics or the mass transport. Therefore, to simplify such models, the best approach is to reduce the PDEs as much as possible. An approach to simplify the model following this idea could be found in [114] has been shown in the state-of-the-art. The resulted ROD calculation equation is shown in (1.49). According to [114], the most important step of the simplification was to assume the exchange current I_0 as a pre-determined function of solely the battery SOC, so that the PDE associated to the electrode kinetics is eliminated. Moreover, assuming a fixed side reaction exchange current density i_{0s}, the PDE associated with the mass transport is eliminated.

In this research, the simplified ROD model introduced in [114] is modified, specifically regarding the calculations of both the I_0 and i_{0s} procedures. As shown in [17], I_0 was not only dependent on the battery SOC, but the temperature was another factor. Further investigations also show that current rate can affect I_0 as well. In this research, I_0 is treated as a function of the current rate, the battery SOC, and the battery temperature, extending from the literature. More details about I_0 characterization can be found in the next section. On the other hand, it might be insufficient to assume fixed i_{0s} for all operating conditions. Though i_{0s} does not seem to be dependent on the battery SOC or the current rate, it may have a dependence on the type of aging mechanism. For the aging mechanisms associated with the SEI layer growth, high temperatures could change the i_{0s} value. Moreover, the i_{0s} value may be different for different for different anode materials.

Adopted from the approach in [114], the following steps and equations show the process

of achieving the reduced-order battery ROD model for this research.

The primary reaction is dominant by the charge transfer process modeled by the Butler-Volmer equation in (4.1).

$$I_1 = I_0(I_{app}, SOC, T_c) \left[\exp\left(\frac{\alpha F}{R_g T_c} \eta_n\right) - \exp\left(-\frac{\alpha F}{R_g T_c} \eta_n\right)\right] \qquad (4.1)$$

I_1 is the intercalation (primary) battery current, I_{app} is the loading battery current, α is assumed to be 0.5 by symmetrical reduction and oxidation reactions, F is the Faraday constant, R_g is the gas constant, T_c is the battery core temperature, and η_n is the overpotential on the anode.

In (4.2), η_n is represented as the difference between the anode potential U_n, and the anode reference potential U_n^{ref}, i.e., anode OCV.

$$\eta_n = U_n - U_n^{ref} \qquad (4.2)$$

The side-reaction kinetics is shown in (4.3), as a Tafel's relationship. I_s is the side reaction current, a_n is the anode specific area, Vol_n is the anode volume, and η_s is the side reaction overpotential. η_s, in (4.4), is calculated similarly to η_n, as the difference between the anode potential and the side reaction reference potential U_s^{ref}.

$$I_s = - i_{0s} a_n Vol_n (T_c) \exp\left(-\frac{\alpha F}{R_g T_c} \eta_s\right) \qquad (4.3)$$

$$\eta_s = U_n - U_s^{ref} \qquad (4.4)$$

The U_s^{ref} is fixed at 0.4 V vs. Li/Li$^+$(ref. electrode), representing the prone anode potential for the 2-electron reduction aging mechanism to occur.

In addition, assuming the reaction on the electrode is a superposition of the primary (intercalation) reaction and the side-reaction. The loading current is the summation of the primary current and the side-reaction current, as shown in ((4.5).

$$I_{app} = I_1 + I_s \qquad (4.5)$$

Among the five equations (4.1)-(4.5), there are five unknown variables when the physical

parameters are excluded. The five unknown variables are I_1, η_n, η_s, U_n, and I_s. Since there are five equations and five unknowns, there exists an exact solution for each of the unknowns. The side-reaction current I_s is the ROD metric, and its calculation is the most important one shown in (4.6).

$$(4.6)$$

$$I_s(I_{app}, SOC, T_c) = -i_{0s}a_nVol_n exp(\frac{-F(U_n^{ref} - U_s^{ref})}{2R_gT_c}) * exp(-asinh(\frac{-i_{app} - I_s(I_{app}, SOC, T_c)}{2I_0(I_{app}, SOC, T_c)}))$$

It is a similar representation as (1.49). Though it is not a direct calculation and I_s exists on both sides of the equation, simple and fast gradient descent type of recursive regression algorithms can be applied to find a solution for I_s.

It should be noted that this ROD equation, as the developed reduced-order ROD model, fulfills the requirements stated at the beginning of this chapter. The current rate, the battery SOC, and the battery core temperature are variables in this equation. Besides the SOC dependence upon I_0, the anode OCV U_n^{ref} also has a strong relationship with the battery SOC. Such relationship can be experimentally determined beforehand and converted into either a look-up table or a fitted function.

Once the $I_s(k)$ is calculated from (4.6) at any given operating point denoted as $(I_{app}(k), SOC(k), T_c(k))$, the fading capacity and increasing resistance of the battery can be calculated in a discrete format, shown in (4.7) and (4.8).

$$Q(k) = Q(k-1) + \Delta t * I_s(k-1) \tag{4.7}$$

$$R(k) = R(k-1) - \frac{M_{SEI}}{a_n^2\rho_{SEI}k_{SEI}F} * \Delta t * \frac{I_s(k-1)}{Vol_n^2} \tag{4.8}$$

4.1.2   Model Simplification: Exchange Current Estimation

As shown in the previous section, I_0 for the developed reduced-order ROD model in this research depends on the current rate, the battery SOC, and the battery core temperature. To bypass the PDE that models the lithium-ion concentration change on the anode during the battery

operation, it is desirable to develop a method to estimate I_0 at different operating points.

Recognizing the fact that I_0 appears in the Butler-Volmer equation modeling the charge transfer process in the battery, I_0 can be calculated based on the inverse form of the Butler-Volmer equation. In [17], a nonlinear Butler-Volmer (BV) battery model in the discrete format is shown below in (4.9).

$$V(z) = V_{ocv} (SOC, T) + I(z) * R_0 + \frac{b_1(I, SOC, T_c)}{1 + a_1 z^{-1}} \text{asinh}(\frac{I(z)}{2I_0(I, SOC, T_c)}) \qquad (4.9)$$

This discrete equation can be further extended to include the Arrhenius relationship. The temperature-dependent form of (4.9) is shown in (4.10), and I_0 is represented as a function of B and G in (4.11).

$$(4.10)$$

$$V(z) = V_{ocv} (SOC, T) + I(z) * A\exp(\frac{E}{T_c}) + \frac{b_1(I, SOC, T_c)}{1 + a_1 z^{-1}} \text{asinh}(I(z)*B(I, SOC, T_c)*\exp(\frac{G}{T_c}))$$

$$I_0(I, SOC, T_c) = \frac{1}{2B(I, SOC, T_c)} \exp(\frac{-G}{T_c}) \qquad (4.11)$$

With fixed A, E, a_1, and G values, (4.10) can be converted into the difference equation form as in (4.12), and I_0 can be estimated via estimating B(I, SOC, T_c) by the recursive estimation algorithms based on the battery experimental data at different operating conditions.

$$V(k) - a_1 V(k-1) = V_{ocv} (SOC, T) + (I(k) + a_1 I(k-1)) * A\exp(\frac{E}{T_c(k)})$$
$$+ b_1(I, SOC, T_c) \text{asinh}(I(k)*B(I, SOC, T_c)*\exp(\frac{G}{T_c(k)})) \qquad (4.12)$$

The experiments to estimate B(I, SOC, T_c) are designed as pulse tests with different current rates starting at different battery SOCs and battery temperatures. Every pulse test last for 10 seconds and the voltage, current, and surface temperature of the battery are recorded.

For the Panasonic 18650PF cell rated at 2.9 Ah, the following Table 4.1 summarizes the pulse test conditions that have been experimentally conducted.

Table 4.1: A summarized table for pulse test conditions

Pulse Current [C]	0.5C, 1C, 2C, 4C, 6C
Start SOC [%]	100%, 95%, 90%, 80%, 70%, 60%, 50%, 40%, 30%, 25%, 20%, 15%, 10%, 5%
Temperature [^{0}C]	25^{0}C, 10^{0}C, 0^{0}C, -10^{0}C, -20^{0}C

After collecting data for each test condition at a 10Hz sampling frequency, the data is analyzed by a nonlinear regression algorithm to fit the best $B(I, SOC, T_c)$ for each test condition. $I_0(I, SOC, T_c)$ is then calculated based on (4.11). The estimated I_0 values for different operating conditions are plotted in Fig. 4.3.
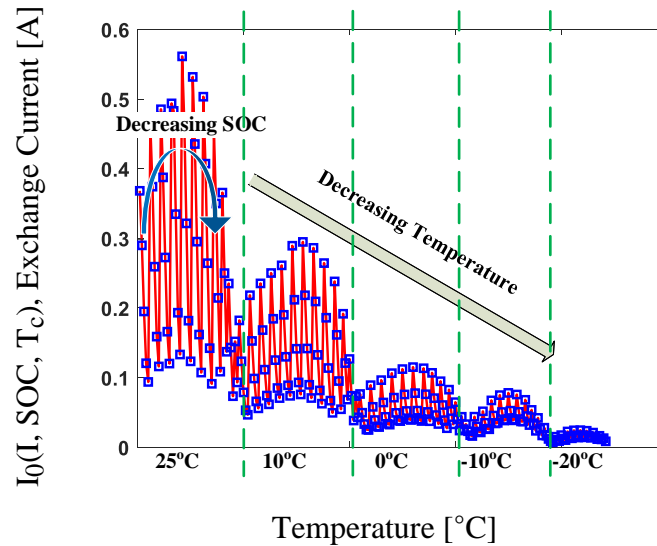
Fig. 4.3: Estimated exchange current I$_0$ at different operating conditions

It should be noted that for each nonlinear regression process, the OCV is assumed not changed over the 10-second pulse and the OCV value is the battery starting voltage ensured by long time rest between tests. Moreover, the core temperature is assumed to be the same as the measured surface temperature. The trends show that I_0 decreases as the temperature decreases and as the pulse current rate increases, while exhibiting U-shape dependence on the battery SOC.

The estimated I_0 data can be used as a look-up table, searched and extrapolated at any operating point denoted by the current rate, the battery SOC, and the estimated battery core temperature. However, the look-up table is quite large and may take a longer time to extrapolate

the I_0 value than expected. In the next section, a fitting function using the separation of variables are applied.

4.1.3   Exchange Current Fitting Using Separation of Variables

To fit the seemingly chaotic curve of I_0 shown in Fig. 4.3 requires a good understanding of the physics and electrochemical theories regarding the potential relationship between the I_0 and the three variables.

By looking at the I_0 trends in Fig. 4.3, the temperature dependence seems to follow the Arrhenius relationship as many other electrochemical parameters. On the other hand, the U-shape relationship between I_0 and the battery SOC could be explained by a break-down version of the Butler-Volmer equation where the I_0 is represented by (4.13), assuming symmetrical reaction, $\alpha_a = \alpha_c = 0.5$. Also, C_{Li} denotes the lithium-ion concentration, which represents the battery SOC. Thus, the relationship between I_0 and the battery SOC would potentially follow a relationship as $I_0 \sim (1 - SOC)^{0.5}*SOC^{0.5}$.

$$I_0 = k_0 C_e^{\alpha_a}(C_{Li\_max} - C_{Li})^{\alpha_a} C_{Li}^{\alpha_c} \tag{4.13}$$

In addition, by extracting a small portion of the estimated I_0 curve, the relationship between the current rate and the I_0 seems to be exponential, as shown in Fig. 4.4.
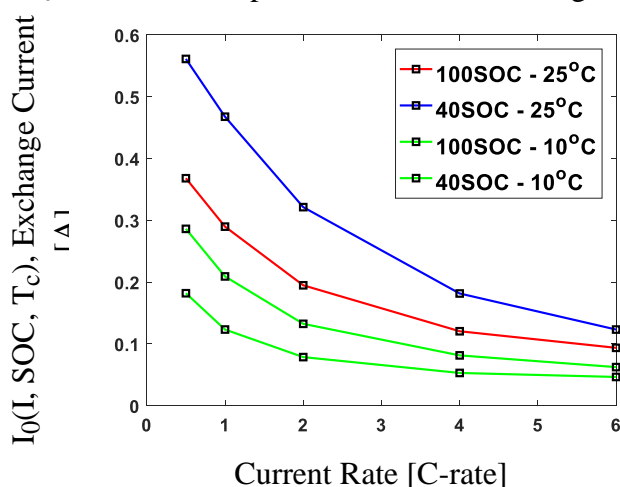
Fig. 4.4: Estimated exchange current I₀ vs. Current rate

As I_0 is the idle current the battery can draw with no overpotential, the idle current is possibly suppressed when the loading current is high, leading to the exponential trend shown above.

Overall, the relationship between I_0 and three operating variables are identified, leading to a fitting approach by the separation of variable technique. The fit function is shown in (4.14), where p_1 - p_6 are parameters fitted by the nonlinear regression.

$$I_0 (I, SOC, T_c) = f_I (I) * f_{soc} (SOC) * f_{T_c} (T_c)$$

$$= [p_1*exp(p_2*I + p_3)] * [p_4*(1.1 - SOC)^{0.5}*SOC^{0.5}] * [p_5*exp(\frac{p_6}{T_c})] \qquad (4.14)$$

The resulted I_{0_fit} is plotted together with the previously estimated I_0 in Fig. 4.5. The fitting error is plotted in Fig. 4.6, and shown to be mostly less than 0.05A. For the cases where the errors are the biggest, battery SOC is low and the battery usually never reaches to such low SOC due to safety and battery protection considerations.
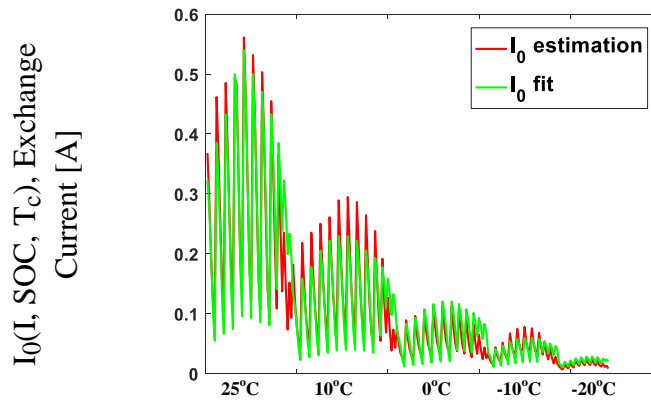
Fig. 4.5: Estimated I_0 and fitted I_{0_fit} comparison
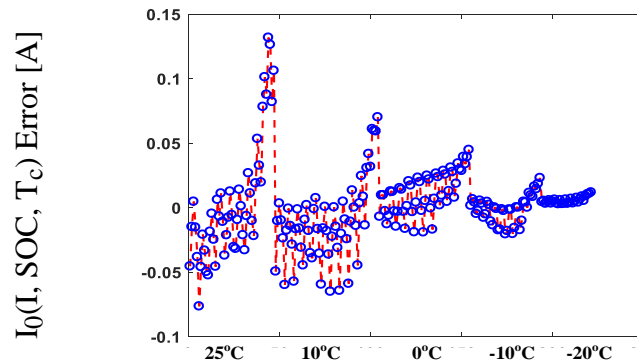
Fig. 4.6: Fitting errors between the estimated I0 and fitted I0_fit

With the fit function available, a quick calculation of the exchange current I_0 is now accessible for any given operating point with a current rate, a battery SOC state, and a measured/estimated battery core temperature.

4.2 Reduced-order ROD Model Validation

In this section, the developed reduced-order ROD model for the Panasonic 18650PF battery is evaluated based on the previously conducted cycling aging tests. As mentioned in the previous section, the side-reaction exchange current density i_{0s} could be slightly different for different batteries since the anode graphite material may not be entirely identical. Therefore, the validation process is divided into two parts, the tuning step, and the evaluation step. In the tuning step, several sets of constant-rate cycling tests data with measured resistance data for the Panasonic 18650PF batteries are compared to the simulated resistance estimations by the developed reduced-order ROD model through the same cycling conditions. The i_{0s} value in (4.6 is tuned until a good agreement is achieved between the estimated resistance and the measured resistance for all cycling conditions. After the tuning step is fixed and the reduced-order ROD model is simulated and compared to another set of experimental results from a set of dynamic-rate cycling aging experiments for model evaluation. It should be noted that the experiments for tuning and evaluation should be run at the same ambient temperature for consistency.

4.2.1   Aging Experimental Design

The aging experiments associated with the tuning step are constant-rate cycling experiments with three different discharge current rates, 0.5C, 1C, and 2C. The aging experiments last for 300 cycles, and the ambient temperature condition is 25°C. In Table 4.2, the aging experiment test conditions are summarized. A total of 6 cells are tested, with 2 cells for each case of the discharge current rate. The 6 cells finish the 300-cycle aging experiments, and the cell resistances are measured by EIS every 30 cycles.

Table 4.2: Cycling experimental design for five Panasonic 18650 lithium-ion cells

Cell #	C Rate	Discharged Capacity %	CCCV Charging Rate	Cycles Per Measurement	EIS Measurement
1	0.5	75	0.3C, 4.2V, 0.05A cut-off	30	R_0
2	0.5	75	0.3C, 4.2V, 0.05A cut-off	30	R_0
3	1	75	0.3C, 4.2V, 0.05A cut-off	30	R_0
4	1	75	0.3C, 4.2V, 0.05A cut-off	30	R_0
5	2	75	0.3C, 4.2V, 0.05A cut-off	30	R_0
6	2	75	0.3C, 4.2V, 0.05A cut-off	30	R_0

The aging experiments used for evaluation are the same as the tests introduced in the previous chapter that investigate aging factors within the drive cycle. The three test conditions include one pure DC discharge, one non-regenerative stepped discharge waveform, and one-stepped discharge with roughly 8% regeneration (i.e., the ratio of regenerative power to discharge power). The two stepped drive profiles were carefully selected to mimic a dynamic drive cycle with the same average current (DC) value as a constant DC discharge condition at 2.9A. The two stepped cycle waveforms have the same RMS value of 3.7Arms, higher than the DC case. The three groups are denoted as "DC", "RMS", and "RMSw/reg", respectively.
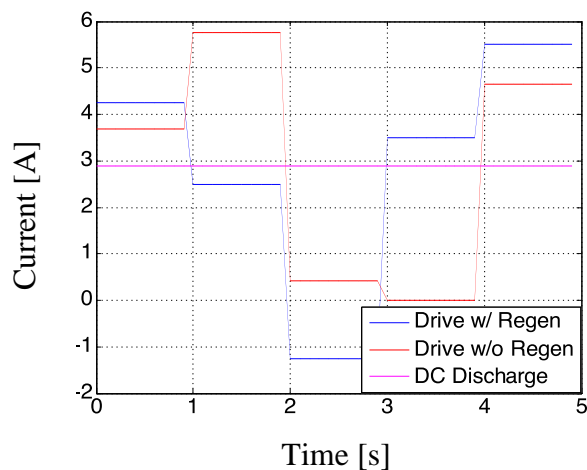
Fig. 4.7: Proposed drive profiles for aging experiments

Table 4.3: Summarized discharge waveform specifications

Treatments	DC	RMS	AC	Regen
AC w/o Regen	2.9 A	3.7 A	+	-
AC w/ Regen	2.9 A	3.7 A	+	+
DC	2.9 A	2.9 A	-	-

Fig. 4.7 shows the one-period current profiles for the three waveforms, and Table 4.3 summarizes the specifications of the different waveforms. For these three waveforms, they are much more dynamic than the constant-rate discharge current waveform. Although it is not a drive cycle, it can still provide useful references to evaluate the developed reduced-order ROD model.

4.2.2   ROD Model Prediction Analysis

The constant-rate cycling data is compared with the estimation results using the reduced-order ROD model. After tuning i_{0s}, the simulated resistances achieve a good agreement with the measured resistance data for all three testing conditions. For the two cells undergoing the same cycling test, the resistance measurements are averaged. The comparison between the resistance estimation and the resistance data is plotted in Fig. 4.8.
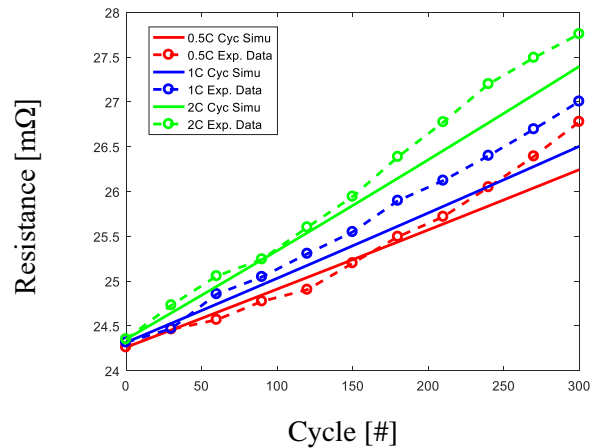
Fig. 4.8: Comparing estimated and measured resistances for the tuning step

Based on the good agreement between the measured resistance and the estimated resistance, the i_{0s} is tuned to be 1.875e-7 A/m^2, about 8 times smaller than the fixed value reported in the literature. The batteries tested in the literature have been the SONY 18650 cells, and they have existed longer than Panasonic 18650PF cells and potentially are inferior in manufacturing qualify and cell performance. The i_{0s} represents the side-reaction rate constant of the battery and tends to be smaller for better cells.

In Fig. 4.9, the incremental resistances for all three cases are plotted, all of which starts from 0. It should be noted that the tuning is intentionally processed to achieve small underestimations for all three cases. This is because considering the other aging mechanisms that have not been modeled in the proposed reduced-order ROD model, the estimated resistance growth should be slower. In addition, the resistance estimation errors for the tuning step are plotted in Fig. 4.10, and generally small errrors are seen.
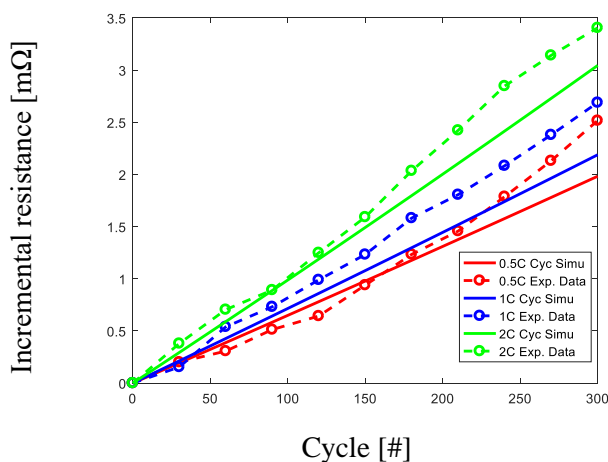
Fig. 4.9: Incremental resistance comparison for the tuning step
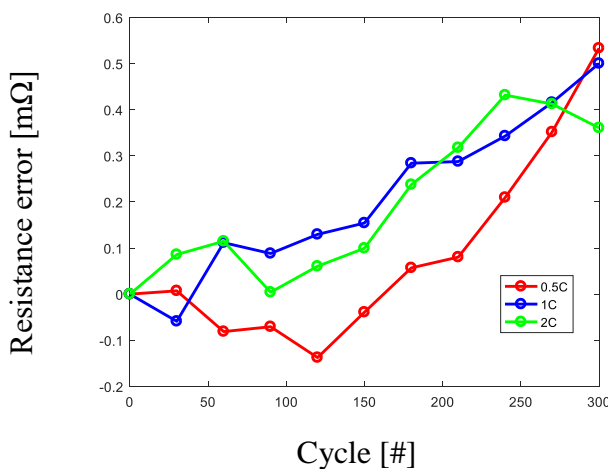
Fig. 4.10: Resistance estimation error for the tuning step

After tuning the i_{0s} for the Panasonic 18650PF cells at 25°C, the reduced-order ROM model is again simulated following the same testing sequence of the dynamic-profile cycling experiments shown in Table 4.3. The estimated resistances are compared to the measured resistance in Fig. 4.11. The estimated resistance shows good agreements with the measured data, confirming the effectiveness of the developed reduced-order ROD model.
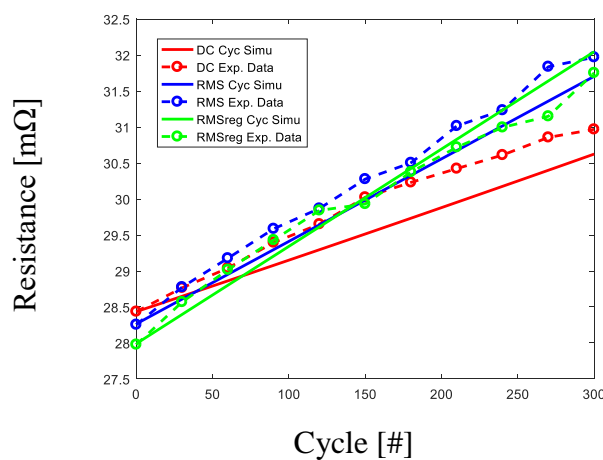
Fig. 4.11: Comparing estimated and measured resistances for the evaluation step
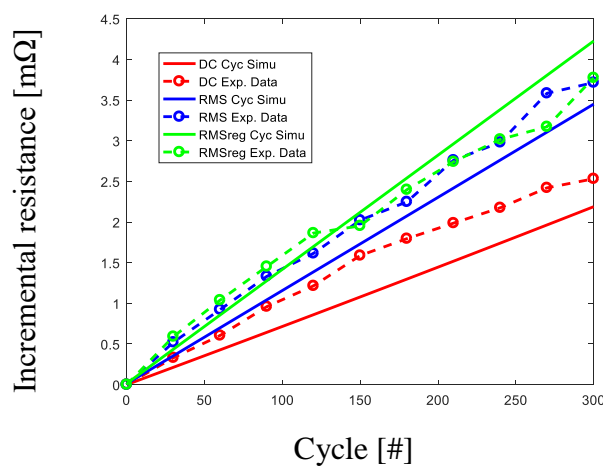
Fig. 4.12: Incremental resistance comparison for the evaluation step
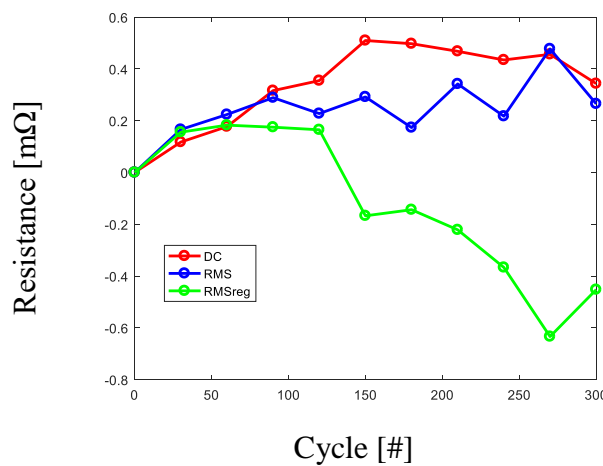
Fig. 4.13: Resistance estimation error for the evaluation step

Moreover, the incremental resistances and the resistance estimation errors for the evaluation step are plotted in Fig. 4.12 and Fig. 4.13. It can be seen from the plots that the estimations tend to usually underestimate the actual degradation progress. This is as expected since the batteries experience other types of aging mechanisms as well, and only the SEI layer growth on the anode is included in the developed model. For now, the developed model is only validated at room temperatures due to two reasons: 1) at low temperatures other aging mechanisms could tamper with the understanding of the degradation state measurements, and 2) although high temperatures aggravate SEI layer growth, however, it is infrequent for batteries in the EV to be operated in such temperature ranges. To avoid too many uncertainties on the developed model, the tuned i_{0s} is kept constant, and the research temperature range is carefully selected. On the other hand, although low temperature does not necessarily aggravate the aging mechanisms for SEI layer growth, it aggravates the aging mechanisms on the cathode significantly, and from a whole cell point of view, the cell resistance would be observed to increase faster. This poses challenges for the degradation control via ROD manipulations, and other aging source-targeted ROD models need to be developed.

4.3   ROD Model Evaluation for Different Batteries

In the previous sections, the proposed ROD model has been evaluated for the Panasonic 18650PF cell. Since it involves a series of steps to formulate the ROD model, it is important to further validate its applicability to different batteries. As introduced in Chapter 2, Sony VTC6 cells are comparable cells with respect to the Panasonic cells. Sony cells are cylindrical 18650 cells and have graphite as the anode material. The biggest difference is that the cathode materials for the Sony cells are different. As shown in Table 2.2, Sony cells' cathode material is NMC, whereas Panasonic cells' cathode material is NCA. Since both cells have the same anode material, the assumptions made earlier in this chapter can be applied to the Sony cells as well. In this section, similar model formulation process is adopted to evaluate the validity of the proposed ROD model

for a different type of batteries.

4.3.1   ROD Model Parameter Identification

As discussed in the previous sections, I_0 and i_{0s} are the two major parameters residing in the intermediate model equations that require identification before achieving a closed-form, real-time solution for the ROD metric, I_s. Starting with identifying I_0 in terms of its dependency on battery load current, SOC, and core temperature, a series of pulse tests has been conducted for the Sony cells. Slightly different from the test conditions chosen for the Panasonic cells, less SOC stages are chosen and the testing temperature range is changed from $-20^0C \sim 25^0C$ to -10^0C to 45^0C. These changes aim to save testing time and accommodate a proper temperature range in which EV batteries operate more often. The test conditions for the Sony cells are summarized in Table 4.4 below.

Table 4.4: A summarized table for pulse test conditions for Sony VTC6

Pulse Current [C]	0.5C, 1C, 2C, 4C, 6C
Start SOC [%]	100%, 90%, 80%, 70%, 60%, 50%, 40%, 30%, 20%, 10%, 5%
Temperature [^0C]	$45^0C, 35^0C, 25^0C, 10^0C, 0^0C, -10^0C$

Based on the BV cell model introduced in the previous section, I_0 is estimated using the nonlinear regression in Matlab Optimization Toolbox such that V(k) in (4.12) can achieve the least squared error with respect to the voltage measurements in each of the test condition. The I_0 estimation results are shown below in Fig. 4.14.

Compared to the I_0 estimation results for the Panasonic cells in Fig. 4.3, I_0 estimation results have similar magnitudes and shapes for the Sony cells. This confirms the potential physical relationships between I_0 and different variables introduced earlier. Meanwhile, the arc-shaped dependency of I_0 on SOC and the Arrhenius-type dependency on temperature are also shown in the plot. Extracting part of the plot, Fig. 4.15 once again shows the exponential relationship between I_0 and the current rate.
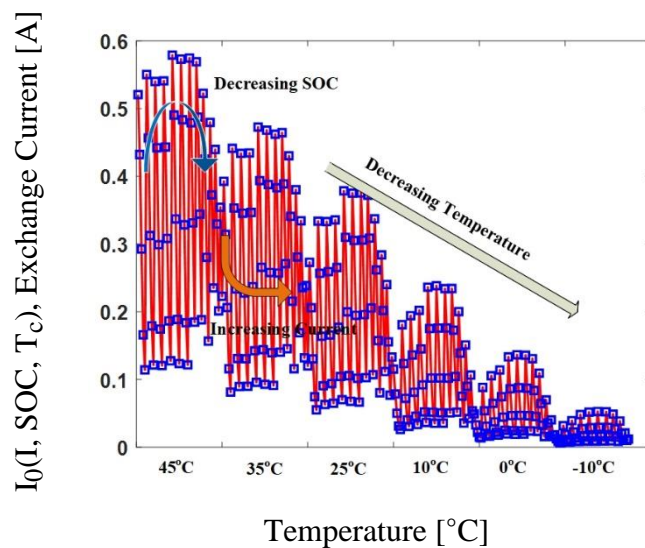
Fig. 4.14: Estimated exchange current I₀ at different operating conditions for Sony cells
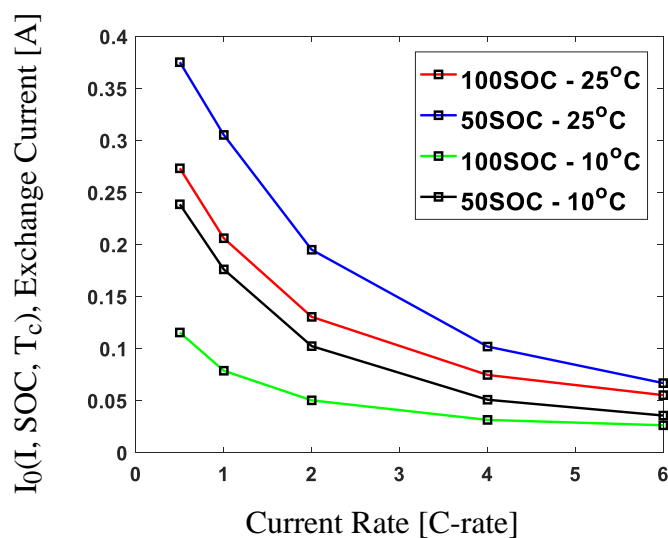
Fig. 4.15: Estimated exchange current I₀ vs. Current rate for Sony cells

Therefore, the separation of variables method is used again to generate a function to quickly calculate I_0 at different operating conditions. The function is formulated as the following, same as (4.14). Using nonlinear regression to identify parameters p_1 to p_6, the fitted I_0 is plotted in Fig. 4.16 together with the previously estimated I_0. The errors between the fitted I_0 and estimated I_0 are shown in Fig. 4.17.

$$I_0 (I, SOC, T_c) = f_I (I) * f_{soc} (SOC) * f_{T_c} (T_c)$$

$$= [p_1*exp(p_2*I + p_3)] * [p_4*(1.1 - SOC)^{0.5}*SOC^{0.5}] * [p_5*exp(\frac{p_6}{T_c})]$$
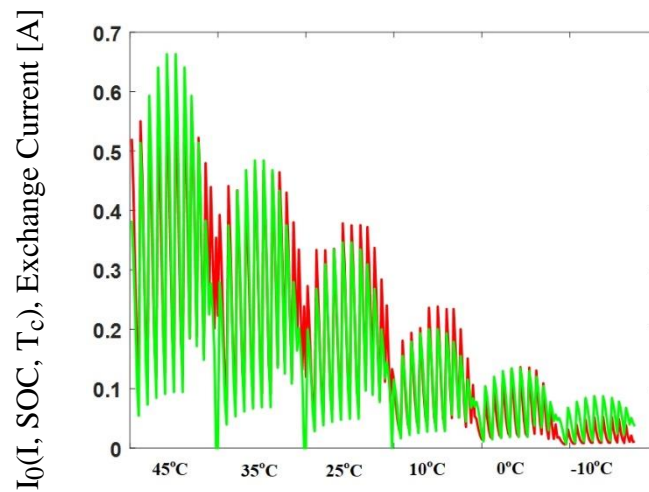
Fig. 4.16: Estimated I0 and fitted I0_fit comparison for Sony cells
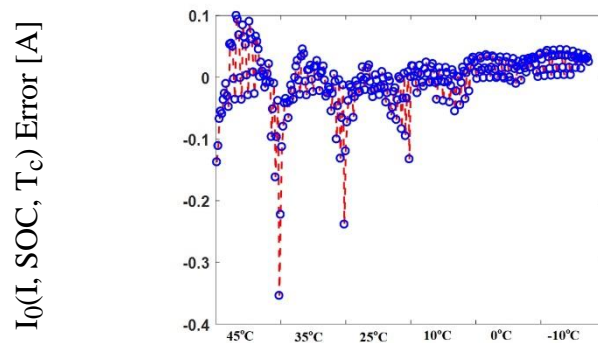
Fig. 4.17: Fitting errors between the estimated I0 and fitted I0_fit for Sony cells

The errors are mostly small with few ones rather large. However, the large errors all appear at operating conditions with very low SOCs ($< 10\%$). When the vehicle is driving, batteries are hardly operating at such conditions. Therefore, the fitted I_0 can be used for the real-time ROD model.

On the other hand, the side-reaction exchange current density i_{0s} also needs to be identified to complete the ROD model formulation. As mentioned earlier, i_{0s} is a battery-specific parameter and will change for different batteries. It required a set of constant-rate cycling test to characterize

i_{0s} for the Panasonic cells and the same approach is used for characterizing i_{0s} for the Sony cells.

Table 4.5: Cycling experimental design for Sony cells

Cell #	C Rate	Discharged Capacity %	CCCV Charging Rate	Cycles Per Measurement	Measured Resistance
1	0.5	75	0.3C, 4.2V, 0.05A cut-off	10	R_{20s}
2	0.5	75	0.3C, 4.2V, 0.05A cut-off	10	R_{20s}
3	1	75	0.3C, 4.2V, 0.05A cut-off	10	R_{20s}
4	1	75	0.3C, 4.2V, 0.05A cut-off	10	R_{20s}
5	2	75	0.3C, 4.2V, 0.05A cut-off	10	R_{20s}
6	2	75	0.3C, 4.2V, 0.05A cut-off	10	R_{20s}

The cycling experiment is summarized in Table 4.5 for characterizing i_{0s} and a total of 300 cycles are performed for each tested cell. Unlike the resistance measuring method used for the Panasonic cells, due to unavailability of the EIS meters, the resistance is measured through a 20 second discharge pulse with 2C discharge current rate. In addition, the resistance is measured every 10 cycles to capture more data points.

Another difference when characterizing i_{0s} for the Sony cells is the range of cycles chosen for the fitting. Due to the fact that the Sony cells are brand new compared to the rather elder Panasonic cells which have been stored for over a year before the cycling experiment, the Sony cells are not expected to suffer noticeably from other aging mechanisms for the whole 300 cycles. Therefore, unlike seeking to achieve the best fit for the first 150 cycles, the i_{0s} for the Sony cells are tuned to achieve a good fit for the whole 300 cycles. After tuning, the resulted modeled incremental resistances are plotted together with the measured resistances for all three testing conditions in Fig. 4.18.
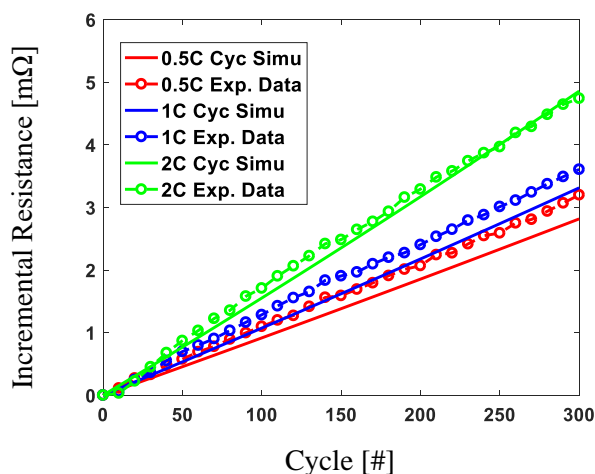
Fig. 4.18: Sony cells' estimated and measured resistances for the tuning step

Since i_{0s} is essentially representing the side-reaction rate constant, it is worthwhile to compare the tuned i_{0s} values for different batteries to have a rough understanding on which batteries tend to age faster. Table 4.6 documents i_{0s} values for both the Panasonic cells and the Sony cells. It shows that i_{0s} of the Panasonic cells is slightly higher than that of the Sony cells, indicating more aging suffered for the Panasonic cells from the SEI layer growth. This is as expected since the Sony cells are newer than the Panasonic cells and cells with NMC cathode materials generally have better battery life.

Table 4.6: Side-reaction exchange current density comparison between tested cells

Panasonic 18650PF (NCA)	Sony VTC6 (NMC)
1.88e-7	1.67e-7

4.3.2   Experimental Evaluation of the ROD Model

With I_0 and i_{0s} are determined, the ROD model can be formulated for the Sony cells. To further validate the ROD model, an aging experiment is conducted cycling the Sony cells with dynamic profiles. Two drive cycle profiles are used, and six Sony cells are separated into two groups with each group cycled with one of the drive cycle profiles. The power profiles for the two drive cycles are shown in Fig. 4.19. The two drive cycles are similar to each other while Drive

cycle #2 contains large discharge power conditions.
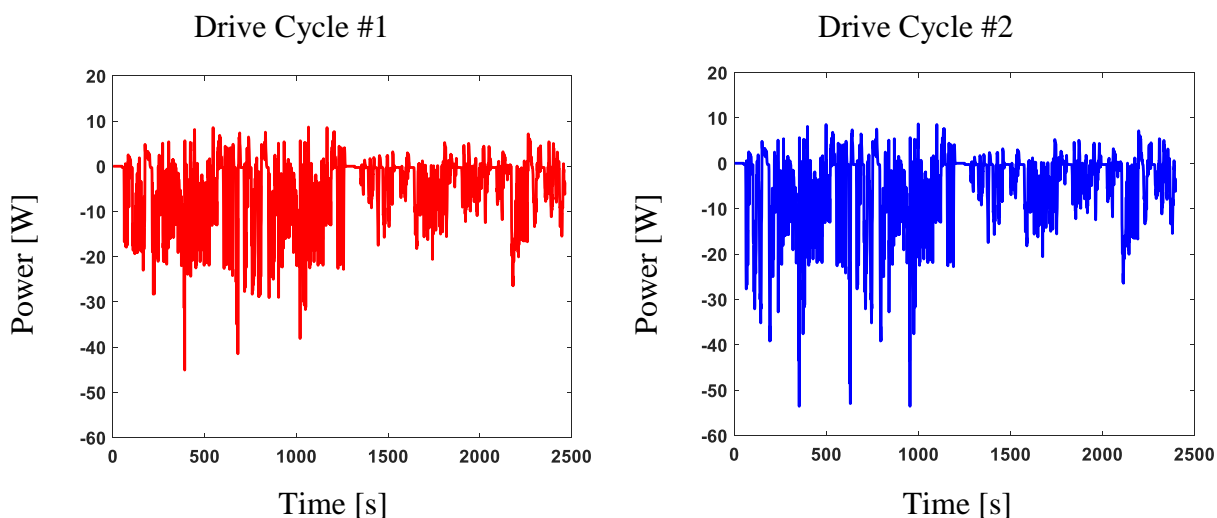
Fig. 4.19: Drive cycle profiles validating the ROD model for Sony cells

The testing conditions are summarized in Table 4.7 and the resistance of each cell is measured every 10 cycles by a 20-sec 2C discharge pulse. The experiment runs a total of 330 cycles.

Table 4.7: 6-cell drive-cycle aging experiments to evaluate ROD model for Sony cells

# of Tested Cell	Op. SOC Range	Drive Cycle #	Op. Temp.	CCCV Charging Rate
3	100% --- 70%	1	25	0.8C, 4.2V, 0.15A cut-off
3	100% --- 70%	2	25	0.3C, 4.2V, 0.15A cut-off

For each group, the measured resistances of the three tested cells are group-averaged. The measured resistance and the estimated resistance are plotted together in Fig. 4.20 and Fig. 4.21, where dotted lines represent the estimated resistances. In addition, the resistance estimation errors are also plotted. The errors are small for both groups, demonstrating the ROD model accuracy.

Drive Cycle #1
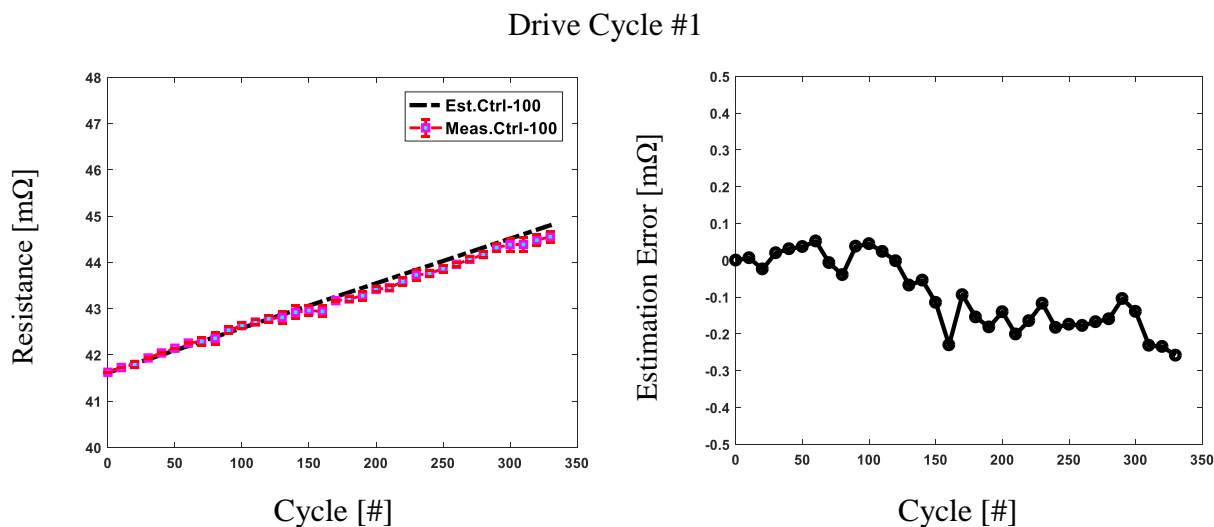
Fig. 4.20: Estimated resistance vs. measured resistance for Sony cells (group 1)

Drive Cycle #2
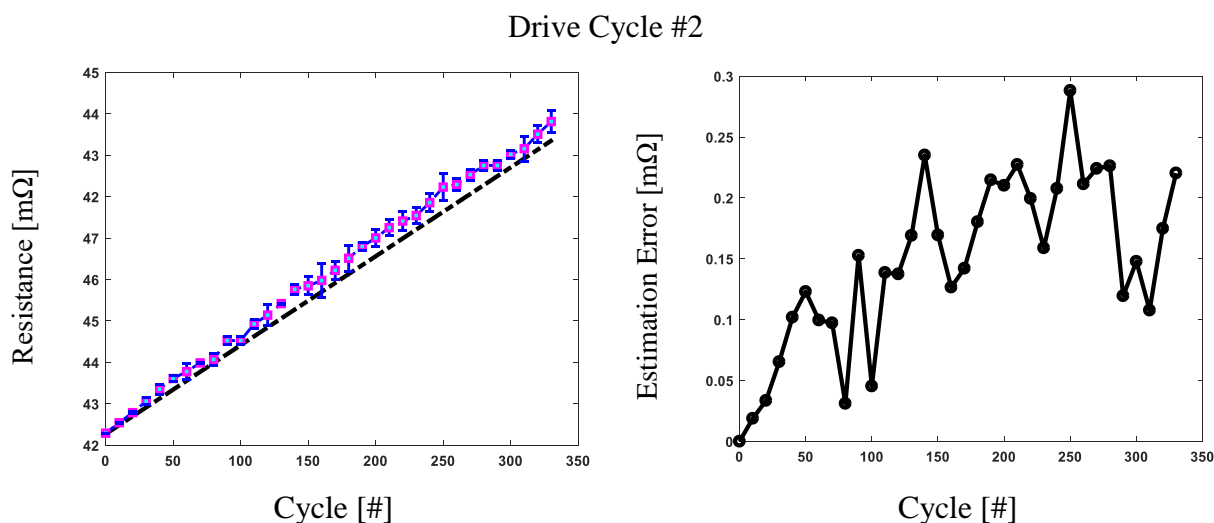
Fig. 4.21: Estimated resistance vs. measured resistance for Sony cells (group 2)

4.4   Chapter Summary

In this chapter, a reduced-order lithium-ion battery rate-of-degradation (ROD) model is developed and experimentally evaluated. The reduced-order ROD model adopts the single-particle model and focuses on modeling the SEI layer growth on the anode. To simplify the conventional electrochemical degradation model, the exchange current I_0 during charge transfer process is estimated by a state estimation technique via the nonlinear regression from various experimental

pulse tests conducted w.r.t the current rate, the battery SOC, and the battery temperature. Adopting a nonlinear battery BV model, I_0 is estimated covering a wide operating range. Also, by fitting the estimated I_0 via a separation of variables, I_0 can be quickly calculated based the current, SOC, temperature values.

Due to cell differences, the side reaction current density i_{0s} used in the literature may not be accurate, a tuning process is conducted via converging the degradation simulation results from the developed reduced-order ROD model to the measured degradation results from one set of constant-rate aging experiments.

The tuned ROD model is further evaluated for two types of cells with different cathode chemistries, and the simulation results of each cell type are compared with the experimental data gathered from another set of aging experiments with dynamic cycling profiles. For both cell types, the simulation results achieve good agreements with the experimental data, validating the proposed reduced-order ROD model.

Meanwhile, one issue that was not discussed in this thesis is the parameter sensitivity of the proposed model. The parameter estimation process introduced in the chapter actually compensates for the potential imperfect parameters as the i_{0s} is the last parameter characterized so that the model output can match with experimental results and therefore compensating for the inaccuracy of other parameters. It is recommended that rigorous chemical experiments can be in the future implemented so that the model parameters can be characterized more accurately.

Chapter 5 Region-based Li-ion Battery ROD Control During Drive Cycles

With a trustworthy rate-of-degradation (ROD) model developed in the previous chapter, the ROD of the battery during the drive cycles can be estimated at any sampling instant, if the current, SOC, and temperature information is available.

In this chapter, the developed reduced-order ROD model is first thoroughly analyzed in terms of its changing trend with respect to different variables. By analyzing the ROD characteristic map over a wide operating range, "comfort zones" in terms of less degradation for the battery to operate at during a drive cycle are identified. Such "comfort zones" identifications would provide insights on how to drive the electrical vehicle efficiently in terms of improving the battery durability. By integrating the reduced-order ROD model with the electro-thermal model developed in a previous chapter, ROD control by monitoring the expected ROD, and manipulating the power and the heat flow for mitigation can be characterized and analyzed. As a result, the drive cycle power profiles can be shaped to extending the battery life on an electric vehicle.

5.1 ROD Equation Analysis

To identify the effects of different battery operating variables on the battery ROD, a holistic sweep of evaluation on the ROD changing trends should be performed. The ROD evaluation equation developed is shown in (4.6). For convenience, the equation is listed below.

$$I_s (I_{app}, SOC, T_c) = -i_{0s}a_nVol_n\exp(\frac{-F(U_n^{ref} - U_s^{ref})}{2R_gT_c}) * \exp(-asinh(\frac{-i_{app} - I_s (I_{app}, SOC, T_c)}{2I_0(I_{app}, SOC, T_c)}))$$

Since a high temperature would potentially change the i_{0s} value, the sweeping temperature window is limited as high as $45^{\circ}C$ to ensure the accuracy of the ROD analysis. Additionally, since

18650 cylindrical cells with graphite anode have similar physical structure, the specific area a_n and the anode volume Vol_n are similar as well. Values from the literature are therefore adopted. For a graphite anode, the OCV vs. SOC relationship has been well documented. One can refer to the appendix for the details.

In the following Table 5.1, the evaluated operating range using (4.6) is summarized, covering the SOC range from 5% to 100%, the current rates from -2C (charge) to 5C (discharge), and battery core temperature from -20°C to 45°C.

Table 5.1: Summary of the ROD evaluation scope	
Current [C-rate]	-2C to 5C (Discharge " - "; Charge " + ";
SOC	100% to 5%
Temperature	-20°C to 45°C

In the next section, the ROD is characterized and calculated within the specified evaluation scope.

5.1.1   Side-reaction Current vs. Temperature * SOC * Current Rate

The ROD metric is the side-reaction current. First, the side-reaction current is calculated over the SOC and current rate windows, while several different temperatures are selected. In this way, the trend of the side-reaction current against temperature can be clearly seen.

It should be noted that in this section, a more positive side-reaction current value means the ROD is more severe. This is just for the convenience of plotting and color-bar adjusting. For the other sections, the sign is inverted, and a more negative side-reaction current value means more severe ROD.

In Fig. 5.1, the side-reaction current becomes larger when the temperature is colder. The characterized temperature range in Fig. 5.1 is from 15°C to 45°C. The trend agrees with the findings from the previous experimental results in Chapter 3, where low-temperature discharge leads to worse battery rate-of-degradation. Moreover, the temperature effect on the side-reaction

current is nonlinear, addressing the importance of the battery pack thermal management system in an electric vehicle.
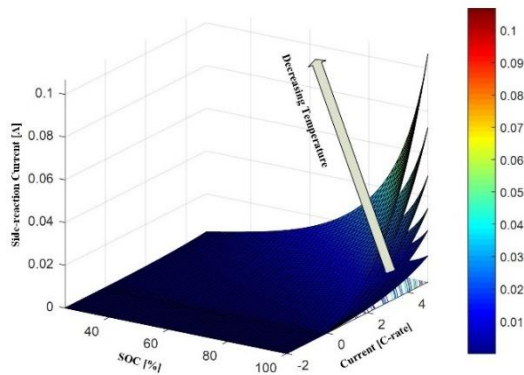
Fig. 5.1: Side-reaction current vs. SOC * I @ different temperatures

In addition, the side-reaction is calculated over the current rate and temperature windows, while several different SOCs are selected. In this way, the trend of the side-reaction current against the SOC can be seen. In Fig. 5.2, the side-reaction current is plotted against the temperature and the current rate. Different side-reaction surfaces are overlaid, representing different SOC cases. It can be seen that the side-reaction current is higher when SOC is high. This agrees with the findings in the literature that the SEI layer grows more when battery SOC is high, generally equivalent to high battery voltage. It can also be seen that typically the almost-full SOC areas cause the most severe ROD, meaning the ROD trend with respect to the SOC is nonlinear. As a result, avoiding operating the battery near full could help improve the battery lifetime.
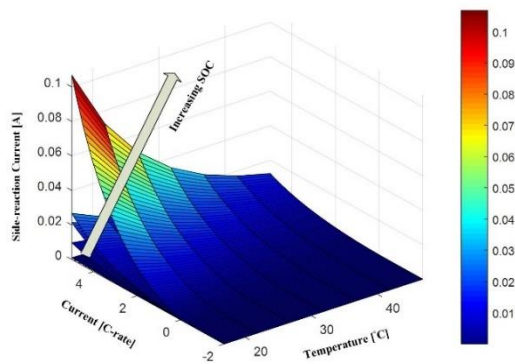
Fig. 5.2: Side-reaction current vs. I*T @ different SOCs

Also, the trend of the side-reaction current with respect to the current rate can be seen from both Fig. 5.1 and Fig. 5.2. A higher discharge current rate results in more severe ROD. This agrees with the full-order electrochemical simulation results and the finding in the literature as well. The relationship between the current rate and the side-reaction current is nonlinear as well, as we can see "exponentially" increasing side-reaction current when the discharge current reaches the area from 3C to 5C. Higher current not only aggravates the battery degradation rate, but also leads to battery internal temperature increase and causes more severe degradation. These coupled effects emphasize the importance of keeping the battery load current benign and the necessity of power control to improve battery lifetime.

As for the charge case, there are other aging mechanisms more dominant than SEI layer growth during charge and can overshadow the estimations from this developed reduced-order ROD model. Therefore, the charge case should be considered separately.

5.1.2   Holistic ROD Characteristic Map Analysis

The side-reaction current changes with respect to the different battery operating variables have been investigated and discussed in the previous section. The central focusing variables are the current rate, the battery SOC, the battery temperature. Based on the trend's analysis, several general suggestions or rules of thumbs are discussed.
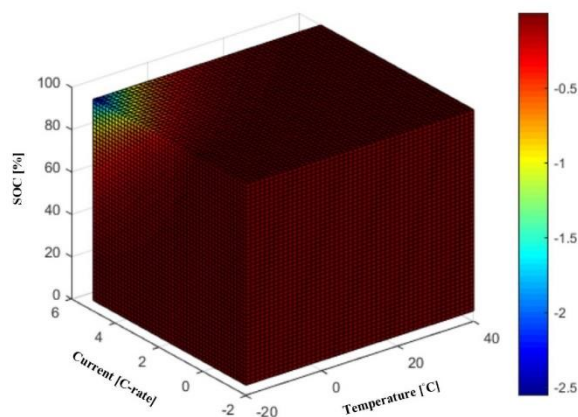
Fig. 5.3: Side-reaction current vs. SOC * I * T (large scope)

However, for quantitative analysis, it is necessary to look at the ROD characteristic map in a more holistic view. In Fig. 5.8, a pseudo-4D plot of the side-reaction current over the 3D operating space (I * SOC * T) is shown, and colder colors represent more severe ROD. However, it is difficult to clearly see the ROD boundaries when almost the whole battery operating range is included.

For EV applications, the battery would be heated up if it is too cold initially. When the vehicle is running, the cooling system usually keeps the battery under $40°C$. Therefore, in Fig. 5.4, the temperature range is limited to $10°C$ to $40°C$. By analyzing different drive cycle experiments, the battery current can be up to about 4.5C. Therefore, the current rate range has been kept from 0 to 4.5C with charging excluded. For an EV, the full SOC range could be used, and therefore the whole SOC range is included still.
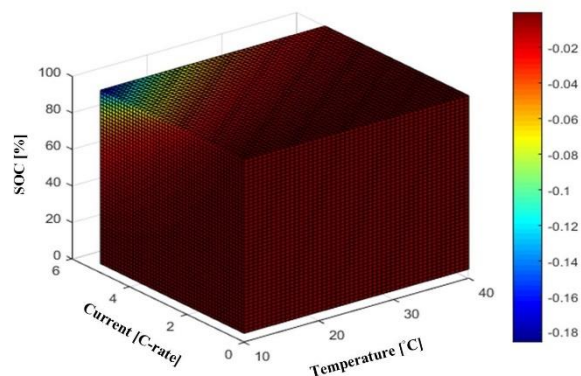
Fig. 5.4: Side-reaction current vs. SOC * I * T (smaller scope)

As shown in Fig. 5.4, there are several boundaries over the operating space. Based on the contour curves, Table 5.2 shows a summary of the various boundaries determined by different levels of the ROD severity.

Table 5.2: Summary of the ROD boundary curves divided by ROD severity

ROD Severity	Current Rate [C]	SOC [%]	Temperature [˚C]
Worst	4.6 – 5	94 – 100	10 - 20
Worse	4 - 4.6	86 – 94	20 – 30
Medium	3 - 4	75 – 86	30 – 33
Benign	1 - 3	35 – 75	33 – 37
More Benign	0 – 1	0 - 35	37 - 40

5.2   Region-based ROD Control Laws Development

Based on the boundary curves identified from the previous sections, several primary ROD control laws are developed in this section.

The control laws can be divided into two categories: 1) hard threshold, and 2) soft (dynamic) threshold. The hard threshold contains the laws that ideally should never be violated when the battery is under operation for EV applications. These laws are mostly based on the battery safety concerns. In Table 5.3, several hard threshold laws are listed in terms of battery's thermal and electrical limitations. As listed, the maximum temperature sensed for the battery surface temperature should be carefully obeyed. A thermal runaway could possibly happen if too much power is continuously drawn from the battery and the driver could be forced to stop the vehicle when the limit is violated. On the other hand, minimum voltage and maximum DOD thresholds are also listed as hard thresholds These two usually are coupled together since the battery voltage would be low when the SOC is low. These thresholds are set to protect the battery from damaging itself operating at low SOC/voltage condition continuously, and another reason is the battery resistance increases at low SOC, and this causes more internal heat generation and may lead to thermal issues. In terms of the battery health, an on-vehicle SOH estimation algorithm should be implemented. Such algorithms could be a look-up table based on the aging data pre-analyzed in the lab for the battery equipped with the vehicle or could be one of the algorithms introduced in

the state-of-the-art review. Usually, 30% of capacity fading would announce the battery no longer suitable for an electric vehicle.

Table 5.3: Hard and soft threshold regarding battery safety and lifetime preservation

Hard Threshold	Soft (dynamic) Threshold
Max. Temperature (Thermal Run-away)	Dynamic Current Threshold
Min. Voltage (Usually 2.5V)	Dynamic SOC Monitoring
Max. Depth-of-discharge (DOD~90%)	Dynamic Core/Surface Temperatures Monitoring
State-of-health Estimator Based on Driving Data	

On the other hand, there could be several soft/dynamic thresholds or ROD control laws. As shown in the previous section, high SOC causes more degradation. It is desirable not to charge the battery to full frequently, and there have been limitations implemented in the charging ports to avoid charging the battery to a nearly full status. However, less available charge in the battery inevitably leads to less mileage from an EV stand of point. Therefore, there is always a trade-off between sacrificing some battery life and wasting some battery energy. Another issue that the developed electro-thermal model could help is to estimate the core temperature of the battery. As mentioned, the surface temperature can be monitored by thermocouples attached. However, in situations like harsh accelerating and hard braking, a significant amount of power is drawn in a brief period of time. While the surface temperature may not quickly respond due to the large battery thermal constant, the core temperature of the battery could increase dramatically in a short time period. This could lead to an unnoticed warning from the thermal management system. With electro-thermal models or other internal temperature estimation methods introduced earlier, this safety concern could be avoided. In addition, the core temperature is usually higher than the surface temperature, and it is the core temperature determining the ROD severity according to (4.6). An electro-thermal model that predicts the core temperature of the battery could help avoid underestimation of the ROD severity.

Moreover, the most direct factor that affects battery ROD is the current since both the SOC

and the temperature are passive factors and are hard to manipulate at will. The current that flows through the battery is an active factor that can be controlled by the current controller in the powertrain system.

A current/power shielding control algorithm is investigated in this thesis. Assuming the battery is undergoing a drive cycle at 25°C, the side-reaction current map at 25°C against different current rates and different SOC stages is shown in Fig. 5.5. As discussed before, the ROD change with respect to current and SOC is not linear. Each of the curves shown in Fig. 5.5 can be separated into two regions, a "fast-grow region" and a "slow-grow region". The "fast-grow region" has a linearly increasing trend, and the "slow-grow region" has a convex down increasing trend. The respective current points associated with each curve that denotes the transition between two regions then form a limiting boundary. For 25°C case, this boundary is then named the "power shielding boundary". The ROD control scheme is then to keep the battery operate on the left side of this power shielding boundary at 25°C to avoid undesirably high ROD. However, this boundary should result in the limiting current at a value that is realistic without compromising the battery performance significantly. A more detailed boundary selection process will be introduced in the next section.

On the other hand, for different temperature cases, this "power shielding boundary" can be different, and the basic idea is searching for this boundary to locate the ROD transition point where the ROD increasing trend changes from convex-down to linear as well as to lead to a reasonable current limit. Overall, whenever the battery at a certain temperature is operating on the left side of the "power shielding boundary" of that temperature, no ROD control will be applied. Whenever there is a command that could push the battery to the right side of the boundary, only the allowable current on the boundary will be available for the battery.
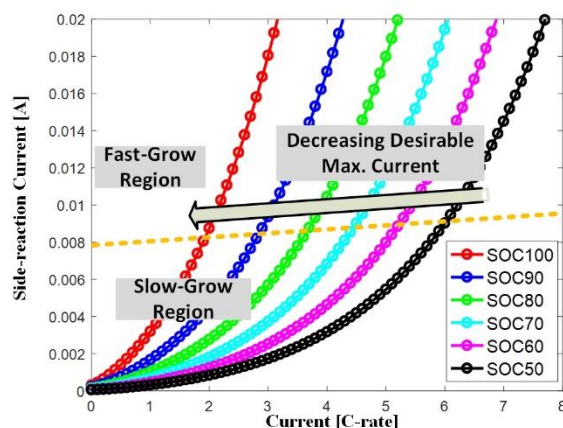
Fig. 5.5: Dynamic current/power shielding boundary curve at 25°C

5.2.1 ROD Boundary Selection Algorithm

The boundary selection can be flexible and needs to be rather realistic, meaning it should not enforce a current limit too small so that the battery performance is dramatically limited. As seen from Fig. 5.5, a side-reaction current ranging from 0.005A to 0.01A can all be treated as the slope-changing region so that an appropriate boundary value should be selected based on the resulting current limit feasibility. As normally seen from EV applications, an average battery load current through a drive cycle would be around 1 to 2C. As shown in a previous section, high SOC can result in worse ROD. Therefore, in this thesis, the minimum discharge current limit for the Panasonic cells is selected at around 1.8C at 25°C, which corresponds to a side-reaction current at 0.0078A.

On the other hand, temperature can dramatically change the ROD curves and since low temperature can result in worse ROD, current limit can be smaller than that at high temperature given the same SOC. However, similar to many other electrochemical parameters that follow the Arrhenius relationship, a 10°C temperature change can lead to half or double of the original parameter. Therefore, keeping the same side-reaction current boundary as of 25°C for the other temperatures may not be appropriate. For temperature conditions higher than 25°C, the side-reaction current limit could be set to a lower value to keep the current limits at different SOCs

close to those at 25°C. Whereas for temperature conditions lower than 25°C, such limits could be set to a higher value so that the corresponding current limits can be mostly feasible. In this thesis, the side-reaction current boundary with respect to the temperature is calculated as in (5.1). This results in the side-reaction current boundary to double the value of 25°C at 10°C.

$$I_{s\_lim}(T) = I_{s\_lim}(25°C) * 1.0473^{(25°C\ -\ T)} \qquad (5.1)$$

Following (5.1), the dynamic battery load current boundary versus temperatures and SOCs is plotted in Fig. 5.6. It can be observed that the discharge current limit is kept larger than 5A so there will not be a significant battery performance compromise. In addition, as expected, lower temperatures and high SOCs enforce more harsh current limits, consistent with the trends found in the previous section.
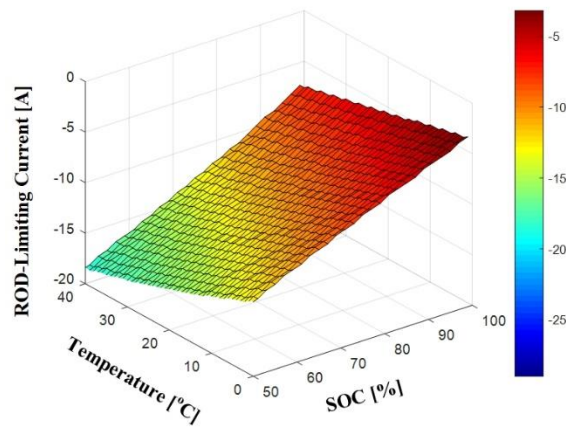
Fig. 5.6: Maximum allowable current vs. SOC and temperature

While the current limits are the value enforced in the proposed ROD control as discussed later in this chapter, it is worthwhile to estimate battery discharge power limits for a more compatible comparison to the commanded drive cycle power. Since the sample frequency is limited to 1Hz for the implementation, the discharge power limit is the 1-sec discharge power and is estimated using (5.2) introduced in [17]. τ here is the estimated charge transfer process time constant and is calculated as in (5.3). The associated parameters in the equation are estimated offline using a Gauss-Newton method based on drive cycle data. Detailed parameter identification

procedure can be found in [17].

$$P_{lim} = I_{lim} * [V_{ocv} (SOC, T) + I_{lim} * A\exp(\frac{E}{T}) + (1 - \exp(-1/\tau))\frac{b_1}{1 + a_1} \operatorname{asinh}(I_{lim}*B*\exp(\frac{G}{T}))] \qquad (5.2)$$

$$\tau = \frac{-1}{\log(-a_1)} \qquad (5.3)$$

In Fig. 5.7 below, the estimated discharge power limit for the Panasonic cells is plotted as it is generally consistent with the trends shown for the current limit. Higher SOC and lower temperature again enforce smaller discharge power limits as expected.
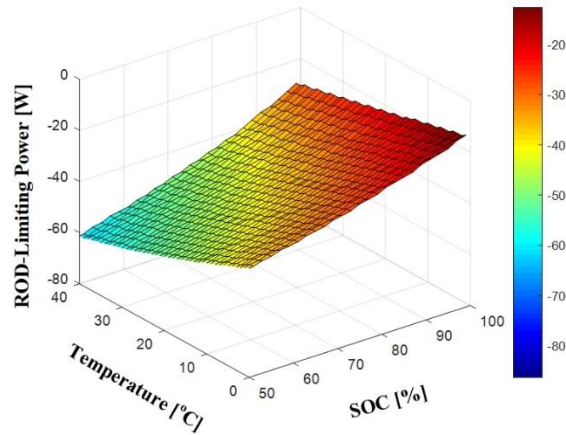
Fig. 5.7: Estimated maximum allowable discharge power vs. SOC and temperature

5.2.2   Integrated Block Diagram for ROD Control Methodology

In Fig. 5.8, a block diagram is shown with the developed integrated system for the battery ROD control. Since the control system is developed for the EV applications, drive cycles are the primary testing profiles. The electro-thermal model developed combining a RNN electrical model with a lumped-parameter thermal model, and the reduced-order ROD model both play crucial roles in the integrated system. Additionally, minor look-up tables such as the OCV-SOC look-up table is also included for necessary SOC estimation via the coulomb counting.
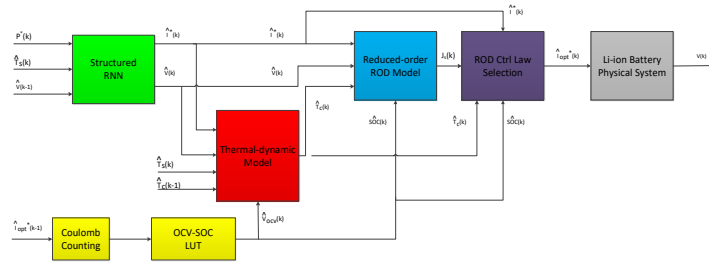
Fig. 5.8: Block diagram of the integrated ROD control schemes

The block diagram represents the whole sequence of the ROD control during a drive cycle simulation environment. With the developed power-commanded electro-thermal model, at any time instant, as soon as the power command is received, the predicted current, the predicted core temperature, and the coulomb-counted SOC value can be fed into the reduced-order ROD model and calculate the predicted side-reaction current. This predicted side-reaction current value will then be fed into the ROD control law and the ROD control law will determine whether the predicted side-reaction current is acceptable. If acceptable, the original power command will be passed to the controller and respective load current will be passed through the battery. If not acceptable, the ROD control law will determine a maximum-allowed power value based on the maximum allowable current limited by the region-based ROD optimization boundary curve. Then, the ROD-optimized maximum allowable power replaces the original power command and gets passed to the controller. This process is called the ROD-optimized Battery Current (Power) Shielding process and will be discussed in the following section.

5.2.3   Dynamic Current (Power) Shielding Algorithm

Assuming at time step k, the power command is P(k). After receiving the power command, the execution sequence of the region-based ROD control algorithm is as follows:

1. The RNN electrical model predicts $\hat{V}(k)$ and $\hat{I}(k)$ based on the input vector [P(k), Wh(k), $\hat{T}_S(k\text{-}1)$, $\hat{V}(k\text{-}1)$]

2. $\hat{I}(k)$ and $\hat{V}(k)$ are fed into the lumped thermal model, $\hat{T}_C(k)$ is predicted

3. $\hat{I}(k)$, $\hat{T}_C(k)$, and SOC(k) are fed into the reduced-order ROD model, and

$I_s(I(k), SOC(k), T_c(k))$ is estimated

4. Compare $\hat{I}(k)$ to $I_{lim}(I(k), SOC(k), T_c(k))$: if $\hat{I}(k) <= I_{lim}(I(k), SOC(k), T_c(k))$, $P(k)$ is acceptable and passed to the controller; if $\hat{I}(k) >= I_{lim}(I(k), SOC(k), T_c(k))$, $P(k)$ is unacceptable and $P_{opt}(k) = I_{lim}(I(k), SOC(k), T_c(k)) * \hat{V}(k)$ replaces $P(k)$ as the command and passed to the controller.

5.3 Experimental Design to Evaluate Proposed ROD Control

Unfortunately, the battery cycler available in the lab is built for testing batteries for standard characterization tests, cycling tests. The way the cycler runs the drive cycle tests requires the user to load the whole sequence of the power profile at once. It is impossible to implement a feedback type of control algorithm in the program that requires sensor feedback signal and manipulate the input at every sample instant. Therefore, the only way to experimentally test the ROD control schemes is first to simulate the whole control system in the Matlab, assuming the actual battery physical system is identical to the battery model developed. Also, the tested batteries are assumed to be identical. By simulating over a drive cycle, the power commands in the drive profile are modified because of the region-based ROD control laws introduced in the previous sections. As a result, with the ROD control algorithm enabled, after simulation a modified drive cycle power profile will be generated.

5.3.1 Combined Testing Drive Cycle

To evaluate the region-based ROD control using the ROD-optimized battery current (Power) shielding algorithm discussed in the previous section, one customized drive cycle power profile is used as the original drive cycle power profile. The original customized drive cycle combines two different drive cycles, US06 and LA92. LA92 drive cycle follows the US06 drive cycle, and each drive cycle lasts for 1200 seconds. In Fig. 5.9 and Fig. 5.10, the speed profiles for the US06 and LA92 drive cycles are shown. Since one US06 drive cycle only lasts for

approximately 600 seconds, two consecutive US06 drive cycles are included to generate 1200 seconds of the drive. On the other hand, one LA92 drive cycle lasts for more than 1200 seconds so that only 1200 seconds of it has been selected.
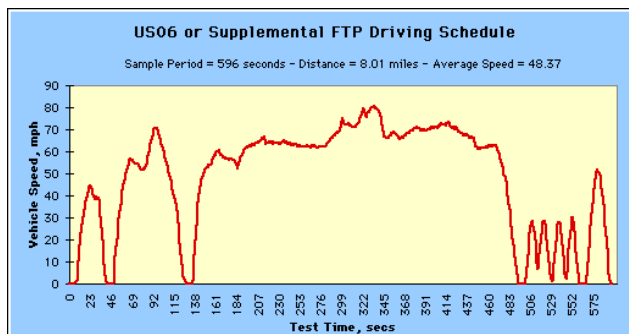
Fig. 5.9: Speed profile for the US06 drive cycle
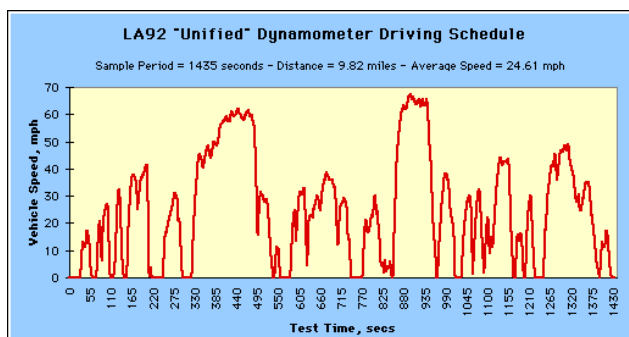
Fig. 5.10: Speed profile for the LA92 drive cycle

The power profiles are scaled for a single cell of a 35kWh electric vehicle battery pack. The drive cycle power profiles are calculated for an electric Ford F150 truck with a 35kWh battery pack [122][123]. The profiles are scaled for a single cell of the 35-kWh battery pack, which is defined to consist of 3680 of the 18650 cells. The transformed power profiles are shown in Fig. 5.11 and Fig. 5.12. The regenerative power is further limited to avoid any overvoltage and fulfill the requirement of discharging 30% of SOC in 2400 seconds.
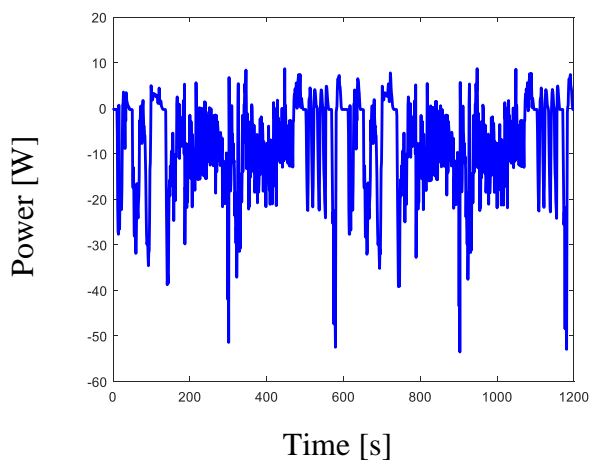
Fig. 5.11: 1200s power profile for the US06 drive cycle

The overall discharge power is higher for the US06 drive cycle since it is a highway drive profile with high speeds and higher accelerations. On the other hand, LA92 is a city drive profile with low speeds and low power. There are more starts and stops for the city drive so that it contains more power transitions. These two 1200s drive cycles are combined to mimic the daily commute scenario, assuming the driver spends about 40 minutes everyday driving to work and the first half of the commute is on the highway and the latter half is in the city. The power profile for the combined drive cycle is shown in Fig. 5.13.
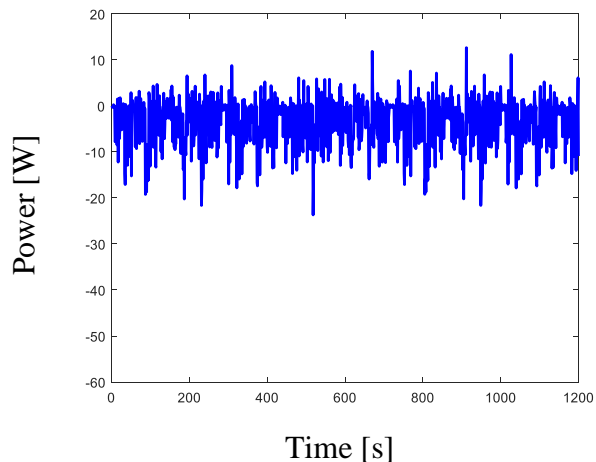
Fig. 5.12: 1200s power profile for the LA92 drive cycle
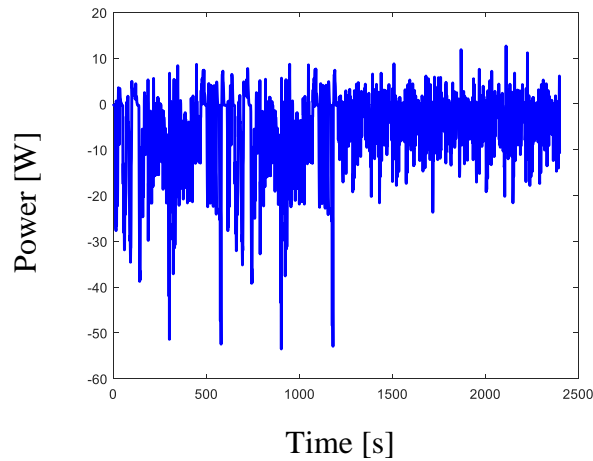
Fig. 5.13: Combined 2400s power profile

5.3.2 Drive Cycle Power Modification by ROD Control

Following the control algorithm sequence introduced in the previous section, the original drive cycle is simulated in the Matlab script with all the components in the block diagram included. Such original drive cycle is simulated for three cases: 1) starting SOC at 100% with the ROD control enabled, 2) starting SOC at 100% without the ROD control, 3) starting SOC at 80% without the ROD control. By comparing 1) and 2), the effect of the developed region-based ROD control algorithm is investigated. By comparing 2) and 3), the SOC effect on ROD for the lithium-ion battery can be investigated. For now, all simulations are carried at 25°C. Based on the region-based ROD control law discussed in the previous sections, the original 2400s power cycle is modified. The modified power profile is shown in Fig. 5.15. The modified power profile shows the power limiting feature mainly for the first half of the drive, where the highway-focus US06 drive cycle is enabled, and the battery is at high SOC.
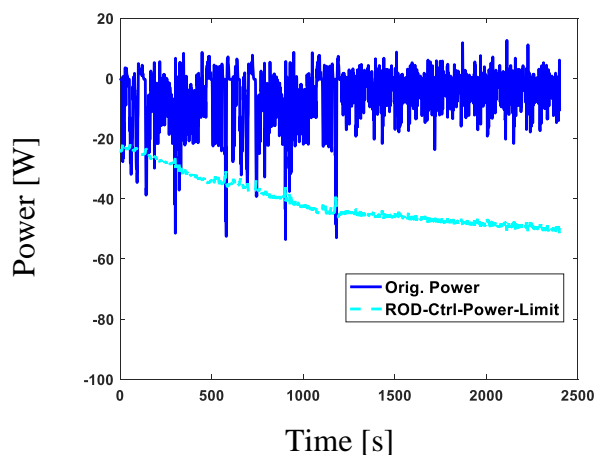
Fig. 5.14: Modified 2400s power profile after applying ROD control
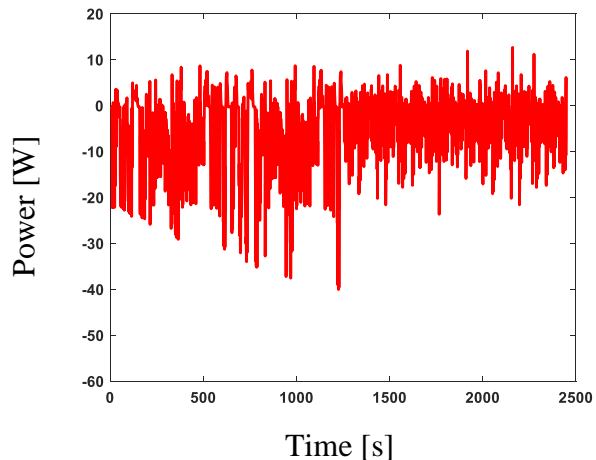
Fig. 5.15: Modified 2400s power profile after applying ROD control

Another difference between the original power profile and the modified power profile is the total time. The modified power profile lasted for 2449 seconds rather than 2400 seconds. Assuming the SOE and SOC are identical, it is important to have the batteries experience the same power load at the same SOC/SOE stage. Otherwise, it is no longer a fair comparison between batteries tested with the original power profile and the modified profile. Therefore, whenever a power-shielding event occurs, the cut power will be supplemented during the next sample time (1s) so that the battery with control will experience the same power load as the battery without control at the same SOE stage, making a fair comparison. In Fig. 5.16, the binary signal denoting the occurrence of activating the ROD-optimized battery current (power) shielding is shown. There

is a total of 98 events recorded.
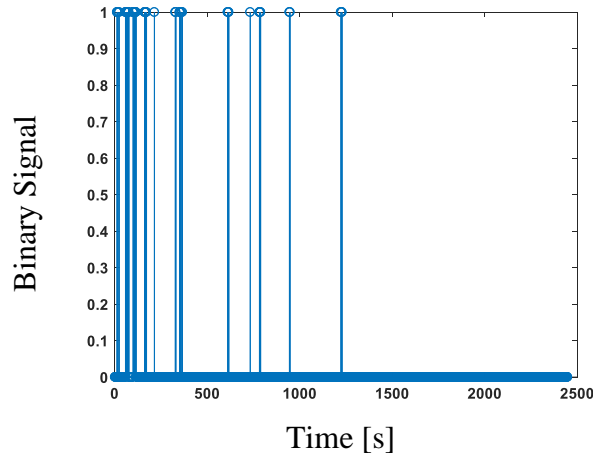
Fig. 5.16: Step-by-step ROD control enabling signal

5.3.3   Comparative Aging Experiment Design

Based on the modified and the original drive cycle power profiles, a set of experiments are designed for 6 cells. For the same three simulation conditions, every 2 cells will be power cycled with either the modified or the original drive cycle power profiles, with the corresponding discharge SOC window in the simulations. Table 5.4 summarizes the aging experiment designs to evaluate the region-based ROD controls. The first and second test sets are designed to evaluate the effectiveness of the developed region-based ROD control, and the second and third test sets are designed to evaluate the SOC effect on ROD.

Table 5.4: 6-cell drive-cycle aging experiments to evaluate region-based ROD controls

# of Tested Cell	Op. SOC Range	With Control?	Op. Temp.
2	100% --- 70%	Yes	25
2	100% --- 70%	No	25
2	80% --- 50%	Yes	25

The total targeted cycle is 450 cycles, and the battery resistance is measured every 10 cycles. Due to the unavailability of the EIS meter, the resistance is measured by applying a 20s pulse of 2C discharge current. The resistance is then calculated by dividing the voltage drop during the 20 seconds with the discharge current, as shown in (5.4).

$$R = \frac{V_{0s} - V_{20s}}{I_{pulse}} \qquad (5.4)$$

Though EIS meter has a better accuracy, the current and voltage sensors of the battery cycler are accurate enough to capture the expected small resistance changes. A sample voltage drop curve during a discharge pulse is shown below in Fig. 5.17. Since the battery resistance changes with respect to SOC and temperature, for this experiment, all the resistance is measured at 80% SOC and 25°C for consistency.

In Fig. 5.18, the 6-cell setup is shown where the cells are placed inside a thermal chamber. During the experiment, the chamber temperature is kept at 25°C. To minimize any thermal unbalance among cells placed at different positions in the thermal chamber, cell 1 and 6 (nearest and farthest) are set to the same group, cell 2 and 5 (2nd nearest and 2nd farthest) are set to the same group, and cell 3 and 4 (3rd nearest and 3rd farthest) are set to the same group.
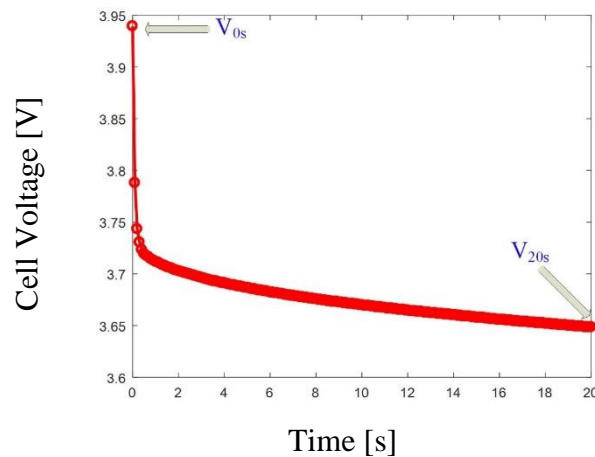
Fig. 5.17: Sample cell voltage curve during a 20s current pulse
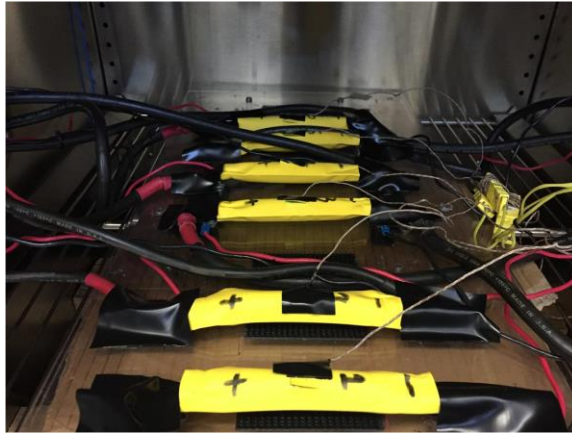
Fig. 5.18: 6-cell experimental setup in a thermal chamber

5.4   ROD Control Evaluation at Room Temperature

The tests listed in Table 5.4 take approximately 2 months to finish. After organizing the test data and calculating the battery resistances, the following evaluation sequence is conducted:

1. Compare the model-estimated battery voltage with the measured voltage data at different cycle numbers.

2. Compare the model-estimated battery current with the measured current data at different cycle numbers.

3. Compare the model-estimated battery surface temperature with the measured surface temperature data at different cycle numbers.

4. Compare the estimated battery resistances with the measured resistances.

5. Compare the increasing rate of the resistances for batteries with different test conditions.

5.4.1.   Electro-thermal Model Evaluation

Since there is no feedback signal available in this experiment, it is important that the electro-thermal model can make accurate estimations of both the cell electrical and thermal responses. In addition, the increasing resistance would have affected the battery electrical

responses as the battery ages, potentially leading to change in the RNN battery electrical model parameters. However, the resistance of the battery is expected to increase about 5mΩ over 450 cycles, leading to less than 0.1V difference with an expected maximum current of less than 15A. This small voltage difference due to resistance change would have been buried in the initial uncertainty from the electrical model. Therefore, the electro-thermal model parameters are kept the same over the 450 cycles, though this inevitably introduces errors.

In Fig. 5.19, Fig. 5.20, and Fig. 5.21, the electro-thermal model is evaluated for cell 1 during cycle #1. Both the voltage and current errors are under 10%, and the temperature error is within 1°C.
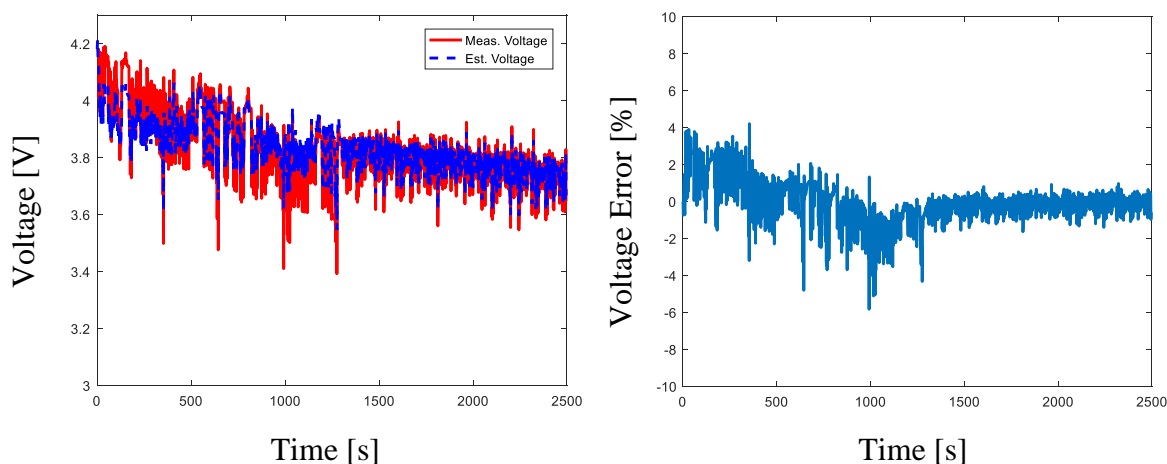
Fig. 5.19: Cell 1 estimated voltage vs. measured voltage at cycle #1
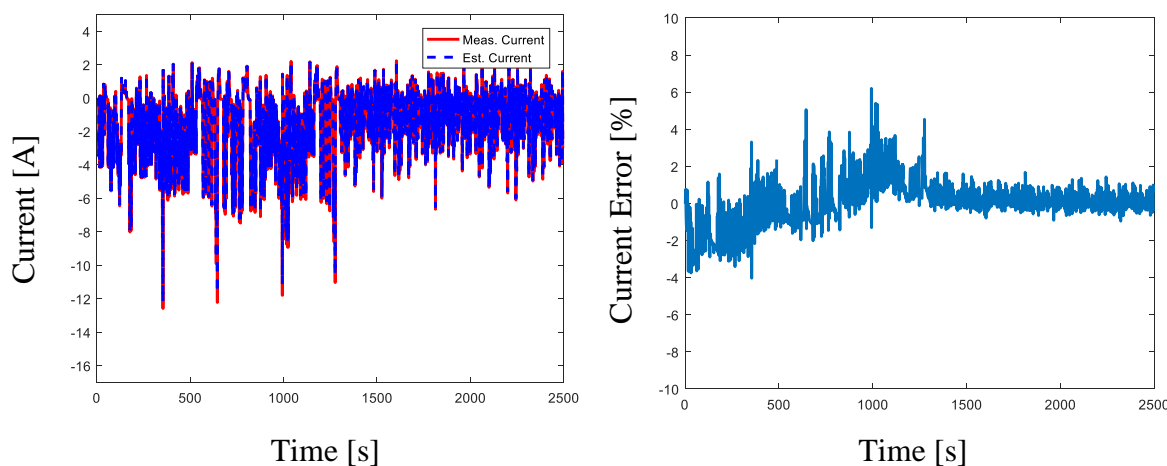
Fig. 5.20: Cell 1 estimated current vs. measured current at cycle #1
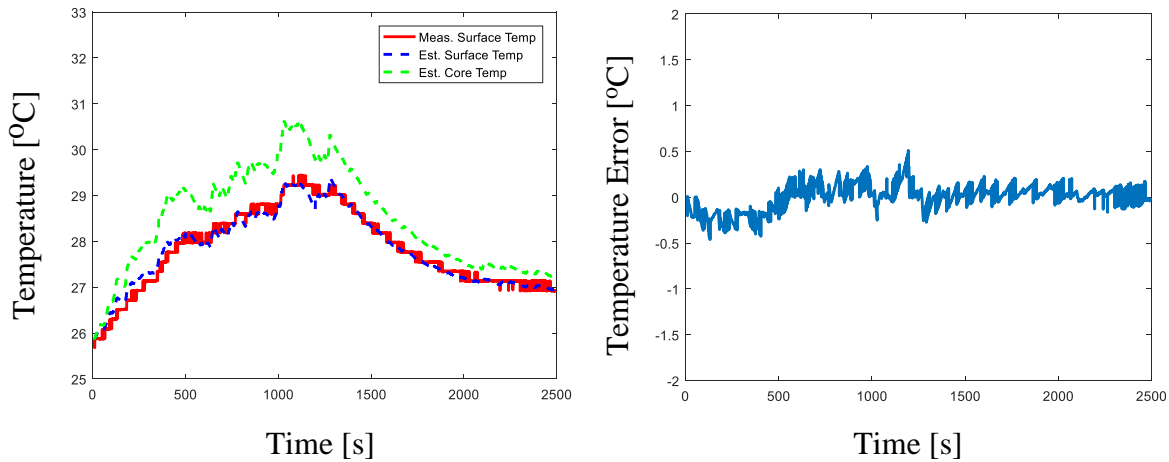
Fig. 5.21: Cell 1 estimated temperature vs. measured temperature at cycle #1
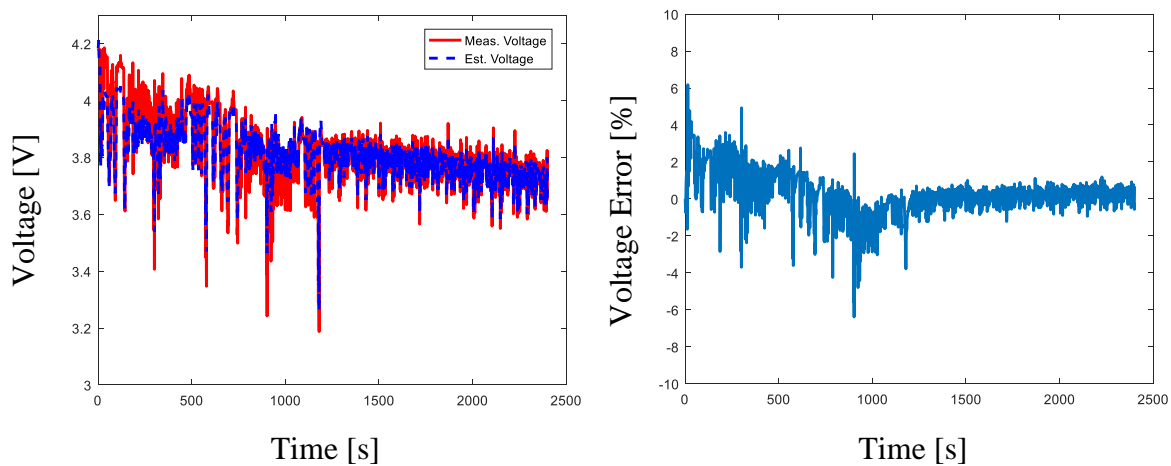
Fig. 5.22: Cell 2 estimated voltage vs. measured voltage at cycle #1
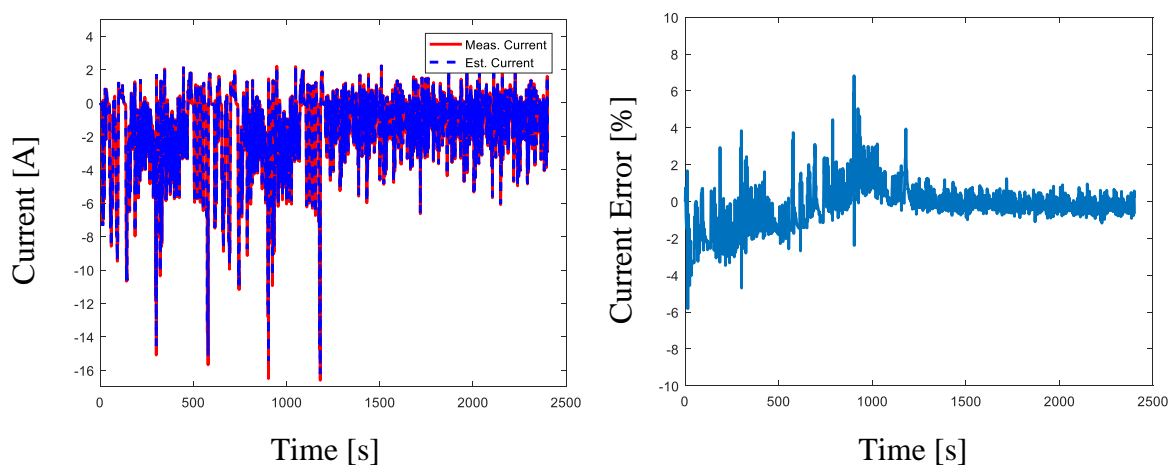
Fig. 5.23: Cell 2 estimated current vs. measured current at cycle #1
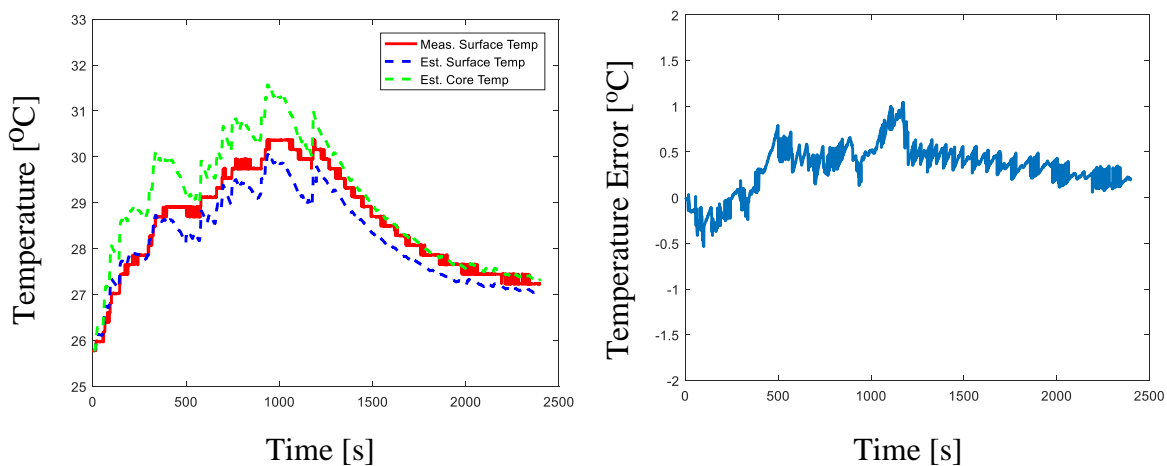
Fig. 5.24: Cell 2 estimated temperature vs. measured temperature at cycle #1

For cell 2 at cycle # 1, the electro-thermal model evaluation results are plotted in Fig. 5.22, Fig. 5.23, and Fig. 5.24. The estimation errors are similar to the errors for cell 1.

For cell 3 at cycle # 1, the electro-thermal model evaluation results are plotted in Fig. 5.25, Fig. 5.26, and Fig. 5.27. The estimation errors are similar to the errors for cell 1 and cell 2.
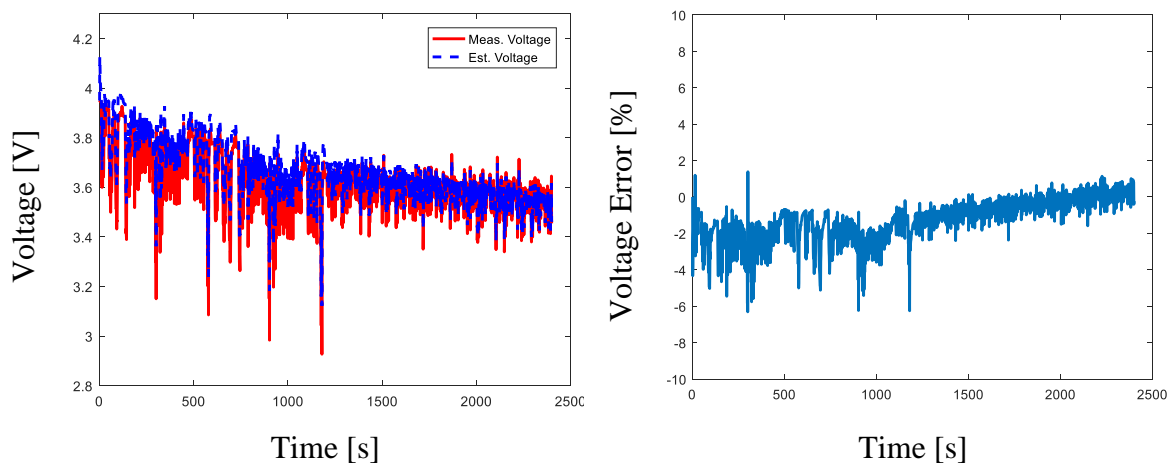
Fig. 5.25: Cell 3 estimated voltage vs. measured voltage at cycle #1
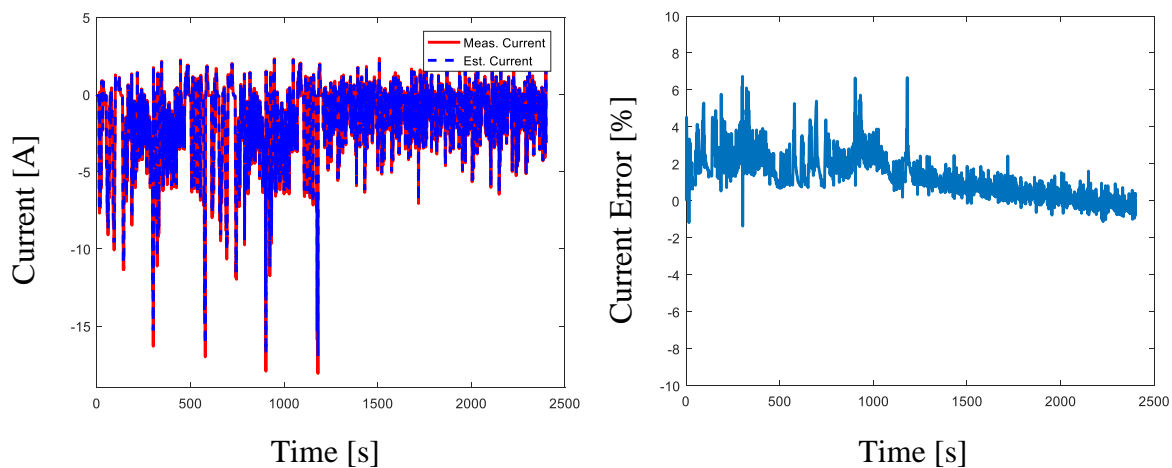
Fig. 5.26: Cell 3 estimated current vs. measured current at cycle #1
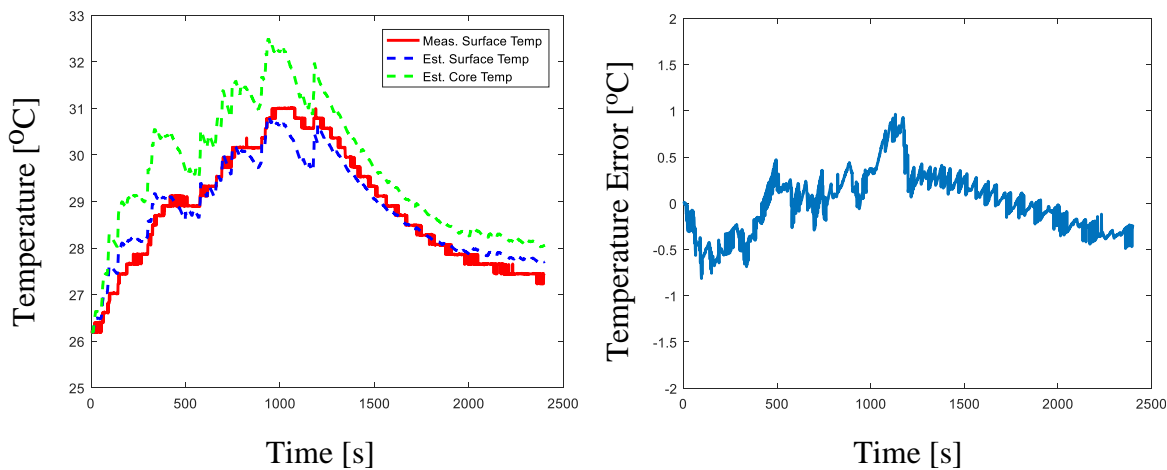
Fig. 5.27: Cell 3 estimated temperature vs. measured temperature at cycle #1

In addition, the electro-thermal model accuracy between cells is evaluated as well. In the following Fig. 5.28, Fig. 5.29, and Fig. 5.30, similar errors result for cell 6 at cycle #1. This result validates the assumption of identical cells.
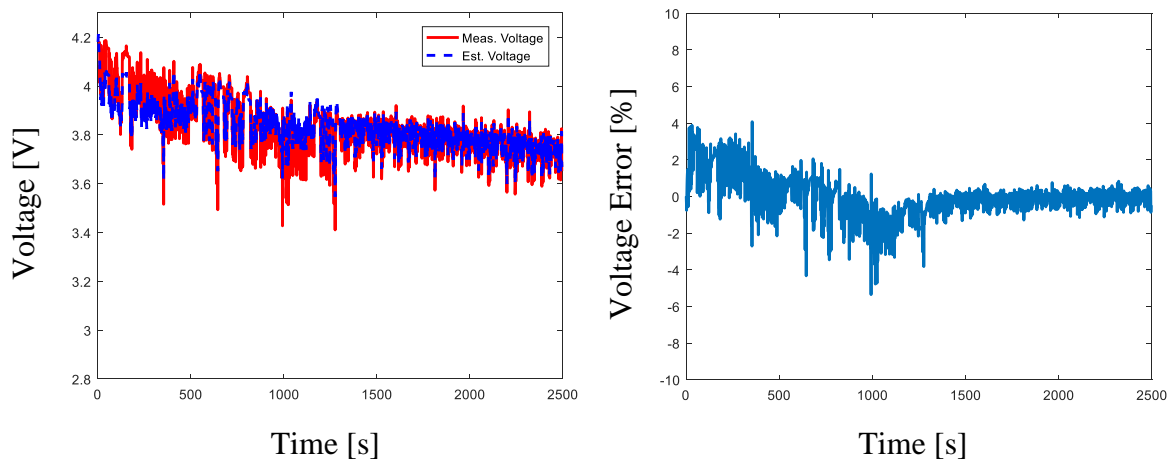
Fig. 5.28: Cell 6 estimated voltage vs. measured voltage at cycle #1
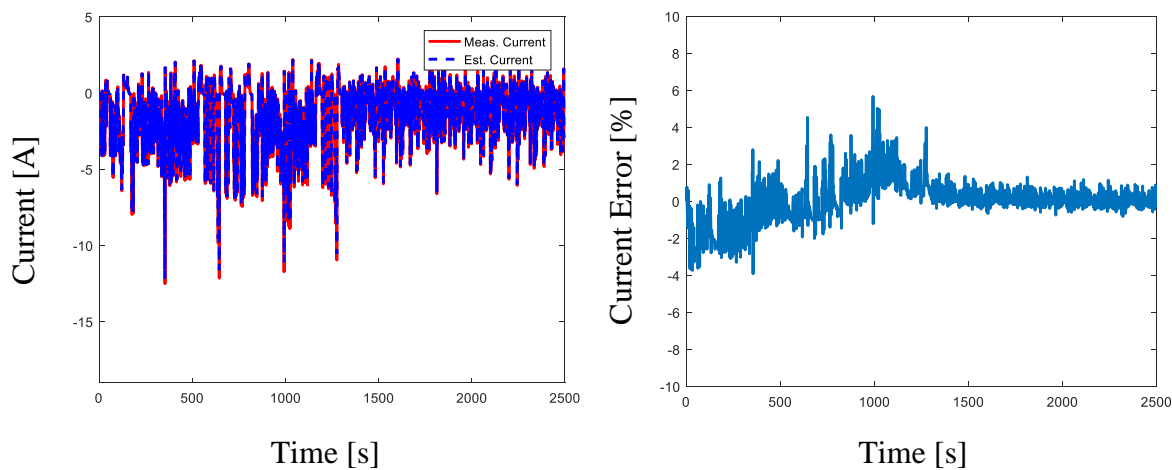
Fig. 5.29: Cell 6 estimated current vs. measured current at cycle #1
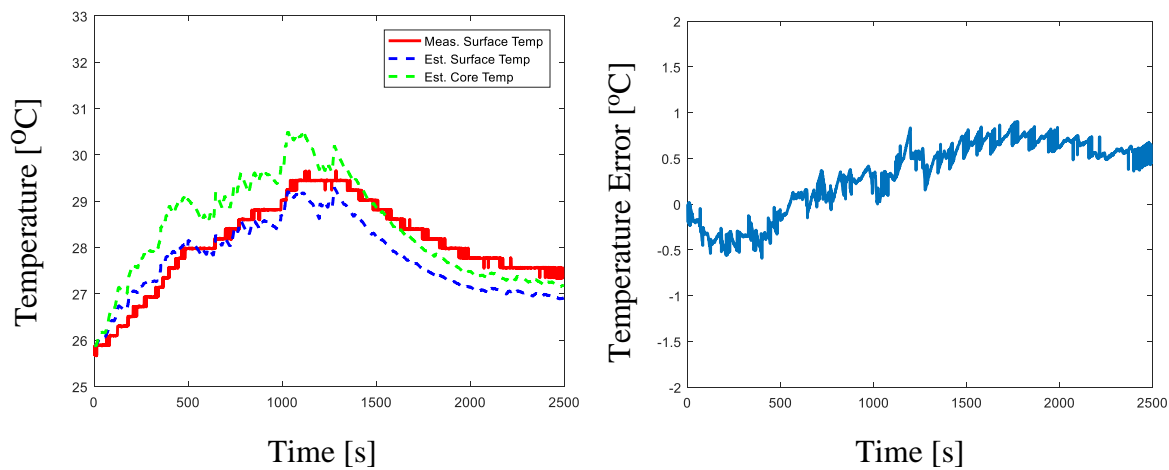
Fig. 5.30: Cell 6 estimated temperature vs. measured temperature at cycle #1

Moreover, as discussed in the previous section, the resistance increase due to aging is expected to introduce unseen change on the cell voltage response that would have been buried from the error initially induced by the electro-thermal model. By comparing the model performances for a cell at different aging stages, this assumption can be further examined.
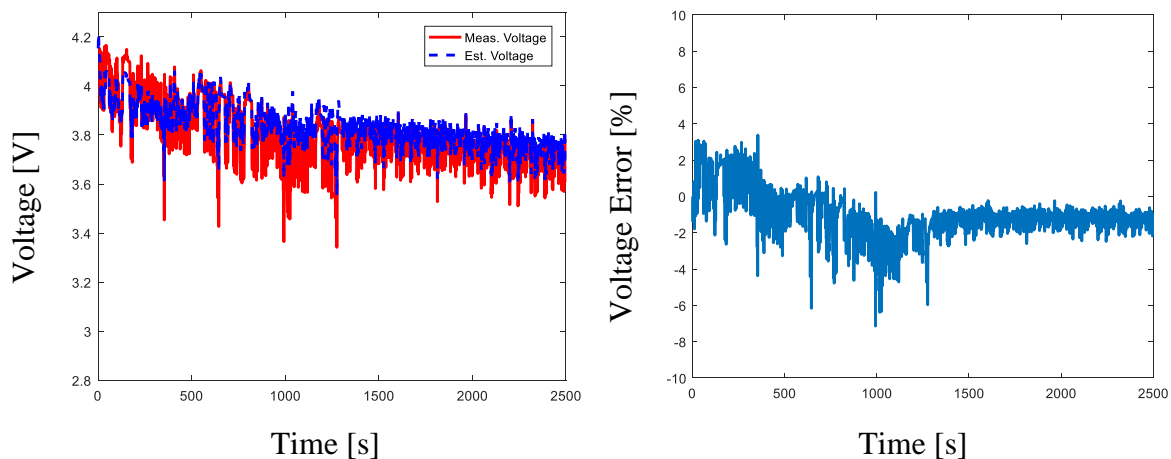
Fig. 5.31: Cell 1 estimated voltage vs. measured voltage at cycle #450
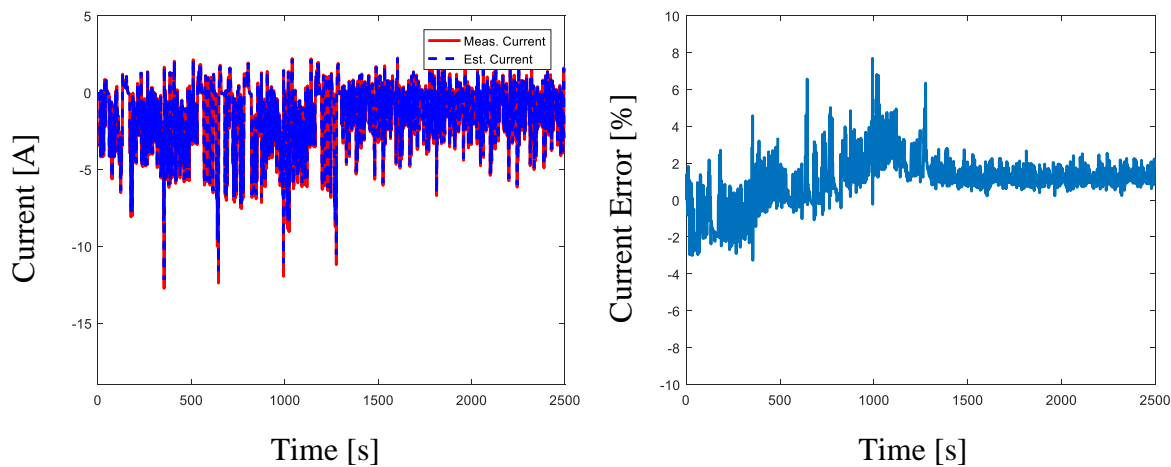
Fig. 5.32: Cell 1 estimated current vs. measured current at cycle #450
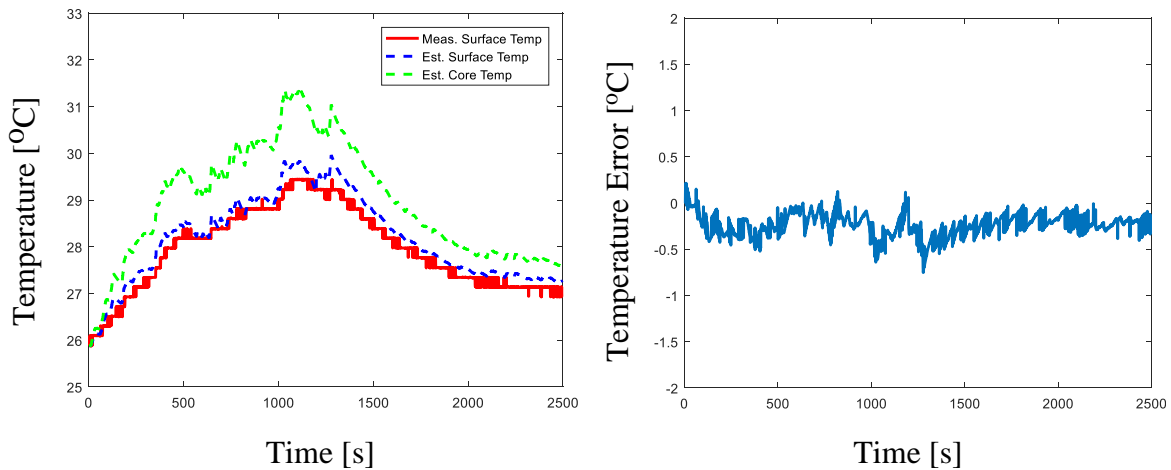
Fig. 5.33: Cell 1 estimated temperature vs. measured temperature at cycle #450

In Fig. 5.31, Fig. 5.32, and Fig. 5.33the electro-thermal model performance at cycle #450 is similar to that at cycle #1. This result shows that the electro-thermal developed does not need significant parameter tuning to account for battery aging.

Overall, the open-loop estimation performance of the electro-thermal model is acceptable, resulting in estimation error less than 10% in terms of battery voltage and current for all cells at different cycles. As the current is the most important variable for applying the region-based ROD control, the current estimation results in less than 0.3C of error, giving confidence for the expected effectiveness of the ROD control. In addition, with the accurate thermal response estimation, any further error induced by the temperature will be minimal.

5.4.2.   Reduced-order ROD Model Evaluation

Since the experiments use two sets of power profiles that have been pre-determined, the original power profile and the modified power profile, the reduced-order ROD model developed in the previous chapter can be used to simulate the battery aging progression. As mentioned before, there has not been any techniques developed to measure the ROD of the battery dynamically. Therefore the resistance growth, instead of the resistance growth rate, is the only measurable variable for model evaluation.

In Fig. 5.34, Fig. 5.35, and Fig. 5.36, the measured resistance and the model predicted

resistance, as well as the error, are plotted for all three battery groups tested. Since there are two cells for each cycling condition, the initial resistance difference between the two cells has been compensated so that the resistance values of the two cells are normalized to start from the same initial value. This normalization reduces the initial cell variance and helps calculate the resistance variance within one group more precisely. In addition, for simulations, the initial resistance for each simulation case is set to be the same as the initially measured resistance of the respective experiment group. For the three test groups, "Ctrl-100" refers to the test condition that the battery cycles from 100% SOC with the modified power profile (ROD control applied), "noCtrl-100" refers to the test condition that the battery cycles from 100% SOC with the original power profile (ROD control NOT applied), and "noCtrl-80" refers to the test condition that the battery cycles from 80% SOC with the original power profile (ROD control NOT applied).
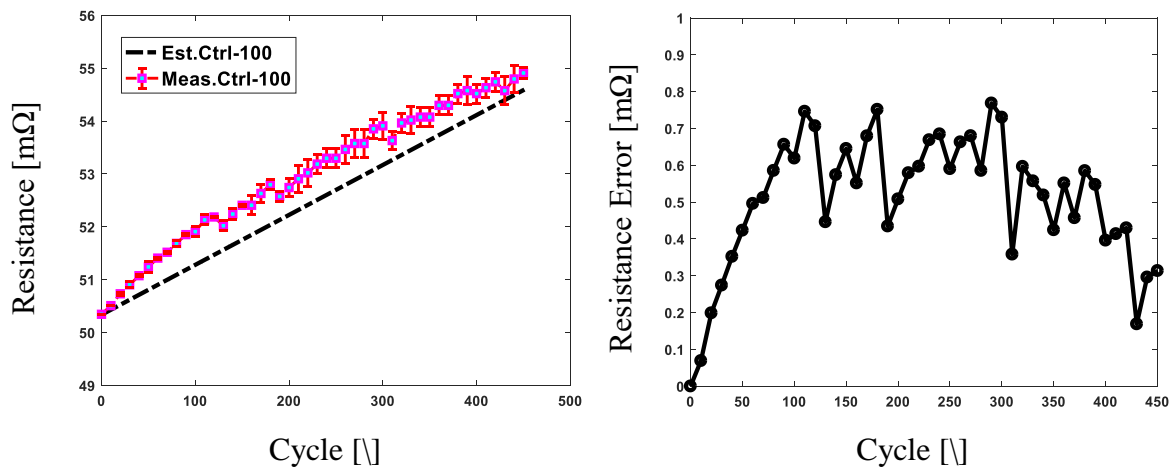
Fig. 5.34: Estimated resistance vs. measured resistance for the "Ctrl-100" group

As seen from Fig. 5.34, for the "Ctrl-100" test case, the estimated resistance generally agrees with the measured resistance. The reduced-order ROD model tends to underestimate the resistance similarly to previous results. The underestimation is due to the other excluded aging mechanisms, as well as unmodeled aging during charge. The resistance estimation error is also plotted, showing errors less than 1mΩ.
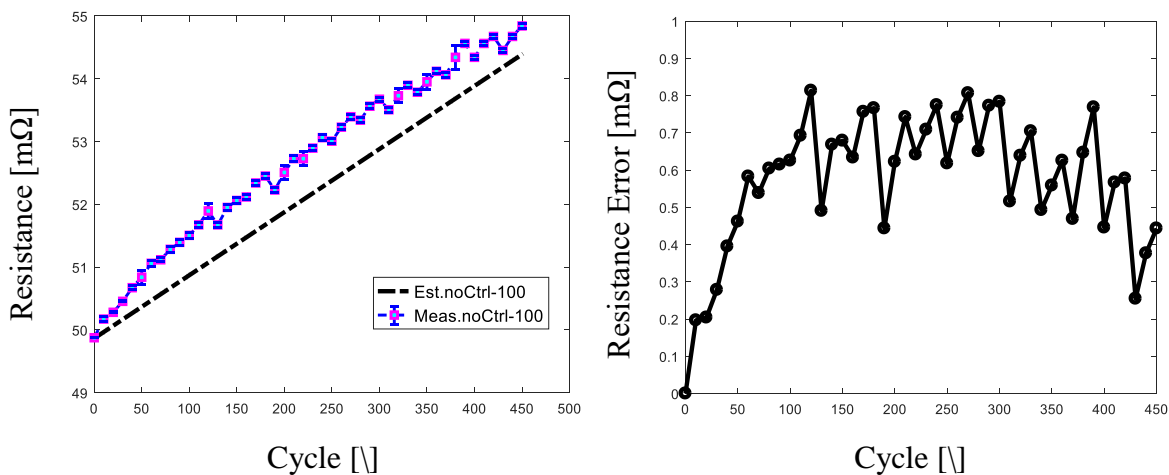
Fig. 5.35: Estimated resistance vs. measured resistance for the "noCtrl-100" group
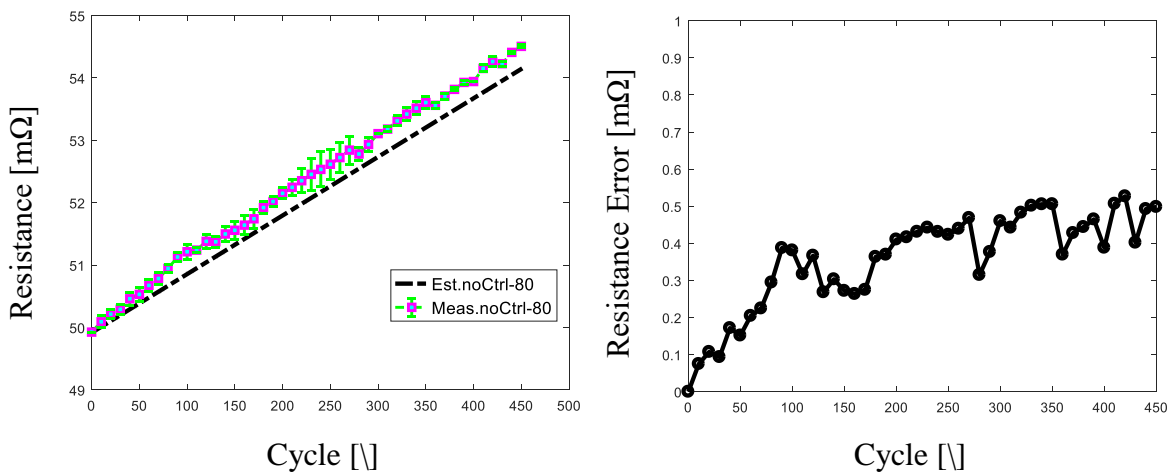
Fig. 5.36: Estimated resistance vs. measured resistance for the "noCtrl-80" group

For the "noCtrl-100" test case, Fig. 5.35 shows similar model performance, and the resistance estimation error is less than 1mΩ as well. For the "noCtrl-80" test case, Fig. 5.36 again shows similar model performance, and the estimation error is less than 0.6mΩ. Comparing the resistance estimation error, "Ctrl-100" group shows the largest error and "noCtrl-80" group shows the smallest error. This result could be due to the following potential reasons:

1. "Ctrl-100" and "noCtrl-100" groups require CC-CV charge during each cycle, and this high-voltage high-SOC charge process may cause more degradation, whereas the "noCtrl-80" group only requires mild charge process at a lower voltage, inducing less

stress.

2. Cells for the "Ctrl-100" group are placed farthest from each other inside the thermal chamber so that they have experienced the most severe thermal unbalance during the experiment, which may lead to higher resistance measurement variance.

5.4.3.   Region-based ROD Control Evaluation

Since the resistance growth rate cannot be measured directly, the proposed region-based ROD control scheme is evaluated by comparing the slopes of the fitted line of the measured resistance data.

In Fig. 5.37, the estimated resistance and measured resistance for all three groups are plotted. The incremental resistances are plotted in Fig. 5.38. The estimated resistance curves are easier to distinguish from each other in terms of their respective slopes.

By linear fitting the estimated resistance curves, Table 5.5 summarizes the respective slopes for the three simulation conditions. It shows that the slope of the "Ctrl-100" group is smaller than the "noCtrl-100" group as expected. On the other hand, the "noCtrl-80" group has a smaller slope than that of the "noCtrl-100" group, showing the SOC effect on ROD characteristics.
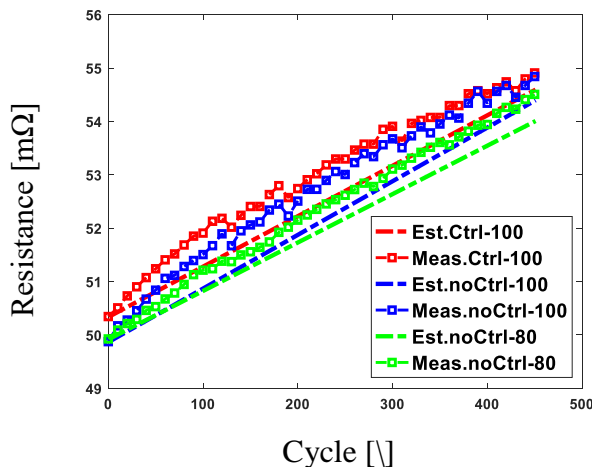
Fig. 5.37: Estimated resistance vs. measured resistance for all groups
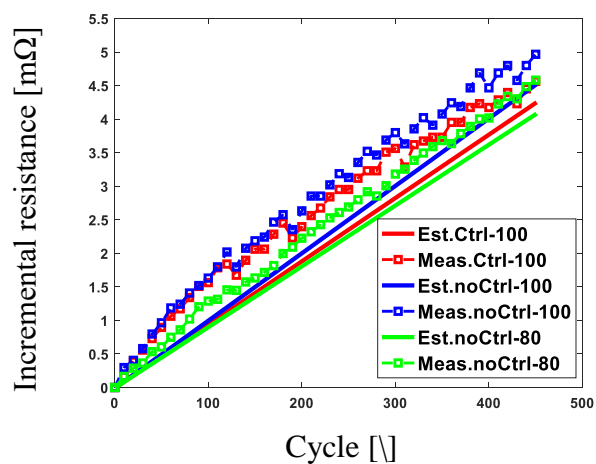
Fig. 5.38: Est. incremental resistance vs. meas. resistance for all groups

Table 5.5: Summary of the linear-fitted slopes of estimated resistance curves

Simulation Case	Ctrl-100	noCtrl-100	noCtrl-80
Slope [$\frac{m\Omega}{Cyc}$]	0.0094	0.0101	0.0091

In addition, linear fitting is also applied to the measured resistance curves. In Fig. 5.39, Fig. 5.40, and Fig. 5.41 respectively, the measured resistance curves and the fitted resistance lines are plotted. The fitted lines are lying through the measured resistance data points.
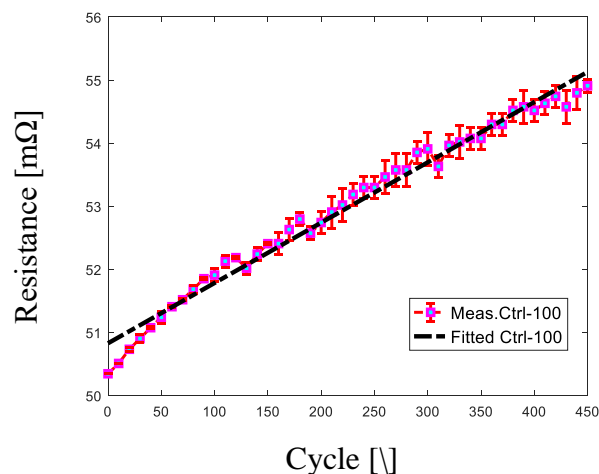
Fig. 5.39: Fitted resistance vs. measured resistance for the "Ctrl-100" group
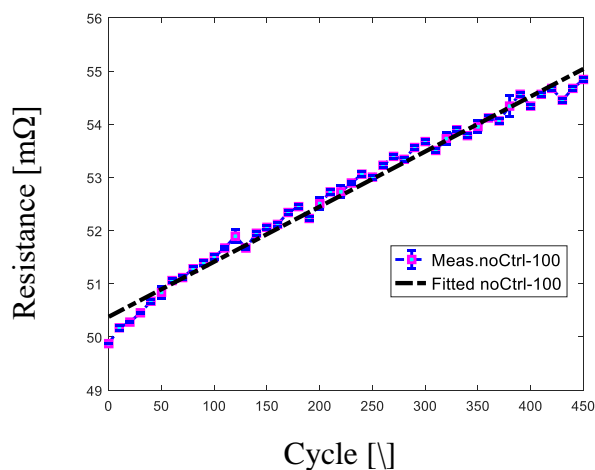
Fig. 5.40: Fitted resistance vs. measured resistance for the "noCtrl-100" group
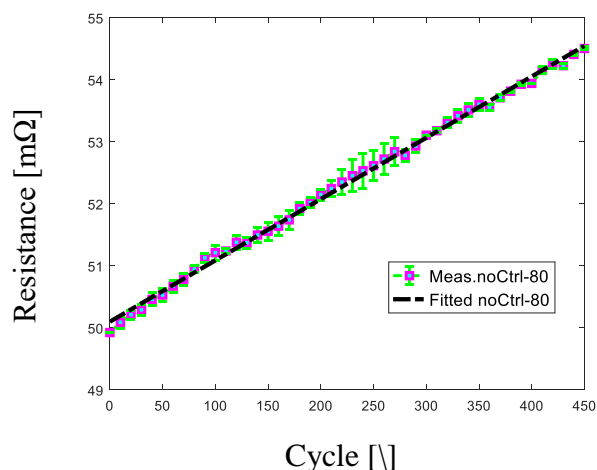
Fig. 5.41: Fitted resistance vs. measured resistance for the "noCtrl-80" group

The slopes of the fitted lines are summarized in the following Table 5.6. It shows that the slope of the "Ctrl-100" group is smaller than the "noCtrl-100" group. This validates the effectiveness of the developed ROD control law, a.k.a ROD-optimized battery current (power) shielding. Based on the slope values, with the ROD control, the battery ages about 8% more slowly. On the other hand, the "noCtrl-80" group has a smaller slope than that of the "noCtrl-100" group, showing that operating the battery at high SOC regularly would lead to more severe degradation. This result agrees with the findings from the ROD characteristics analyzed in the previous section.

Table 5.6: Summary of the linear-fitted slopes of measured resistance data

Test Case	Ctrl-100	noCtrl-100	noCtrl-80
Slope [$\frac{m\Omega}{Cyc}$]	0.0096	0.0104	0.0099

5.5   ROD Control Evaluation for Different Batteries

As discussed previously, both the power-commanded electro-thermal model and the ROD model can be applied to different batteries. Since the ROD control schemes proposed earlier in this chapter are built based on both models, the ROD control schemes are also evaluated for the Sony cells and the results are compared with the Panasonic cell results.

5.5.1.   Power Modification Under ROD Control for Sony Cells

Since Sony cells have similar ratings as the Panasonic cells, the evaluation drive cycle is not changed. The 2400s drive cycle combined with 1200s US06 and 1200s LA92 is used. As mentioned in the previous chapter, Sony cells, since they are newer and have potentially better cathode materials, appear to have better life with relatively lower I_s. In Fig. 5.42, based on the ROD model formulated for the Sony cells, the side-reaction current I_s vs. different load current for different SOCs at 25°C is plotted. Since Sony cells are relatively newer than the Panasonic cells and the side-reaction exchange current density is smaller, the chosen boundaries are more generous for the Sony cells so that the allowable current/power for Sony cells can be similar to that of the Panasonic cells.

Fig. 5.43 shows the maximum allowable current at different SOCs and temperatures for the Sony cells. The determination of such dynamic boundaries follows the algorithm introduced earlier for the Panasonic cells. The estimated maximum allowable discharge power at different SOCs and temperatures is plotted in Fig. 5.44.
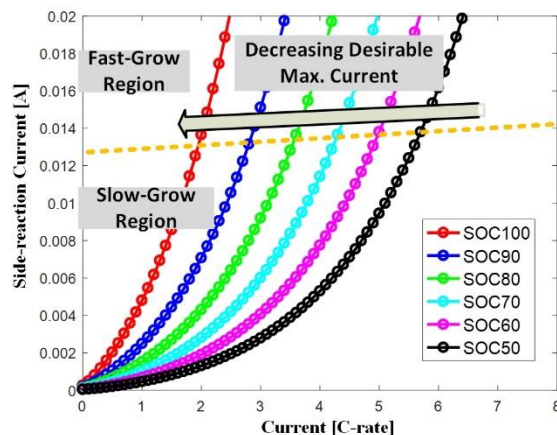
Fig. 5.42: Dynamic current/power shielding boundary curve at 25°C for Sony cells
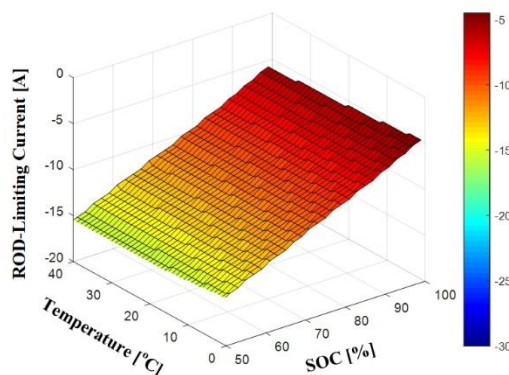
Fig. 5.43: Maximum allowable current vs. SOC and temperature for Sony cells

Compared to Fig. 5.6, it can be observed that generally the maximum allowable current for the Sony cells is similar to that of the Panasonic cells.

Following the simulation of the proposed integrated ROD control system in Fig. 5.8 for the Sony cells at 25°C, the original 2400s drive cycle can be modified as well. In Fig. 5.45, the original drive cycle power profile is superimposed with the power limits imposed by the ROD control. It can be seen that most of the interventions happen during the first half of the drive cycle where SOC is relatively high and the load power is more aggressive. The power profile modified after the ROD control is plotted in Fig. 5.46. The discharge power is overall contained under 40W, whereas the original power profile shows up to 60W of the discharge power.
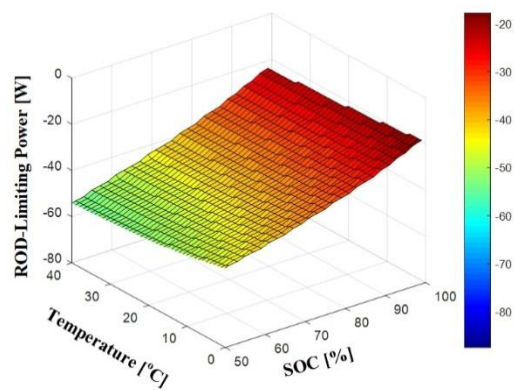
Fig. 5.44: Estimated maximum allowable power vs. SOC and temperature for Sony cells
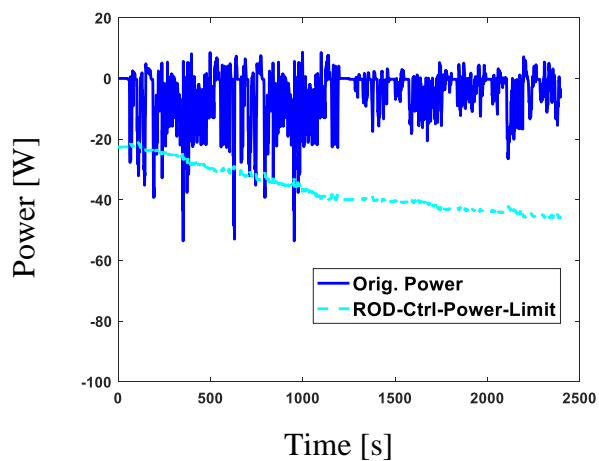
Fig. 5.45: Original 2400s power profile with ROD control power limits
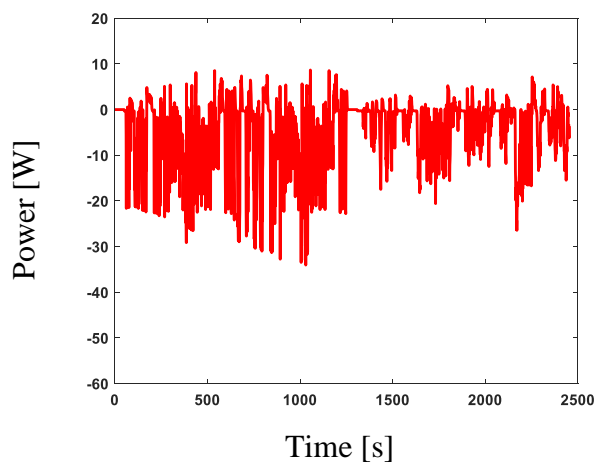
Fig. 5.46: Modified 2400s power profile after applying ROD control

In Fig. 5.47, the binary control signal is plotted through the whole 2400s drive cycle. A

total of 116 ROD control events occurs while for the Panasonic cells there had been a total of 98 events.
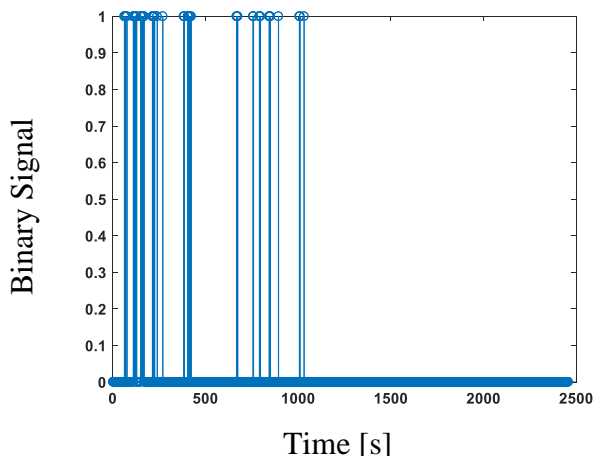
Fig. 5.47: ROD control enabling signal for Sony cells

5.5.2. Aging Experimental Setup for Sony Cells

A comparative aging experiment is then designed for the Sony cells to evaluate the effectiveness of the proposed ROD control schemes. Unlike the three-way comparable aging experiment designed for the Panasonic cells, the experiment for the Sony cells aims to solely evaluate the ROD control performance, excluding the investigation of cycling SOC range's effect on battery aging. A total of 6 Sony cells is used in the experiment and is grouped into two. The operating SOC range is kept from 100% to 70% per 2400s drive cycle and the ambient temperature is set to $25°$C. One group of cells is cycled with the 2400s original drive cycle, while the other group is cycled with the modified power profile. Table 5.7 summarizes the testing conditions for the two groups of Sony cells in this experiment.

Table 5.7: 6-cell aging experiments to evaluate region-based ROD controls for Sony cells

# of Tested Cell	Op. SOC Range	With Control?	Op. Temp.	Group Name
3	100% --- 70%	Yes	25	Ctrl-100
3	100% --- 70%	No	25	noCtrl-100

To characterize the aging status, 2C 20-sec pulse test is used and the resistances are measured every 10 cycles. The resistance is measured when the cells are at 80% SOC with $25°$C

ambient temperature. The measured resistances of the cells in each group are normalized and group averaged for analysis.

5.5.3. ROD Control Experimental Evaluation for Sony Cells

The aging experiment runs for a total of 330 cycles for all the 6 cells. Resistances estimated by the ROD model were all initialized with the first measured resistances averaged for each group. The estimated resistances are plotted together with the measured resistances for both groups in Fig. 5.48 and Fig. 5.49. For both cases, the estimated resistances agree well with the measured resistances. The estimation error for the "Ctrl-100" group is well under 0.3mΩ through the 330 cycles, while the estimation error for the "noCtrl-100" group is similar.
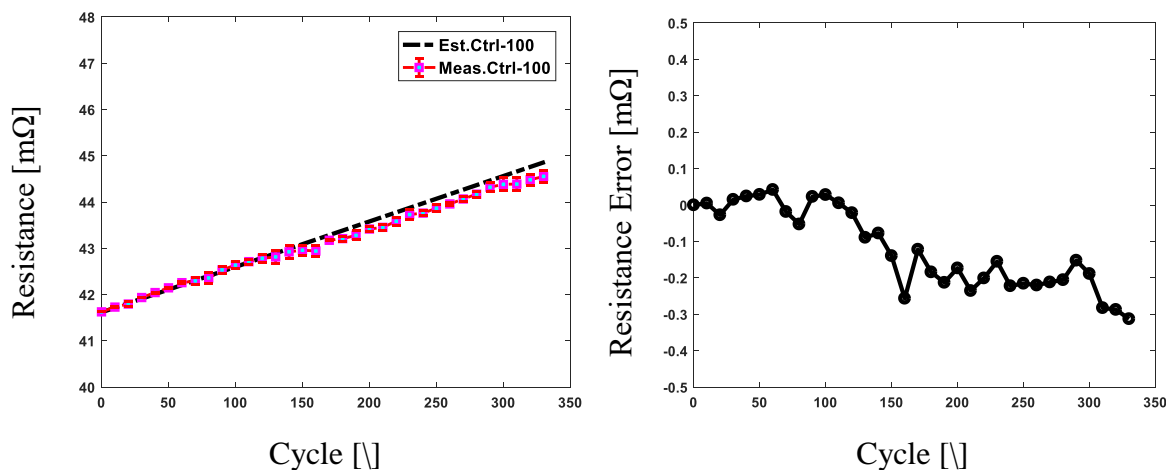
Fig. 5.48: Estimated resistance vs. measured resistance for the "Ctrl-100" group (Sony)

In order to quantitatively analyze the effectiveness of the proposed ROD control scheme, the measured resistances are also linearly fitted for each group since the slopes of the linear fitted lines can be used to indicate the aging rates. In Fig. 5.50 and Fig. 5.51, the measured resistances are plotted together with the respective first-order linear fitted lines. The slopes of the linear fitted lines are summarized in Table 5.12 and the slope for the fitted "Ctrl-100" group line is lower than that of the fitted "noCtrl-100" group by approximately 21%. This indicates that quite significant degradation reduction can be achieved by applying the limiting-type ROD control schemes.
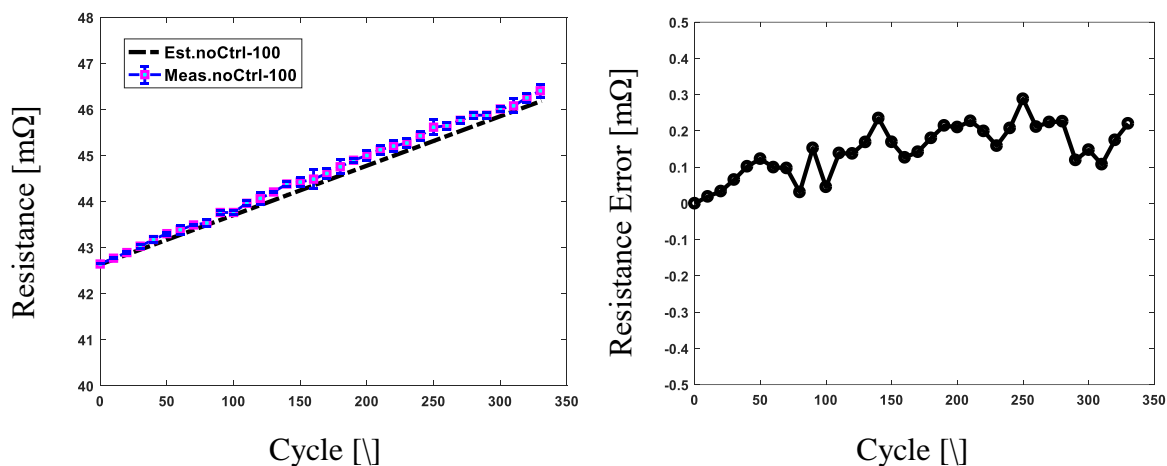
Fig. 5.49: Estimated resistance vs. measured resistance for the "noCtrl-100" group (Sony)
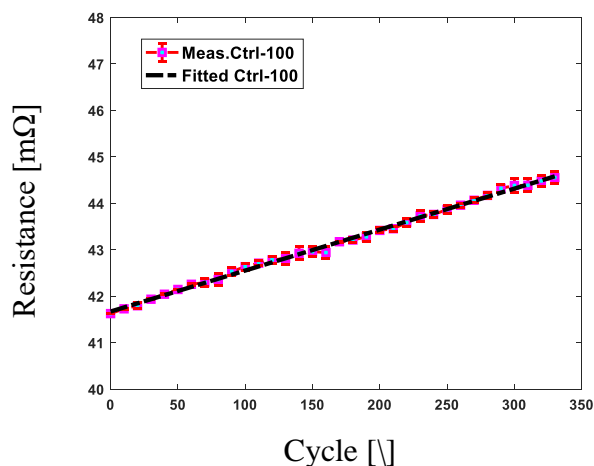
Fig. 5.50: Fitted resistance vs. measured resistance for the "Ctrl-100" group (Sony)

In Fig. 5.52, the incremental resistances of both the measured resistance and the estimated resistance for both groups are plotted together, showing clear aging reduction with the ROD control enabled. Table 5.9 summarizes the fitted slopes for the modeled resistance curves for both groups. The slopes are close to those for the measured resistances, confirming the accuracy of the ROD model.
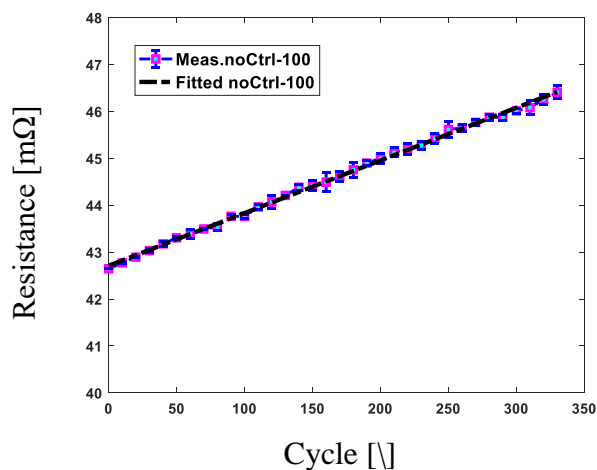
Fig. 5.51: Fitted resistance vs. measured resistance for the "noCtrl-100" group (Sony)
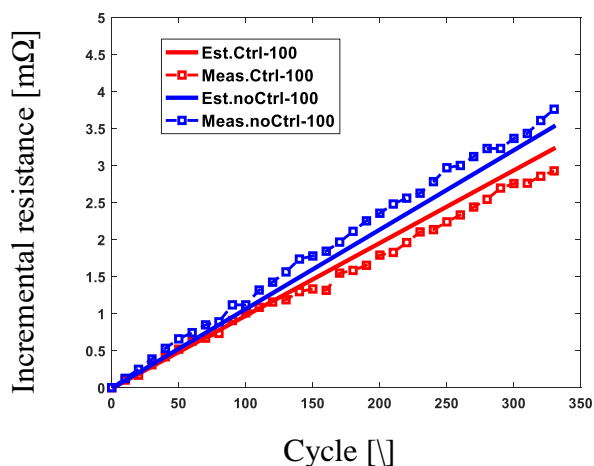
Fig. 5.52: Est. incremental resistance vs. meas. resistance for all groups (Sony)

Overall, it can be seen that the proposed ROD control can be applied for a battery with different cathode chemistry and aging reduction can be achieved as well. Based on the results, it suggests that Sony VTC6 cells are less vulnerable to SEI layer growth related aging mechanisms and can benefit more from the proposed ROD control schemes.

Table 5.8: Summary of the linear-fitted slopes of estimated resistance curves (Sony)

Simulation Case	Ctrl-100	noCtrl-100
Slope [$\frac{m\Omega}{Cyc}$]	0.0098	0.0107

Table 5.9: Summary of the linear-fitted slopes of measured resistance data (Sony)

Test Case	Ctrl-100	noCtrl-100
Slope [$\frac{m\Omega}{Cyc}$]	0.0088	0.0112

5.6 ROD Control Evaluation at Low Temperature

As the batteries in an EV can operate at different temperatures, it is worthwhile to analyze the suitability of the proposed ROD control at different operating temperature conditions. As the batteries can be particularly limited in terms of its power/energy capability at low temperatures, in this section, the proposed ROD control is evaluated for its low temperature applicability.

To avoid significant power capability restriction, normally EV battery pack will be pre-heated to approximately 10°C before driving. Therefore in this section, 10°C is chosen as the testing temperature condition to evaluate the low temperature ROD control.

5.6.1. Low Temperature Power Modification

As discussed in a previous section, the limited side-reaction current at different temperatures is tuned according to (5.1). In Fig. 5.53, the side-reaction current boundary at 10°C is shown and is double of the value at 25°C. As a result, the current limits, though harsher, are kept within a feasible range.
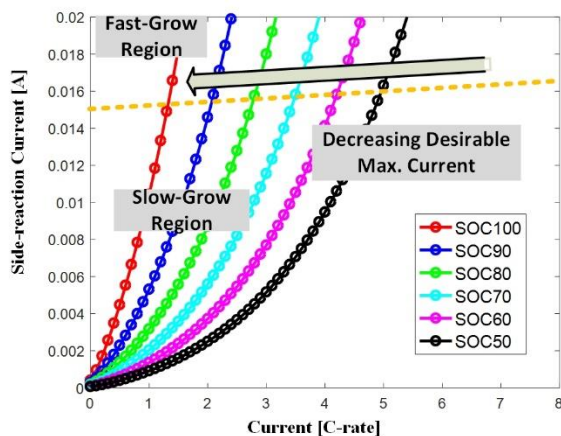
Fig. 5.53: Dynamic current/power shielding boundary curve at 10°C

The tested drive cycle remains the same as in the previous experiments, consisted of 1200s US06 and 1200s LA92. The original 2400s drive cycle is again plotted below. It is expected that by applying the dynamic ROD current (power) shielding, more control events would occur. Since the ROD is more severe at low temperature, by applying an even more strict boundary, more battery performance compromise is expected but would ideally lead to more degradation reduction.

Fig. 5.55 superimposes the ROD-limited dynamic power limit with the original drive cycle power profile. The limit is overall smaller than 25°C case.
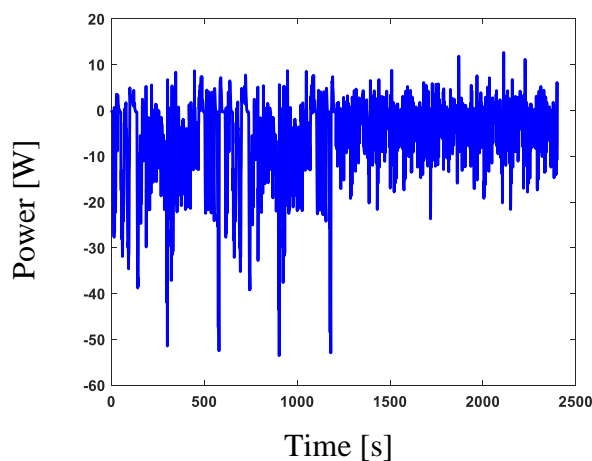
Fig. 5.54: Combined 2400s power profile
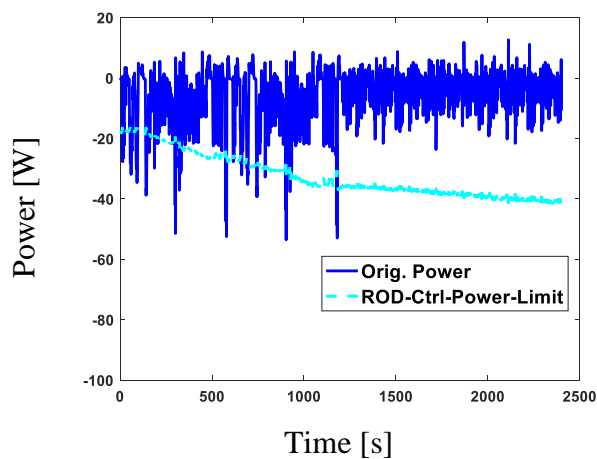
Fig. 5.55: Original power profile imposed with ROD control power limits at 10°C
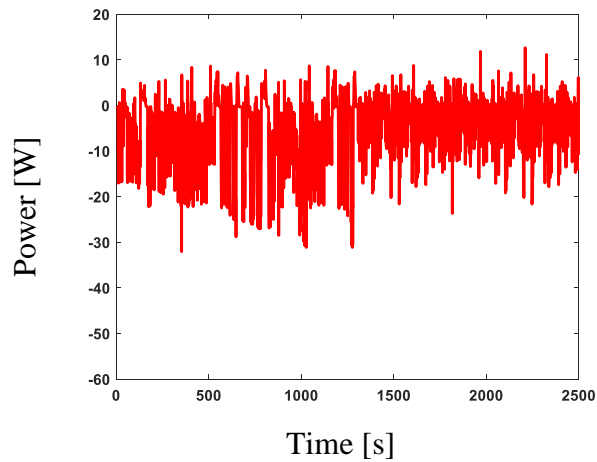
Fig. 5.56: Modified 2400s power profile after applying ROD control at 10°C

Fig. 5.56 and Fig. 5.57 show the modified drive cycle power profile at 10°C as well as the binary control signal over the whole drive cycle. Same as previous tests, whenever a control event occurs, the truncated power will be supplemented during the next second so that SOC/SOE will not be affected.

As expected, 198 control events occur for the 10°C case, about twice the occurrence at 25°C. This also leads to more performance compromises.
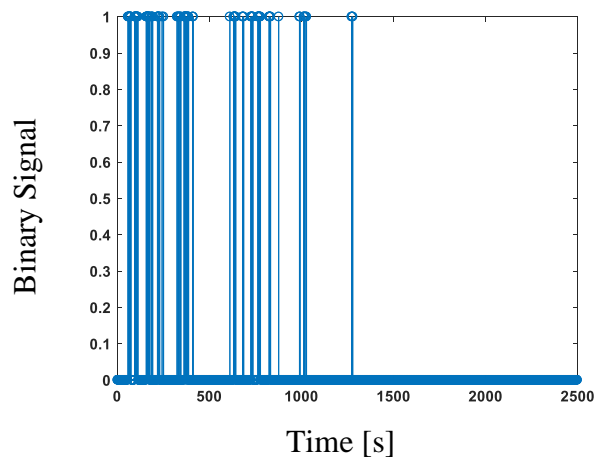
Fig. 5.57: ROD control enabling signal for Panasonic cells at 10°C

5.6.2.   Low Temperature Aging Experimental Design

The experimental design for 10°C ROD control evaluation is similar to the previous

experiments. Six Panasonic cells are divided into two groups. The discharge SOC range is from 100% to 70%. Resistances of all cells are measured every 10 cycles using a 20-sec 2C discharge pulse.

Since low temperature charging can trigger another Li-ion battery aging mechanism, lithium plating, the charging temperature is set to 20°C by relaxing the batteries for a period of time until the chamber temperature rises from 10°C to 20°C. This change however will prolong the total test time quite significantly. A summary of the experiment is provided in Table 5.10 below.

Table 5.10: 6-cell drive-cycle aging experiments to evaluate region-based ROD controls

# of Tested Cell	Op. SOC Range	With Control?	Op. Temp.
3	100% --- 70%	Yes	10°C
3	100% --- 70%	No	10°C

Eventually the test runs for a total of 180 cycles both due to the prolonged single cycle duration and limited by the testing equipment availability. Since SEI layer growth is more dominant during the early stages, 180 cycles are enough for ROD control evaluation.

5.6.3.   Low Temperature ROD Control Evaluation

After gathering the resistance data for all cells, the data are group averaged. Two evaluations are applied. One is to compare the group-averaged resistance data for both groups with the estimated resistances based on the ROD model. The second evaluation is to compare the two data groups to determine whether the ROD control achieves degradation reduction.

In Fig. 5.58 and Fig. 5.59, the modeled resistances are compared with the resistance data for both the "Ctrl-100" group and the "noCtrl-100" group. In both cases, accurate estimation is achieved. The estimation error overall is slightly higher for the "Ctrl-100" group but in both cases the estimation errors are kept well under 1mΩ.

In Fig. 5.60 and Fig. 5.61, linear-fitted resistances are plotted together with the original

resistance data. The slopes of the linear-fitted resistances can be compared to determine the effectiveness of the proposed ROD control on degradation reduction.
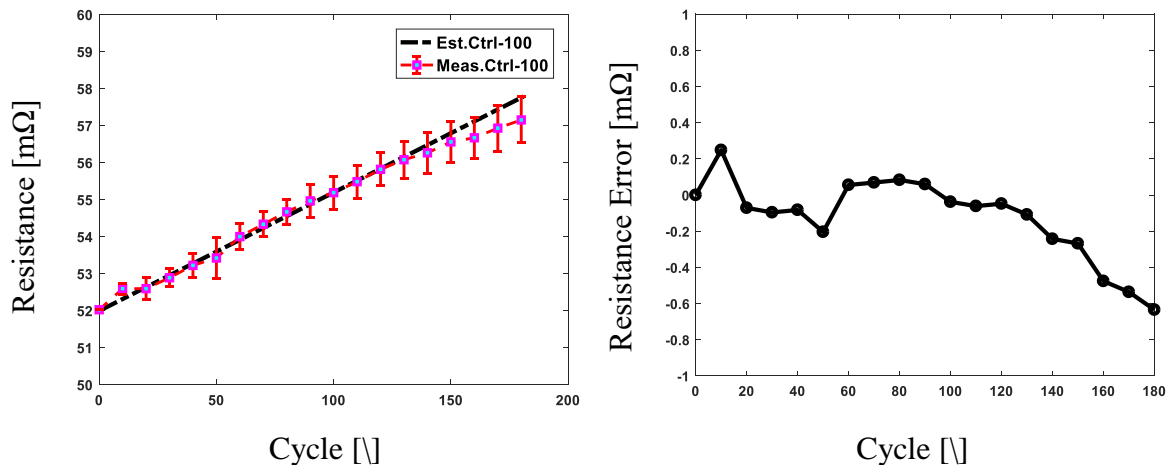
Fig. 5.58: Estimated resistance vs. measured resistance for the "Ctrl-100" group
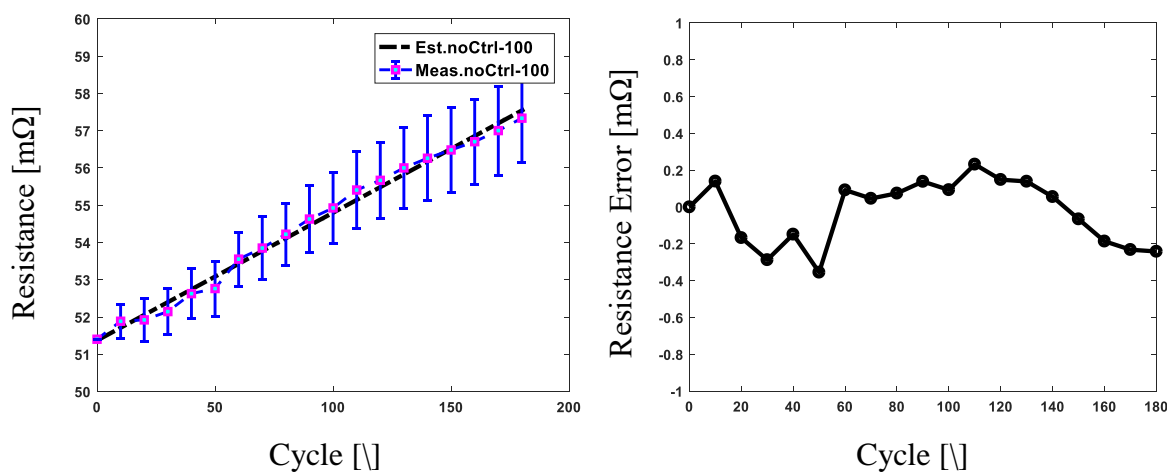
Fig. 5.59: Estimated resistance vs. measured resistance for the "noCtrl-100" group
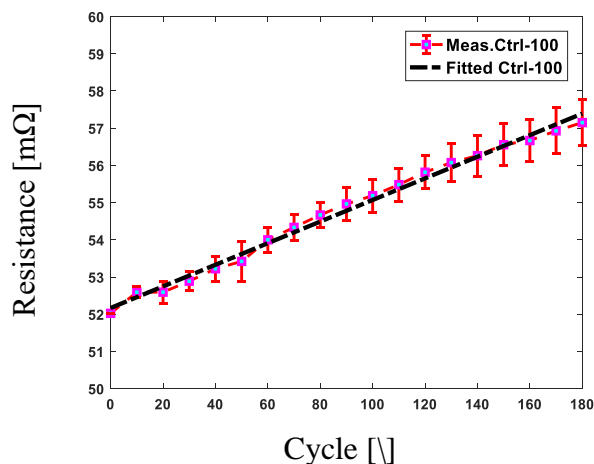
Fig. 5.60: Fitted resistance vs. measured resistance for the "Ctrl-100" group
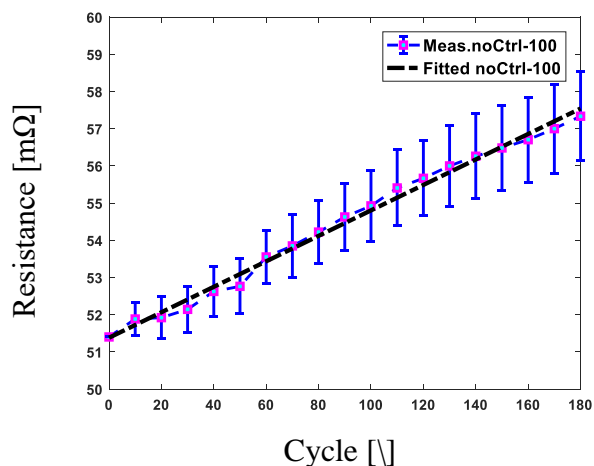
Fig. 5.61: Fitted resistance vs. measured resistance for the "noCtrl-100" group

Table 5.11 summarizes the estimated slopes based on the modeled resistance with or without ROD control and the slope of the "Ctrl-100" group is slightly smaller. Such small difference may not be evident enough to confirm the degradation reduction capability. However, in Table 5.12, the slopes based on the linear fits for the measured resistance data show that a noticeable degradation reduction can be achieved by the proposed ROD control at low temperatures. It shows an approximately degradation reduction of 15%. The resulting degradation reduction is more than that at room temperatures as expected since the current limiting boundary is harsher at low temperatures as shown previously. In addition, it requires more battery performance compromise at low temperatures as seen from the doubled control events.

In summary, the proposed ROD control has been evaluated for low temperature conditions and shown noticeable battery degradation reduction capability as well.

Table 5.11: Summary of the linear-fitted slopes of estimated resistance curves

Simulation Case	Ctrl-100	noCtrl-100
Slope $[\frac{m\Omega}{Cyc}]$	0.0320	0.0343

Table 5.12: Summary of the linear-fitted slopes of measured resistance data

Test Case	Ctrl-100	noCtrl-100
Slope $[\frac{m\Omega}{Cyc}]$	0.0290	0.0342

5.7   Chapter Summary

In this chapter, the reduced-order ROD model is analyzed quantitatively on its relationship with changing current rate, battery SOC, and battery temperature. It shows that larger current rates, higher battery SOC, and lower battery temperature lead to worse ROD based on the model equation evaluations. A holistic characteristic map of the ROD over a large battery operating region has been evaluated, and several stages of the ROD severity are identified with their respective ROD severity boundary curves. Based on the characteristic map, it has been determined at any given temperature, a ROD transitioning boundary curve with respect to both the battery current and SOC is identified indicating the dramatic transition of the side-reaction current from a "slow-grow region" to a "fast-grow region". A boundary selection algorithm is developed to further generate useful look-up table of ROD-limited current limits in terms of different SOC and temperature conditions. Secondary algorithms are also developed to adjust the side-reaction current boundary for different temperatures to generate reasonable and pragmatic current limits during drive cycles.

A block diagram including the integration of the power-commanded electro-thermal model and the reduced-order ROD model is developed, feeding the side-reaction current as the ROD metric to the region-based ROD control block. A ROD-optimized battery current (power) shielding

control law is developed based on only allowing the battery to operate within the proposed ROD-limited current limits. This ROD-optimized battery current (power) shielding control law serves as the core part of the region-based ROD control schemes. An algorithm dynamically calculating the allowable loading power for the battery at any sampling instant is developed for the shielding control law as well.

A power-commanded drive cycle is customized to mimic a daily commuting scenario, consisting of 20-minute US06 drive cycle and 20-minute LA92 drive cycle. Evaluation simulations for the Panasonic 18650PF batteries undergoing this customized drive cycle with or without the shielding control law, as well as over different SOC ranges to evaluate the effect of battery SOC on battery ROD. A slower degradation progress of the battery with the ROD control is seen from the simulation, and a slower degradation progress of the battery operating during a medium-SOC range rather than in a high-SOC range is seen as well.

Drive cycle aging experiments have been designed and conducted for six Panasonic 18650PF cells, undergoing the same simulated operating sequences. The three different aging experiments at 25°C include power cycling 2 batteries with the ROD control starting from 100% SOC, 2 batteries without the ROD control starting from 100% SOC, and 2 batteries without the ROD control starting from 80% SOC. The resistances of the batteries are measured every 10 cycles. After 450 cycles, the experimental resistance data agree well with the estimated resistance for the three testing conditions, validating the accuracy of the developed ROD model and the effectiveness of the developed ROD-optimized battery current (power) shielding control law.

Meanwhile, similar aging experiments have been conducted to validate the ROD control law for a battery with different chemistries. Sony VTC6, which has a different cathode chemistry compared to the Panasonic 18650, has been tested and degradation reduction is shown achievable at room temperature. In addition, low temperature experiment of Panasonic cells also shows the effectiveness of the ROD control schemes, achieving a degradation reduction.

Chapter 6 Trade-off Between ROD Control and Battery Performance Compromise

As seen in Chapter 5, the proposed ROD control strategy results in a limiting-type control and can compromise the battery performance in terms of the loading current and power. For EV applications, these particular limitations lead to situations that when the driver is stepping heavily on the acceleration pedal, the vehicle would not deliver the desired amount of power because of the ROD control limits. One may argue that this type of limitation should not be applied since it is against the driver's requests while driver should have the complete decision privileges. However, one would understand that such performance limits have been existed for automobile industry for a long time. For the conventional internal combustion engine (ICU), torque limits are always applied to consider factors such as performance and emission [128]. Fig. 6.1 shows a block diagram about ICE cruise control. It can be seen that a torque saturation block is included. Similar limits are also applied to other variables of ICE such as velocity, emission, and injection ratio. Therefore, applying current or power limits to EVs in order to keep the degradation rate reasonable could be acceptable for the drivers even though the drivers may feel underpowered.
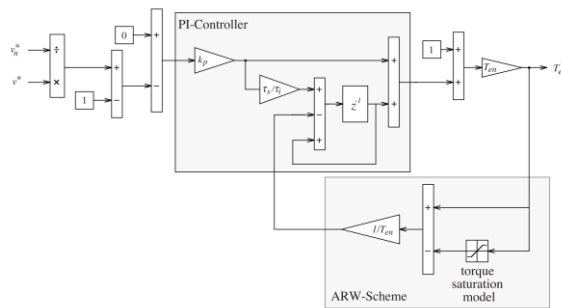
Fig. 6.1: Discrete-time PI controller with anti-reset windup circuit

In this chapter, a trade-off analysis between the battery degradation reduction capability and the battery performance based on simulations is conducted. As briefly shown in the previous chapter, the ROD-limited current envelope for a battery can be modified so that the resulting

controlled battery current can be more practical. Consequently, the battery degradation reduction capability changes and this can be also driving-scenario dependent. In this chapter, different levels of current limits at different temperatures are investigated for scenarios including highway and city drive cycles. The resulting trade-off between the degradation reduction level and the battery performance compromise level is showcased and summarized.

6.1   ROD-limited Current Manipulation

As discussed in chapter 5, the proposed ROD control essentially enforces limits on either the current or the power that discharges the battery. However, since there is much freedom in terms of setting the ROD boundary, there are opportunities to manipulate such a boundary for different operating conditions to achieve the desirable level of battery degradation reduction. On the other hand, since the battery current and power outputs are limited when the ROD control algorithm is enabled, battery performance compromises, though not desirable, are inevitable. As briefly discussed in chapter 5, as the proposed ROD control algorithm is applied for low temperature cases, there can be a temperature-dependent adjusting factor applied so that the resulting current limit is within a reasonable range. In this section, the effects of different adjustment factors on the ROD-limit current boundary at different temperature conditions are investigated.

6.1.1   Temperature-dependent ROD-limited Current Adjustment

Based on the characterization of the proposed ROD model, temperature can be one significant factor affecting the ROD curves. While developing the ROD control law, if one fixed ROD value limit were to be used, the associated current limits, especially for the high SOC region, could be quite small and somewhat unrealistic for practical usages as the EV performance would have been significantly restricted.

In Fig. 6.2, the current limits at different conditions based on a fixed ROD limit are plotted. As indicated from this figure, in the high SOC region, the discharge current limit can be as low as

only 2A at low temperature conditions, while at room temperature or higher the discharge current limit can range from 5A to 8A.
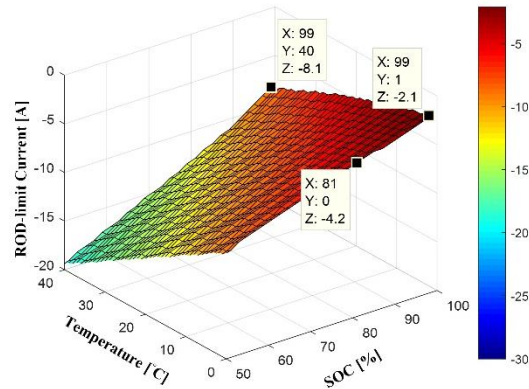
Fig. 6.2: ROD-limit current boundary map with no adjustment factor

Such a low current limit at low temperature conditions can be troublesome for EV application as the battery pack can be routinely at a high SOC region and the ambient temperature can be quite cold sometimes. As drive cycles can have an average discharge current of about 1C, 2A, or equivalently 0.67C for the Sony cell, can dramatically limit the battery performance and frequently trigger ROD control if the vehicle is running in cold environment. In other words, the performance compromise in such a situation is too heavy not to be felt by the driver. A temperature-dependent adjustment on the current limits is preferred so that a balance between the degradation reduction and performance compromise can be achieved.

6.1.2   Current Limit Adjustment Factor

As introduced in section 5.2.1, the ROD-limit current boundary was adjusted with respect to temperature as the low temperature performance was too heavily limited with the evaluation drive cycle used. Moreover, the Arrhenius relationship was also considered and help lead to an adjustment that changes the previously-fixed ROD limit to a temperature-dependent varying quantity. The adjustment factor was set to 2 so that at low temperature conditions, the ROD-limit current can be more than 1C to lessen the limitation.

However, the practice of adjusting the ROD-limit current focused on achieving a

reasonable power profile for low temperature ROD control evaluation. There has not been a more complete investigation on how different levels of the adjusting factor can affect either the degradation reduction level or the battery performance compromise level. Moreover, different driving scenarios can favor different adjusting factors. Specifically, highway drive cycles and city drive cycles may have different levels of adjusting factor enforced but still achieve similar results. Also, temperatures can be another factor dimension to be considered.

Table 6.1: Summary of the operating conditions considered

Adjusting factor	Drive cycle type	Temperature
1 (no adjustment), 1.5, 2, 3	highway, city	$35°C$, $25°C$, $10°C$, $0°C$

In Table 6.1, a summary of different agjusting factor levels, drive cycle scenarios and temperature conditions is provided. The adjusting factor is divided into four levels. The value of each factor level refers to the case in which the ROD limit value, $I_{s\_lim}(T)$, is increased by such a factor as temperature decreases $15°C$. (6.1) is the mathematical expression that represents this adjustment. The "1" case is the baseline and essentially there is no adjustment. The "1.5" case leads to a small adjustment for the low temperature ROD-limit current boundary. At the same time, since other aging mechanisms that favor high temperatures can be worsen if the battery discharge current is high, a similar adjustment can be enforced simultaneously for high temperature conditions. The "1.5" case, as a result, can also lead to a more aggressive ROD boundary at high temperature conditions. Overall, the "1.5" factor can be somewhat recognized as slightly "favoring" the low temperature. Similarly, the "2" and "3" cases "favor" the low temperature conditions even more, while the "2" case results in a ROD-limit current boundary map that is almost independent of temperature.

$$\text{root} = \sqrt[15]{\text{factor}}$$
$$I_{s\_lim}(T) = I_{s\_lim}(25°C) * \text{root}^{(25°C - T)}$$

(6.1)

In Fig. 6.3, the ROD-limit current boundary maps with different adjustment factors are

plotted. The boundary surface is rotating towards the direction where larger discharge current is allowed for the low temperature conditions. With a factor of 1.5, slightly over 1C current rate is allowed for low temperature cases in a high SOC region. With an increasing factor, the boundary map results in harsher limits for the high temperature conditions. This may not be necessary if only the characterized aging mechanism is considered, but can be helpful as it compensates, to some extent, the effects from other high-temperature-favorable aging mechanisms such as mechanical disintegration and material decomposition.
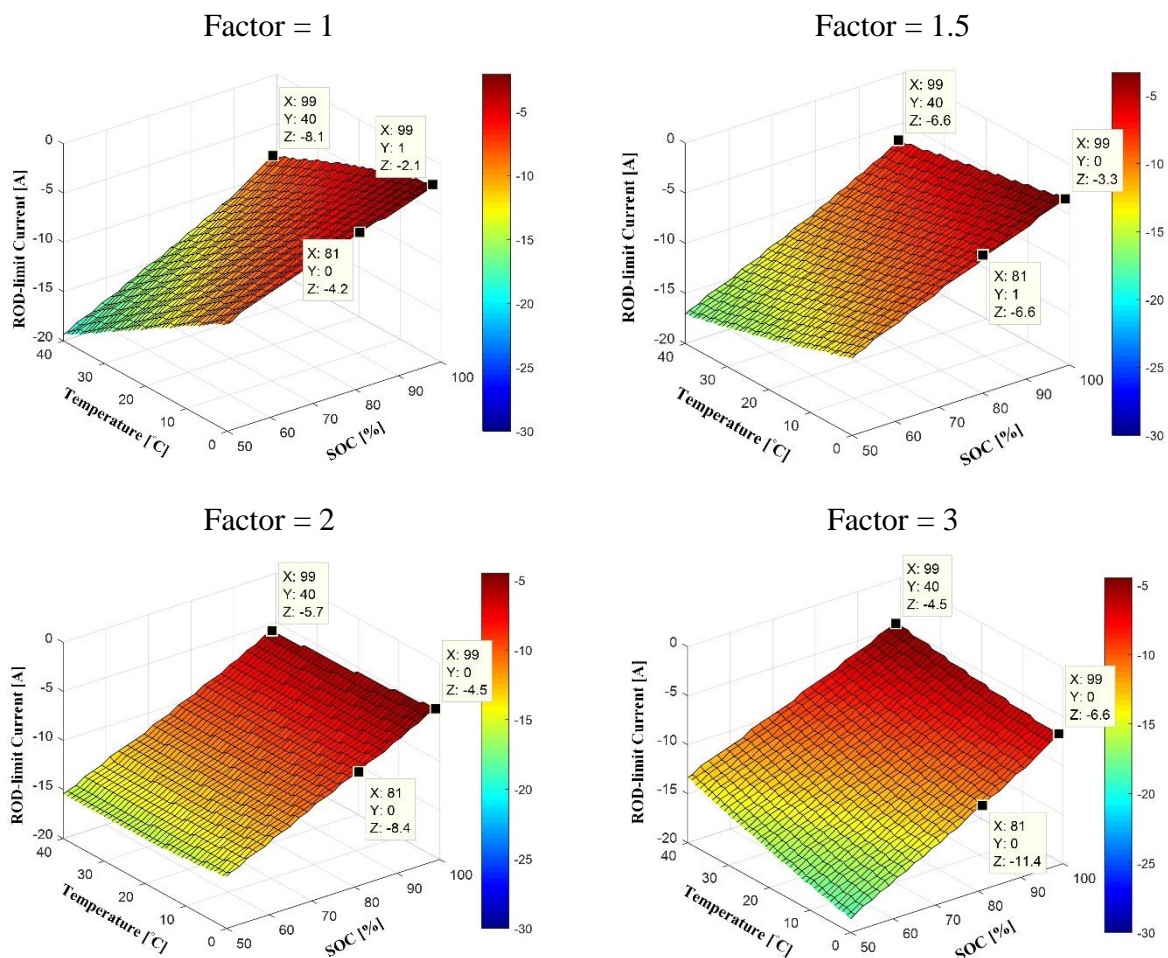
Fig. 6.3: ROD-limit current boundary maps with different adjustment factors

In the next section, these ROD-limit current boundary maps will be evaluated through simulations in terms of the resulting trade-off between the degradation reduction level and the

battery performance compromise level. Different drive cycle scenarios and different temperature conditions will be investigated.

6.2   Trade-off Analysis

The design factors for the evaluation include four adjustment factors, two different drive cycles, and four different temperature conditions. US06 drive cycle is used as the highway drive cycle and LA92 drive cycle is used as the city drive cycle. For various conditions, the simulation follows the sequence as in Fig. 5.8. For each cycle, the power profile is applied recursively until 20% SOC. The initial battery resistance is assumed to be 45mΩ and a total of 300 cycles are simulated. The ratio between the linearly-fitted slopes of the simulated resistances with or without ROD control is used to quantitively represent the degradation reduction level. The occurrence count of the ROD control enabling signal per cycle is used to represent the performance compromise level.

6.2.1   Degradation Reduction vs. Performance Compromise

In Fig. 6.4, the power profiles for both the highway and the city drive cycles are plotted. The highway drive cycle contains overall higher power values. It is expected that the ROD control would be enabled more frequently during a highway drive cycle.

In Table 6.2 and Table 6.3, the respective degradation reduction ratio and the control event occurrence for each test condition is recorded. Comparing the two tables, as expected, the ROD control event is much more often triggered for highway drive conditions. Both tables indicate that at low temperatures the proposed ROD control algorithm gets enabled more often. Meanwhile, a clear relationship between the degradation reduction level and the control event occurrence can be observed. As expected, more control events can occur, and more degradation reduction can be achieved.
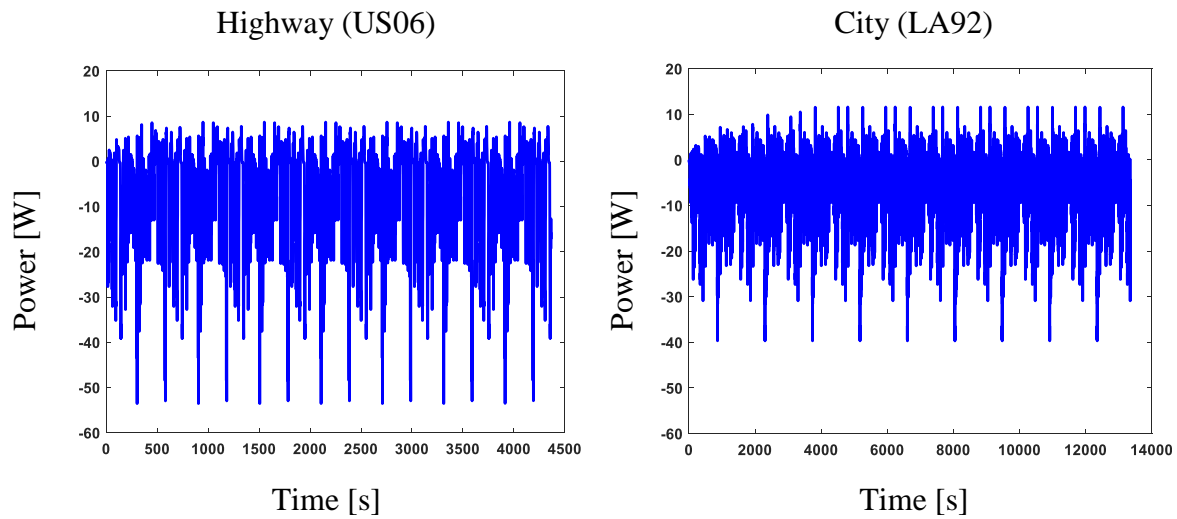
Fig. 6.4: Evaluation power profiles for both highway and city drive cycles

Table 6.2: Trade-off summary for the highway driving scenario

	35°C	25°C	10°C	0°C
Factor 1	0.97 - 44	0.92 - 124	0.78 - 432	0.67 - 890
Factor 1.5	0.94 - 92	0.91 - 140	0.84 - 264	0.78 - 434
Factor 2	0.92 - 136	0.91 - 148	0.88 - 194	0.85 - 246
Factor 3	0.88 - 224	0.90 - 158	0.92 - 106	0.92 - 106

Table 6.3: Trade-off summary for the city driving scenario

	35°C	25°C	10°C	0°C
Factor 1	0.99 - 6	0.99 - 68	0.92 - 538	0.83 - 1346
Factor 1.5	0.99 - 36	0.99 - 80	0.95 - 244	0.92 - 560
Factor 2	0.99 - 72	0.98 - 90	0.97 - 176	0.95 - 234
Factor 3	0.97 - 172	0.98 - 110	0.98 - 78	0.98 - 70

The ratio in both tables can be translated into percentages indicating how much degradation reduction is achieved. The translated tables are shown in Table 6.4 and Table 6.5.

Table 6.4: Translated trade-off summary for the highway driving scenario

	35°C	25°C	10°C	0°C
Factor 1	3% - 44	8% - 124	22% - 432	33% - 890
Factor 1.5	6% - 92	9% - 140	16% - 264	22% - 434
Factor 2	8% - 136	9% - 148	12% - 194	15% - 246
Factor 3	12% - 224	10% - 158	8% - 106	8% - 106

Table 6.5: Translated trade-off summary for the city driving scenario

	35°C	25°C	10°C	0°C
Factor 1	1% - 6	1% - 68	8% - 538	17% - 1346
Factor 1.5	1% - 36	1% - 80	5% - 244	8% - 560
Factor 2	1% - 72	2% - 90	3% - 176	5% - 234
Factor 3	3% - 172	2% - 110	2% - 78	2% - 70

For each temperature condition, both the degradation reduction percentage and the control event occurrence as in the "Factor 1" scenario are used as the baseline and the values in the other "Factor" levels are normalized. In Fig. 6.5, the normalized ratios for either the degradation reduction or the ROD control event are plotted against different adjusting factors respectively for different temperature conditions. Both the highway and the city scenarios are plotted as well. Specifically, with a higher adjusting factor, the performance compromise level can increase significantly for the 35°C case during a city drive cycle, while the corresponding degradation reduction capability does not change noticeably. This is due to the fact that the ROD control targeting limiting the current can be enabled multiple times as the battery current command is only slightly over the current limit. Therefore, the degradation reduction is not obvious, but the ROD control events occurrence is high. As a result, the 35°C case holds little interest for analysis and therefore are removed from the plot. Fig. 6.6 then plots 25°C, 10°C and 0°C cases for city drive cycle situation.

Highway

City (LA92)
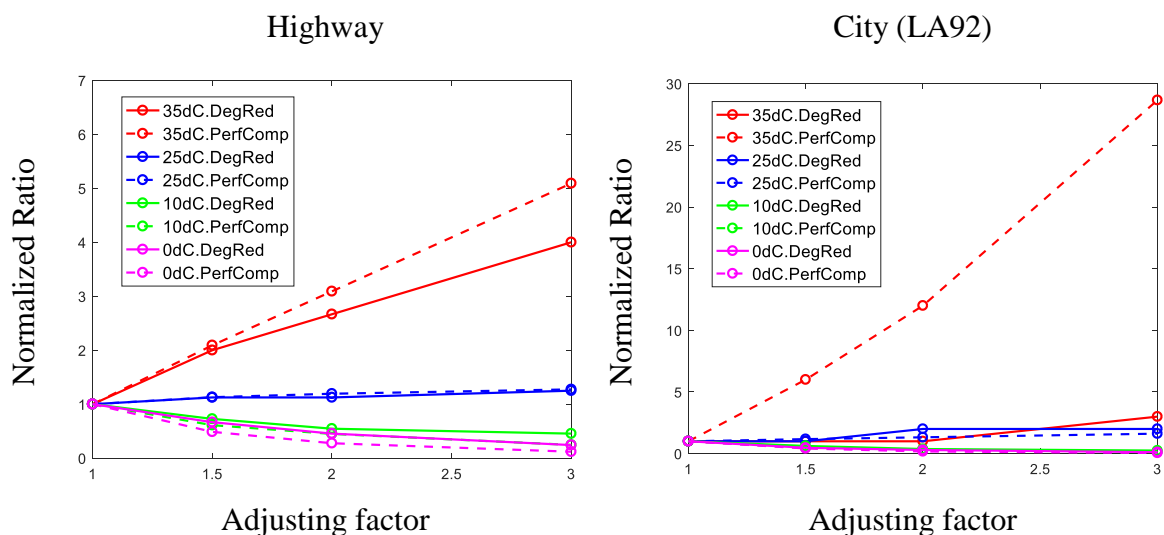
Fig. 6.5: Normalized trade-off ratios for both highway and city scenarios
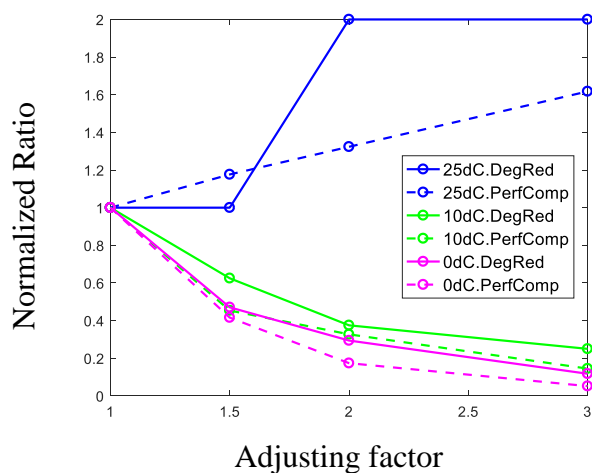
Fig. 6.6: Truncated normalized trade-off ratios for city scenarios

As seen from Fig. 6.5 and Fig. 6.6, the balance between the degradation reduction level and the performance compromise level does not appear to be linear and therefore at different temperature conditions different adjusting factors can be chosen to achieve a more optimal trade-off.

6.2.2   ROD Control Strategy Selection at Different Op. Conditions

To select a more suitable adjusting factor for different temperature conditions, the difference between the two normalized ratios at different adjusting levels can be a useful indicator.

Another indicator can be useful sometimes is the estimated ROD control event occurrence at an operating condition during one drive cycle and such value should not be too large otherwise the driver would clearly feel the current/power/torque limited.

In Table 6.6 and Table 6.7, different adjusting factors are selected as the more desirable factors for different operating conditions, namely different driving scenarios and different temperature conditions. It shows that for highway drive cycles, usually enforcing a higher adjusting factor can help achieve a better balance between the degradation reduction and the performance compromise. Typically, at low temperature conditions, enforcing the original factor can lead to strict constraints so that it would not be ideal for driver experience. An adjusting factor of 2 or 3 can help achieve a better balance while still imposing proper ROD limitations.

Table 6.6: Summary of desirable adjusting factors for highway scenario

Temperature	Desirable Factor	Reason
35°C	1.5/2	moderate limit, prevent overtemperature
25°C	1.5	good balance, moderate limit
10°C	2/3	good balance, high limit, low temperature enforcement
0°C	2	high limit, low temperature enforcement

For the city drive cycles, at 25°C a factor of 2 achieves the best trade-off balance and therefore is selected. For the 10°C and 0°C cases, either a factor of 1.5 or a factor of 3 can be chosen, depending on the situation. Both factors can help achieve a good balance while enforcing a factor of 1.5 can lead to quite a significant amount of ROD limiting events. If the drive is not time sensitive, a factor of 1.5 can be selected. However, for a purpose such as commute, a factor of 3 can be selected so the driver can arrive at work promptly.

Table 6.7: Summary of desirable adjusting factors for city scenario

Temperature	Desirable Factor	Reason
35°C	1	no significant improvement when elevating the factor
25°C	2	good balance, moderate limit
10°C	1.5/3	situation-dependent, good balance
0°C	1.5/3	situation-dependent, good balance

6.3   Chapter Summary

In this chapter, the trade-off between the proposed current/power limiting ROD control and the resulting battery performance compromise has been emphasized. A temperature-dependent ROD-limit boundary selection procedure is proposed. An adjustable ROD limit is discussed in terms of its relationship to the Arrhenius equation as well as its calculation procedure. To standardize the boundary adjustment process, different adjusting factors are introduced that the ROD limit can be tuned to favor different temperature conditions.

Extensive simulations have been conducted to evaluate the trade-off between the degradation reduction capability and the battery performance compromise for both highway and city driving scenarios at different temperature conditions. Quantitative summaries have been included to show both the degradation reduction level and the performance compromise level (i.e., ROD control event occurrence) for different operating conditions. As a result, desirable adjusting factors for different conditions are suggested to achieve a better trade-off.

Overall, enforcing a cell-level ROD control as proposed will inevitably lead to battery performance compromises although there is plenty of flexibility to manipulate the balance between the battery life-saving and the performance limitation. If a separate energy storage device such as a supercapacitor is also present in the system, effective power splitting can help improve the overall system durability while maintaining the system performance.

Chapter 7 Li-ion Battery State Estimation Algorithms Integrated with the ROD Control

As introduced in the state-of-the-art review, state estimation algorithms such as SOC and SOP estimation are an important branch of a battery management system. While the proposed ROD control algorithm can be an independent algorithm that does not necessarily require the information from the state estimation, it is worthwhile to investigate the integration compatibility between the proposed ROD control algorithm and the conventional state estimation algorithms proposed in the literature. In this chapter, a widely-used voltage-based SOC estimation algorithm using the extended Kalman filter (EKF) and an industry-tested SOP estimation algorithm using a linear Kalman filter (LKF) are adopted and integrated with the proposed ROD control algorithm. The compatibility, as well as potential limitations, is analyzed through simulations.

7.1   State Estimation Using Kalman Filters

There have been numerous algorithms developed in the literature focusing on Li-ion battery state estimation. These algorithms have different complexities, structures, and implementation difficulties. Though they are not the focal point of this research, they can still be potentially integrated with the proposed ROD control algorithm and interact with each other. In this section, two conventional state estimation algorithms for both SOC and SOP estimation are adopted and reconfigured for the Sony VTC6 cells that have been heavily tested throughout this research. In order to test various drive cycles at different temperature conditions in a convenient way, first an accurate 2RC equivalent circuit model is constructed for the Sony cells, enabling fast simulation capability. Subsequently, SOC and SOP algorithms are formulated, validated with real drive cycle data, and confirmed their accuracy by replacing the data with simulated drive cycle results.

7.1.1   2RC Battery Equivalent Circuit Model

Various battery equivalent circuit models (ECMs) have been published in the literature. Among them, 2RC ECM is commonly-used for its excellent balance between model complexity and model accuracy. Fig. 7.1 shows the 2RC equivalent circuitry containing the OCV component, a series resistance R_0, and two RC-parallel components $R_1\|C_1$ and $R_2\|C_2$.
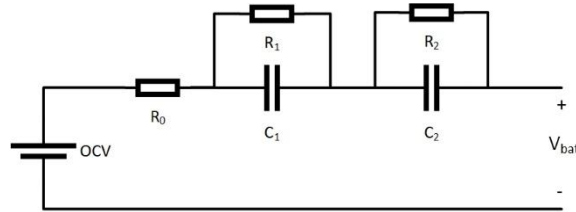
Fig. 7.1: 2RC equivalent circuit for the Sony cells

The OCV is measured for the Sony cells at different SOCs and different temperatures. The resulting OCV data table is further fitted with the function shown below, in which SOC ranges from 0 to 1 and temperature has the unit of Kelvin.

$$OCV_{fit} = f(SOC,T)$$

$$= p_0 + p_1 SOC + p_2 SOC^2 + p_3 SOC^3 + p_4 SOC^4 + p_5 SOC^5 + p_6 SOC*T + p_7 T + p_8 T^2$$

(7.1)

The resulting fitted OCV is plotted below, as well as the measured OCV and the fitting error between them. As shown in Fig. 7.2, the fitted OCV is close to the OCV data and the error is kept within 0.05V. Therefore, using the function to estimate OCV values for different algorithms can be accurate enough.

The other five circuit components are dependent on current, SOC, and temperature. It requires an extensive amount of characterization experiment to formulate necessary look-up tables. For this research, discharge pulse tests with different current rates at different SOCs and temperature conditions are conducted.
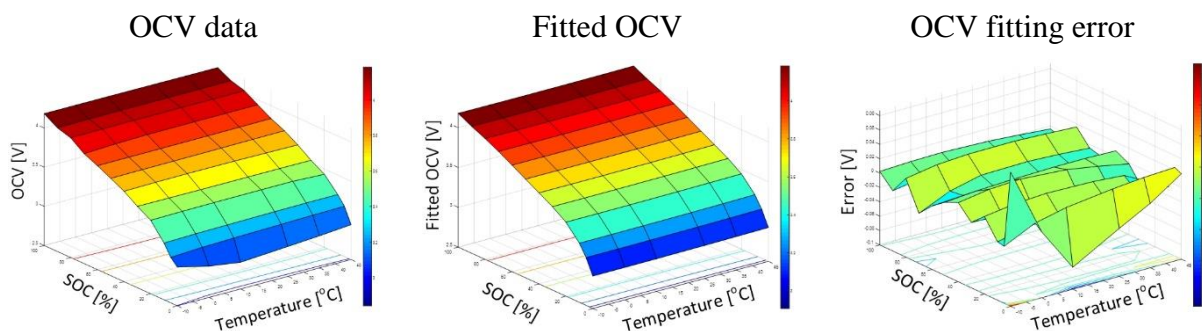
Fig. 7.2: Sony cell OCV fitting and error

A nonlinear least-square optimization process is used to estimate the five parameters by matching the estimated battery voltage with the measured voltage over each pulse test. Fig. 7.3, Fig. 7.4, and Fig. 7.5 show example plots of different equivalent circuit components at different current, SOC, and temperature conditions. Due to either the Arrhenius relation or the Butler-Volmer equation, different resistance components show higher variabilities at low temperature conditions.
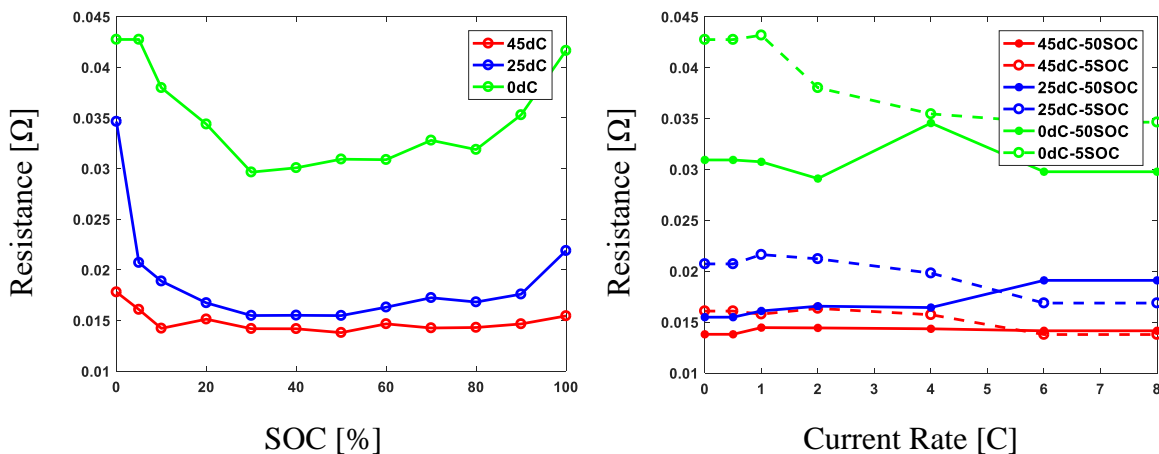
Fig. 7.3: Identified Sony cell R_0 for different conditions
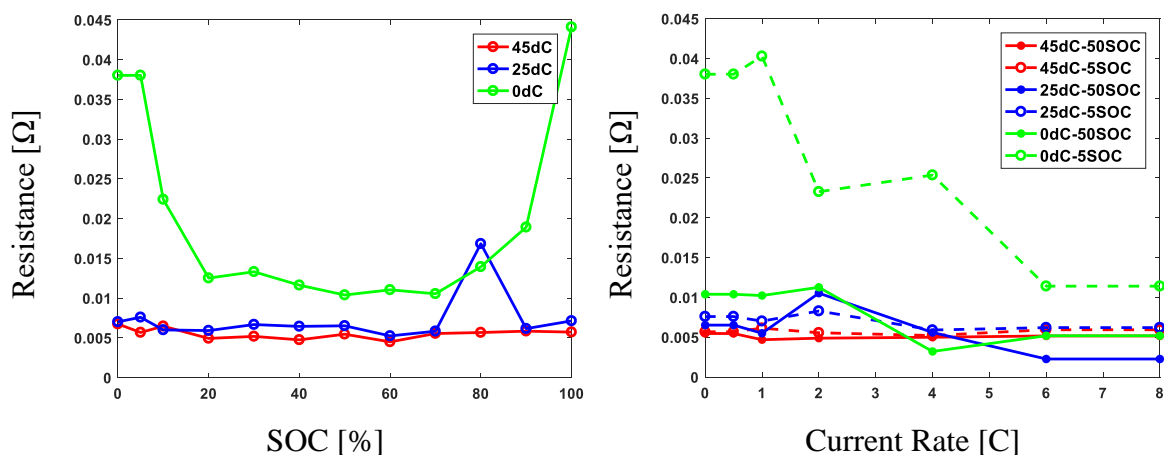
Fig. 7.4: Identified Sony cell R_1 for different conditions
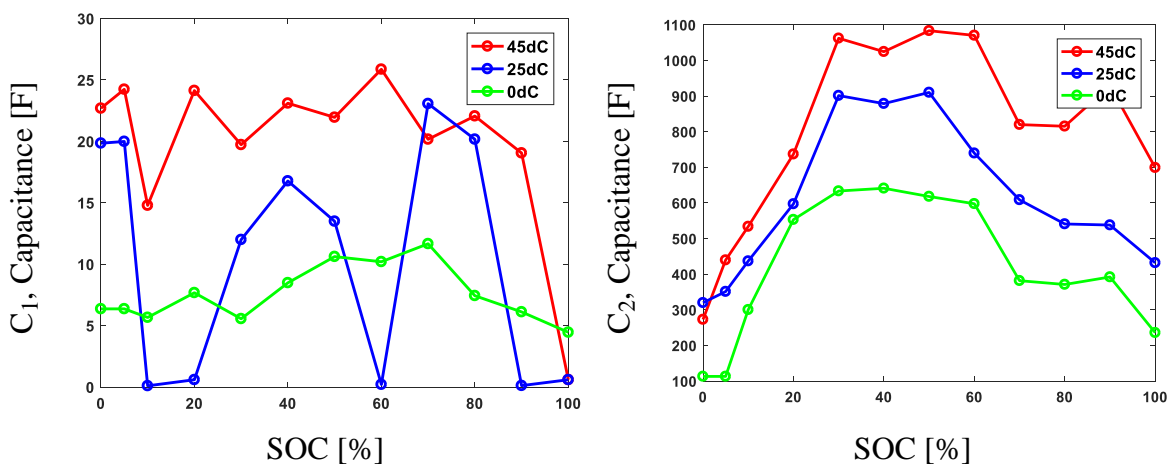
Fig. 7.5: Identified Sony cell C_1 and C_2 for different conditions

On the other hand, since the battery has different time constants related to either the charge transfer process or the diffusion process, C_2 is about ten times bigger than C_1. As all equivalent circuit components are identified, the battery electrical model is formulated. In Fig. 7.6 and Fig. 7.7, the model is validated with a validation drive cycle combined by four different drive cycles, in which each drive cycle makes up a quarter of the whole validation profile. At both 25°C and 0°C ambient temperature cases, the modeled battery voltage is compared with the measured voltage, showing accurate estimation and errors well within 200mV.
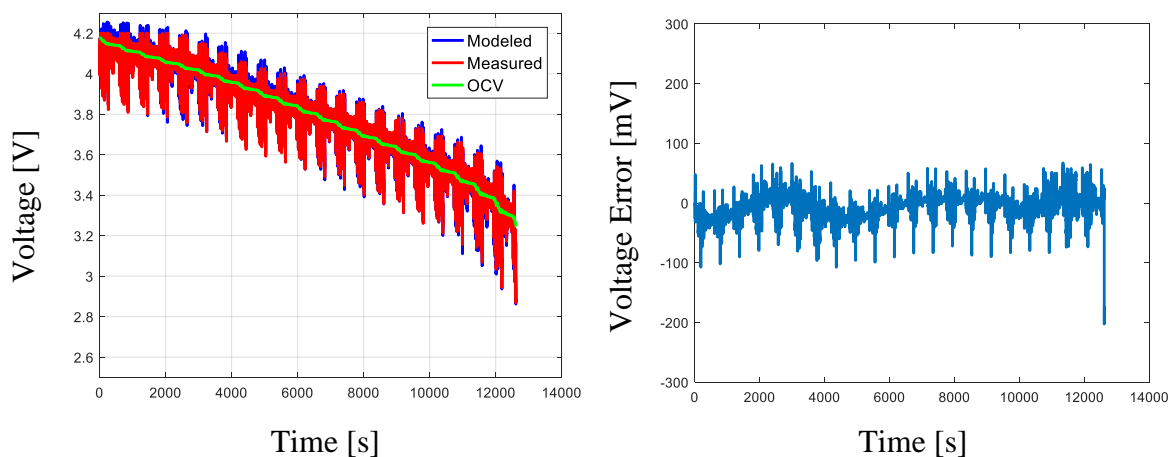
Fig. 7.6: 2RC ECM voltage estimation at 25°C
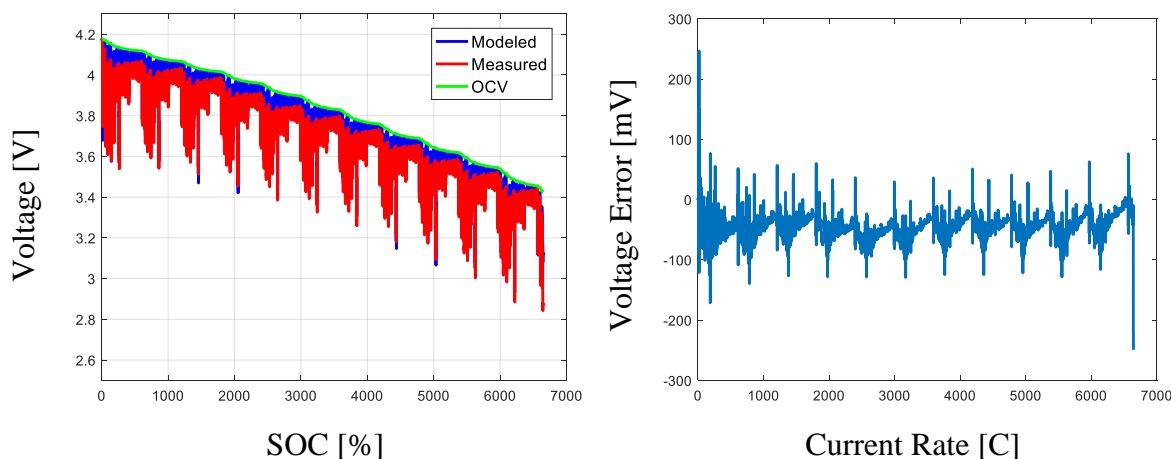
Fig. 7.7: 2RC ECM voltage estimation at 0°C

The successful formulation of the 2RC ECM, more importantly the identified battery model parameters, can be then utilized extensively for the other state estimation procedures.

7.1.2   SOC Estimation Using an Extended Kalman Filter

A standard practice for Li-ion battery SOC estimation is using an extended Kalman filter. Without knowing the battery model parameters, a more complex dual extended Kalman filter can be used. Since the focus of this research is about degradation control algorithm development, only the extended Kalman filter with known model parameters is adopted as the SOC estimation algorithm basis. In [42], EKF algorithm was introduced for Li-ion battery SOC estimation and the

general EKF algorithm procedure is shown in Fig. 7.8.
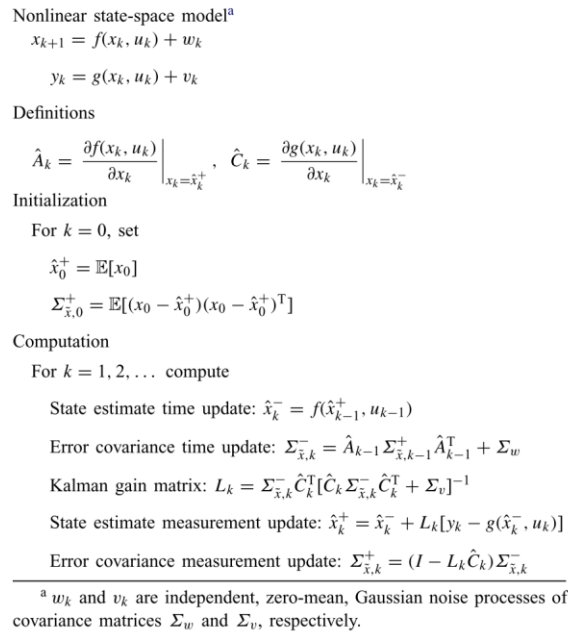
Fig. 7.8: Summary of the nonlinear EKF algorithm

Based on the 2RC battery model, the state-space model required can be formulated as the following.

$$x_{k+1} = \begin{bmatrix} u_1(k+1) \\ u_2(k+1) \\ SOC(k+1) \end{bmatrix} \qquad u_k = I_k$$

$$A_k = \begin{bmatrix} e^{\frac{-\Delta t}{R_1(k)C_1(k)}} & 0 & 0 \\ 0 & e^{\frac{-\Delta t}{R_2(k)C_2(k)}} & 0 \\ 0 & 0 & 1 \end{bmatrix} \qquad B_k = \begin{bmatrix} R_1(k)(1 - e^{\frac{-\Delta t}{R_1(k)C_1(k)}}) \\ R_2(k)(1 - e^{\frac{-\Delta t}{R_2(k)C_2(k)}}) \\ \frac{\Delta t}{C_{rated}} \end{bmatrix} \qquad (7.2)$$

$$C_k = \begin{bmatrix} 1 \\ 1 \\ \frac{dOCV}{dSOC}|SOC_k^- \end{bmatrix} \qquad D_k = R_0(k) \qquad y_k = V_k - OCV_k$$

The third element in C_k can be calculated by partial-differentiating the fitted OCV function in (7.1) with respect to SOC. In addition, the initial (co)variance matrices of the state noise, process

noise, and measurement noise are determined based on the suggestions in [129]. A summarized table is provided below.

Table 7.1: Summary of the (co)variance matrices used for the EKF

state covariance matrix	diag[10e-12, 10e-12, 5e-4]
process covariance matrix	diag[10e-9, 10e-9, 10e-15]
measurement variance	5e-7

Evaluation of the EKF for the Sony cells on its SOC estimation accuracy during a drive cycle is performed at different temperature conditions. The selected evaluation drive cycle is the same as in the last section for 2RC ECM evaluation. $0°C$ and $25°C$ cases are both evaluated.

Fig. 7.9 shows the SOC estimation compared with the measured SOC using the coulomb counting method. The estimation has errors due to both the model parameter inaccuracy and the battery hysteresis phenomenon.
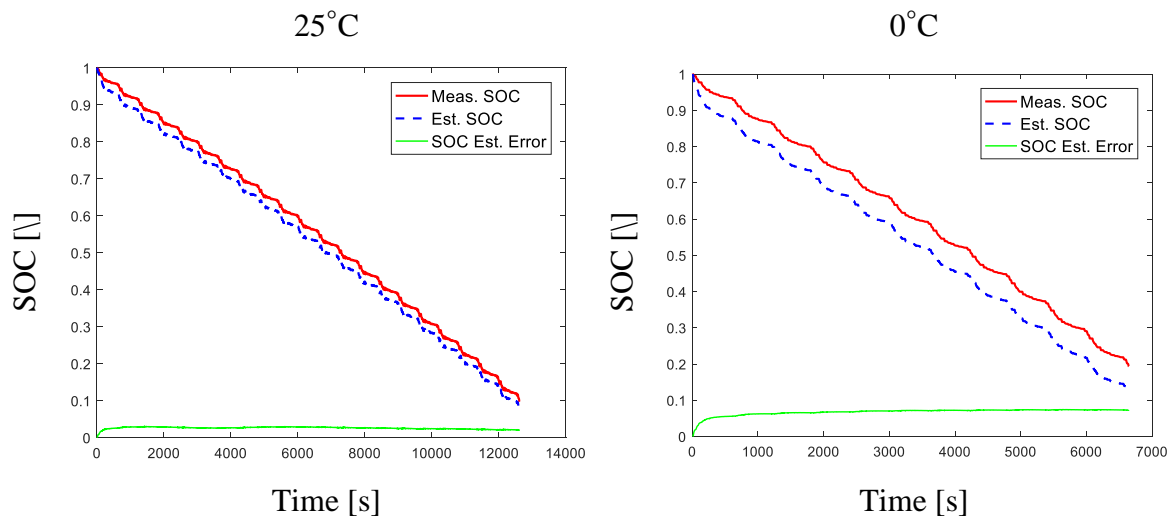
Fig. 7.9: SOC estimation for the evaluated drive cycle at $0°C$ and $25°C$
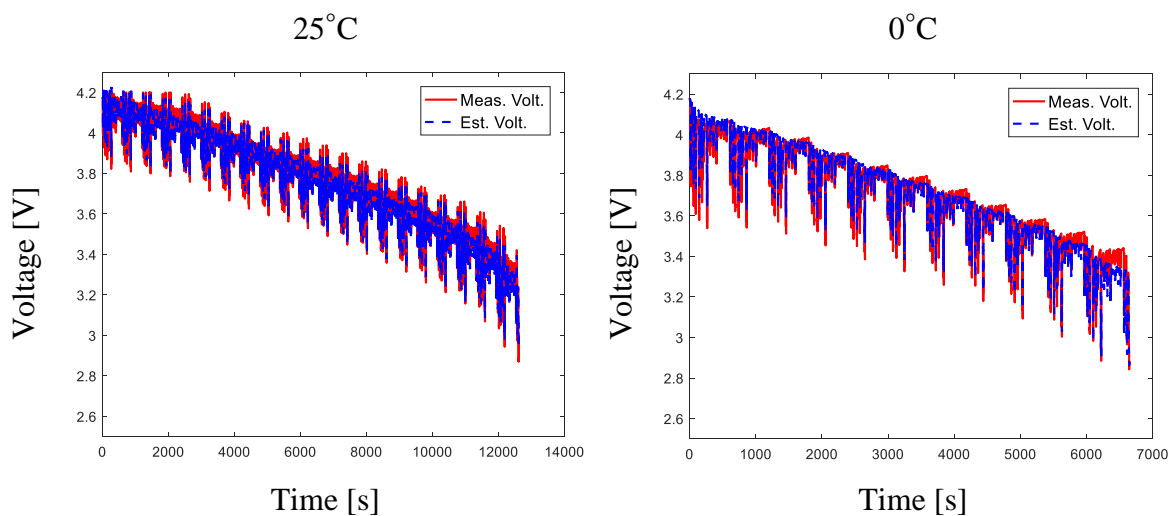
Fig. 7.10: Voltage filtering for the evaluated drive cycle at $0°$C and $25°$C
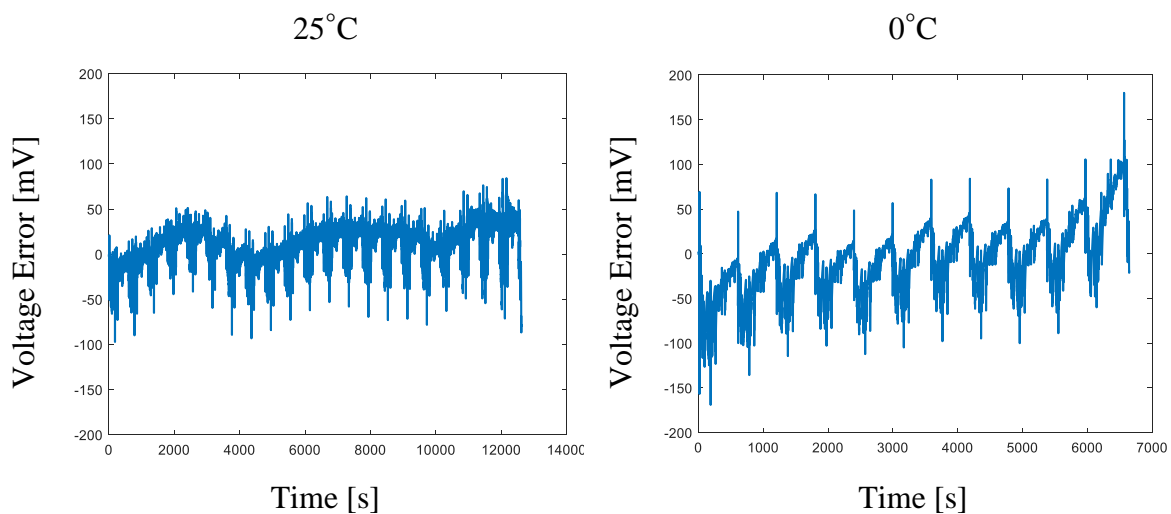
Fig. 7.11: Voltage filtering error for the evaluated drive cycle at $0°$C and $25°$C

It can be seen for either the SOC estimation accuracy or the filtered voltage accuracy, the results are better for the $25°$C case. This can be because the battery internal resistance is higher at low temperatures and leads to more severe hysteresis.

Overall, the EKF performs well and the SOC estimation is quite accurate with only 3% of error at $25°$C and less than 10% at $0°$C. This SOC estimation algorithm is then ready for integration with the extra capability of providing an estimated SOC value for other algorithms if necessary.

7.1.3 SOP Estimation Using a Linear Kalman Filter

Normally battery power capability refers to either the max charge power or the max discharge power that will not cause the battery to exceed the maximum or minimum voltages. It can be particularly interesting when integrated with the ROD control algorithm. As shown before, the ROD control algorithm is enforced based on current or power limit. Therefore, the voltage-protected power limits that are estimated using an estimation algorithm for SOP can interact with the power limits posed by the ROD control algorithm. By adopting an estimation algorithm for SOP using a linear Kalman filter with a nonlinear Butler-Volmer (BV) battery model, a standard SOP estimation algorithm is evaluated for the Sony cells.

The SOP algorithm adopted in this research was introduced in [17], where a nonlinear battery BV model was used. The following Fig. 7.12 shows the equivalent circuit of the battery BV model. The associated discrete-time model equation can be found in (4.10).
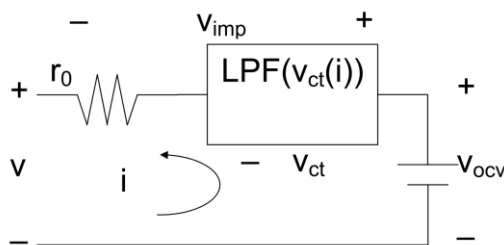
Fig. 7.12: Nonlinear battery BV model [17]

A linear Kalman filter (LKF) is formulated based on the difference form of the model equation. Fig. 7.13 summarizes the LKF structure based on the battery BV model, in which the identified parameters can be used for SOP estimation. As seen in Fig. 7.13, R is the gas constant and can be eventually combined with either E_a or G and the difference form of the model can be expressed as in (4.12).

As introduced in [17], a_1, E_a, B, and G are predetermined via a Gauss-Newton optimization algorithm based on different drive cycle datasets at different temperatures. A similar procedure is used in this research to pre-identify these four values for the Sony cell. A summary regarding the

four predetermined parameters is provided in Table 7.2.

$$v(k) + a_1 v(k-1) = v_{ocv}(1 + a_1) - \frac{1}{A}(i(k) + a_1 i(k-1))\exp\left(\frac{E_a}{RT(k)}\right)$$
$$- b_1 T(k)\sinh^{-1}\left(\frac{i(k)}{2B\exp\left(\frac{-G}{RT(k)}\right)}\right)$$
$$v(k) + a_1 v(k-1) = \theta\varphi(k)$$

$$\varphi(k) = \begin{bmatrix} 1 + a_1 \\ -(i(k) + a_1 i(k-1))\exp\left(\frac{E_a}{RT(k)}\right) \\ -T(k)\sinh^{-1}\left(\frac{i(k)}{2B\exp\left(\frac{-G}{RT(k)}\right)}\right) \end{bmatrix}$$

$$\theta = [v_{ocv}, \frac{1}{A}, b_1]$$

Fig. 7.13: LKF structure based on the battery BV model [17]

Table 7.2: Summary of predetermined BV model parameters

Predetermined Parameter	a_1	E_a	B	G
Value	-0.921	2.135e+3	8.7e-7	3.628e+3

To estimate the power capability, [17] introduced a V_{low} estimator, which represents the predicted low voltage at any sample instant with a certain amount of current for a period of time of interests. (7.3) shows the dynamic estimation equation of V_{low}. With the LKF-estimated parameters $[V_{ocv}, \frac{1}{A}, b_1]$ at each sample instant, V_{low} can be dynamically estimated.

$$v_{low} = v_{ocv} - \frac{1}{A}\exp\left(\frac{E_a}{RT}\right)i_{max} - \frac{b_1 T}{1 + a_1}\sinh^{-1}\left(\frac{i_{max}}{2B\exp\left(\frac{-G}{RT}\right)}\right) \tag{7.3}$$

There are two issues regarding using this LKF for SOP estimation. The first issue involves the determination of the i_{max} in (7.3). In [17], i_{max} was chosen as the maximum discharge current during the drive cycle. This can be a reasonable number given the prior knowledge of the whole drive cycle and the SOP, typically the maximum discharge power can be estimated using (7.4). It also had been suggested in [17] that V_{low} could be compared with V_{min}, the battery operational minimum voltage, to determine whether the battery has the power capability to deliver a current

of i_{max}. This can lead to a potential adjustment of i_{max} as V_{low} is close to V_{min}.

$$P_{disMax} = V_{low} * i_{max} \tag{7.4}$$

The other issue is that the fact that the standard battery power capability characterizations result in an indication of capable maximum (dis)charge power for a certain amount of time until the battery reach either the upper or the lower voltage limits. One standard time period is 10 seconds, referring to maximum 10-second (dis)charge power. However, (7.3) is not predicting the battery voltage exactly after 10 seconds, and neither is (7.4) predicting the 10-second power capability. With a small modification of (7.3), however, the 10-second standard can be complied.

As the third term in (7.3) is essentially a low pass filter, the time constant τ that can be calculated based on a_1 and the data sample frequency T_s following (7.5). Therefore, the voltage response after 10 seconds can be easily estimated by modifying the third term in (7.3). The modified V_{low_10s} can be calculated following (7.6). It should be noted that (7.6) can be easily changed for predicting the power capability with a different time period.

$$\tau = \frac{-T_s}{\log(-a_1)} \tag{7.5}$$

$$V_{low\_10s} = V_{ocv} + i_{max} * A\exp(\frac{E}{T}) + \frac{b_1}{1 + a_1} \operatorname{asinh}(i_{max}*B*\exp(\frac{G}{T}))*(1\text{-}\exp(\frac{-10}{\tau})) \tag{7.6}$$

As V_{low_10s} can be estimated, 10-second discharge power capability can be calculated using (7.7).

$$P_{disMax\_10s} = V_{low\_10s} * i_{max} \tag{7.7}$$

To evaluate this SOP estimation algorithm, the drive cycle evaluated in the previous section for SOC estimation is used again. Both $25°C$ and $0°C$ cases are evaluated.
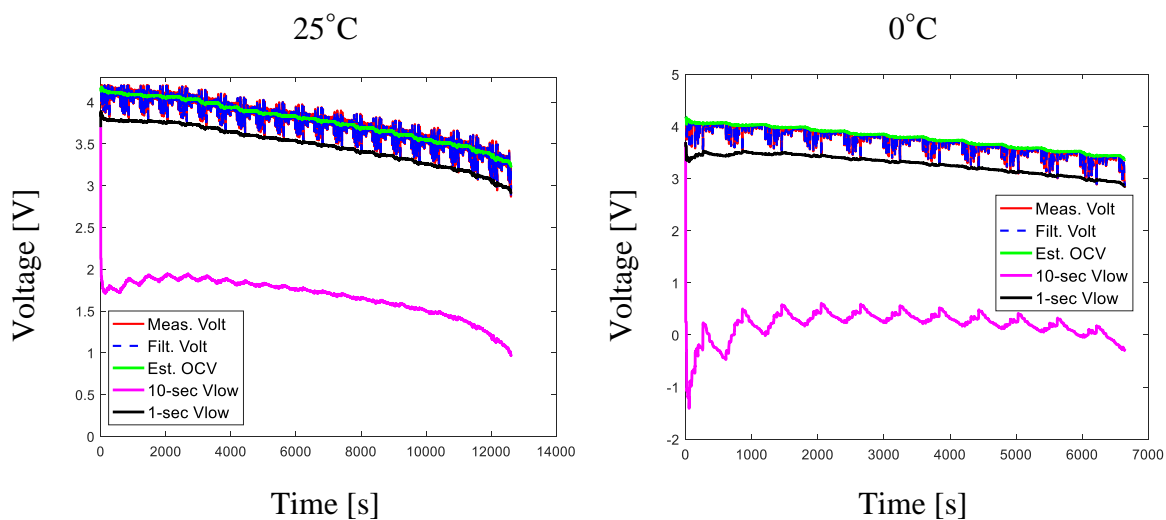
Fig. 7.14: Meas./filt. volt., est. OCV, and Vlow for the evaluated drive cycle at 0°C and 25°C
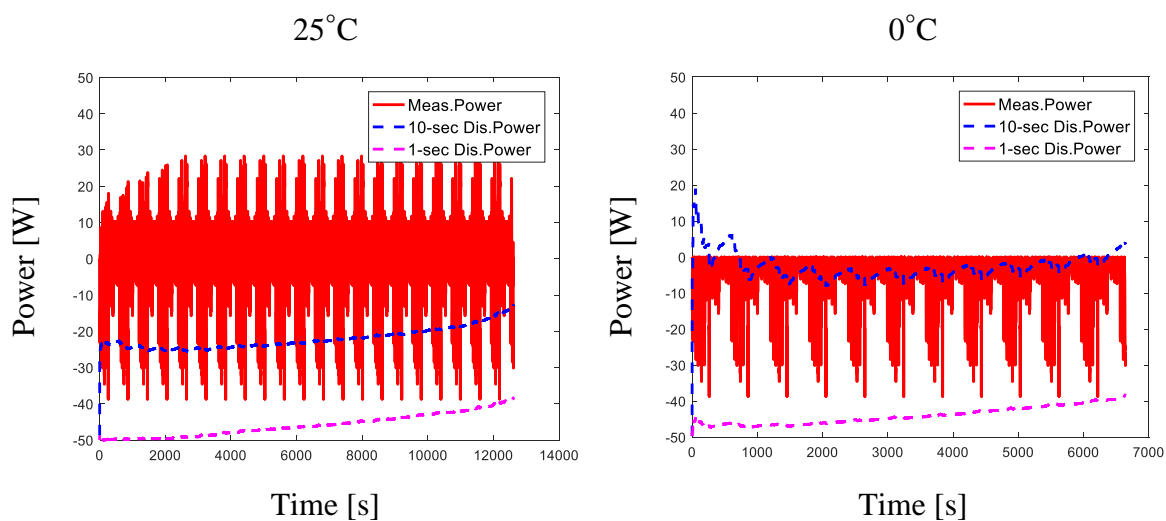
Fig. 7.15: Power capability predictions for the evaluated drive cycle at 0°C and 25°C

Fig. 7.14 plots the measured voltage, estimated voltage with the KF, estimated OCV, 1-sec V_{low}, and 10-sec V_{low} for both temperature cases. For both cases, the OCV and 1-sec V_{low} estimation is quite stable, confirming the effectiveness of the applied LKF. It can be seen that the 10-sec V_{low} for the 0°C case can be extremely low and less than 0V. This is due to the large resistance of batteries at low temperatures and resulting limited power capability especially for the 10-second case. This also causes the 10-second power capability estimation at 0°C shown in Fig.

7.15 to be unstable. This instability can be also attributed to the fact that the i_{max} had been set to a constant value and is actually not a realistic value at low temperature conditions. This drawback can be resolved by combining a different power capability calculation procedure with an iterative algorithm calculating the suitable i_{max} dynamically. Such an approach will be discussed in a later section.
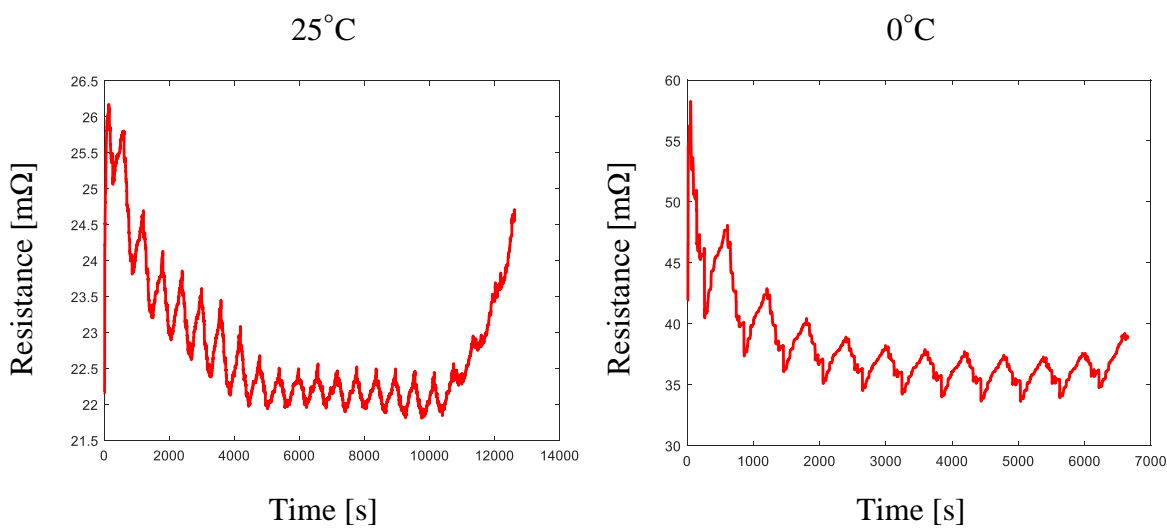
Fig. 7.16: Estimated series resistance for the evaluated drive cycle at 0°C and 25°C
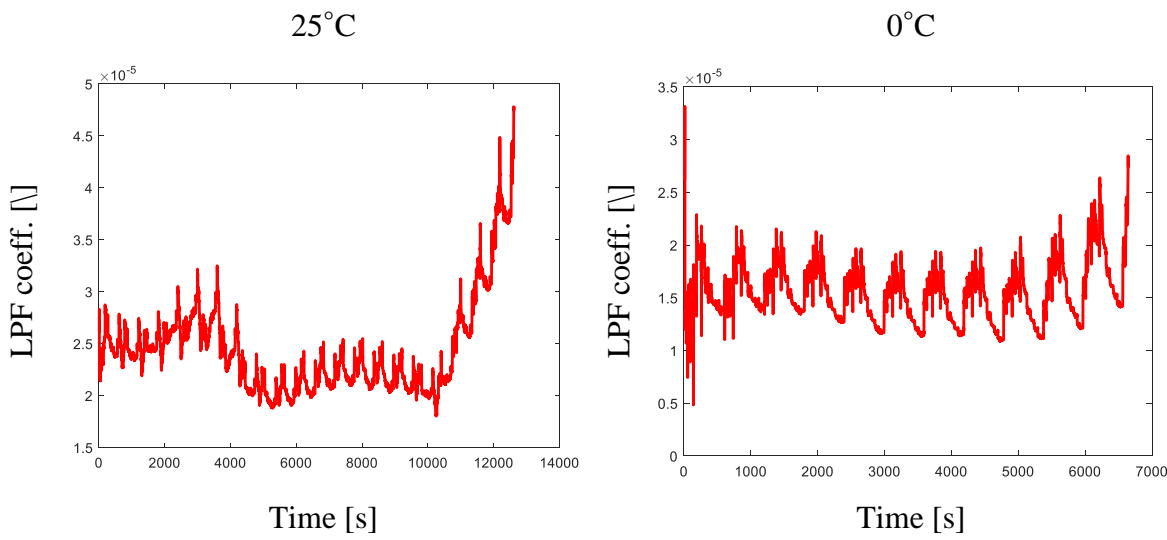
Fig. 7.17: Estimated LPF coeff. for the evaluated drive cycle at 0°C and 25°C

7.1.4   Improved SOP Estimation Combining LKF and Imax Adjustment

In [130], the commonly-used standard discharge power characterization procedure is introduced and (7.8) shows the equation to calculate the maximum discharge pulse for 10 second. As the discharge resistance, R_{dis}, requires previous characterization and can be dependent on current, SOC, temperature, and aging status, it cannot be accurately characterized beforehand and can lead to inaccuracy especially during a dynamic profile like a drive cycle.

$$P_{disMax\_10s} = \frac{V_{min}*(V_{ocv} - V_{min})}{R_{dis}} \tag{7.8}$$

An alternative equation of (7.8) that can be used during a dynamic condition is shown in (7.9), where I_{max_iter} refers to an estimated maximum discharge current that, after being applied for 10 seconds, would result in the battery voltage dropping to V_{min}, i.e., 2.5V. However, based on (7.6), usually the current is the input variable and the voltage is the output variable. It requires an iterative process to estimate the required maximum current that results in a voltage of V_{min}.

$$P_{disMax\_10s} = V_{min}*I_{max\_iter} \tag{7.9}$$

In order to better utilize the proposed SOP estimation algorithm in [17] especially for low temperature conditions, an iterative process is inserted in the LKF process to replace the original V_{low} estimation algorithm to achieve a more stable SOP estimation. In Matlab specifically, a "fzero" function is used to iteratively calculate the I_{max_iter} at every sample instant and estimate the maximum 10-second discharge power. Typically, the iterative calculation is to find the i_{max_iter} that forces "f" in (7.10) to be almost zero. The subsequent SOP estimation is then calculated by (7.9).

$$f = V_{ocv} + i_{max\_iter} * Aexp(\frac{E}{T}) + \frac{b_1}{1 + a_1} asinh(i_{max\_iter}*B*exp(\frac{G}{T}))*(1-exp(\frac{-10}{\tau})) - V_{min} \tag{7.10}$$

The improved SOP algorithm is evaluated for the same validation drive cycle previously for both 25°C and 0°C temperature conditions. The maximum 10-second discharge power for both

temperatures is plotted in Fig. 7.18. For the 25°C case, the improved SOP estimation achieves similar values as that using the previous method shown in Fig. 7.15. For the 0°C, however, the improved algorithm results in a stable SOP estimation and the estimation is reasonable, generally lower than the 25°C SOP values as expected.
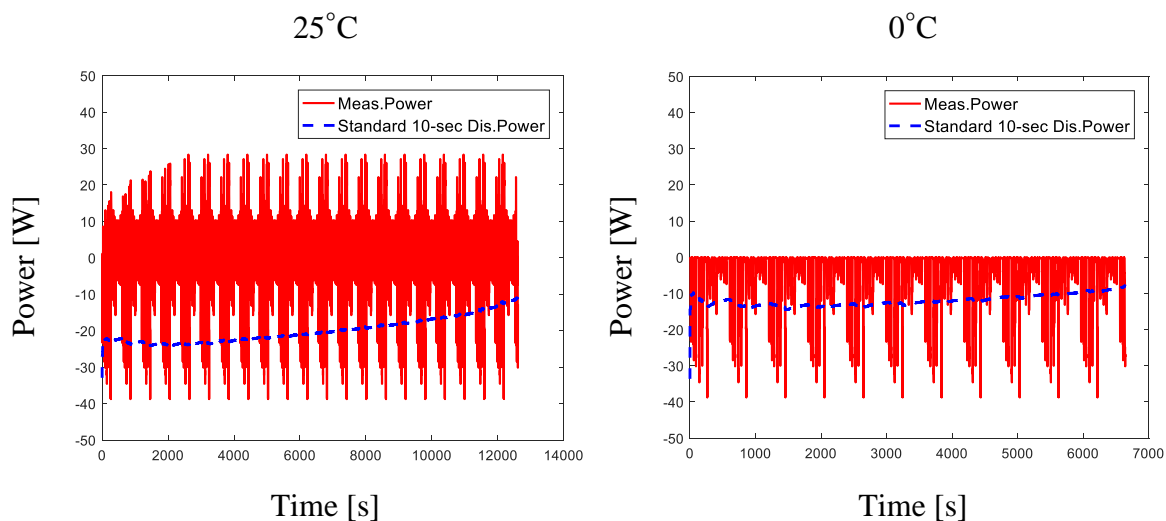
Fig. 7.18: Improve SOP for the evaluated drive cycle at 0°C and 25°C
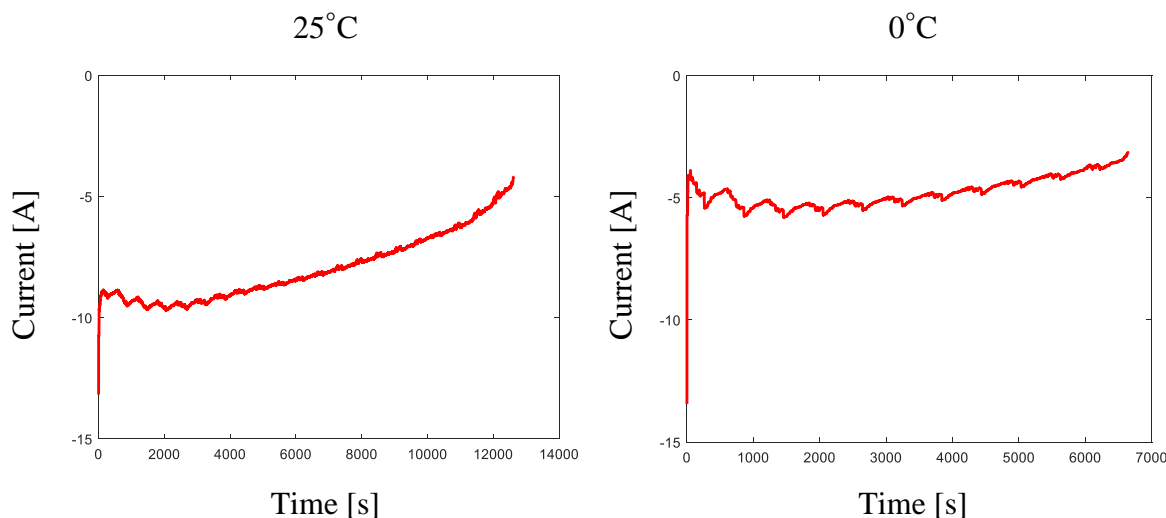
Fig. 7.19: Iterative maximum discharge current for the evaluated drive cycle at 0°C and 25°C

In Fig. 7.19, the maximum discharge current, i_{max_iter}, resulting from the iterative process, is plotted for both temperature cases. The values are now realistic and generally at 0°C, it allows

lower maximum discharge current rates as expected.

The improved SOP estimation algorithm and the previously-introduced SOC estimation algorithm using EKF will then be integrated with the ROD control algorithm. The performance and interactions within such an integrated algorithm will be discussed in the next section.

7.2 Integration of ROD Control and SOC/SOP Estimation

As seen from Chapter 5, the ROD control algorithm proposed mostly enforces current or power limits at the high SOC region and high discharge current conditions. This can be supplemental to the standard SOP algorithms since most SOP algorithms can provide crucial information as the battery reaches to low SOC region and has a low voltage. Moreover, the proposed ROD control algorithm used coulomb counting as the SOC estimation method, while in practical it would be better to have a voltage-based SOC estimation algorithm available to provide battery SOC information. Therefore, in this section, the 2RC battery ECM is used as the pseudo-battery system and an integration of the ROD control with the SOC/SOP algorithms introduced in the previous sections is evaluated with drive cycle simulations.

7.2.1 Integrated Algorithm System Structure

The integrated algorithm system structure is shown in Fig. 7.20 below, where the SOC estimation, SOP estimation, and ROD control algorithm are integrated together.

As shown in Fig. 7.20, the actual battery physical system is replaced by the 2RC battery equivalent circuit model and therefore the evaluation of the integrated algorithm system is done in simulation only, aiming for a proof of concept. Moreover, to avoid additional model error sources, current profiles, instead of power profiles, of the drive cycle is used.

The algorithm sequence at one typical sample instant can be described as the following Table 7.3. At one sample instant, the operation sequence can be divided into six steps, resulting in a selection of the optimal current value that may or may not be modified from the current command

based on the limitations enforces by both the ROD control algorithm and the SOP algorithm.
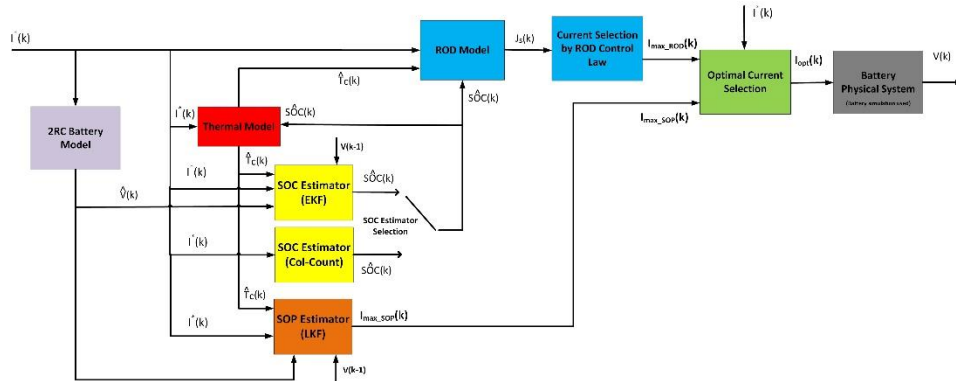
Fig. 7.20: Integrated battery algorithm system structure

Table 7.3: Sample operation sequence of the proposed integrated algorithm system

Step 1	Receive the current command $I^*(k)$ and the 2RC battery model estimates the voltage $\hat{V}(k)$
Step 2	Either the EKF method or the coulomb-counting method estimates $S\hat{O}C(k)$
Step 3	Thermal model estimates the core temperature $\hat{T}_c(k)$ based on $I^*(k)$, $\hat{V}(k)$, and $S\hat{O}C(k)$
Step 4	The LKF SOP method estimates the maximum allowed current $I_{max\_SOP}(k)$
Step 5	The ROD model and ROD control law estimate the maximum ROD-allowed current $I_{max\_ROD}(k)$ based on the ROD-limiting current boundary.
Step 6	$I^*(k)$, $I_{max\_SOP}(k)$, and $I_{max\_ROD}(k)$ are compared and the minimum value is chosen as the optimized current command $I_{opt}(k)$ to feed into the pseudo-battery (2RC model in simulation).

To evaluate the proposed integrated algorithm system, the drive cycle used in the previous sections is adopted. Both 25°C and 0°C cases are evaluated.

7.2.2 Integrated Algorithm System Evaluation

The integrated algorithm system is evaluated at two different temperature conditions. Coulomb-counting method is used for SOC estimation and provide the SOC information to the

other algorithms, while the EKF is also running and provides another independent SOC estimation.

Fig. 7.21 shows the control signal during the evaluation drive cycle. The control signal is enabled whenever the current command "violates" the current limit enforced by either the ROD control or the SOP 10-second requirement. The SOP 10-second requirement refers to the maximum discharge current allowed for 10 seconds before the battery voltage reaches the low voltage limit. For the 25°C case, a total of 324 control events are observed while 601 control events are observed for the 0°C case. This is as expected since current limits enforced by either the ROD control law or the SOP 10-second requirement are stricter at low temperatures.
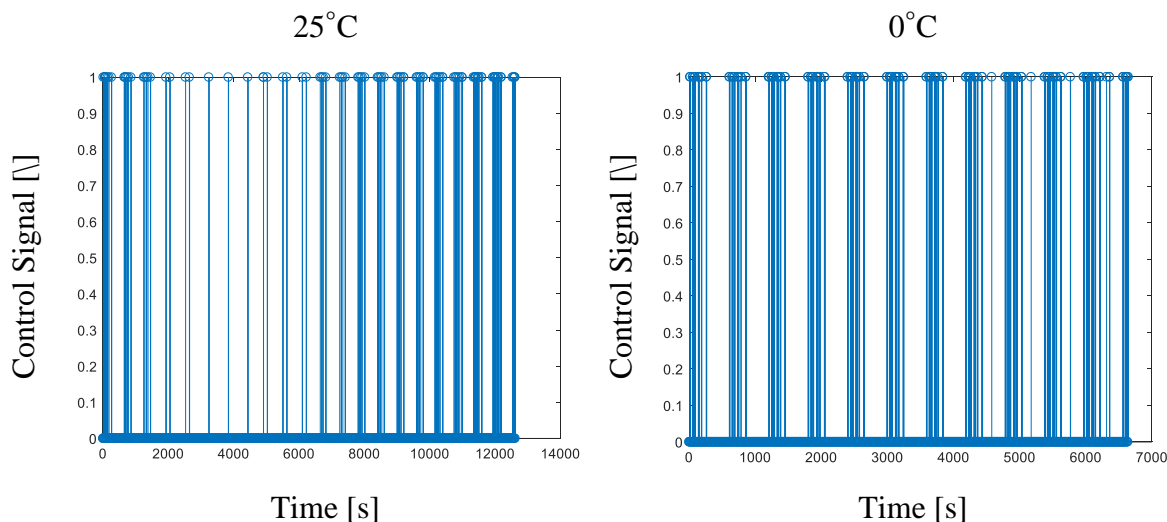
Fig. 7.21: Control signal during the evaluated drive cycle at 0°C and 25°C

Fig. 7.22 shows the original current profile, the modified current profile, the ROD-limit current, the SOP-limit current, and the final current limit considering both current limits. In both temperature cases, the final current limits both exhibit a "V" shape meaning that more control events occur either at the high SOC or at the low SOC. Comparing the final limit to the two current limits, the ROD control is more dominant at high SOC and the SOP algorithm is more dominant at low SOC.
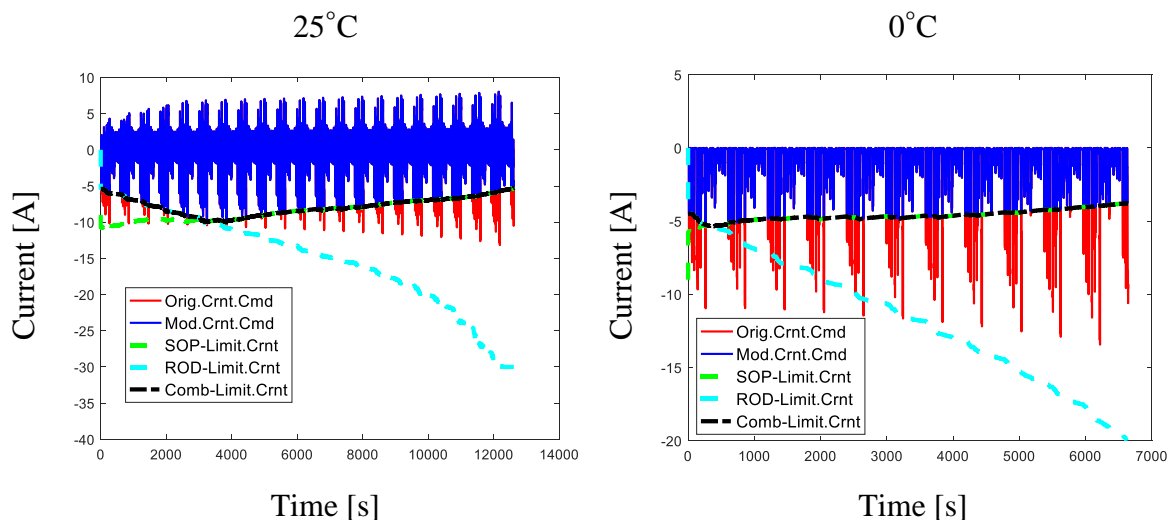
Fig. 7.22: Current modification and limits during the evaluated drive cycle at 0°C and 25°C
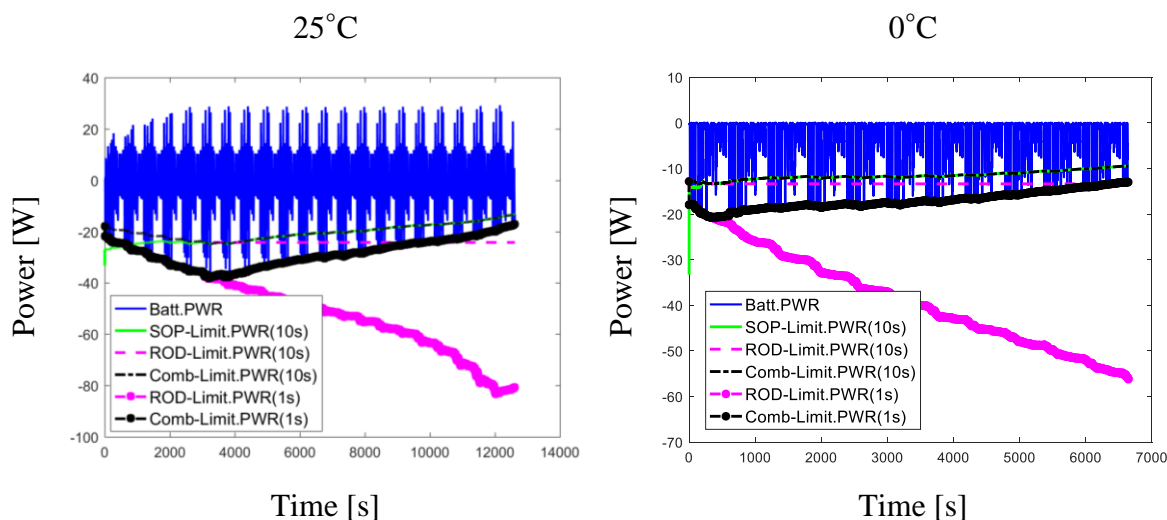
Fig. 7.23: Power modification and limits during the evaluated drive cycle at 0°C and 25°C

Fig. 7.23, instead of current, shows the similar quantities of power during the drive cycle. As expected, similar observations can be made compared to the results for the battery current. One difference is that both 1-second and 10-second power limits are plotted here, and the resulting battery power profile follows the 1-second power limits since the sample frequency is 1Hz. In practical, however, 1-second power limits do not hold much significance since mostly the SOP considers a longer duration of discharge power.

25°C   0°C
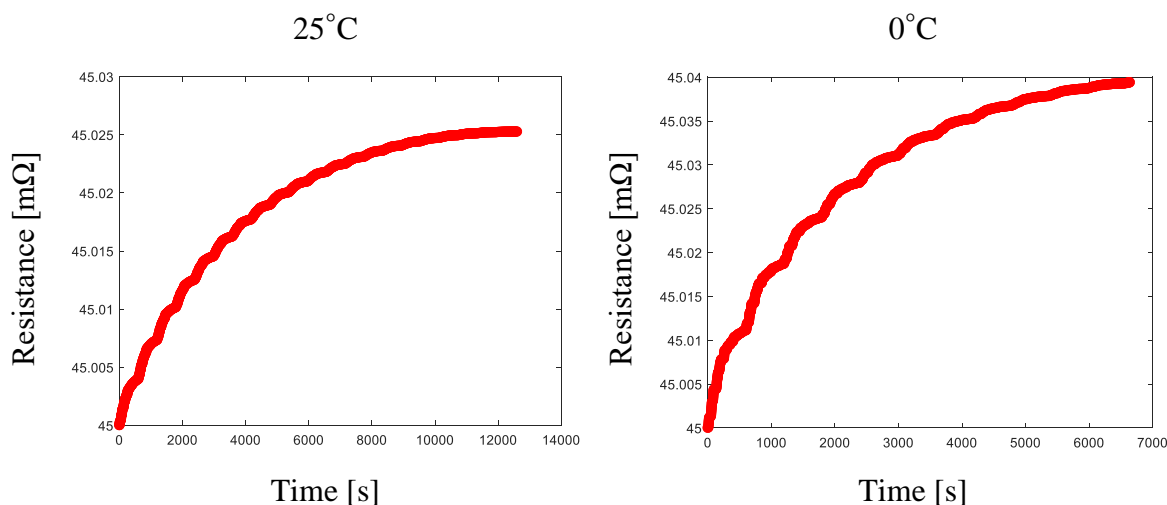
Fig. 7.24: Estimated aging resistance growth for the evaluated drive cycle at 0°C and 25°C

25°C   0°C
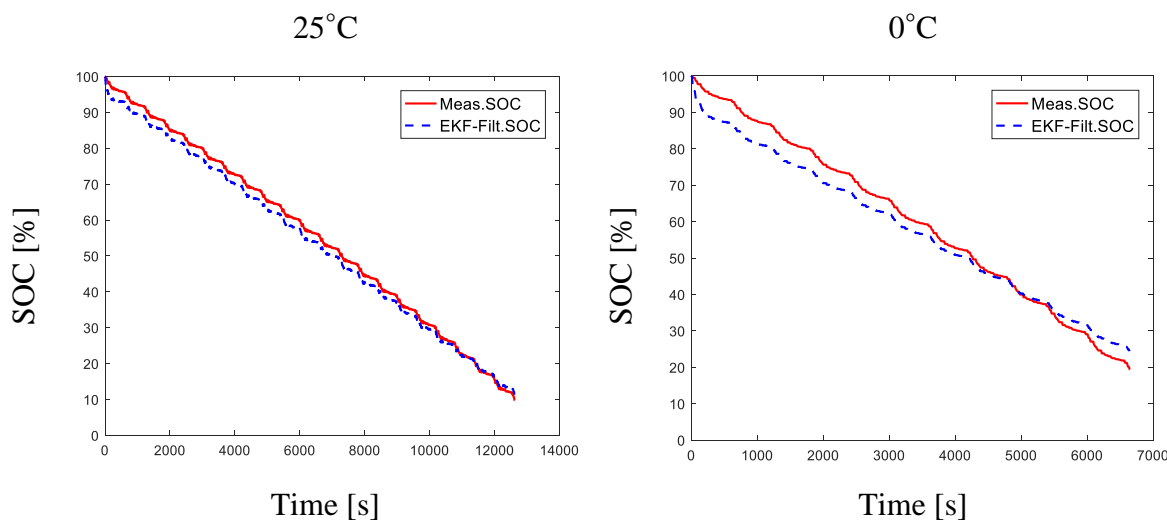
Fig. 7.25: SOC estimation by EKF for the evaluated drive cycle at 0°C and 25°C

In Fig. 7.24, the estimated aging resistance growth during one cycle for both temperature cases are plotted. It can be seen that the resistance grows slightly faster at 0°C, consistent with the results shown in Chapter 5 that low temperature can lead to faster aging.

In Fig. 7.25 and Fig. 7.26, the coulomb counted SOC referred as the "true" SOC is compared to the estimated SOC by the EKF approach and the estimation error is within 5% for 25°C case and within 10% for 0°C case. This result also suggests that if the SOC values estimated

by the EKF were provided to the other algorithms in the system, instead of the "true" SOC, slightly degraded performance would have been achieved for the 25°C, while worse performance would the 0°C case have had.

25°C   0°C
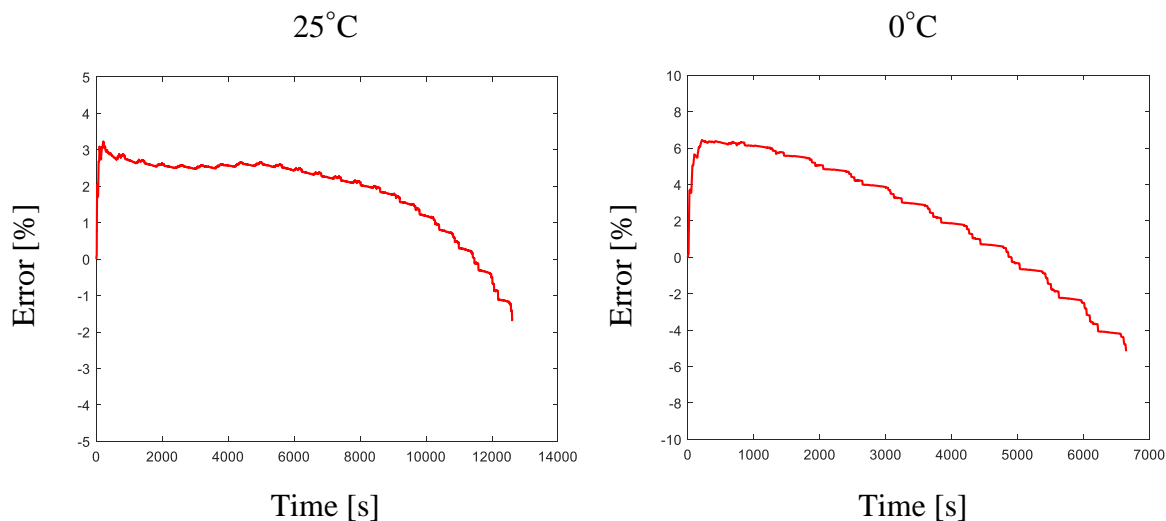
Fig. 7.26: SOC estimation error for the evaluated drive cycle at 0°C and 25°C

7.3   Chapter Summary

In this chapter, the potential of integrating the proposed ROD control algorithm with more conventional state estimation algorithm in the literature has been investigated.

An accurate 2RC equivalent circuit model (ECM) is formulated for the Sony cell to fast conduct investigations about the algorithm integration over a wide range of simulation conditions. An extended Kalman filter (EKF) based on the 2RC battery ECM is formulated for the Sony cell to construct a voltage-based SOC estimator. By selecting correct tuning parameters, the SOC estimator based on a EKF can achieve excellent SOC estimation accuracy with less than 10% errors.

Moreover, an estimation for SOP based on a linear Kalman filter (LKF) from the literature is adopted. It has been shown that such an algorithm for SOP had one drawback that the maximum

discharge current value was predetermined at a constant value and was not dynamically adjusted based on different operating conditions. An improved version of this SOP estimation algorithm has been proposed, adding an iterative maximum discharge current estimation algorithm. The resulting improved SOP algorithm can be more robust for different operating conditions and achieve accurate power capability diagnosis.

Both the SOC estimator and the improved SOP estimator are then integrated with the previously proposed ROD control algorithm, formulating an integrated algorithm system. Different algorithms interact with each other and provide necessary battery state or parameter information among them. Typically, the improved SOP estimator heavily cooperates with the ROD control algorithm and provide the current and power limits over the whole SOC range. Such an integrated system has been evaluated through simulations and has shown effective current and power control, as well as accurate SOC/SOP estimation during drive cycles.

Chapter 8 Conclusions, Contributions, and Recommended Future Work

8.1   Conclusions

The following lists summarize the key conclusions of this research. The conclusions are listed based on significant topics.

8.1.1   Key Conclusions from the State-of-the-Art Review

- Conventional battery equivalent circuit models (ECMs) and physics-based electrochemical models commonly have utilized battery current as the input.

- Testing batteries with drive cycles commonly have used power command profiles, and the resulting measured current has been used to evaluate conventional battery models.

- Lumped thermal models based on the battery thermal equivalent circuit have been formulated to estimate both the battery surface temperature and core temperature.

- Fading capacity and increasing electrical resistance have been used as the two major battery degradation indicators.

- Solid-electrolyte-interphase (SEI) layer growth due to insoluble components formed by side-reactions has been shown to be a major source of lithium-ion battery anode aging.

- The SEI layer thickness has been used as a metric to describe the anode aging and estimate battery aging quantitatively.

- The side-reaction current, proportional to the rate-of-change of SEI layer thickness, has been considered as a metric to evaluate the lithium-ion battery ROD.

- Pack-level active degradation controls such as electrical and thermal loading equalization have been commonly utilized to improve the overall battery pack durability.

- For battery charge and constant low-rate discharge cases, cell-level active degradation controls

by manipulating battery ROD have been investigated.

8.1.2   Power-commanded Battery Electro-thermal Modeling

- Machine learning technique such as neural networks (NN) can be promising candidates to model the battery electrical responses during drive cycles with a power input.

- A recurrent neural network (RNN) with gated recurrent unit (GRU) and deep feature selection (DFS) can model the time-dependent battery system with long time constants.

- A thermal equivalent circuit with proper modeling of the internal heat sources such as the reaction heat and the entropy change can accurately model battery thermal responses.

- The RNN model and a lumped battery thermal model can be cross-coupled to formulate an electro-thermal battery model.

- The developed battery electro-thermal model can accurately model both the electrical and thermal responses during drive cycles over a wide range of temperature conditions.

- The electro-thermal model can be applicable for different batteries and achieve comparable model accuracy as the conventional equivalent circuit models.

8.1.3   Drive Cycle Properties Affecting Battery Rate-of-degradation

- Aging effects of the current RMS, the presence of regeneration, and their interaction effects with temperature can be investigated by a three-way design of experiments.

- An analysis methodology containing ANCOVA, log regression, and Student's t-test can be used to statistically analyze the significance of interested aging factors.

- The analysis suggests that higher RMS current can result in faster aging, while the presence of regeneration in the current profile may not affect aging.

- The analysis suggests that low-temperature can result in faster aging, and the interacting aging effect between the RMS current and temperature appears to be significant.

8.1.4   Reduced-order Lithium-ion Battery ROD Model

- The partial differential equations (PDEs) related to charge transfer and mass transport can significantly complicate the physics-based lithium-ion battery ROD models.

- The exchange current and the side-reaction exchange current density resulting from the PDEs can be both offline estimated using battery experimental data.

- The resulting exchange current estimation can be formulated as a function of the battery current, the battery state-of-charge (SOC), and the battery core temperature.

- The proposed reduced-order ROD model can be PDE free by incorporating the exchange current function and the estimated side-reaction exchange current density.

- The reduced-order ROD model can accurately predict battery resistance growth due to SEI layer growth during dynamic-cycling aging tests.

- Variables such as battery current, voltage, and temperature of the developed reduced-order ROD model can be manipulated input candidates for battery active ROD controls.

8.1.5   Region-based Lithium-ion Battery ROD Control

- Thresholds that monitor and control battery current, voltage, SOC, and temperature, can be enabled to maintain the battery in acceptable safe and durable ranges.

- The reduced-order ROD model characterization suggests that high current, high SOC, and low temperature can result in worse side reaction current (i.e., worse ROD).

- ROD transition curves shown from the characterization can be used as the current/power shielding boundaries to manipulate battery ROD during operations.

- The electro-thermal model, reduced-order ROD model, and region-based current (power) shielding ROD control can be integrated to an active ROD control methodology.

- The proposed sequential ROD control method can be enabled to detect ROD boundary crossing events, limit the allowed battery power, and actively reduce battery ROD.

- Slower resistance growth (degradation) can be observed for batteries cycled with the proposed active ROD control enabled, or lower operating SOC range.

- The reduced-order ROD model can be applied to different batteries but requires separate characterization tests to identify the battery-specific side-reaction exchange current density.

- The proposed ROD control method can be applied to different batteries and achieve degradation reduction for other lithium-ion batteries.

- The proposed ROD control method can be extended to low temperature conditions, showing degradation reduction capability while limiting the battery performance more frequently.

8.1.6   Trade-off Between ROD Control and Performance Compromise

- Different ROD thresholds can be utilized for different temperature conditions to allow practically reasonable current (power) over regions where ROD is most severe.

- Temperature-dependent ROD boundary limits can be formed by an adjustable factor that manipulates current limits at various temperatures and keep a smooth boundary transition.

- Quantitative summaries based on simulations suggest that desirable balance can be achieved by selecting a suitable adjusting factor for different operating conditions.

- More flexibility from the ROD boundary manipulations can be observed for highway driving scenarios, while city drives have limited flexibility at low temperatures.

8.1.7   ROD Control Algorithm Integration with State Estimation

- 2RC equivalent circuit model (ECM) with offline parameter identification can be used to accurately model lithium-ion battery electrical responses during drive cycles.

- A voltage-based SOC estimation algorithm using the extended Kalman filter (EKF) can be effective for lithium-ion battery online SOC estimation.

- An algorithm for SOP using a linear Kalman filter (LKF) and a nonlinear Butler-Volmer (BV) battery model can effectively predict battery power capability in real-time.

- An iterative maximum discharge current estimation algorithm can improve the robustness of the SOP algorithm for power capability prediction at low temperatures.

- The proposed ROD control algorithm can be combined with the SOC/SOP estimation algorithms to formulate an integrated battery algorithm system.

- The ROD control algorithm can interact with the SOC/SOP estimation algorithms, providing consistent power monitoring and managing over a wide operating range.

8.2   Contributions

Contributions of this research are listed in this section. Several major contributions are first listed as follows.

- Developed an integrated lithium-ion battery ROD control methodology

This work developed an integrated battery ROD control system that incorporates the power-commanded electro-thermal model, the reduced-order ROD model, and the region-based battery current (power) shielding ROD control via a sequential method. Such ROD control system can reduce battery aging progression during drive cycles and can be extended to different batteries and various temperature conditions.

- Developed a reduced-order, control-oriented lithium-ion battery ROD model

This work developed a reduced-order lithium-ion battery ROD model that is applicable for different batteries and can estimate battery ROD in real time during drive cycles. The developed model is PDE free and has the capability to be integrated to the real-time active ROD control of lithium-ion batteries.

- Developed an enhanced electro-thermal model for EV drive cycle simulation

This work developed a power-commanded RNN battery electrical model integrated with a lumped battery thermal model. This electro-thermal model can accurately predict both the

electrical responses and the thermal responses of the battery during different power-commanded drive cycles over a wide range of temperature conditions.

• Developed an integrated ROD/SOC/SOP control & monitoring algorithm system

This work developed an integrated algorithm system combining the proposed ROD control with the filter-type lithium-ion battery SOC and SOP estimation algorithm. The associated algorithms interact with each other, extending the power monitoring and managing capabilities to a wide operating range.

• Proposed a ROD limit selection guideline for desirable control-performance balance

This work analyzed the trade-off between the degradation reduction due to active ROD control and battery performance (power) compromises. A temperature-dependent ROD boundary selection procedure based on an adjusting factor is proposed to achieve a desirable trade-off balance for different driving scenarios and temperature conditions.

• Determined the aging impacts from less well-known drive cycle properties

The work investigated the battery aging impacts from unique factors related to drive cycles. The individual aging effects from the current RMS value and the presence of regeneration, as well as the interaction effects between the current RMS value and the temperature, have been identified.

The following part summarizes the other contributions that support the major contributions listed above.

• Developed parameter estimation algorithms for exchange current estimation

This work proposed a set of algorithms that includes nonlinear regression and separation of variables to estimate the exchange current in terms of battery current rate, SOC, and temperature.

• Developed a methodology evaluating both individual and interacting aging effects

This work proposed a comparable three-way design of experiment based on the factorial experimental design approach. The proposed design of experiment efficiently allows explicit identification of the individual aging effects and the interacting aging effects.

- Improve SOP algorithm robustness with iterative maximum current estimation

This work proposed an iterative algorithm that estimates the max allowable discharge current in real-time. Such current values can be used for battery SOP estimation, improving the algorithm robustness over a wide temperature range.

- Developed a temperature-dependent ROD boundary shifting procedure

This work proposed an algorithm that uses an adjusting factor to manipulate the ROD thresholds at different temperatures. The resulting temperature-dependent ROD thresholds can lead to practically reasonable battery current (power) limits at different temperatures.

- Developed a battery modeling approach for power-commanded drive cycles

This work recognized the time dependency and long time constant feature of the batteries and developed a suited modeling approach incorporating the gated recurrent unit (GRU) and the deep feature selection (DFS) structures.

8.3 Recommended Future Work

Based on the work presented in this document, the following is a list of the recommended future work.

- Investigate system level means to reduce required battery performance compromises

The region-based ROD control laws developed in Chapter 5 require compromises from battery performance, and this could be undesirable for EV operators. Methods such as incorporating a hybrid-energy system, or active cell-level thermal management should be investigated for their potential to reduce the performance compromises.

- Investigate real-time battery ROD estimation methods to enhance ROD control

    The proposed ROD control method is limited to open-loop due to the difficulty of measuring battery ROD. There is a need to investigate using data-based state estimation methods to extract battery ROD information. This can facilitate the online tuning of the ROD model parameters, as well as the formulation of a closed-loop control structure.

- Investigate the capability of extending the ROD control method to charge process

    The aging mechanisms during charge can be more complicated compared to discharge, and more sensitive to the temperature. An investigation can be made to enhance the proposed ROD modeling by including other aging mechanism such as lithium plating. The ROD control methodology can be potentially extended to charge case as well.

- Investigate module/pack level ROD control algorithm integration

    The proposed ROD control algorithm is evaluated for single cells. However, as cells are connected together either in series or in parallel, inherent cell difference and thermal unbalance require adjustments from the algorithm. Additional algorithms may be needed to compensate such differences.

- Investigate the aging effect of operating SOC range through statistical experiment

    The proposed reduced-order ROD model suggests the battery SOC has a significant effect on battery aging. A statistical aging experiment can be conducted to investigate the SOC effect on the lithium-ion battery aging more comprehensively.

Bibliography

[1] J.W. Tester, E.M. Drake, M.J. Driscoll, M.W. Golay, W.A. Peters, "Sustainable energy: choosing among options," MIT Press, 2005

[2] H.J. Bergveld, W.S. Kruijt, P.H.L. Notten, "Battery Management Systems, Design by Modelling," Kluwer Academic Publishers, 2002.

[3] B.B. Battery, BP5-12, datasheet, as of 8/30/2009. Website: http://www.bb-battery.com/productpages/BP/BP5-12.pdf

[4] Panasonic, "Lithium Ion Batteries," April 2008, http://industrial.panasonic.com/www-data/pdf/ACI4000/ACI4000PE5.pdf

[5] D. Aurbach, "Review of selected electrode-solution interactions which determine the performance of Li and Li-ion batteries," Journal of Power Sources, vol. 89, pp. 206-218, 2000.

[6] K. Takeno, M. Ichimura, K. Takano, J. Yamaki, "Influence of cycle capacity deterioration and storage capacity deterioration on Li-ion batteries used in mobile phones," Journal of Power Sources, vol. 142, pp. 298-305, 2005.

[7] Panasonic, "Overview of Lithium Ion Batteries," January 2007. Website: www.panasonic.com/industrial/includes/pdf/Panasonic_LiIon_Overview.pdf

[8] J. Dahn, G.M. Ehrlich, "Chapter 26 - Lithium-Ion Batteries," in Linden's Handbook of Batteries, 4th ed., McGraw-Hill, 2011.

[9] A.J. Bard, L.R. Faulkner, "Electrochemical Methods, Fundamentals and Applications", 2nd ed., John Wiley & Sons, Inc., New York, 2001.

[10] John Alfred Valentine Butler– Wikipedia: the Free Encyclopedia, as of 10/12/12. Website: http://en.wikipedia.org/wiki/John_Alfred_Valentine_Butler

[11] Max Volmer– Wikipedia: The Free Encyclopedia, as of 11/20/2017. Website: http://en.wikipedia.org/wiki/Max_Volmer

[12] D. Aurbach, "Review of selected electrode-solution interactions which determine the performance of Li and Li ion batteries," Journal of Power Sources, vol. 89, pp. 206-218, 2000.

[13] D. Aurbach, B. Markovsky, I. Weissman, E. Levi, Y. Ein-Eli, "On the correlation between surface chemistry and performance of graphite negative electrodes for Li ion batteries," Electrochimica Acta, vol 45, pp 67-86, 1999.

[14] M.D. Levi, D. Aurbach, "Simultaneous Measurements and Modeling of the Electrochemical Impedance and the Cyclic Voltammetric Characteristics of Graphite Electrodes Doped with Lithium," The Journal of Physical Chemistry B, vol 101, pp 4630-3640, 1997.

[15] D. Aurbach, M.D. Levi, E. Levi, H. Teller, B. Markovsky, G. Salitra, U. Heider, L. Heider, "Common Electroanalytical Behavior of Li Intercalation Processes into Graphite and Transition Metal Oxides," Journal of the Electrochemical Society, vol 145(9), pp 3024-3034, 1998.

[16] D. Aurbach, B. Markovsky, A. Rodkin, M. Cojocaru, E. Levi, H. Kim, "An analysis of rechargeable lithium-ion batteries after prolonged cycling," Electrochimica Acta, vol 47(12), pp 1899-1911, 2002.

[17] L.W. Juang, "Investigation of the Role of Battery Resistance and Overpotential on Performance Models, Power Capability Prognostics and Aging Behavior," Ph.D Thesis,

2014.

[18] U. Tröltzsch, O. Kanoun, Hans-Rolf Tränkler, "Characterizing aging effects of lithium ion batteries by impedance spectroscopy," Electrochimica Acta, vol 51, pp. 1664-1672, 2006.

[19] J. Li, E. Murphy, J. Winnick, P.A. Kohl, "The effects of pulse charging on cycling characteristics of commercial lithium-ion batteries," Journal of Power Sources, vol 102, pp. 302-309, 2001.

[20] Z. Rao, S. Wang, "A review of power battery thermal energy management," Renewable and Sustainable Energy Reviews, vol. 15, pp. 4554-4571, 2011.

[21] P. Suresh, A.K. Shukla, N. Munichandraiah, "Temperature dependence studies of a.c. impedance of lithium-ion cells," Journal of Applied Electrochemistry, vol 32, pp 267-273, 2002.

[22] M. Doyle, T.F. Fuller, J. Newman, "Modeling of Galvanostatic Chargen and Discharge of the Lithium/Polymer/Insertion Cell," Journal of Electrochemical Society, vol. 140, pp. 1526-1533, 1993.

[23] R. Srinivasan, B.G. Carkhuff, M.H. Butler, A.C. Baisden, "Instantaneous measurement of the internal temperature in lithium-ion rechargeable cells," Electrochimica Acta, vol. 56, pp. 6198-6204, 2011.

[24] C. Forgez, D. V. Do, G. Friedrich, M. Morcrette, C. Delacourt, "Thermal modeling of a cylindrical LiFePO4/graphite lithium-ion battery," Journal of Power Sources, vol. 195, pp. 2961-2968, 2010.

[25] L.H.J. Raijmakers, D. L. Danilov, J.P.M. van Lammeren, M.J.G. Lammers, "Sensorless battery temperature measurements based on electrochemical impedance spectroscopy," Journal of Power Sources, vol. 247, pp. 539-544, 2014.

[26] J. P. Schmidt, S. Arnold, A. Loges, D. Werner, T. Wetzel, E. Ivers-Tiffee, "Measurement of the internal cell temperature via impedance: Evaluation and application of a new method," Journal of Power Sources, vol. 243, pp. 110-117, 2013.

[27] Arrhenius Equation– Wikipedia: the Free Encyclopedia, as of 11/20/2017. Website: https://en.wikipedia.org/wiki/Arrhenius_equation

[28] R. Zhao, R.D. Lorenz, T.M. Jahns, L. Juang, "Separating Key Less Well-Known Properties of Drive Profiles that Affect Lithium-ion Battery Aging by Applying the Statistical Design of Experiments," in 2016 IEEE Energy Conversion Congress and Exposition (ECCE), 2016.

[29] V. Ramadesigan, P.W.C. Northrop, S. De, S. Santhanagopalan, R.D. Braatz, V.R. Subramanian, "Modeling and Simulation of Lithium-Ion Batteries from a Systems Engineering Perspective," Journal of The Electrochemical Society, vol. 159 (3), pp. R31-R45, 2012.

[30] T.M. Bandhauer, S. Garimella, T.F. Fuller, "A Critical Review of Thermal Issues in Lithium-Ion Batteries," Journal of The Electrochemical Society, vol. 58, pp. R1-R25, 2011.

[31] K.A. Murashko, A.V. Mityakov, V.Y. Mityakov, S.Z. Sapozhnikov, J. Jokiniemi, J. Pyrhonen, "Determination of the entropy change profile of a cylindrical lithium-ion battery by heat flux measurements," Journal of Power Sources, vol. 330, pp. 61-69, 2016.

[32] P.W.C. Northrop, M. Pathak, D. Rife, S. De, S. Santhanagopalan, V.R. Subramanian, "Efficient Simulation and Model Reformulation of Two-Dimensional Electrochemical Thermal Behavior of Lithium-Ion Batteries," Journal of The Electrochemical Society, vol. 162, pp. A940-A951, 2015.

[33] L. Cai, R.E. White, "Mathematical modeling of a lithium ion battery with thermal effects in COMSOL Inc. Multiphysics (MP) software," Journal of Power Sources, vol. 196, pp. 5985-5989, 2011.

[34] M. Guo, G. Sikha, R.E. White, "Single-Particle Model for a Lithium-Ion Cell: Thermal Behavior," Journal of The Electrochemical Society, vol. 158, pp. A122-A132, 2011.

[35] P. Amiribavandpour, W. Shen, D. Mu, A. Kapoor, "An improved theoretical electrochemical-thermal modelling of lithium-ion battery packs in electric vehicles," Journal of Power Sources, vol. 284, pp. 328-338, 2015.

[36] Y. Xiao, "Model-Based Virtual Thermal Sensors for Lithium-ion Battery in EV Applications," IEEE Transactions on Industrial Electronics, vol. 62, pp. 3112-3122, 2015.

[37] X. Lin, H.E. Perez, S. Mohan, J.B. Siegel, A.G. Stefanopoulou, Y. Ding, M.P. Castanier, "A lumped-parameter electro-thermal model for cylindrical batteries," Journal of Power Sources, vol. 257, pp. 1-11, 2014.

[38] J. Zhang, J. Lee, "A review on prognostics and health monitoring of Li-ion battery," Journal of Power Sources, vol. 196, pp. 6007-6014, 2011.

[39] T. Torikai, T. Takesure, Y. Toyota, K. Nakano, "Research and Development of the Model-Based Battery State of Charge Indicator," in Proc. of 1992 International Conference on Power Electronics and Motion Control, pp. 996-1001, 1992.

[40] S. Santhanagopalan, R.E. White, "Online Estimate of the State of Charge of a Lithium Ion Cell," Journal of Power Sources, vol. 161, pp. 1346-1355, 2006.

[41] G. Welch, G. Bishop, "An Introduction to the Kalman Filter," University of North Carolina at Chapel Hill, 1995.

[42] G.L. Plett, "Extended Kalman filtering for battery management systems of LiPB-based HEV battery packs Part 3. State and parameter estimation," vol. 134, pp. 277-292, 2004.

[43] S. Schwunk, N. Armbruster, S. Straub, J. Kehl, M. Vetter, "Particle filter for state of charge and state of health estimation for lithium-iron phosphate batteries," Journal of Power Sources, vol. 239, pp. 705-710, 2013.

[44] X. Chen, W. Shen, Z. Cao, A. Kapoor, "A novel approach for state of charge estimation based on adaptive switching gain sliding mode observer in electric vehicles," Journal of Power Sources, vol. 246, pp. 667-678, 2014.

[45] B. Xia, C. Chen, Y. Tian, W. Sun, Z. Xu, W. Zheng, "A novel method for state of charge estimation of lithium-ion batteries using a nonlinear observer," Journal of Power Sources, vol. 270, pp. 359-366, 2014.

[46] S. Dey, B. Ayalew, P. Pisu, "Nonlinear Robust Observers for State-of-Charge Estimation of Lithium-Ion Cells Based on a Reduced Electrochemical Model," IEEE Transactions on Control System Technology, vol. 23, pp. 1935-1942, 2015.

[47] F. Huet, R.P. Nogueira, L. Torcheux, P. Lailler, "Simultaneous real-time measurements of potential and high frequency resistance of a lab cell," Journal of Power Sources, vol. 113, pp. 414-421, 2003.

[48] H. Blanke, O. Bohlen, S. Buller, R.W. De Doncker, B. Fricke, A. Hammouche, D. Linzen, M. Thele, D.U. Sauer, "Impedance measurements of lead-acid batteries for state-of-charge, state-of-health and cranking capability prognosis in electric and hybrid electric vehicles," Journal of Power Sources, vol. 144, pp. 418-425, 2005.

[49] A. Hammouche, E. Karden, R.W. De Doncker, "Monitoring state-of-charge of Ni-MH and

Ni-Cd batteries using impedance spectroscopy," Journal of Power Sources, vol. 127, pp. 105-111, 2004.

[50] M. Hughes, R.T. Barton, S.A.G.R. Karunathilaka, N.A. Hampson, R. Leek, "The Residual Capacity estimation of Fully Sealed 25Ah Lead/Acid Cells," Journal of Power Sources, vol. 17, pp. 305-329, 1986.

[51] T. Hansen and C.-J. Wang, "Support vector based battery state of charge estimator," J. Power Sources, vol. 141, no. 2, pp. 351–358, 2005.

[52] J. A. Anton, P. G. Nieto, F. de Cos Juez, F. S. Lasheras, M. G. Vega, and M. R. Gutierrez, "Battery state-of-charge estimator using the SVM technique," Appl. Math. Model., vol. 37, no. 9, pp. 6244–6253, 2013.

[53] Y. S. Lee, W. Y. Wang, and T. Y. Kuo, "Soft computing for battery stateof-charge (BSOC) estimation in battery string systems," IEEE Trans. Ind. Electron., vol. 55, no. 1, pp. 229–239, Jan. 2008.

[54] W.-Y. Chang, "Estimation of the state of charge for a LFP battery using a hybrid method that combines a RBF neural network, an OLS algorithm and AGA," Int. J. Elect. Power Energy Syst., vol. 53, pp. 603–611, 2013.

[55] I. Sutskever, "Training recurrent neural networks," Ph.D. dissertation, Univ. of Toronto, Toronto, ON, Canada, 2013.

[56] S. Hochreiter and J. Schmidhuber, "Long short-term memory," Neural Comput., vol. 9, no. 8, pp. 1735–1780, 1997.

[57] E. Chemali, P.J. Kollmeyer, M. Preindl, R. Ahmed, A. Emadi, "Long Short-Term Memory Networks for Accurate State-of-Charge Estimation of Li-ion Batteries", IEEE Transaction on Industrial Electronics, 65(8), 2018

[58] A. Eddahech, O. Briat, JM. Vinassa, "Adaptive Voltage Estimation for EV Li-ion Cell Based on Artificial Neural Networks State-of-Charge Meter," IEEE International Symposium on Industrial Electronics, pp. 1318-1324, 2012.

[59] G. Capizzi, F. Bonanno, G.M. Tina, "Recurrent Neural Network-Based Modeling and Simulation of Lead-Acid Batteries Charge-Discharge," IEEE Transactions on Energy Conversion, vol. 26, pp. 435-443, 2011.

[60] C. Sbarufatti, M. Corbetta, M. Giglio, F. Cadini, "Adaptive prognosis of lithium-ion batteries based on the combination of particle filters and radial basis function neural networks," Journal of Power Sources, vol. 344, pp. 128-140, 2017.

[61] S. Yanqing, "Adaptive online state-of-charge determination based on neuro-controller and neural network," Energy Conversion and Management, vol. 51, pp. 1093-1098, 2010.

[62] L. Kang, X. Zhao, J. Ma, "A new neural network model for the state-of-charge estimation in the battery degradation process," Applied Energy, vol. 121, pp. 20-27, 2014.

[63] P.J. van Bree, A. Veltman, W.H.A. Hendrix, P.R.J. van den Bosch, "Prediction of Battery Behavior Subject to High-Rate Partial State of Charge," IEEE Transactions on Vehicular Technology, vol. 58, 2009.

[64] E. Meissner, G. Richter, "Battery monitoring and electrical energy management precondition for future vehicle electric power systems," Journal of Power Sources, vol. 116, pp. 79-98, 2003.

[65] G.L. Plett, "High-performance battery-pack power estimation using a dynamic cell model," IEEE Transactions on Vehicular Technology, vol. 53, pp. 1586-1693, 2004.

[66] A. Farmann, D.U. Sauer, "A comprehensive review of on-board State-of-Available-Power

prediction techniques for lithium-ion batteries in electric vehicles," Journal of Power Sources, vol. 329, pp. 123-137, 2016.

[67] W. Zhang, W. Shi, Z. Ma, "Adaptive unscented Kalman filter based state of energy and power capability estimation approach for lithium-ion battery," Journal of Power Sources, vol. 289, pp. 50-62, 2015.

[68] W. Waag, C. Fleischer, D.U. Sauer, "Adaptive on-line prediction of the available power of lithium-ion batteries," Journal of Power Sources, vol. 242, pp. 548-559, 2013.

[69] L.W. Juang, P.J. Kollmeyer, T.M. Jahns, R.D. Lorenz, "Improved Modeling of Lithium-Based Batteries using Temperature-Dependent Resistance and Overpotential," in Proc. of IEEE Transportation Electrification Conference and Expo (ITEC 2014), 2014.

[70] K. Mamadou, E. Lemaire, A. Delaille, D. Riu, S. E. Hing, Y. Bulter, "Definition of a State-of-Energy Indicator (SoE) for Electrochemical Storage Devices: Application for Energetic Availability Forecasting," Journal of Electrochemical Society, vol. 159, pp. A1298-A1307, 2012.

[71] X. Liu, J. Wu, C. Zhang, Z. Chen, "A method for state of energy estimation of lithium-ion batteries at dynamic currents and temperatures," Journal of Power Sources, vol. 270, pp. 151-157, 2014.

[72] H. He, Y. Zhang, R. Xiong, C. Wang, "A novel Gaussian model based battery state estimation approach: State-of-Energy," Applied Energy, vol. 151, pp. 41-48, 2015.

[73] Y. Wang, C. Zhang, Z. Chen, "A method for joint estimation of state-of-charge and available energy of LiFePO4 batteries," Applied Energy, vol. 135, pp. 81-87, 2014.

[74] J. Vetter, P. Novak, M.R. Wagner, C. Veit, K.C. Moller, J.O. Besenhard, M. Winter, M. Wohlfahrt-Mehrens, C. Vogler, A. Hammouche, "Ageing mechanisms in lithium-ion batteries," Journal of Power Sources, vol. 147, pp. 269-281, 2005.

[75] M. Broussely, W.A. van Schalwijk, B. Scrosati, "Advances in Lithium-Ion Batteries," Academic/Plenum Publishers, New York, pp. 393–432, 2002.

[76] M. Salomon, H. Lin, E.J. Plichta, M. Hendrickson, "Advances in Lithium-Ion Batteries," pp. 309–344, 2002.

[77] D. Aurbach, "Electrode-solution interactions in Li-ion batteries: a short summary and new insights," Journal of Power Sources, vol. 119–121, pp. 497–503, 2003.

[78] M. Winter, K.C. Moeller, J.O. Besenhard, G.A. Nazri, G.Pistoia, "Lithium Batteries Science and Technology," Kluwer Academic, Dordrecht, 2003.

[79] Y. Wang, X. Guo, S. Greenbaum, J. Liu, K. Amine, "Solid Electrolyte Interphase Formation on Lithium-Ion Electrodes: A 7Li Nuclear magnetic Resonance Study," Journal of The Electrochemical Society, vol. 4(6), pp. A68–A70, 2001.

[80] R. S. Rubino, H. Gan, E.S. Takeuchi, "A Study of Capacity Fade in Cylindrical and Prismatic Lithium-Ion Batteries," Journal of The Electrochemical Soceity, vol. 14, pp. A1029–A1033, 2001.

[81] A. Du Pasquier, F. Disma, T. Bowmer, A.S. Gozdz, G. Amatucci, J.M. Tarascon, "Differential Scanning Calorimetry Study of Carbon Anodes in Plastic Li-Ion Batteries," Journal of Electrochemical Society, vol. 145, pp. 472–477, 1998.

[82] R. Spotnitz, J. Franklin, "Abuse behavior of high-power lithium-ion cells," Journal of Power Sources, vol. 113, pp. 81–100, 2003.

[83] G. Li, R. Xue, L. Chen, "The influence of polytetrafluorethylene reduction on the capacity

loss of the carbon anode for lithium ion batteries," Solid State Ionics, vol. 90, pp. 221–225, 1996.

[84] J.W. Braithwaite, A. Gonzales, G. Nagasubramanian, S.J. Lucero, D.E. Peebles, J.A. Ohlhausen, W.R. Cieslak, "Corrosion of Lithium-ion Battery Current Collectors," J. Electrochem. Soc., vol. 146, pp. 448–456, 1999.

[85] M. Wohlfahrt-Mehrens, C. Vogler, J. Garche, "Aging mechanisms of lithium cathode materials," J. Power Sources, 127, 2004, 58–64.

[86] W. Feng, O. J. Kwon, C-Y Wang, "Electrochemical-thermal modeling of automotive Li-ion Batteries and Experimental Validation Using a Three-Electrode Cell," International Journal of Energy Research, vol. 34, pp. 107-115, 2010.

[87] P. Atkins, J. de Paula, "Physical Chemistry, 9th ed," Oxford University Press, 2010.

[88] K. Takeno, M. Ichimura, K. Takano, J. Yamaki, S. Okada, "Quick testing of batteries in lithium-ion battery packs with impedance-measuring technologs," Journal of Power Sources, vol. 128, pp. 67-75, 2004.

[89] E. Prada, D. Di Domenico, Y. Creft, J. Bernardi, V. Sauvant-Moynot, F. Huet, "Physics-based modelling of LiFeP04-graphite Li-ion batteries for Power and Capacity fade predictions: Application to calendar aging of PHEV and EV," 2012 IEEE Vehicle Power and Propulsion Conference, Oct. 9-12, 2012, Seoul, Korea.

[90] M. Ecker , J.B. Gerschler, J. Vogel, S. Käbitz, F. Hust, P. Dechent, D.U. Sauer, "Development of a lifetime prediction model for lithium-ion batteries based on extended accelerated aging test data," Journal of Power Sources, vol. 215, pp. 248–257, 2012

[91] E. Prada, D. Di Domenico, Y. Creft, J. Bernardi, V. Sauvant-Moynot, F. Huet, "A Simplified Electrochemical and Thermal Aging Model of LiFePO4-Graphite Li-ion Batteries: Power and Capacity Fade Simulations," Journal of The Electrochemical Society, vol. 160 (4), pp. A616-A628, 2013

[92] "Battery Test Manual For Plug-In Hybrid Electric Vehicles," Rev. 0, March 2008, U.S. Department of Energy, contract DE-AC07-051D14517.

[93] A. Jossen, "Fundamentals of battery dynamics," Journal of Power Sources, vol 154, pp 530-538, 2006.

[94] P. Singh, R. Vinjamuri, X. Wang, D. Reisner, "Fuzzy logic modeling of EIS measurements on lithium-ion batteries," Electrochimica Acta, vol 51, pp. 1673-1679, 2006.

[95] C.G. Hochgraf, J.K. Basco, T.P. Bohn, I. Bloom, "Effect of Ultracapacitor-Modified PHEV Protocol on Performance Degradation in Lithium-Ion Cells," Journal of Power Sources, vol. 246, pp. 965-969, 2014.

[96] E. V. Thomas, I. Bloom, J.P. Christophersen, V.S. Battaglia, "Statistical methodology for predicting the life of lithium-ion cells via accelerated degradation testing," Journal of Power Sources, vol. 184, pp. 312-317, 2008.

[97] M. Safari, M. Morcrette, A. Teyssot, C. Delacourt, "Multimodal Physics-Based Aging Model for Life Prediction of Li-Ion Batteries," Journal of The Electrochemical Society, vol. 156(3), pp. A145-A153, 2009.

[98] R. Darling, J. Newman, "Modeling Side Reactions in Composite LiyMn2O4 Electrodes," Journal of The Electrochemical Society, vol. 145(3), pp. 990-998, 1998.

[99] H. Ploehn, P. Ramadass, R. White, "Solvent Diffusion Model for Aging of Lithium-Ion Battery Cells," Journal of The Electrochemical Society, vol. 151(3), pp. A456-A462, 2004.

[100] P. Ramasamy, J. Lee, B. Popov, "Simulation of capacity loss in carbon electrode for lithium-ion cells during storage," Journal of Power Sources, vol. 166, pp. 266-272, 2007.

[101] P. Ramadass, B. Haran, P. Gomadam, R. White, B. Popov, "Development of First Principles Capacity Fade Model for Li-Ion Cells," Journal of The Electrochemical Society, vol. 151(2), pp. A196-A203, 2004.

[102] Z. Chen, C. C. Mi, Y. Fu, J. Xu, X. Gong, "Online battery state of health estimation based on Genetic Algorithm for electric and hybrid vehicle applications," Journal of Power Sources, vol. 240, pp. 184-192, 2013.

[103] Z. Guo, X. Qiu, G. Hou, B. Y. Liaw, C. Zhang, "State of health estimation for lithium ion batteries based on charging curves," Journal of Power Sources, vol. 249, pp. 457-462, 2014.

[104] A. Farmann, W. Waag, A. Marongiu, D.U. Sauer, "Critical review of on-board capacity estimation techniques for lithium-ion batteries in electric and hybrid electric vehicles," Journal of Power Sources, vol. 281, pp. 114-130, 2015.

[105] G.L. Plett, "Recursive approximate weighted total least squares estimation of battery cell total capacity," Journal of Power Sources, vol. 196, pp. 2319-2331, 2011.

[106] J. Remmlinger, M. Buchholz, M. Meiler, P. Bernreuter, K. Dietmayer, "State-of-health monitoring of lithium-ion batteries in electric vehicles by on-board internal resistance estimation," Journal of Power Sources, vol. 196, pp. 5357-5363, 2011.

[107] D. Andre, A. Nuhic, T. Soczka-Guth, D.U. Sauer, "Comparative study of a structured neural network and an extended Kalman filter for state of health determination of lithium-ion batteries in hybrid electric vehicles," Engineering Applications of Artificial Intelligence, vol. 26, pp. 951-961, 2013.

[108] S. Zhang, "A review on electrolyte additives for lithium-ion batteries," Journal of Power Sources, vol. 162, pp. 1379-1394, 2006.

[109] L. Lu, X, Han, J. Li, J. Hua, M. Ouyang, "A review on the key issues for lithium-ion battery management in electric vehicles," Journal of Power Sources, vol. 226, pp. 272-288, 2013.

[110] J. Cao, N. Schofield, A. Emadi, "Battery Balancing methods: A Comprehensive Review," IEEE Vehicle Power and Propulsion Conference, Sept. 3-5, 2008, Harbin, China.

[111] S. Santhanagopalan, Q. Guo, P. Ramadass, R. White, "Review of models for predicting the cycling performance of lithium ion batteries," Journal of Power Sources, vol. 156, pp. 620-628, 2006.

[112] S.K. Rahimian, S.C. Rayman, R.E. White, "Maximizing the Life of a Lithium-Ion Cell by Optimization of Charging Rates," Journal of The Electrochemical Society, vol. 157, pp. A1302-A1308, 2010.

[113] R.D. Perkins, A.V. Randall, X. Zhang, G.L. Plett, "Controls oriented reduced order modeling of lithium deposition on overcharge," Journal of Power Sources, vol. 209, pp. 318-325, 2012.

[114] A.V. Randall, R.D. Perkins, X. Zhang, G.L. Plett, "Controls oriented reduced order modeling of solid-electrolyte interphase layer growth," Journal of Power Sources, vol. 209, pp. 282-288, 2012.

[115] S.J. Moura, J.C. Forman, S. Bashash, J.L. Stein, H.K. Fathy, "Optimal Control of Film Growth in Lithium-Ion Battery Packs via Relay Switches," IEEE Trans. on Industrial Electronics, vol. 58, pp. 3555-3566, 2011.

[116] S. Yuan, H. Wu, X. Ma, C. Yin, "Optimal Charging Strategy Development Based on Solid Electrolyte Interface (SEI) Film Growth Model and Dynamic Programming," EVS28

International Electric Vehicle Symposium and Exhibition, Korea, pp. 1-12, 2015

[117] L.L. Lam, R.B. Darling, "Determining the optimal discharge strategy for a lithium-ion battery using a physics-based model," Journal of Power Sources, vol. 276, pp. 195-202, 2015.

[118] "Recurrent neural network tutorial, Part 3-Backpropagation through time and vanishing gradients":http://www.wildml.com/2015/10/recurrent-neural-networks-tutorial-part-3-backpropagation-through-time-and-vanishing-gradients/, 2015.

[119] R. Pascanu, T. Mikolov, Y. Bengio, "On the difficulty of training recurrent neural networks", ICML, 2013.

[120] "Recurrent neural network tutorial, Part 4 – Implementing a GRU/LSTM RNN with Python and Theano", http://www.wildml.com/2015/10/recurrent-neural-network-tutorial-part-4-implementing-a-grulstm-rnn-with-python-and-theano/, 2015.

[121] Y. Li, CY. Chen, W.W. Wasserman, Deep Feature Selection: Theory and Application to Identify Enhancers and Promoters. In: Przytycka T. (eds) Research in Computational Molecular Biology. RECOMB 2015. Lecture Notes in Computer Science, vol 9029. Springer, Cham.

[122] P.J. Kollmeyer, "Development and implementation of a battery-electric light-duty class 2a truck including hybrid energy storage," Ph.D. dissertation, Univ. Wisconsin-Madison, Madison, WI, USA, 2015.

[123] P.J. Kollmeyer, W. Lamb, L.W. Juang, J.D. McFarland, T.M. Jahns, B. Sarlioglu, "Design of an electric powertrain for a ford f150 crew cab truck utilizing a lithium battery pack and an interior pm synchronous machine drive," in Proc. IEEE Transp. Electrific. Conf. Expo., 2012, pp. 1-8.

[124] P.J. Kollmeyer, A. Hackl, A. Emadi, "Li-ion battery model performance for automotive drive cycles with current pulse and EIS parameterization," in Proc. IEEE Transp. Electrific. Conf. Expo., 2018.

[125] C.F.J. Wu, M.S. Hamada, "Experiments: Planning, Analysis, Optimization," 2nd ed., John Wiley & Sons Inc., Hoboken, NJ, 2009.

[126] M.C. Smart, B.V. Ratnakumar, S. Surampudi, "Electrolytes for Low-Temperature Lithium Batteries Based on Ternary Mixtures of Aliphastic Carbonates," Journal of The Electrochemical Society, vol. 146(2), pp. 486-492, 1999.

[127] M.C. Smart, B.V. Ratnakumar, S. Surampudi, Y. Wang, X. Zhang, S.G. Greenbaum, A. Hightower, C.C. Ahn, B. Fultz, "Irreversible Capacities of Graphite in Low-Temperature Electrolytes for Lithium-ion Batteries," Journal of The Electrochemical Society, vol. 146(11), pp. 3963-3969, 1999.

[128] L. Guzzella, C.H. Onder, "Introduction to Modeling and Control of Internal Combustion Engine System," 2nd ed., Springer-Verlag Berlin Heidelberg, Germany, 2010.

[129] C. Campestrini, T. Heil, S. Kosch, A. Jossen, "A Comparative study and review of different Kalman filters by applying an enhanced validation method," Journal of Energy Storage, vol. 8, pp. 142-159, 2016.

[130] "U.S Department of Energy Vehicle Technologies Program: Battery Test Manual For Electic Vehicles", Idaho National Laboratory, Rev. 3, 2015

Appendix

Battery Test Equipment:

Most of the experiment results in this thesis are obtained in the Johnson Controls Advanced Systems Test Lab located in the High-bay lab on the first floor of the Wisconsin Energy Institute (WEI) building. An overview of the battery test lab is shown in Fig. A.1, including three battery cyclers, three thermal chambers, and a workstation.

Fig. A.1: Johnson Controls Advanced Systems Test Lab

Safety systems are also equipped with the test system including hexane/hydrogen gas sensing and CO_2 fire suppression. Fig. A.2 shows the schematic of the whole test system including the safety equipment.
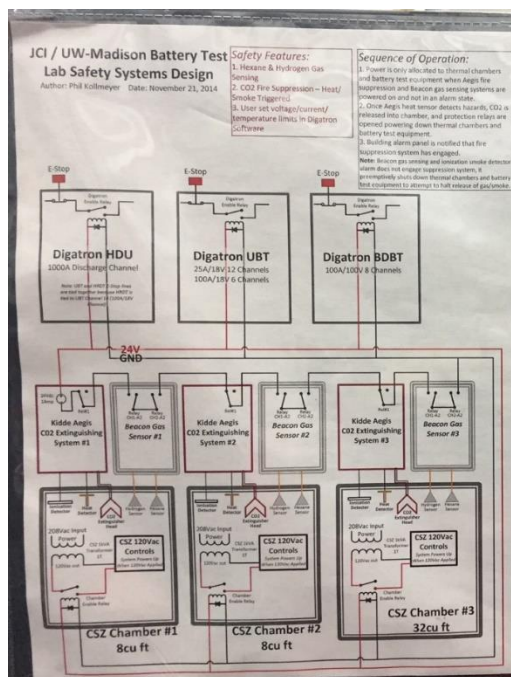
Fig. A.2: JCI/UW-Madison battery test lab safety systems design

Three Digatron battery testing power units are available for testing batteries or other energy storage devices with different ratings. The three power units are shown in Fig. A.3, and the specifications are listed in Table A.1. Besides the voltage sensors equipped with each channel, there are extra 96 voltage sensing channels and 48 temperature sensing channels available.

Table A.1: Channel specs for the Digatron testing units

	Current / Voltage Limits	# of Channels
Low Rating Circuits	25A / 18V	12
Medium Rating Circuits	100A / 18V	6
High Rating Circuits	100A / 100V	8
Ultra-high Rating Circuits	1000A	1

Fig. A.3: Digatron testing power units

There are two medium-size thermal chambers and one large-size thermal chamber available for placing the batteries of different sizes, shown in Fig. A.4. All three CSZ thermal chambers are fully monitored and can be controlled either through the on-surface screen or through the software installed in the computer on the workstation.

Fig. A.4: Fully-monitored thermal chambers from CSZ

There are also 12 channels of EIS-meters which perform electrochemical impedance spectroscopy. Fig. A.5 shows a picture of the EIS-meter and its specs are listed below.

Fig. A.5: Digatron EIS-meter

Table A.2: Digatron EIS-meters specs

Resistance range	$0.3 - 3000$ mΩ
Output current AC	2 A (max. peak)
Resolution AC current	< 100 µA
Frequency range AC current	10 mHz – 6.5 kHz
Accuracy frequency	0.005 % from displayed value
Voltage range measurement	0 V – 20 V
Input impedance (typical)	10 GΩ
Resolution voltage channel	5 µV
Meas. accuracy abs{Z}	< 1 %
Meas. accuracy arg(Z)	< 1 °
Power consumption	65 W per channel / EIS card (typical)
Power supply	115 V / 60 Hz, 2.3 A for 4 EIS cards
Casing (W x D x H)	500 x 500 x 150 mm
Weight	4,43 kg + 2.47 kg per channel
Environment temperature	0 °C – 40 °C

Battery Graphite Anode Characteristics

The OCV-SOC curve of the graphite anode is shown in Fig. A.6, and the associated equations are shown in (A.1).
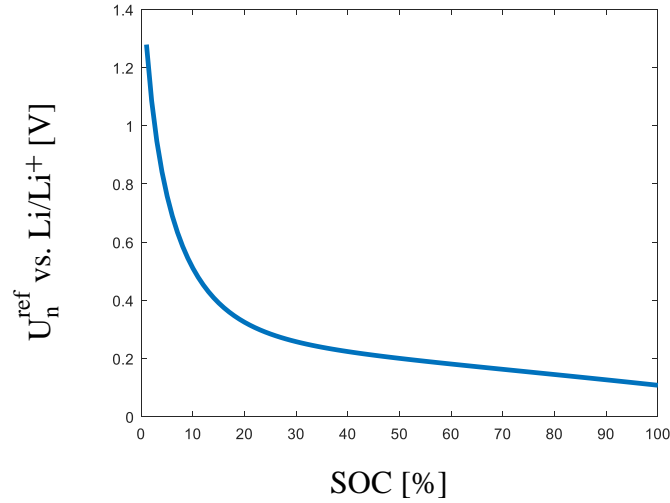
Fig. A.6: Graphite anode OCV vs. SOC

$\theta_{min} = 0.03$

$\theta_{max} = 0.886$

$\theta = \theta_{min} + SOC * (\theta_{max} - \theta_{min})$

$U_n^{ref} = 0.7222 + 0.1387*\theta + 0.029*\theta^{0.5} + \dfrac{0.0172}{\theta}$

$+ \dfrac{0.0019}{\theta^{1.5}} + 0.2808*\exp(0.9 - 15*\theta) - 0.7984*\exp(0.4465*\theta - 0.4108)$

(A.1)